Assessment of *ex-situ* degradation of perfluorosulfonic acid membranes in water electrolysis

J van den Heever


orcid.org/0000-0002-2082-3739

Dissertation accepted in fulfilment of the requirements for the degree *Master of Science* in Engineering Sciences with Chemical Engineering at the North-West University

Supervisor: Prof DG Bessarabov

Co-supervisor: Dr SP du Preez

Graduation: July 2026

DECLARATION

I, **Jason van den Heever**, declare that the dissertation entitled: **Assessment of *ex-situ* degradation of perfluorosulfonic acid membranes in water electrolysis** which I herewith submit to the North-West University (NWU) in fulfilment of the requirements set for the **Master of Science in Engineering Sciences with Chemical Engineering** degree, that my work is my own, unless specifically indicated otherwise, has been text edited as required, and has not been submitted to any other tertiary institution other than the NWU.

Signature of candidate:_____ University Number: **31703607**

Signed at **Potchefstroom** on **4 March 2026**

DEDICATION

2 Timothy 1:7

For God gave us not a spirit of fearfulness but of power, love, and discipline.

PREFACE

The transition to a sustainable, decarbonised energy economy is a major global challenge. Within this shifting landscape, hydrogen gas has emerged not merely as an alternative fuel but as a critical energy vector capable of coupling renewable resources with hard-to-abate industrial sectors. Proton Exchange Membrane Water Electrolysis (PEMWE) technology holds immense promise for large-scale green hydrogen production, but its widespread deployment is currently constrained by cost and durability challenges.

This dissertation, titled "Assessment of *ex-situ* degradation of perfluorosulfonic acid membranes in water electrolysis," was motivated by an interest in understanding the fundamental limits of the materials relied upon, such as Perfluorosulfonic Acid (PFSA) membranes.

While the scientific literature contains numerous studies on the chemical degradation of PFSA membranes, a distinct gap was observed in PEMWE between fundamental *ex-situ* chemical stability tests and the practical, electrochemical reality of an operating electrolyser.

This study addresses the disconnect between *ex-situ* chemical stability assessments and *in-situ* electrochemical performance by systematically linking the two. Industry-standard Nafion® membranes were subjected to controlled Fenton-based Accelerated Stress Tests (ASTs), followed by fabrication into Catalyst Coated Membranes (CCMs) for single cell PEMWE evaluation. This approach enables direct comparison between chemically induced structural selective degradation and subsequent electrochemical behaviour. Particular focus is placed on identifying backbone and side-chain scission pathways and evaluating how these molecular-level alterations translate into measurable changes in ohmic resistance, charge-transfer behaviour, and overall cell performance.

This research was conducted at North-West University (NWU), utilising the facilities of the Hydrogen South Africa (HySA) Infrastructure Centre of Competence. It represents a synthesis of chemical engineering principles, polymer science, chemistry, and electrochemistry. It is believed that the findings and correlations attempted in this work, specifically regarding the impact of ferrous ion (Fe^{2+}) contaminants and the chemo-mechanical nature of membrane failure, will contribute meaningfully to the fundamental understanding of the degradation process in PEM water electrolysers, the development of more durable electrolyser components, and refining accelerated test protocols.

Jason van den Heever

Potchefstroom, 2026

ACKNOWLEDGEMENTS

It is an honour to thank the following persons and entities for their vital role in the completion of this dissertation:

- My mentors, **Professor Dmitri Bessarabov** and **Doctor Stephanus Petrus du Preez,** for the two years of exceptional guidance, expertise, supervision, and assistance in this study.
- **Hydrogen South Africa (HySA) Infrastructure Centre of Competence**, for making laboratories and equipment available.
- **Chemical Resource Beneficiation (CRB)**, for making laboratories available.
- Laboratory staff at **North-West University (NWU)** and the **University of Tokyo**, for performing SEM and Raman analyses on samples.
- The **University of Tokyo** and the **Catalysis for Energy Conversion (CatEC)** research group for hosting me, and the **Japan International Cooperation Agency (JICA)** for the arrangement thereof.
- The **NWU**, **HySA Infrastructure,** and the **Science and Technology Research Partnership for Sustainable Development (SATREPS)** program, hosted by **Japan Science and Technology Agency (JST),** for approving this study.
- **Doctor Artem Pushkarev** for the training and assistance in using RelaxIS3 software.
- My fellow **postgraduate students**, **colleagues**, **friends**, and **family** for the motivation, love, and friendship, and specifically **Maryna Mari Pelser** for the love, support, friendship, and food provided during late nights, and finally **Ms Deliana Kruger** for motivating me.

NOTES TO THE READER

To facilitate navigation within the electronic version of this dissertation, internal cross-references have been hyperlinked. Underlined numbers denote these links and can be accessed by pressing Ctrl + Left Click. To return to the original text after following a link, press Alt + Left Arrow.

This dissertation is structured as follows: Chapter 1 introduces the research background, problem statement, and primary objectives of this study; Chapter 2 establishes the theoretical framework of radical-induced degradation; Chapter 3 details the experimental methodology and AST protocols; Chapter 4 presents the core physicochemical and electrochemical results; and Chapter 5 evaluates the project's success against its initial objectives.

For the reader's convenience, each chapter concludes with its own dedicated bibliography rather than a cumulative list at the end of the document. All citations and references are formatted in accordance with the American Chemical Society (ACS) style guide, with the use of EndNote 20.

Throughout Chapter 4, degraded membrane samples are referenced using the following shorthand convention: [Fe^{2+} Concentration (ppm)] - [Degradation Duration (h)]. For *in-situ* testing, a third variable is added: - [Cell Temperature (°C)]. For example, a sample labelled '30-72-40' refers to a membrane that was degraded in 30 ppm Fe^{2+} for 72 hours and then tested at 40 °C.

Although this dissertation is written in British English, the IUPAC nomenclature system will be used; for example, ‘Sulphur’ (British) vs ‘Sulfur’ (IUPAC).

ABSTRACT

The escalating energy demands and environmental concerns associated with fossil fuel consumption have resulted in various national policies and technical targets for green hydrogen production as a viable energy carrier and green chemical feedstock. Proton Exchange Membrane Water Electrolysis (PEMWE) is a promising technology for hydrogen production due to its high efficiency and compact design. However, the operational lifetime of PEMWE systems is hindered by the degradation of components, including PFSA membranes, under oxidising, acidic operating conditions.

This study investigates the chemical degradation of PFSA membranes via an *ex-situ* AST using Fenton's reagent. Nafion® 115 and 117 membranes were subjected to varying ferrous (Fe^{2+}) concentrations and exposure durations to simulate degradation caused by metallic impurities and radical species. Changes in key membrane properties, including Ion Exchange Capacity (IEC), Fluoride Release Rate (FRR), and surface morphology, were analysed. The *in-situ* performance of degraded membranes in PEMWE cells was also evaluated, focusing on polarisation behaviour, charge-transfer resistance, and ohmic resistance.

Multi-modal characterisation revealed a dose-dependent degradation mechanism characterised by concurrent side-chain and main-chain scission, evidenced by a Fluoride-to-Sulfur ratio of ~18.6:1, at 30ppm Fe^{2+}, and the simultaneous loss of backbone (728 cm^{-1}) and side-chain (1060 cm^{-1}) Raman signals. Profilometry identified a chemo-mechanical synergy, in which mechanical defects from cutting methods served as initiation sites for radical attack. *In-situ* testing of degraded membranes confirmed that these chemical and structural defects manifest as nonlinear increases in ohmic resistance and potential failure.

The findings provide insights into the degradation mechanisms and establish correlations between *ex-situ* chemical degradation markers and the *in-situ* electrochemical performance of PEMWE cells.

Keywords: Proton exchange membrane (PEM), water electrolysis (WE), Perfluorosulfonic acid (PFSA), Accelerated stress testing (AST), Fenton test, Ion exchange capacity (IEC), Fluoride release rate (FRR), Sulfur emission rate (SER)

OPSOMMING

Die toenemende energienavraag en omgewingsbekommernisse wat met fossielbrandstofverbruik gepaardgaan, het gelei tot verskeie nasionale beleide en tegniese teikens vir groen waterstofproduksie as 'n lewensvatbare energiedraer en groen chemiese voerstof. Protonuitruilmembraan-waterelektrolise (PUMWE) is 'n belowende tegnologie vir waterstofproduksie weens die hoë doeltreffendheid en kompakte ontwerp daarvan. Die bedryfsleeftyd van PUMWE-stelsels word egter beperk deur die degradasie van perfluoorsulfoonsuur (PFSS)-membrane onder strawwe bedryfstoestande.

Hierdie studie ondersoek die chemiese degradasie van PFSS-membrane deur middel van 'n *ex-situ* versnelde spanningstoets (VST) met behulp van Fenton se reagens. Nafion® 115- en 117-membrane is aan wisselende yster(II)-ione (Fe^{2+}) konsentrasies en blootstellingstye onderwerp om degradasie wat deur metaalonsuiwerhede en radikaalspesies veroorsaak word, te simuleer. Veranderinge in membraan-eienskappe, insluitend ioonuitruilkapasiteit (IUK), fluoriedvrystellingstempo (FVT) en oppervlakmorfologie, is ontleed. Die *in-situ* werkverrigting van gedegradeerde membrane in PUMWE-selle is ook geëvalueer, met die fokus op polarisasiegedrag, ladingsoordragweerstand en ohmiese weerstand.

Multimodale karakterisering het 'n dosis-afhanklike degradasiemeganisme aan die lig gebring wat gekenmerk word deur gelyktydige syketting- en hoofkettingsplitsing, soos blyk uit 'n fluoried-tot-swael-verhouding van ~18.6:1 en die gelyktydige verlies van rugraat- (728 cm^{-1}) en syketting- (1060 cm^{-1}) Raman-seine. Van kardinale belang is dat profilometrie 'n chemo-meganiese sinergie geïdentifiseer het, waar meganiese defekte as gevolg van sny-metodes as inisiëringsterreine vir radikaalaanvalle gedien het. *In-situ* toetsing van gedegradeerde membrane het bevestig dat hierdie chemiese en strukturele defekte manifesteer as nie-lineêre toenames in ohmiese weerstand en potensiële faling.

Die bevindinge bied insig in die degradasiemeganismes en vestig korrelasies tussen *ex-situ* chemiese degradasiemerkers en die *in-situ* elektrochemiese werkverrigting van PUMWE-selle.

Sleutelterme: Protonuitruilmembraan (PUM), Waterelektrolise (WE), Perfluoorsulfoonsuur (PFSS), versnelde spanningstoets (VST), Fenton-toets, Ioonuitruilkapasiteit (IUK), Fluoriedvrystellingstempo (FVT), Swaelvrystellingstempo (SVT)

LIST OF ABBREVIATIONS AND ACRONYMS

ACS	American Chemical Society
AEMWE	Anion Exchange Membrane Water Electrolysis
ASR	Area Specific Resistance
AST	Accelerated Stress Test
ATR	Attenuated Total Reflectance
AWE	Alkaline Water Electrolysis
BPP	Bipolar Plate
CatEC	Catalysis for Energy Conversion
CCM	Catalyst Coated Membrane
CP-MAS NMR	Cross-Polarisation Magic Angle Spinning Nuclear Magnetic Resonance
CRB	Chemical Resource Beneficiation
DI	Deionised
EC	European Commission
ECM	Equivalent Circuit Model
ECSA	Electrochemically Active Surface Area
EDX	Energy Dispersive X-ray
EPR	Electron Paramagnetic Resonance
EW	Equivalent Weight
FRR	Fluoride Release Rate
FT-IR	Fourier Transform Infrared Spectroscopy
GC	Gas Chromatograph
GC-MS	Gas Chromatography-Mass Spectroscopy
GDL	Gas Diffusion Layer
HDPE	High-Density Polyethylene
HE	Hydrogen Embrittlement
HER	Hydrogen Evolution Reaction

HFR	High-Frequency Resistance
HySA	Hydrogen South Africa
HTSE	High-Temperature Steam Electrolysis
ICR	Interfacial Contact Resistance
IEC	Ion Exchange Capacity
JICA	Japan International Cooperation Agency
JST	Japan Science and Technology Agency
LDPE	Low-Density Polyethylene
MEA	Membrane Electrode Assembly
MEMS	Micro-Electromechanical Systems
MS	Mass Spectrometer
NHE	Normal Hydrogen Electrode
NMR	Nuclear Magnetic Resonance
NWU	North-West University
OCV	Open Circuit Voltage
OER	Oxygen Evolution Reaction
PE	Polyethylene
PEMFC	Proton Exchange Membrane Fuel Cell
PEMWE	Proton Exchange Membrane Water Electrolysis
PFSA	Perfluorosulfonic Acid
PGM	Platinum Group Metals
PP	Polypropylene
PTFE	Polytetrafluoroethylene
PTL	Porous Transport Layer
PVC	Polyvinyl Chloride
RSC	Royal Society of Chemistry
SATREPS	Science and Technology Research Partnership for Sustainable Development

SECM	Scanning Electrochemical Microscopy
SEM	Scanning Electron Microscopy
SER	Sulfur Emission Rate
SOE	Solid-Oxide Electrolysis
SOEC	Solid-Oxide Water Electrolysis Cell
SMR	Steam Methane Reforming
SPE	Solid Polymer Electrolyte
TPB	Triple Phase Boundary
VHTR	Very-High-Temperature Reactor
X-ray CT	X-ray Computed Tomography

LIST OF CHEMICAL ELEMENTS AND SYMBOLS

Ar	Argon
Ca^{2+}	Calcium (II)
C	Carbon
CO_2	Carbon Dioxide
CF_{bb}	Carbon-Fluoride Backbone
CF_{sc}	Carbon-Fluoride Sidechain
CO	Carbon Monoxide
Co^{2+}	Cobalt (II)
Cu^{2+}	Cupric Copper
$\bullet CF_2\text{-}R$	Difluoroalkyl radical
CF_2	Difluorocarbene
$R\text{-}OCF_2$	Difluoromethoxy
e^-	Electron
C-O-C	Ether Linkage
Fe^{3+}	Ferric Iron
Fe^{2+}	Ferrous Iron
$FeSO_4.xH_2O$	Ferrous Sulfate
F^-	Fluoride
HCl	Hydrochloric Acid
HF	Hydrofluoric Acid
H_2	Hydrogen (Diatomic)
H_2O_2	Hydrogen Peroxide
•H	Hydrogen Radical
H_2S	Hydrogen Sulfide
H_3O^+	Hydronium Ion
•OOH	Hydroperoxyl Radical
OH^-	Hydroxide

•OH	Hydroxyl Radical
Ir	Iridium
$Ir(OH)_3$	Iridium Hydroxide
Ir_2O_3	Iridium (III) Oxide
IrO_2	Iridium (IV) Oxide
$FeCl_2.4H_2O$	Iron (II) Chloride Tetrahydrate
Pb	Lead
Pb^{2+}	Lead (II)
CH_4	Methane
Ni^{2+}	Nickel (II)
O_2	Oxygen (Diatomic)
$-OCF_2$	Perfluoroalkyl Ether
PO_4^{3-}	Phosphate
KOH	Potassium Hydroxide
Pt	Platinum
Pt^{2+}	Platinum (II)
H^+	Proton
Ru	Ruthenium
Na^+	Sodium (I)
NaCl	Sodium Chloride
NaOH	Sodium Hydroxide
SO_4^{2-}	Sulfate
S^{2-}	Sulfide
SO_3^-	Sulfonate
$-SO_3H$	Sulfonic Acid
O_2^-	Superoxide
Ti	Titanium
TiO_x	Titanium Oxide

CF_3	Trifluoromethyl
H_2O	Water

LIST OF NOMENCLATURE

Activation energy	E_a	$kJ.mol^{-1}$
Capacitance	C	F
Characteristic Frequency	f_x	Hz
Charge Transfer Resistance	R_{ct}	$m\Omega.cm^2$
Chemical Shift	δ	ppm
Current Density	j	$A.cm^{-2}$
Duration	t	h min sec
Equivalent Weight	EW	$g.eq^{-1}$
Fluoride Release Rate	FRR	$\mu mol.cm^{-2}.h^{-1}$
Hydration Number	λ	
Ion Exchange Capacity	IEC	$meq.g^{-1}$
Molarity	M	$mol.dm^{-3}$
Ohmic Resistance	R_Ω	$m\Omega.cm^2$
Parts Per Billion	ppb	$\mu g.L^{-1}$
Parts Per Million	ppm	$mg.L^{-1}$
Pre-exponential Factor	A	$L.mol^{-1}.s^{-1}$
Rate Constant	k	$L.mol^{-1}.s^{-1}$
Relaxation Time	τ_x	s
Revolutions Per Minute	rpm	$rev.min^{-1}$
Sulfur Emission Rate	SER	$\mu mol.cm^{-2}.h^{-1}$
Temperature	T	°C / K
Voltage	V	Volts
Volume Percentage	v/v%	%
Weight Percentage	wt%	%
Water Uptake	WU	%

TABLE OF CONTENTS

DECLARATION ..... **I**

DEDICATION ..... **II**

PREFACE ..... **III**

ACKNOWLEDGEMENTS ..... **IV**

NOTES TO THE READER ..... **V**

ABSTRACT ..... **VI**

OPSOMMING ..... **VII**

CHAPTER 1: BACKGROUND, MOTIVATION, AND OBJECTIVES **1**

1.1 Project Background **1**

1.2 Problem Statement **2**

1.3 Aims and Objectives **3**

CHAPTER 2: LITERATURE SURVEY **7**

2.1 Hydrogen Production **7**

2.1.1 Biological or Bio-hydrogen 9

2.1.2 Steam Methane Reforming 9

2.1.3 Hydrocarbon Gasification 10

2.1.4 Nuclear Energy 11

2.2 Water Electrolysis Technologies **12**

2.2.1 Alkaline Water Electrolysis (AWE) 13

2.2.2 Proton Exchange Membrane Water Electrolysis (PEMWE) 14

2.2.3 Solid-Oxide Water Electrolysis (SOE) 14

2.2.4 Anion Exchange Water Electrolysis (AEMWE) 15

2.2.5 Comparison of Existing Water Electrolysis Technologies..... 15

2.3 Proton Exchange Membrane Water Electrolysis (PEMWE) Components..... 17

2.3.1 Catalyst Coated Membrane (CCM)..... 18

2.3.2 Membrane Electrode Assembly (MEA)..... 19

2.3.3 Porous Transport Layer (PTL)..... 19

2.3.4 Bipolar Plates (BPPs)..... 20

2.4 Proton Exchange Membrane Water Electrolysis (PEMWE) Degradation Modes 20

2.4.1 Degradations Within the Catalyst Layer..... 21

2.4.1.1 Catalyst Dissolution..... 21

2.4.1.2 Particle Agglomeration and Migration in the Catalyst Layer..... 23

2.4.2 Hydrogen Embrittlement (HE)..... 23

2.4.3 Titanium Passivation..... 23

2.4.4 Porous Transport Layer (PTL)..... 24

2.4.4.1 Chemical Degradation..... 24

2.4.4.2 Mechanical Degradation..... 25

2.4.5 Proton Exchange Membrane (PEM)..... 26

2.4.5.1 Thermal Degradation..... 26

2.4.5.2 Mechanical Degradation..... 26

2.4.5.3 Chemical Degradation..... 27

2.5 PEMWE Accelerated Stress Testing (AST)..... 30

2.5.1 Accelerated Stress Tests (ASTs) for Proton Exchange Membrane Water Electrolysis (PEMWE) Cell Components..... 30

2.5.2 Accelerated Stress Tests (ASTs) for Single Cell 32

2.5.3 Accelerated Stress Tests (AST) for Electrolysis Stacks 34

2.6 Fenton-Based *Ex-situ* Degradation 34

2.6.1 Generation and Kinetics of •OH, •OOH and H_2O_2 35

2.6.2 Summary 39

CHAPTER 3: METHODOLOGY 56

3.1 Materials 56

3.1.1 Membranes 56

3.1.2 Chemicals 56

3.2 Membrane Pre-treatment 57

3.2.1 Membrane Preparation 57

3.2.2 Protonation 58

3.2.3 Cutting 58

3.2.4 Storage 58

3.3 Fenton degradation 58

3.3.1 Degradation Procedure 59

3.3.2 Post-Degradation Treatment 60

3.4 Membrane Characterisation 60

3.4.1 Ion Exchange Capacity (IEC) Measurement 60

3.4.2 Water Uptake Measurement 61

3.4.3 Fourier Transform Infrared Spectroscopy (FT-IR) Analysis 61

3.4.4 Raman Spectroscopy 62

3.4.5 CP-MAS NMR Spectroscopy Measurement 62

3.4.6 Profilometry 63

3.4.7 Effluent Analysis 63

3.5 PEMWE Single Cell *In-situ* Testing 64

3.5.1 Catalyst Coated Membrane (CCM) Fabrication 64

3.5.2 Porous Transport Layer (PTL) Preparation and Flow Fields 65

3.5.3 Single Cell Assembly 66

3.6 Electrochemical Conditioning and Testing Protocol: 67

3.6.1 Gas-Crossover Testing 69

3.6.2 Electrochemical Impedance Spectroscopy (EIS) 69

CHAPTER 4: RESULTS AND DISCUSSION 75

4.1 Virgin Membrane Characterisation 75

***4.2 Ex-Situ* Degradation: Impact on Physicochemical Properties 79**

4.2.1 Ion Exchange Capacity (IEC) Loss 79

4.2.2 Effluent Analysis: Fluoride Release Rate (FRR) and Sulfur Emission Rate (SER) 81

4.2.3 Spectroscopic Results 85

4.2.3.1 Raman Spectroscopy Results 85

4.2.3.2 ATR FT-IR spectroscopy Results 87

4.2.3.3 CP-MAS NMR Analysis 88

4.2.4 Morphological Analyses 90

4.2.5 Summary 98

4.3 *In-Situ* Electrochemical Performance 100

4.3.1 Baseline Characterisation 100

4.3.1.1 Polarisation Behaviour of Non-Degraded CCMs 100

4.3.1.2 Electrochemical Impedance Spectroscopy (EIS) Analysis of Non-Degraded CCMs .. 101

4.3.1.3 Hydrogen Crossover 104

4.3.2 Degraded CCM Characterisation 105

4.3.2.1 CCM Break-In Procedure 105

4.3.2.2 Polarisation Behaviour 108

4.3.2.3 Electrochemical Impedance Spectroscopy (EIS) Analysis of Degraded Catalyst Coated Membranes (CCMs) 112

4.3.2.4 Hydrogen Crossover 115

4.4 Correlating *Ex-Situ* Degradation with *In-Situ* Performance 119

4.4.1 Fluoride Release Rate (FRR) and Voltage Degradation 120

4.4.2 Correlation of *Ex-Situ* Degradation with Electrochemical Impedance Spectroscopy (EIS) 121

4.4.2.1 Ion Exchange Capacity (IEC) Loss and Ohmic Resistance (R_{Ω}) 121

4.4.2.2 Sulfur Emission and Ohmic Resistance (R_{Ω}) 122

4.4.2.3 Sulfur Emission and Charge Transfer Resistance R_{ct} 123

CHAPTER 5: PROJECT EVALUATION AND FUTURE PROSPECTS 135

5.1 Project evaluation 135

5.2 Limitations Of The Study 137

5.2.1 The *Ex-Situ* Versus *In-Operando* Gap 137

5.2.2 Aggressiveness and Mechanism of the AST 138

5.2.3 Scope of Materials and *In-Situ* Testing 138

5.3 Recommendations for Future Research 138

5.3.1 Development of an In-Operando Contamination AST 139

5.3.2 Investigation of Contaminant Synergies 139

5.3.3 Mapping Degradation Mechanisms at Realistic Contaminant Concentrations 139

5.3.4 Evaluation of Modern Reinforced Membranes 139

5.3.5 Study of Chemical Mitigation Strategies 139

5.3.6 Advanced *In-Situ* Diagnostics 140

CHAPTER 6: ANNEXURE 141

6.1 Annexure A: *Ex-situ* analysis 141

6.1.1 IEC Loss 141

6.1.2 Fluoride Release Rate (FRR) 142

6.1.3 Raman 143

6.2 Annexure B: Programmed Break-In Script and I*n-Situ* Analysis 144

6.2.1 Automated Break-In Script 144

6.2.2 Virgin CCM Polarisation Data 145

6.2.3 Degraded CCM Polarisation Data 146

6.2.4 Degraded CCM Electrochemical Impedance (EIS) Data 148

6.2.5 Post-Mortem Imaging 150

6.3 Annexure C: Membrane Physical Parameters and Experimental Conditions 151

6.4 Annexure D: Recent Development in Hydrocarbon-Based PEMs 154

LIST OF TABLES

Table 1: Comparison of H_2 production technologies via water electrolysis. 16

Table 2: Summary of cell components AST for PEMWE 32

Table 3: Summary of single cell AST for PEMWE 34

Table 4: Summary of kinetic data of simultaneous reactions present during radical-induced PFSA degradation. 36

Table 5: Chemicals, suppliers, concentration, purity, and % contaminants of chemicals used. 57

Table 6: Summative table of CCM fabrication, cell assembly and pre-conditioning parameters 69

Table 7: Virgin Nafion® samples including IEC, EW, Water uptake (%) and Hydration number (λ). Based on 60 analyses, with averages and deviations shown. 75

Table 8: Table of identification for characteristic chemical shift present in PFSA structure in NMR, FT-IR and Raman spectroscopy. 79

Table 9: Comparative table of previous degradation studies on Nafion® membranes 85

Table 10: Nomenclature for membranes exposed to different experimental conditions 100

Table 11: Processed EIS data from non-degraded CCM at 0.1 and 0.5 A.cm^{-2} at 40, 60 and 75 °C 102

Table 12: EIS results with absolute error for Nafion® 115 CCMs tested in PEMWE single cell at j=0.5 A.cm^{-2} 113

Table 13: EIS results with absolute error for Nafion® 115 CCMs tested in PEMWE single cell at j=0.1 A.cm^{-2} 114

Table 14: Compiled results of Nafion® 115 samples used in CCM fabrication. 120

Table 15: IEC loss at varying Fe^{2+} concentration and duration for small-scale 4 cm^2 samples. 141

Table 16: IEC loss at varying Fe^{2+} concentration and duration for large-scale 336.44 cm^2 samples. 141

Table 17: Table of automation breaking-in script with comments 144

Table 18: Baseline parameters for virgin non-degraded PEMWE cells. 145

Table 19: Table of Polarisation results at 40, 60 and 75 °C for large-scale membranes 146

Table 20: Average potential difference in mV vs reference data at each datapoint with standard deviations shown. 147

Table 21: Potential difference in mV at 1.85V vs reference data with standard deviations 147

Table 22: EIS data for degraded CCMs at j=0.1 $A.cm^{-2}$ 148

Table 23: EIS data for degraded CCMs at j=0.5 $A.cm^{-2}$ 149

Table 24: Parameters for large-scale Nafion® 115 virgin membranes and their corresponding experimental conditions 151

Table 25: Parameters for small-scale Nafion® 117 virgin membranes and their corresponding experimental conditions 152

Table 26: A comparison of physicochemical properties of fluorinated and hydrocarbon-based PEMs 154

LIST OF FIGURES

Figure 1: a) Schematic representation of a proton exchange membrane water electrolyser, and b) the monomeric molecular structure of Nafion® 1

Figure 2: The colour-coding system of H_2 production methods. 8

Figure 3: Schematic representation of water electrolysis by different technologies. a) alkaline, b) PEM, c) solid oxide and d) AEM water electrolysis..... 13

Figure 4: Schematic representation of the main PEM electrolysis cell components 17

Figure 5: Bipolar plate with a) flow field facing upwards and b) back of bipolar plate..... 20

Figure 6: Degradation effects, conditions, and mechanisms of PFSA membranes, ... 21

Figure 7: Pourbaix diagram for the iridium-water system at 25 °C and its dependence on pH and potential. 22

Figure 8: An in-house profilometric imaging of an oxidised (top) and fresh (bottom) bipolar plate/flow field, zoomed in sections indicated in red, magnifying the water inlet regions. Single pins from each are further magnified to illustrate the formation of suspected TiO_x..... 24

Figure 9: a) Summary of the radical attack mechanism of the Nafion® structure b) Main chain unzipping mechanism. BB represents the backbone of the PFSA membrane. 27

Figure 10: a) Side chain degradation mechanism. b) Mechanism of ether cleavage with subsequent fragmentation and side-chain unzipping. BB represents the backbone of the PFSA ionomer 29

Figure 11: Sidechain degradation of PFSA via Fenton solution 37

Figure 12: a) Hydrogen peroxide reaction sequence in the presence of 1ppm Fe and PFSA. b) Dominant reactions of *ex-situ* Fenton test at 1M H_2O_2 and 1ppm Fe. 39

Figure 13: Membrane size and experimental setup for a) small-scale degradations, with the dotted line on the membrane representing the region that was cut and b) experimental setup for large-scale degradations. 59

Figure 14: Perkin Elmer Spectrum 3 FT-IR/NIR Spectrometer..... 62

Figure 15: ARPChem Raman spectrophotometer used for Raman spectral acquisition. 62

Figure 16: KLA Zeta-20 optical profilometer used for topographical analysis. 63

Figure 17 Dionex ICS-3000 used for IC (from left to right in the image: computer, autosampler carousel, Dionex ICS-3000, Dionex EGC 500 KOH eluent generator). 63

Figure 18: SonoTek Exacta coat used for CCM fabrication..... 64

Figure 19: a) Post-degradation (5 ppm Fe^{2+} 24h), uncoated Nafion® 115 membrane, and b) a fabricated CCM prepared using the degraded membrane shown in a)..... 65

Figure 20: Image of sintered passivated PTL utilised in this study, placed on the flow field (right) and bipolar plate with the flow field visible (left). 66

Figure 21: Assembled PEMWE cell 67

Figure 22: Greenlight Innovations® PEMWE/FC testing station 68

Figure 23: Equivalent circuit diagram used for EIS processing of PEMWE cells with use of two Constant Phase Elements (CPE)..... 70

Figure 24: ATR FT-IR transmittance spectrum of as-received Nafion® 117 in the spectral range of 1800-550 cm^{-1}..... 76

Figure 25: Raman spectrum of as-received Nafion® 117 77

Figure 26: Virgin a) ^{1}H Liquid NMR spectrum and b)^{19}F liquid NMR spectrum of a virgin Nafion® 117 membrane..... 78

Figure 27: Virgin ^{13}C CP-MAS NMR spectrum 78

Figure 28: a) IEC loss of small-scale Nafion® 117 as a) function of exposure duration, and b) percentage IEC loss per hour as a function of Fe^{2+} concentration. IEC loss of large-scale Nafion® 115 as c) function of exposure duration, and d) percentage IEC loss per hour as a function of Fe^{2+} concentration..... 80

Figure 29: Fluoride release and sulfur emission per exposed surface area of the degraded membranes, as a) a function of degradation duration and b) average, normalised for degradation duration, release as a function of Fe^{2+} concentration..... 82

Figure 30: Comparative Figure of previous studies of total fluoride release in terms of *ex-situ* Fenton test duration. 84

Figure 31: Raman spectrum of the dose-response effect of Fe^{2+} concentration on Nafion®117 in the spectral range of 0-1340(cm^{-1}) for the a) 72 h degraded and the b) 30 ppm membranes. 86

Figure 32: ATR FT-IR spectrum of the dose-response effect of Fe^{2+} concentration on Nafion® 117 in the spectral range of 550-1800(cm^{-1}) 87

Figure 33: ^{13}C CP-MAS NMR spectrum of samples degraded for a) 24 h at Fe^{2+} concentrations of 5, 15, 30 ppm and b) for 24, 48 and 72h at 30 ppm Fe^{2+} concentration..... 89

Figure 34: Flow diagram of membrane swelling and shrinkage during hydration and degradation..... 91

Figure 35: Image grid of 2x2cm Nafion® 117 membranes under varying Fenton test conditions. 92

Figure 36: Profilometric imaging of Fenton degraded membranes at a) 5 ppm, b) 15 ppm and c) 30 ppm for 24 hours 93

Figure 37: SEM imaging of a) Virgin, non-degraded, b) 15 and c) 30 ppm Fe^{2+} degraded membranes for 72h 93

Figure 38: (a) Schematic illustration of notch area, fatigue crack growth area and fracture area. (b)–(d) are surface morphologies of notch area, fatigue crack growth area and fracture area of 48 h chemically-degraded Nafion® 212 membrane, respectively; (e)–(g) are corresponding cross-section morphologies. The contours of each part are indicated with dashed lines. 94

Figure 39: Thinning of an SPE membrane caused by various stressors, resulting in pinhole formation 95

Figure 40: Post-degradation (30 ppm 72h) Nafion® 115 with indicated regions 1-6 in which rupturing can be seen. 96

Figure 41: Post-degradation (15 ppm 72h) of 168.2 cm2 Nafion® 115 with visible bubble formation and the corresponding magnified region of 1787µm x 1340 µm showing bubble development from left to right 97

Figure 42: Post-degradation (5 ppm 48h) a) of 168.2 cm^2 Nafion® 115 with no visible notch or rupture formation, and the corresponding counterpart b) of 4 cm^2 Nafion® 117 with severe bubble formation present..... 98

Figure 43: Polarisation curve for reference cells at 40, 60 and 75 °C. 101

Figure 44: Nyquist plot for reference cell a) variable current density at 40 °C and b) variable temperature at 0.1 $A.cm^{-2}$..... 102

Figure 45: Hydrogen gas crossover of 2 reference cells from cathode to anode (H_2 in O_2) at a) variable temperature and b) variable current density 104

Figure 46: Potential and applied current as a function of time for cell a) 30-48, with automation script absent, and b) 15-48, with automation script present 106

Figure 47: Potential and applied current as a function of time for cell 30-72, with automation script present..... 107

Figure 48: Polarisation curve for a) 5-ppm degraded and b)15 ppm degraded CCMs at 40, 60, and 75 °C. 109

Figure 49: Polarisation curve for 30-ppm degraded CCMs at 40, 60, and 75 °C 110

Figure 50: Nyquist plot of reference cell vs a) 5 ppm, b) 15 ppm, and c) 30 ppm degraded cells at 40 °C 114

Figure 51: Nyquist plot of reference cell vs a) 24 h, b) 48 h, and c) 72 h degraded cells at 40 °C 115

Figure 52: Hydrogen gas crossover data for 5 ppm Fe^{2+} degraded CCMs at variable a) temperature (T= 40, 60 and 75°C) and b) current density(*j*= 0.35, 0.5 and 0.7A.cm^{-2}), and 15 ppm Fe^{2+} degraded CCMs at variable c) temperature(T= 40, 60 and 75°C) and d) current density (*j*= 0.35, 0.5 and 0.7A.cm^{-2}). 117

Figure 53: Hydrogen gas crossover data for 30 ppm Fe^{2+} degraded CCMs at variable a) temperature and b) current density. 118

Figure 54: Ohmic resistance increase per % IEC loss as a function of degradation duration 122

Figure 55: Sulfur emission per R_{Ω} and R_{ct} as a function of degradation duration 123

Figure 56: Comparative figure of previous studies of total fluoride release in terms of *ex-situ* Fenton test duration. 142

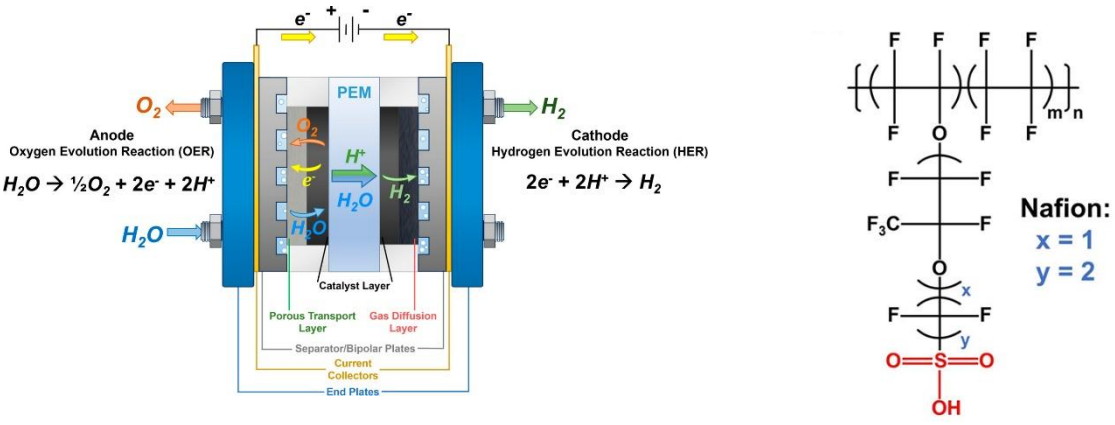
Figure 57: Raman spectrum of Fenton degraded Nafion® 117 at variable duration in the spectral range of 0-1340(cm^{-1}) 143

CHAPTER 1: BACKGROUND, MOTIVATION, AND OBJECTIVES

1.1 Project Background

With escalating global energy demand, the incentive to mitigate greenhouse gas emissions from fossil fuel combustion has intensified the search for sustainable, environmentally friendly alternative energy sources.[1] Renewable energy technologies, harnessing abundant resources such as wind and solar power, offer a promising pathway to displace fossil fuels. Consequently, significant global investments are being directed towards the generation and utilisation of renewable energy. Notably, green hydrogen gas (H_2) was identified as a crucial energy carrier in this transition.[2-4] Currently, global production of hydrogen is ~100 million tonnes. However, the fraction of green hydrogen remains very low at present.[5, 6] Hydrogen production reached 97 Mt in 2023, of which less than 1% was low-emissions.

Proton Exchange Membrane Water Electrolysis (PEMWE) is a promising technology for the efficient, high-purity production of H_2. As illustrated in Figure 1 a), PEM electrolysers utilise a Solid Polymer Electrolyte (SPE) membrane, typically a Perfluorosulfonic Acid (PFSA) ionomer such as Nafion®, Flemion®, Aciplex® and Aquivion® sandwiched between two catalysed electrodes. [7] This configuration allows the membrane to act as a selective proton conductor and a physical barrier separating the anodic (oxygen-evolving) and cathodic (hydrogen-evolving) compartments. PEMWE technology has garnered considerable attention due to its inherent advantages, including a relatively simple design, high power density (favourable weight-to-space ratio), and potential for high energy efficiency.[8, 9, 10]



(a) (b)

Figure 1: a) Schematic representation of a proton exchange membrane water electrolyser, and b) the monomeric molecular structure of Nafion® (Reproduced from [11] with permission from Royal Society of Chemistry (RSC) under CC BY-NC-ND license: https://creativecommons.org/licenses/by-nc-nd/4.0/)

PFSA membranes, often characterised by a three-digit Equivalent Weight (EW) designation (where the first two digits indicate the EW and the final digit indicates thickness in fractions of inches), are crucial to PEMWE performance. The EW, defined as polymer mass per mole of sulfonic acid (SO_3H) functional groups, significantly influences key membrane properties.[12] Generally, increasing EW correlates with higher crystallinity and a reduction in Water Uptake (WU) and glass transition temperature (T_g).[13, 14] Another critical parameter is the Ion Exchange Capacity (IEC), representing the molar concentration of exchangeable ions (protons in this context) per unit mass of dry membrane. Given the strong dependence of membrane characteristics on IEC, it is a fundamental property for assessing and monitoring membrane performance in research and development.[14]

1.2 Problem Statement

The degradation of non-reinforced PFSA membranes, such as Nafion®, represents a significant obstacle limiting the long-term performance and operational lifetime of PEM electrolysers. During PEM electrolysis, the membrane is subjected to a harsh environment characterised by acidic, oxidative conditions, the presence of radical species, elevated temperature, mechanical stressors, and high electrochemical overpotentials, all of which contribute to component degradation. This can manifest as membrane thinning, catalyst dissolution, and passivation of Bipolar Plates (BPPs) and Porous Transport Layers (PTLs), among other issues.[1] Operational parameters such as elevated temperature, pressure cycling, and fluctuating current density (j*)* and power load cycles can significantly accelerate the degradation rate of PEM electrolyser components.

Impurities in the water feed pose a considerable threat to the longevity of PEM electrolysers. Common cationic impurities present in the feed water, with a reported degradation rate in the order of Fe^{2+}>>Cu^{2+}>>Co^{2+}>Pt^{2+}>Ni^{2+} and Na^+, Ca^{2+}, Pb^{2+}, can lead to metallic cationic poisoning of the PEMWE system.[1] These cations migrate to and occupy the active sulfonic acid ion-exchange sites within the membrane and catalyst layer, thereby increasing charge-transfer resistance, overpotential, and the overpotential penalty, reducing catalytic activity, and decreasing proton conductivity. Furthermore, these cationic impurities catalyse the formation of highly reactive hydroxyl (•OH) and hydroperoxyl (•OOH) radicals upon the crossover of reactant gases, leading to further oxidative degradation of the PFSA ionomer and the subsequent release of fluoride ions (F^-) into the feed water system.

The release of F^-, often termed "forever chemicals" due to their environmental persistence, into the feed water is a significant environmental concern, as the typical F^- concentration in drinking water is regulated to be within the range of 0.5-1 ppm.[15] Studies have indicated that operating a PEMWE at 80 °C can result in a F^- release rate of approximately 3 μg. $h^{-1}\cdot cm^{-2}$ of

membrane area.[8] Consequently, the restriction or outright ban of polyfluorinated substances is currently being debated and implemented in various regions.[16-19] Another challenge associated with PEMWE technology is the reliance on specialised materials, particularly Platinum-Group Metals (PGMs) such as platinum (Pt) and iridium (Ir) as electrocatalysts, which significantly increase the costs and hinder the potential for large-scale deployment.

Considering the complex interplay of operating conditions in PEMWEs, including the presence of radicals, cationic metallic impurities, and an oxidative environment, a representative and selective Accelerated Stress Test (AST) is required to effectively analyse the degradation behaviour of PFSA membranes. The Fenton test, which utilises Fenton's reagent (a mixture of hydrogen peroxide (H_2O_2) and ferrous iron (Fe^{2+})), is a widely employed method for this purpose.[20-27] The reaction between H_2O_2 and Fe^{2+} generates highly reactive •OH and •OOH radicals, accelerating PFSA membrane degradation and mimicking the chemical degradation processes occurring within a PEMWE.

1.3 Aims and Objectives

The overarching objective of this study is to elucidate the impact of chemically induced degradation, simulated via *ex-situ* Fenton treatment, on the subsequent performance of PFSA membranes in a PEMWE system. To achieve this primary objective, the following specific aims will be addressed:

- Subject Nafion® 115 and 117 membranes to controlled *ex-situ* Fenton degradation under varying Fe^{2+} concentrations and exposure durations, mimicking the accelerated chemical degradation induced by metallic contaminants and reactive radical species encountered during PEMWE operation.
- Characterise the alterations in the Nafion® 115 and 117 membranes resulting from the *ex-situ* Fenton degradation, focusing on key properties such as IEC, FRR, SER, surface morphology, and chemical structure alterations.
- Evaluate the *in-situ* electrochemical performance of PEMWE single cells employing Catalyst Coated Membranes (CCMs) fabricated from the pre-degraded Nafion® 115 membranes, assessing parameters including polarisation behaviour, hydrogen gas crossover, and Electrochemical Impedance Spectroscopy (EIS) under relevant operating conditions.
- Establish a correlation between the extent of *ex-situ* Fenton degradation, as determined by changes in membrane properties, and the resulting *in-situ* PEMWE performance metrics.

Bibliography

(1) Qi, F.; Xiao−Zi, Y.; Gaoyang, L.; Bing, W.; Zhen, Z.; Hui, L.; Haijiang, W. A review of proton exchange membrane water electrolysis on degradation mechanisms and mitigation strategies. *Journal of Power Sources* **2017**, *366*, 33-55. DOI: https://doi.org/10.1016/j.jpowsour.2017.09.006.

(2) sakthimurugan, V.; Lakshmikanth, G.; Balaji, N.; Roopashree, R.; Kumar, D.; Devarajan, Y. Green hydrogen revolution: Advancing electrolysis, market integration, and sustainable energy transitions towards a net-zero future. *Results in Engineering* **2025**, *26*, 104849. DOI: https://doi.org/10.1016/j.rineng.2025.104849.

(3) Curcio, E. Techno-economic analysis of hydrogen production: Costs, policies, and scalability in the transition to net-zero. *International Journal of Hydrogen Energy* **2025**, *128*, 473-487. DOI: https://doi.org/10.1016/j.ijhydene.2025.04.013.

(4) Zavala, V. R.; Pereira, I. B.; da Silva Vieira, R.; da Silva Aires, F. I.; Dari, D. N.; da Silva Félix, J. H.; de Lima, R. K. C.; Sousa dos Santos, J. C. Challenges and innovations in green hydrogen storage technologies. *International Journal of Hydrogen Energy* **2025**, *113*, 322-339. DOI: https://doi.org/10.1016/j.ijhydene.2025.02.472.

(5) Abbasian Hamedani, E.; Alenabi, S. A.; Talebi, S. Hydrogen as an energy source: A review of production technologies and challenges of fuel cell vehicles. *Energy Reports* **2024**, *12*, 3778-3794. DOI: https://doi.org/10.1016/j.egyr.2024.09.030.

(6) (IEA), I. E. A. *Global Hydrogen Review 2024*. 2024. https://www.iea.org/reports/global-hydrogen-review-2024 (accessed 2026 08-03).

(7) Wu, J.; Yuan, X. Z.; Martin, J. J.; Wang, H.; Zhang, J.; Shen, J.; Wu, S.; Merida, W. A review of PEM fuel cell durability: Degradation mechanisms and mitigation strategies. *Journal of Power Sources* **2008**, *184* (1), 104-119. DOI: https://doi.org/10.1016/j.jpowsour.2008.06.006.

(8) Kuhnert, E.; Heidinger, M.; Sandu, D.; Hacker, V.; Bodner, M. Analysis of PEM Water Electrolyzer Failure Due to Induced Hydrogen Crossover in Catalyst-Coated PFSA Membranes. *Membranes* **2023**, *13* (3), 348.

(9) Shaygan, M.; Ehyaei, M. A.; Ahmadi, A.; Assad, M. E. H.; José Luz, S. Energy, exergy, advanced exergy and economic analyses of hybrid polymer electrolyte membrane (PEM) fuel cell and photovoltaic cells to produce hydrogen and electricity. *Journal of Cleaner Production* **2019**, *234*, 1082-1093. DOI: https://doi.org/10.1016/j.jclepro.2019.06.298.

(10) Jian, Z.; Xianguo, L. A review of polymer electrolyte membrane fuel cell durability for vehicular applications: Degradation modes and experimental techniques. *Energy*

Conversion and Management **2019**, *199*, 112022. DOI: https://doi.org/10.1016/j.enconman.2019.112022.

(11) Wang, C. R.; Stansberry, J. M.; Mukundan, R.; Chang, H.-M. J.; Kulkarni, D.; Park, A. M.; Plymill, A. B.; Firas, N. M.; Liu, C. P.; Lang, J. T.; et al. Proton Exchange Membrane (PEM) Water Electrolysis: Cell-Level Considerations for Gigawatt-Scale Deployment. *Chemical Reviews* **2025**, *125* (3), 1257-1302. DOI: 10.1021/acs.chemrev.3c00904.

(12) Maximilian, M.; Dunia, A.; Miriam, K.; Muhammad Solihul, M. m.; Simon, T.; Thomas, B. A comprehensive study on the ionomer properties of PFSA membranes with confocal Raman microscopy. *Journal of Membrane Science* **2023**, *669*, 121244. DOI: https://doi.org/10.1016/j.memsci.2022.121244.

(13) Marianne, P. R.; Benjamin, P. P.; Nahid, M.; Leonard, J. B.; Darlene, K. S. Effect of perfluorosulfonic acid membrane equivalent weight on degradation under accelerated stress conditions. *Electrochimica Acta* **2013**, *100*, 180-187. DOI: https://doi.org/10.1016/j.electacta.2013.03.112.

(14) Mauritz, K. A.; Moore, R. B. State of Understanding of Nafion. *Chemical Reviews* **2004**, *104* (10), 4535-4586. DOI: 10.1021/cr0207123.

(15) Organization, W. H. INADEQUATE OR EXCESS FLUORIDE: A MAJOR PUBLIC HEALTH CONCERN. (2019), W. H. O., Ed.; 2019.

(16) Bessarabov, D. Hydrogen production by water electrolysis: Challenges and

opportunities. National Science and Technology Forum: 2023; p 6.

(17) Agency, T. E. C. *Registry of restriction intentions until outcome*. 2021. https://echa.europa.eu/registry-of-restriction-intentions/-/dislist/details/0b0236e18663449b (accessed.

(18) Scheuer, S. *EU bans sub-group of PFAS used in food packaging and clothing*. ChemTrust, 2024. https://chemtrust.org/eu_pfhxa_ban/ (accessed.

(19) Spyrakis, F.; Dragani, T. A. The EU's Per- and Polyfluoroalkyl Substances (PFAS) Ban: A Case of Policy over Science. *Toxics* **2023**, *11* (9). DOI: 10.3390/toxics11090721 From NLM.

(20) Ghassemzadeh, L.; Kreuer, K. D.; Maier, J.; Müller, K. Evaluating chemical degradation of proton conducting perfluorosulfonic acid ionomers in a Fenton test by solid-state 19F NMR spectroscopy. *Journal of Power Sources* **2011**, *196* (5), 2490-2497. DOI: https://doi.org/10.1016/j.jpowsour.2010.11.053.

(21) Kremer, M. L. An Upper Limit to O2 Evolution as Test for Radical and Nonradical Mechanisms for the Fenton Reaction. *Reactions* **2021**.

(22) Tsuneda, T. Fenton reaction mechanism generating no OH radicals in Nafion membrane decomposition. *Scientific Reports* **2020**, *10* (1), 18144. DOI: 10.1038/s41598-020-74646-0.

(23) Kuhnert, E.; Hacker, V.; Bodner, M. A Review of Accelerated Stress Tests for Enhancing MEA Durability in PEM Water Electrolysis Cells. *International Journal of Energy Research* **2023**, *2023*, 3183108. DOI: 10.1155/2023/3183108.

(24) Kundu, S.; Simon, L. C.; Fowler, M. W. Comparison of two accelerated Nafion™ degradation experiments. *Polymer Degradation and Stability* **2008**, *93* (1), 214-224. DOI: https://doi.org/10.1016/j.polymdegradstab.2007.10.001.

(25) Ishimoto, T.; Koyama, M. A review of molecular-level mechanism of membrane degradation in the polymer electrolyte fuel cell. *Membranes (Basel)* **2012**, *2* (3), 395-414. DOI: 10.3390/membranes2030395 From NLM.

(26) Lorenz, G.; Willem, H. K. Kinetic Simulation of the Chemical Stabilization Mechanism in Fuel Cell Membranes Using Cerium and Manganese Redox Couples. *Journal of The Electrochemical Society* **2011**, *159* (2), B211. DOI: 10.1149/2.075202jes.

(27) Alhassan Salami, T.; Rahim, A. H. A. Numerical Modeling the Effect of Operating Variables on Faraday Efficiency in PEM Electrolyzer. *Procedia Technology* **2016**, *26*, 419-427. DOI: https://doi.org/10.1016/j.protcy.2016.08.054.

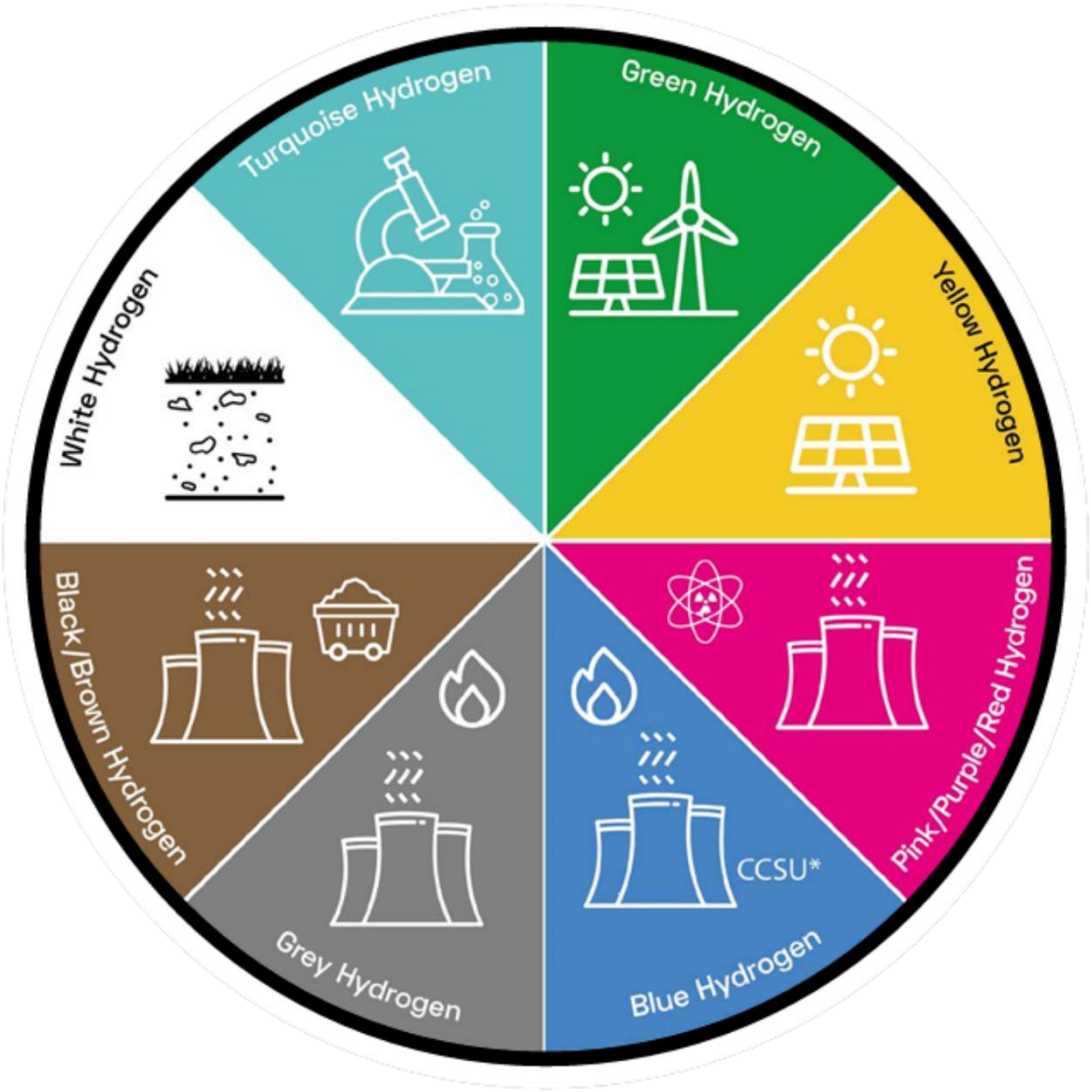
CHAPTER 2: LITERATURE SURVEY

This literature survey provides a detailed discussion of the background information and previous research relevant to the themes explored in this thesis. It establishes the context for the current work, focusing primarily on H_2 production via PEMWE and the associated degradation phenomena. This survey commences with a broad overview of H_2 production, outlining the prevalence of hydrogen, its various sources, and the established colour-coding system that classifies production methods by environmental impact. Following this general introduction, the survey narrows its focus specifically to PEMWE. It delves into the fundamental components of a PEM electrolyser; A substantial section is dedicated to a comprehensive review of the critical degradation mechanisms that affect PEMWE durability and performance. This includes literature addressing the degradation of the electrocatalyst layer, the polymer membrane, hydrogen embrittlement, metal passivation, and the gas-diffusion and porous transport layers. Finally, the survey introduces the concept and importance of AST as a vital methodology for investigating and understanding these degradation processes. Specifically, the Fenton test, as an AST, is reviewed for the PFSA membrane. This thorough review of the existing literature sets the foundation for the specific investigations and contributions presented in this dissertation.

2.1 Hydrogen Production

Hydrogen, the most prevalent element in the universe, exists on Earth predominantly in compound form, with diatomic H_2 being relatively scarce. Hydrogen gas can be produced through diverse methods that utilise both non-renewable (e.g., fossil fuels) and renewable sources (e.g., biomass and water). The annual global H_2 production of ~100 Mt[1] is estimated to be produced from 47-60% natural gas, 22-30% from coal, 19-27% from oil (as a by-product), and approximately1-4% from electrolysis.[2] Despite the growing demand for H_2, the production of low-C-emission H_2 is still scarce.[3] In 2022, the average emission intensity of H_2 production was 12-13.5kg CO_2-eq/kg H_2.[4]

To better categorise the diverse H_2 production methods and their environmental impact, a colour-coded classification system has emerged, as shown in Figure 2.



*CCSU: Carbon capture, storage, and usage

Figure 2: The colour-coding system of H_2 production methods. Reproduced from Western Gateway Partnership "Western Gateway Hydrogen Ecosystem 2022".[5]

Currently, grey hydrogen is the most widely utilized production route, with 40% of produced hydrogen being a by-product of other chemical processes such as Steam Methane Reforming (SMR).[6, 7] White hydrogen refers to naturally occurring hydrogen gas found in underground deposits, it is suspected that the Precambrian continental lithosphere could generate ~554 million tons of white H_2 per year via serpentinization with ultramafic deposits and radiolysis, for which no large-scale utilization methods have yet been developed.[8, 9] Green, pink, and yellow hydrogen are produced via water electrolysis using different energy sources, whereas turquoise hydrogen is generated through methane pyrolysis. Brown and black hydrogen are produced by gasification, with the colour designation indicating the type of coal used. This method is popular due to the

availability of coal sources. Blue hydrogen is produced using fossil fuels but incorporates CCSU technologies, currently offering a lower production cost than green hydrogen.[6]

Section 2.1 will briefly discuss the most common industrial methods for H_2 production, providing a foundational understanding for the context of this dissertation, which focuses on hydrogen production via PEMWE.

2.1.1 Biological or Bio-hydrogen

Biological hydrogen production presents a promising avenue for sustainable energy generation, primarily categorised into two distinct pathways: water bio-photolysis by algae and bio-photolysis (photo-fermentation) by other microorganisms.[10]

Direct water bio-photolysis harnesses the natural photosynthetic machinery of specific microorganisms, such as algae, to convert water into molecular H_2 under anaerobic conditions using light energy.[11] In contrast, indirect bio-photolysis involves a two-stage process. First, photosynthetic microorganisms utilise sunlight to capture carbon dioxide (CO_2) and store it as carbohydrates, releasing O_2 as a byproduct. Subsequently, when these carbohydrate-rich microorganisms are placed under anaerobic conditions in a separate step, they metabolise the stored compounds, producing H_2.[10]

The use of microorganisms is considered a promising source for hydrogen-based energy as it is more efficient and less energy-intensive than other traditional methods. The high startup capital requirements and running costs of the bioreactor currently limit the economic feasibility of this method.[8]

2.1.2 Steam Methane Reforming

Steam reforming of natural gas is a commercially established method of H_2 production. The cost of H_2 production from natural gas depends on the availability and price of the natural gas feedstock.[12] Steam reforming is a highly endothermic gas-phase conversion process that requires temperatures >823 °C in the presence of a Fe- or Ni-based catalyst at a pressure of 3 MPa. From this, syngas is produced, containing 70-75% H_2, 2-6% methane (CH_4), 6-14% CO2, and 7-10% CO. The general steam reforming reaction is described by equation 1:[12]

$$C_nH_m + nH_2O \rightarrow \left(\frac{(n+m)}{2}\right)H_2 + nCO\,,\ \ \Delta H^0 > 0 \qquad \text{Reaction 1}$$

Steam reforming is currently a predominant industrial method for hydrogen production; however, for a future hydrogen economy, this method is not ideal, as it emits approximately 9kg CO_2 / kg H_2 and may deplete global CH_4 storage, thereby increasing hydrogen production costs.[13, 14]

2.1.3 Hydrocarbon Gasification

The escalating accumulation of plastic waste, with an estimated 79% discarded into the environment, presents a significant and growing pollution challenge.[15] In response to this issue, hydrocarbon gasification offers a promising technology for converting carbonaceous materials, such as waste plastics, coal, and oil, into syngas, which contains H_2, CO, CO_2, and CH_4.[16]

The gasification process involves a series of steps that transform hydrocarbon structures/polymers into simpler gaseous products. Initially, the feedstock is mechanically homogenised to increase its surface area. This then undergoes pyrolysis under anaerobic conditions.[17] During pyrolysis, thermal decomposition breaks down the long polymer chains (plastics) into a mixture of volatile compounds, including tars, oils, and char.[17]

The pyrolysis products are subsequently introduced into a gasifier, where they react with a gasifying agent at elevated temperatures. Common gasifying agents include air, O_2, steam, CO_2, or mixtures thereof. This high-temperature reaction further breaks down the materials into a gaseous mixture known as syngas, which primarily comprises CO and H_2, along with other gases such as CO_2 and CH_4. The composition of the syngas is influenced by the specific gasifying agent used and the operating conditions.

An alternative reaction for the gasification process is partial oxidation, particularly when O_2 or air is used as the gasifying agent. These reactions are generally faster than traditional steam reforming, exothermic in the presence of oxygen, and require moderately high temperatures. While this exothermic operation offers significant energy benefits over endothermic steam reforming, the literature warns that these temperatures generally require robust catalyst design to prevent rapid deactivation via coking and to ensure complete tar cracking, which otherwise reduces downstream efficiency.[18-20] Depending on the specific hydrocarbon feedstock, partial oxidation can be carried out with or without a catalyst. Studies have shown that the type of plastic feedstock significantly affects the hydrogen yield, with Polypropylene (PP) and Polyethylene (PE) typically yielding the highest hydrogen production rates.[21]

While hydrocarbon gasification of carbonaceous materials and waste plastics offers a potential solution to mitigate plastic pollution and produce valuable H_2, several challenges hinder its widespread industrialisation. These challenges include: i) the formation of tars, which can cause fouling and operational problems in downstream equipment, ii) the nature of the produced syngas, which inevitably contains corrosive gaseous impurities derived from heteroatoms in the plastic waste. Notable contaminants include Hydrogen Chloride (HCl) from Polyvinyl Chloride (PVC) dechlorination and Hydrogen Sulfide (H_2S) from sulfur-based additives. These species induce corrosion of reactor alloys and downstream piping, and poison the active Nickel and Iron

sites of catalytic systems utilised for syngas production.[22-24] These contaminants require specialised materials and handling procedures, thereby altering overall economic viability, which is influenced by feedstock costs, plant capital expenditures, and operational expenses.[17]

2.1.4 Nuclear Energy

Nuclear energy presents a compelling method for producing hydrogen on a large scale with minimal greenhouse gas emissions. Unlike intermittent renewable energy sources such as solar and wind, nuclear power provides a continuous and reliable supply of electricity and high-temperature process heat, making it well-suited for industrial hydrogen production facilities. Hydrogen produced using nuclear energy is typically classified as pink, purple, or red hydrogen, depending on the specific production method employed. There are three primary strategies for nuclear-assisted hydrogen production.

The most direct and technologically mature method is the use of electricity from a nuclear power plant to drive conventional low-temperature water electrolysis systems, such as Alkaline Water Electrolysis (AWE) or PEMWE.[25] In this configuration, the nuclear reactor functions as an emission-free energy source, with turbine power driving the electrolyser systems. While this approach is readily deployable, with current reactor and electrolyser technologies, its overall system efficiency is constrained by the combined efficiencies of the thermodynamic power generation cycle (typically 30-40%) and the electrolysis process itself (typically 60-80%).[26]

A more efficient approach is High-Temperature Steam Electrolysis (HTSE), which leverages both electricity and high-quality heat generated by advanced Generation IV nuclear reactors, such as Very-High-Temperature Reactors (VHTRs). These reactors can produce heat, in the form of steam, at temperatures between 750−1000 ˚C.[27] In HTSE, this heat is used to create high-temperature steam, which is then fed to a Solid-Oxide Water Electrolysis Cell (SOEC). By supplying a portion of the energy needed to split water as thermal energy, the electrical energy requirement is significantly reduced, leading to much higher overall production efficiencies that can exceed 50%.[27] The primary challenges for HTSE lie in developing and scaling up durable stainless steel materials for SOEs that can withstand the demanding high-temperature and corrosive steam environment for extended operational lifetimes.[28, 29]

The third major pathway involves thermochemical water-splitting cycles. These processes use high-temperature heat directly from a nuclear reactor to drive a series of chemical reactions that collectively decompose water into hydrogen and oxygen.[30] All chemical intermediates are regenerated and reused within a closed-loop cycle, meaning the only net inputs are water and heat, and the only net outputs are hydrogen and oxygen. More than 100 cycles have been proposed, but the Sulfur-Iodine (S-I) cycle is among the most extensively studied. It requires a

heat input >800 °C, making it compatible with VHTRs. While thermochemical cycles theoretically offer very high efficiencies and eliminate the electricity-generation step, they face considerable technical hurdles, including managing highly corrosive reagents (e.g., sulfuric acid) and the engineering complexities of large-scale, high-temperature chemical plants.[30]

While technologies such as SMR and hydrocarbon gasification currently dominate industrial hydrogen supply, they remain fundamentally tethered to carbon-based feedstocks. Despite CCSU's potential to mitigate emissions, these methods often perpetuate reliance on fossil fuels and face challenges related to tar formation and syngas purity. Consequently, to achieve a truly decarbonised energy vector, the industry must pivot toward technologies that decouple hydrogen production from carbon entirely. Water electrolysis represents this necessary shift, offering a pathway to generate high-purity hydrogen using only water and renewable electricity as inputs.

2.2 Water Electrolysis Technologies

Water electrolysis is an electrochemical process that utilises electrical energy to dissociate water (H_2O) into its constituent elements: hydrogen (H_2) and oxygen (O_2). While the overall reaction ($H_2O \rightarrow H_2 + \frac{1}{2} O_2$) is consistent, the specific technology employed dictates the operating conditions, electrolyte, and charge-carrying species. The four primary technologies for water electrolysis, i.e., AWE, PEMWE, SOEC, and Anion Exchange Membrane Water Electrolysis (AEMWE), are distinguished by their core components and operational principles, as illustrated in Figure 3. Each technology presents a unique set of advantages and disadvantages with respect to efficiency, cost, durability, and operational flexibility.

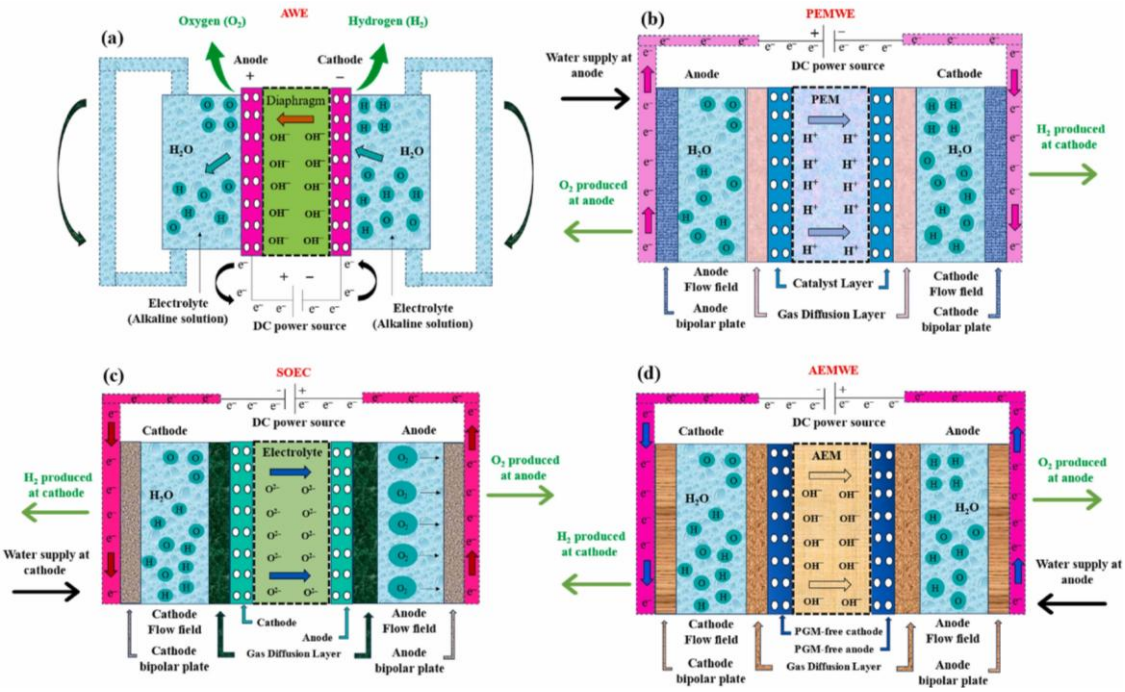


Figure 3: Schematic representation of water electrolysis by different technologies. a) alkaline, b) PEM, c) solid oxide and d) AEM water electrolysis (Reproduced from [31] with permission from ScienceDirect, under license no.6174110713788)

2.2.1 Alkaline Water Electrolysis (AWE)

First demonstrated in 1789 by Troostwijk and Diemann, AWE is the most mature and commercially established technology for large-scale, megawatt-level hydrogen production.[32, 33] As depicted in Figure 3 a), AWE systems utilise an alkaline solution (KOH or NaOH) as an electrolyte to facilitate ion transport between two electrodes separated by a porous diaphragm. During operation, an external electric current is applied across the cell. At the cathode, water molecules are reduced to produce hydrogen gas and hydroxide ions (OH^-):

$$2H_2O + 2e^- \rightarrow H_2 + 2OH^- \qquad \text{Reaction 2}$$

The hydroxide ions, serving as the charge carriers, migrate through the liquid electrolyte and across the diaphragm to the anode, where they are oxidised to form oxygen gas and water:

$$2OH^- \rightarrow \frac{1}{2}O_2 + H_2O + 2e^-,\ Ev = 1.23\ V \qquad \text{Reaction 3}$$

The primary advantages of AWE technology are its long operational lifetime, low cost, non-precious-metal electrocatalyst, and scalability to larger stacks.

AWE presents several challenges, including gas crossover between the electrodes, decreased hydrogen purity, low current densities, and limited adaptability to variable loads.

2.2.2 Proton Exchange Membrane Water Electrolysis (PEMWE)

The first PEMWE was idealised in the early 1950s by Grubb and was developed by General Electric Co. in 1966, after the release of DuPont's perfluorinated ion-exchange membrane (Nafion®), to overcome the limitations of AWE.[34, 35] The operational principle of a PEMWE cell is schematically shown in Figure 3 b). The core of this technology is the MEA, which consists of a SPE (Solid Polymer Electrolyte)/PFSA membrane sandwiched between two electrodes coated with PGM-based catalysts. In a PEMWE cell, high-purity deionised water is supplied to the iridium-based anode. Under an applied external current, water is oxidised on an iridium-based catalyst to produce oxygen gas, electrons, and protons, according to Reaction 4:

$$H_2O \rightarrow \frac{1}{2}O_2 + 2H^+ + 2e^- \qquad \text{Reaction 4}$$

The protons act as the charge carriers, migrating through the hydrated PFSA membrane to the cathode. At the platinum-based cathode, the protons are reduced with electrons from the external circuit to form high-purity hydrogen gas.[36]:

$$2H^+ + 2e^- \rightarrow H_2 \qquad \text{Reaction 5}$$

PEMWE offers significant advantages over AWE and SOEL, including a compact design, the ability to operate at high current densities (j = 1.0-2.2 A/cm^2), and a rapid response to dynamic power fluctuations, making it exceptionally well-suited for integration with renewable energy sources. The main disadvantages are the high capital cost, driven by the reliance on expensive PGM catalysts (iridium and platinum), the use of titanium in the PTLs and BPPs, the PFSA membrane, and a comparatively shorter operational lifetime than AWE due to material degradation in the harsh acidic and oxidative environment.

2.2.3 Solid-Oxide Water Electrolysis (SOE)

SOEs are a highly efficient third-generation technology that operates at elevated temperatures, typically between 600 and 900 °C. As shown in Figure 3 c), an SOE cell is composed of two porous electrodes (a fuel electrode and an oxygen electrode) separated by a dense, solid, ceramic electrolyte that is exclusively conductive to oxide ions.[37]

During operation, steam is supplied to the porous fuel electrode (cathode), where it is electrochemically reduced, producing pure hydrogen gas and superoxide (O_2^-):

$$H_2O + 2e^- \rightarrow H_2 + O_2^- \qquad \text{Reaction 6}$$

The negatively charged oxide ions serve as charge carriers, migrating through the solid electrolyte to the anode. At the anode, these ions are oxidised to form oxygen gas (O_2), releasing electrons into the external circuit:

$2O_2^- \rightarrow O_2 + 4e^-$ Reaction 7

The primary advantage of SOE technology is its exceptionally high current efficiency (81-90%)[38]. The high operating temperature yields favourable thermodynamic and reaction kinetic conditions, thereby significantly reducing the electrical energy required for the endothermic water-splitting reaction.[37] A portion of the required energy can be supplied as high-quality waste heat from external industrial processes, further enhancing overall system efficiency. Additionally, SOECs do not require expensive precious-metal catalysts and instead rely on abundant ceramic and metallic materials.

The main challenges for SOE are linked to its high operating temperature. These include material degradation and long-term stability issues.[37] Other drawbacks include slower start-up times and complex sealing requirements to ensure gas-tightness and prevent thermomechanical failure.

2.2.4 Anion Exchange Water Electrolysis (AEMWE)

AEMWE, represented in Figure 3 d), makes use of an alkali electrolyte and an anion exchange membrane to split water into H_2 and O_2 gas. Water is fed into the Nickel (Ni) foam anode, where it oxidises to produce O_2 (reaction 3) and OH^- ions. The OH^- ions then migrate through the membrane (which acts as a selective barrier), where they recombine at the Ni-Fe cathode to produce H_2.[39-42] The AEM operates at lower pressure and temperature than the previously discussed techniques, thereby reducing system complexity.[31]

Due to the unique nature of each technology, a comparative table (Table 1) presents differences in parameters such as electrode material, operating temperature, pressure, and efficiency.

2.2.5 Comparison of Existing Water Electrolysis Technologies

While the fundamental thermodynamic principles of water splitting remain consistent across all electrolysis methods, the practical implementation and engineering requirements vary significantly between technologies. These distinctions are primarily determined by the nature of the electrolyte and the charge-carrying species, which, in turn, influence material selection, operating conditions, and system complexity. To elucidate the relative merits and limitations of the primary electrolysis technologies, AWE, PEMWE, SOEC, and AEMWE, a comparative summary of their key operational and economic parameters is presented in Table 1.

Table 1: Comparison of H_2 production technologies via water electrolysis. Adapted from[43, 44] with permission from Elsevier under licence Number: 6027530328773.

	AWE[45-47]	PEM[34,48]	SOEC[49, 50]	AEMWE[48, 51, 52]
Electrolyte	NaOH/KOH (aq)	water	Y_2O_3	Akali solution
Charge carrier	OH^-	H^+	O^{2-}	OH^-
Electrode material	Ni and Ni alloys	PGMs	Cermet and doped metal composites	Transition metals
Operational temperature (˚C)	60-90	50-90	600-1000	40-90
Operational pressure (bar)	2-10	15-30	<30	1-30
Cell voltage (V)	1.8-2.4	1.8-2.2	0.95-1.3	1.5-2.3
Current Density (A/cm^2)	0.2-0.7	1.0-2.2	1.0-1.4	1-2
Current Efficiency (%)	62-82	67-84	81-90	39.7
Investigated durability (kh)	~100	~10	~2	~2
Maximum hydrogen production (Nm^3/h)	1-760	0.265-30	>100	0.25-1
Cost (estimation by 2050) ($/kW)	600	750	200	-
H_2 Production cost ($/kg)	2.36-6.98	2.5-6.8	2.99 -7.02	3.0-7.0
Capital cost at MW scale (USD/kW)	500-1000	700-1400	>2000	-
Technology status	Mature	Commercial	Pilot project	R&D
Advantages	Long lifetime	Higher current density	High energy efficiency	Low cost
	Low cost	Compact design	Less electrical consumption	Non-PGM catalyst
	Large stack size	Rapid response	Low expected cost	Low operational temperature
Disadvantages	Low current density	Requires noble metals	Unstable electrodes	Lower durability
	Corrosive electrolyte	Short lifetime	Sealing issues	Lower efficiency
	Gas crossover	High membrane cost	Severe environment	Technologically immature

As detailed in Table 1, the selection of an electrolysis technology necessitates trade-offs among maturity, efficiency, and operational flexibility. AWE, while commercially mature and cost-effective, is limited by low current density (j=0.2-0.7 $A.cm^{-2}$) and limited dynamic response, making it less ideal for fluctuating power inputs. Conversely, SOEC offers superior thermodynamic efficiency but is currently constrained by severe material degradation at high operating

temperatures (600-1000 °C), limiting its commercial readiness. AEMWE aims to combine the low material cost of alkaline systems with the compact design of PEMWE; however, it remains in the research and development phase and faces durability challenges.

PEMWE, therefore, emerges as the most viable candidate for a sustainable hydrogen economy powered by renewables. Its capacity to operate at high current densities (j=1.0-2.2 A.cm^{-2}), combined with rapid response times to fluctuating power loads, makes it uniquely suitable for coupling with wind and solar energy. However, this performance comes at the cost of durability in harsh, oxidising, acidic environments. Thus, this study focuses exclusively on PEMWE, specifically addressing the material degradation challenges that currently impede its long-term deployment.

2.3 Proton Exchange Membrane Water Electrolysis (PEMWE) Components

As PEMWE is of interest in this study, the technology will be disseminated in the following section. A PEMWE is a complex electrochemical device composed of several integral components, each with specific functions crucial for efficient and durable operation. A schematic representation illustrating the assembly of these primary components is shown in Figure 4. The core of the device is the MEA, which is supported and supplied with reactants by the PTLs and BPPs. A detailed description of each component is shown in Figure 4. The following discussion adopts a spatial structure, commencing at the core of the device, the MEA, and progressing outward toward the BPPs.

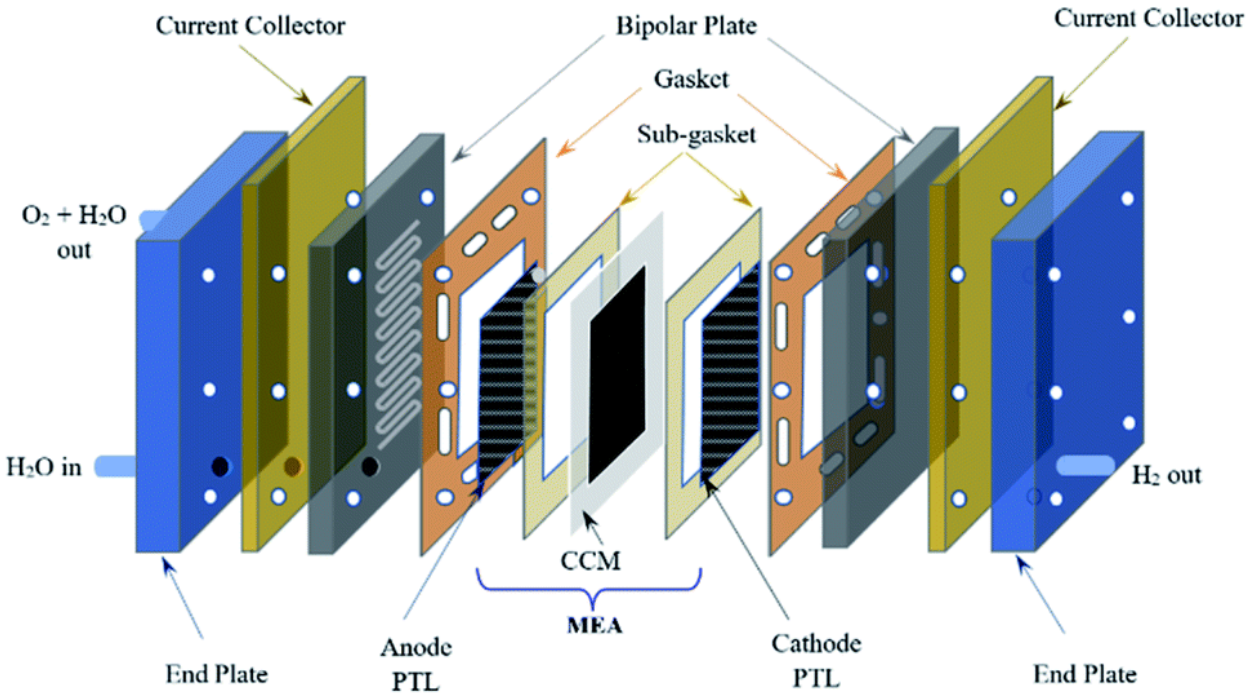


Figure 4: Schematic representation of the main PEM electrolysis cell components (Reproduced from [53] with permission from RSC, License ID: 1609413-1)

2.3.1 Catalyst Coated Membrane (CCM)

The PEM is an SPE that serves a dual function within the cell. Firstly, it acts as a selective proton (H^+) conductor, facilitating proton transport from the anode to the cathode while remaining an electronic insulator.[54] Secondly, it functions as a physical barrier to limit the crossover of the product gases, hydrogen and oxygen, thereby ensuring high-purity hydrogen production and safe operation.[55] The most widely used materials are PFSA ionomers, with DuPont's Nafion® as the benchmark. The PEM's performance depends on its hydration level, as water molecules facilitate proton transport via the sulfonic acid (SO_3H) functional groups. Consequently, key properties such as high proton conductivity, low gas permeability, excellent chemical stability in the harsh oxidative and acidic environment, and robust mechanical strength are required for a durable PEM.

While PFSA ionomers, such as Nafion®, exhibit excellent proton conductivity and mechanical strength, their chemical structure is not impervious. The ether linkages and tertiary carbons within the polymer side chains represent specific sites of vulnerability. Under the harsh oxidative environment of the electrolyser, these sites are susceptible to attack by radical species, a degradation mechanism that ultimately dictates the operational lifetime of the membrane and is the primary focus of the *ex-situ* investigations in this study.

The catalyst layers are thin, porous structures applied to both sides of the PEM, designed to accelerate the electrochemical half-reactions of water electrolysis by lowering their activation energies. The anode catalyst facilitates the Oxygen Evolution Reaction (OER) via Reaction 4.

This reaction occurs under harsh conditions. While the thermodynamic limit is 1.23 V, practical water splitting typically requires cell voltages exceeding the thermoneutral voltage of ~1.48 V. Consequently, the anode operates at potentials (often >1.6 V to 2.0 V at nominal current densities) to overcome the significant kinetic overpotential of the OER, exposing the catalyst to a severely oxidative environment.[56, 57] These conditions restrict the choice of materials. PGMs, specifically Ir and ruthenium (Ru) based metals and oxides, are materials known to possess a reasonable balance of catalytic activity and stability. Currently, iridium oxide (crystalline IrO_2 or amorphous IrO_x)[58] is considered the state-of-the-art OER catalyst due to its superior durability compared to Ru-oxides.[59] However, even Ir-based catalysts are susceptible to dissolution over time, which is a major contributor to performance degradation.[57, 60]

The cathode catalyst facilitates the Hydrogen Evolution Reaction (HER) via Reaction 5. The cathodic environment is less corrosive than the anode. Platinum (Pt), typically dispersed on a high-surface-area carbon support (Pt/C), is the most common and highly effective catalyst for the HER due to its excellent activity and stability in the acidic environment of the PEMWE cathode.

The electrochemical efficiency of the PEMWE catalyst layer is governed by the Triple Phase Boundary (TPB), defined as the active geometric locus where the electron-conducting electrocatalyst, the proton-conducting ionomer, and the mass transport network (pores) converge.[61] Unlike the gaseous environment of fuel cells, the liquid-fed PEMWE anode presents a unique multiphase challenge: while water diffusivity through the hydrated ionomer suggests a theoretical volumetric "Two-Phase Boundary" reaction zone, the efficient removal of the gaseous oxygen product practically limits activity to sites with direct pore access to prevent bubble-induced masking and ionic isolation.[59, 62]

Optimising the catalyst layer architecture requires a precise balance of the Ionomer-to-Catalyst (I/C) ratio. Empirical studies demonstrate a relationship for cell performance, with optimal loadings typically falling between 10–25 wt%.[63, 64]

Furthermore, the catalyst-ionomer interface is subject to intrinsic limitations known as ionomer poisoning.[65] The specific adsorption of sulfonate groups (SO_3^-) onto the Ir-oxide surface sterically hinders water access and alters the electronic structure of active sites, elevating the activation energy for the OER.[66] Consequently, advanced electrode designs are shifting toward gradient ionomer structures and ionomer-free Porous Transport Electrodes (PTE) to decouple proton-transport requirements from catalytic kinetics and mitigate interfacial degradation mechanisms, such as radical attack and viscoelastic creep.[65]

2.3.2 Membrane Electrode Assembly (MEA)

The MEA is the electrochemical core of the PEMWE cell, where the fundamental processes of water splitting occur. The core of the MEA is the CCM. In the full cell assembly, the MEA typically refers to the five-layer structure comprising the CCM sandwiched between two PTLs.[67]. The careful design and fabrication of the MEA are paramount, as their integrity and interfacial properties directly dictate the electrolyser's performance, efficiency, and operational lifetime.[68]

2.3.3 Porous Transport Layer (PTL)

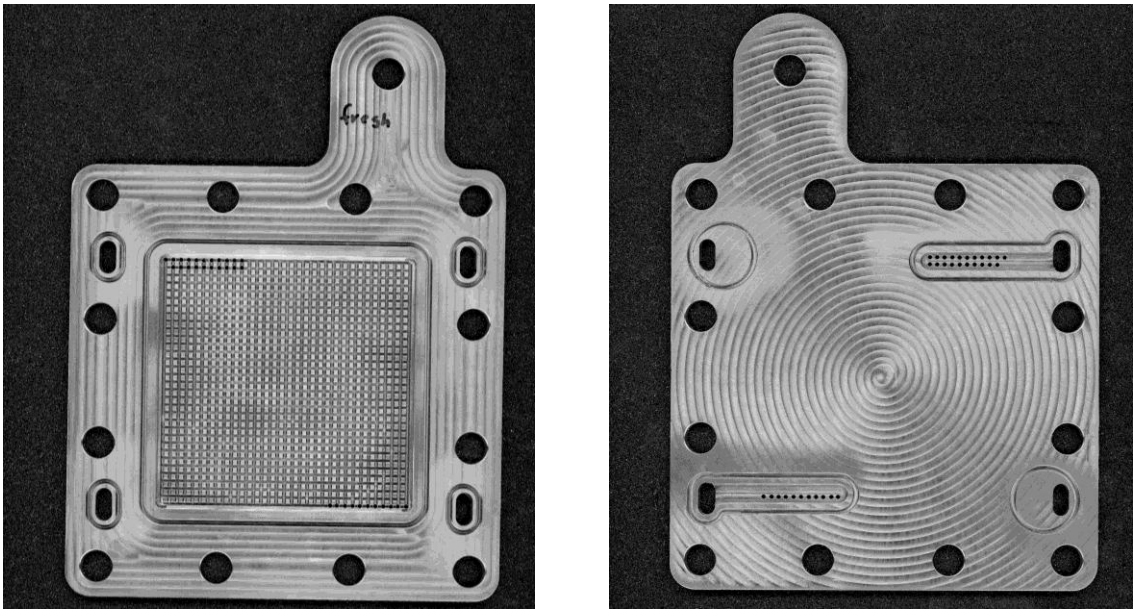
Positioned between the catalyst layers and the BPPs, the PTLs are multifunctional components assisting cell operation. Their primary roles are to provide a conductive pathway for electrons between the BPP and the catalyst layers, to offer mechanical support to the CCM, and to facilitate the efficient transport of reactants (water) and products (H_2 and O_2).[53]

On the anode side, the PTL must transport liquid water to the catalyst layer and allow *in-situ* generated O_2 gas to escape. Due to the high potential and corrosive environment, sintered titanium (Ti) felts or foams are typically used. On the cathode side, the Gas Diffusion Layer (GDL) must efficiently allow unrestricted flow of the produced hydrogen gas and manage water. Here,

carbon-based materials like carbon paper or cloth are commonly employed. The microstructure of the PTLs, including their porosity, tortuosity, and thickness, significantly impacts mass transport and ohmic losses, and is therefore carefully engineered to optimise performance.

2.3.4 Bipolar Plates (BPPs)

The BPPs, positioned between the current collectors and PTLs, serve several functions. Machined or stamped into their surface are flow channels that distribute reactant water across the anode PTL and collect the hydrogen and oxygen gas products from their respective outlets. The material requirements are stringent, demanding high electrical conductivity, excellent corrosion resistance, high mechanical strength, and impermeability to gases.[69, 70] Titanium is the most common material for PEMWE BPPs due to its ability to form a thin, conductive, and protective passive oxide layer (TiO_2). However, it can be susceptible to Hydrogen Embrittlement (HE) on the cathode side and to further passivation on the anode side, which increases contact resistance over time.[70]



a) b)

Figure 5: Bipolar plate with a) flow field facing upwards and b) back of bipolar plate (source, HySA Infrastructure, NWU).

2.4 Proton Exchange Membrane Water Electrolysis (PEMWE) Degradation Modes

Despite the efficiency and dynamic response capabilities of PEMWE, its widespread commercialisation is currently impeded by significant challenges related to the system's long-term durability and degradation. As mentioned earlier, the harsh operating conditions within the electrolyser, characterised by high anodic potentials, an acidic and oxidising environment, and

elevated temperatures, induce a variety of complex and often interconnected degradation mechanisms across all key components, as illustrated in Figure 6.

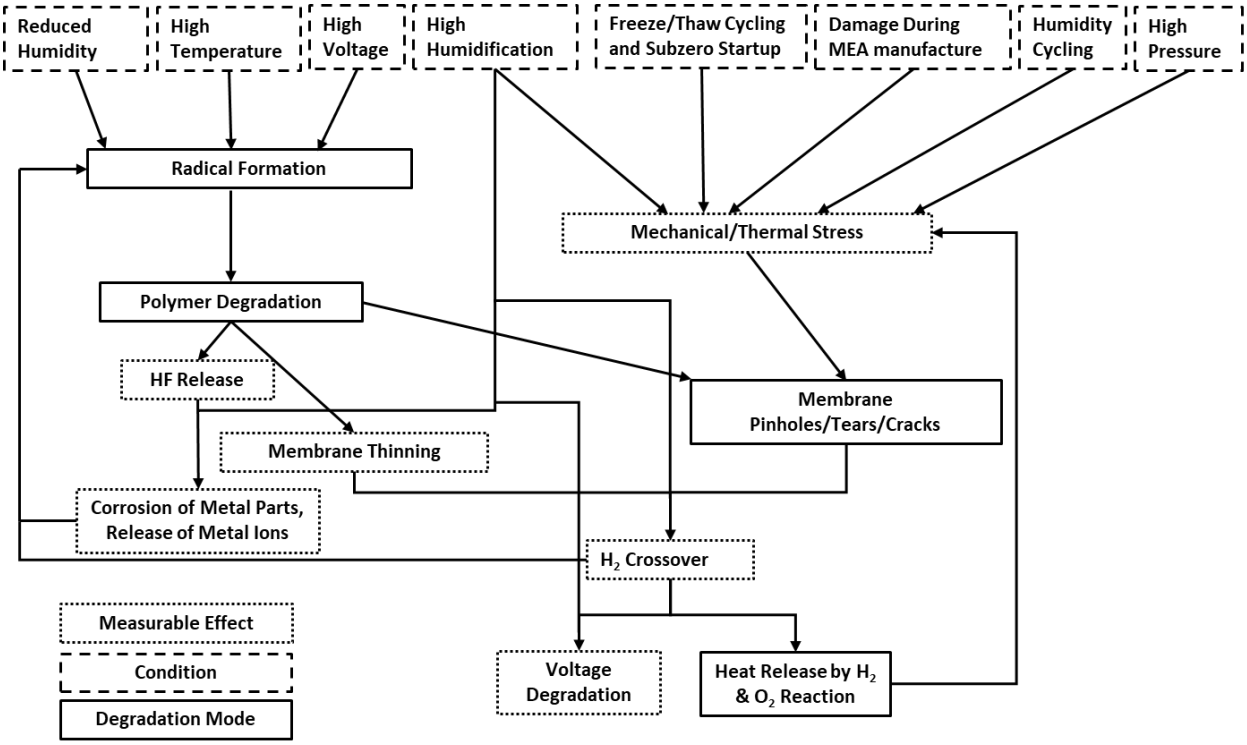


Figure 6: Degradation effects, conditions, and mechanisms of PFSA membranes, (Reproduced from [71] with permission, Copyright 2008 John Wiley and Sons, License ID: 6052981353871)

A thorough understanding of these failure modes is paramount for developing effective mitigation strategies, enhancing component longevity, and ultimately improving the economic viability and reliability of PEMWE systems. This section provides a comprehensive survey of the primary degradation phenomena affecting PEMWE, systematically examining the chemical, mechanical, and thermal degradation pathways within the electrocatalyst layers, the polymer electrolyte membrane, and the porous transport layers.

2.4.1 Degradations Within the Catalyst Layer

2.4.1.1 Catalyst Dissolution

Given the operational conditions of the PEMWE, characterised by its acidic environment, potentials exceeding 1.5 V, and elevated oxygen concentration at the anode, the choice of electrocatalyst is limited to PGMs.[72] As mentioned in Section 2.3.1, currently Ir-oxides are considered the most viable anodic OER materials.[73-75] However, the harsh environment causes dissolution of the iridium oxide catalyst, leading to progressive thinning of the catalyst layer and subsequent loss of electrolyser performance.[75]

Understanding this phenomenon is deemed essential for the commercialisation of PEMWE. Cherevko *et al.* identified that the formation of the unstable, water-soluble (at low pH) $Ir(OH)_3$ and Ir_2O_3 complexes as the primary cause for the iridium catalyst dissolution.[76, 77] Thomassen *et al.* observed that the mass activity and Electrochemically Active Surface Area (ECSA) degrades most at high voltages (>1.8 V), with mass activity loss initiating at medium voltages (1.4-1.6 V).[77] This is further confirmed by the Pourbaix diagram illustrated in Figure 7**,** as the stable IrO_2 begins to turn to soluble iridium at a potential of approximately 1.8 V.

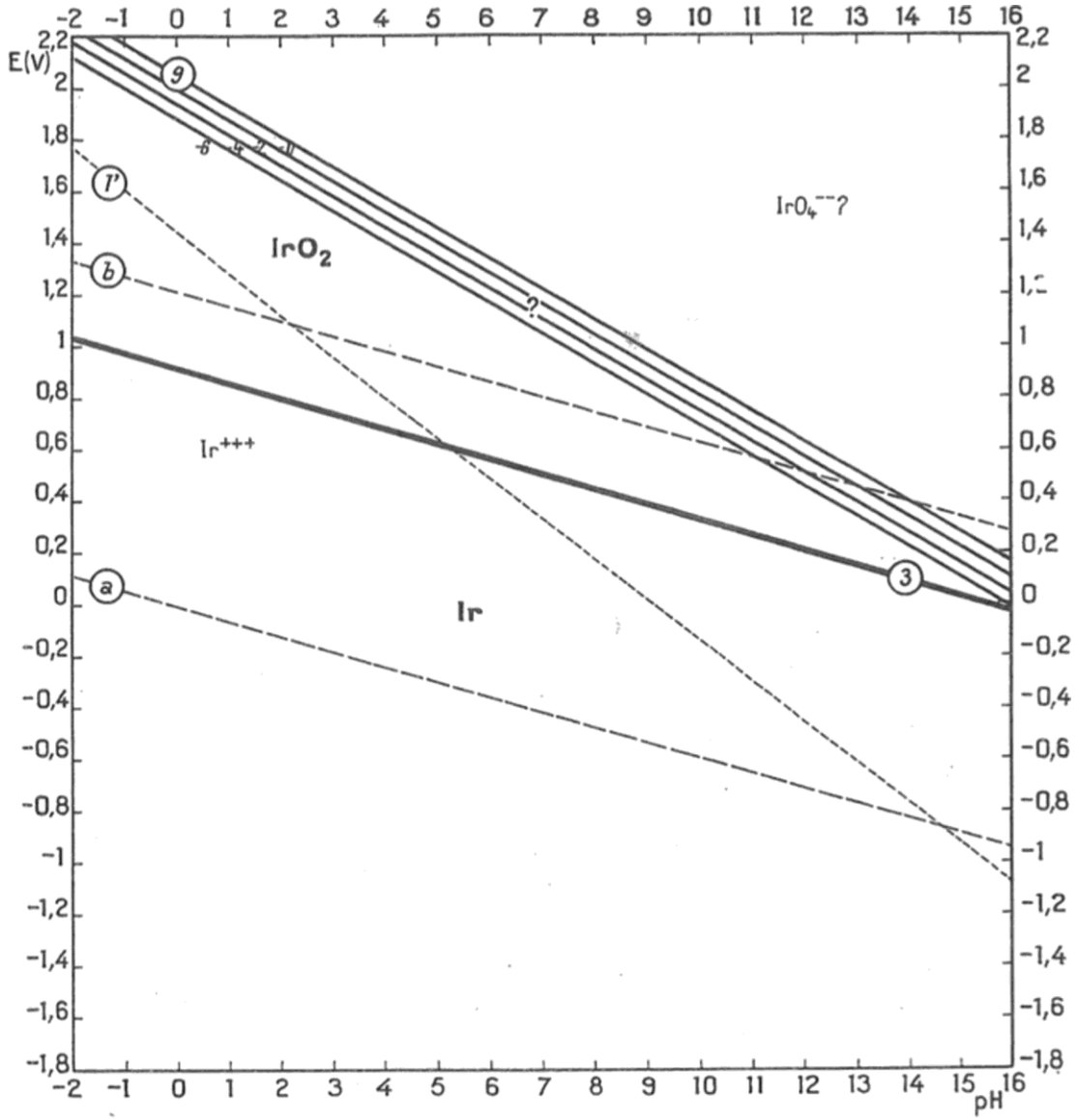


Figure 7: Pourbaix diagram for the iridium-water system at 25 °C and its dependence on pH and potential. (Reproduced with permission from NACE International [78], Houston, TX. All rights reserved. M. Pourbaix, Atlas of electrochemical equilibria in aqueous solutions, National Association of Corrosion Engineers, Houston, TX (1974)).

Research on platinum dissolution is less prevalent; however, it has been found that at Open Circuit Voltage (OCV) above 0.85 V (against Normal Hydrogen Electrode (NHE)), platinum undergoes dissolution due to oxygen scattering from the anode. At cathodic potentials of 1.02 V (vs NHE), the rate of platinum dissolution reaches a maximum of ~4.5 $ng.cm^{-2}.h^{-1}$.[79]

2.4.1.2 Particle Agglomeration and Migration in the Catalyst Layer

Nanoparticle growth can occur via two primary mechanisms: migration and agglomeration. In the context of the catalyst layer, agglomeration refers to an increase in average particle size, driven by sintering or crystal growth.[80] This phenomenon has been thoroughly investigated in PEM fuel cells; however, its fundamental causes in electrolysis systems are not as well established, despite being an observed degradation mode in PEMWE.[81] The principal consequence of catalyst agglomeration is a substantial reduction in ECSA, thereby directly reducing overall cell efficiency. This degradation mode has been observed on both the anode and cathode catalyst layers. Evidence suggests that the rates of agglomeration and migration are exacerbated by demanding operational parameters, with the applied voltage being a particularly significant accelerating factor.[82]

2.4.2 Hydrogen Embrittlement (HE)

HE is a degradation process characterised by a metal hardening and a simultaneous loss of ductility.[83] While titanium is often chosen for its excellent mechanical stability and corrosion resistance (especially compared to graphite), it remains susceptible to HE. In BPPs, HE manifests as the formation of non-conductive hydrides on the component surface.[84] These hydrides lead to material weakening, compromised electron transport, and increased contact resistance.[85] The cathode side of the cell is reportedly the most susceptible to HE. This process is strongly promoted by cycling between elevated temperatures and pressure, which facilitates the formation of hydride species.[86] High potential can further drive hydride formation. One proposed mitigation technique for this high-voltage degradation is to pre-treat the BPPs with noble metals; however, this approach significantly increases the electrolyser's manufacturing costs.[87]

2.4.3 Titanium Passivation

The passivation of BPPs involves the growth of a thin, 2-3 nm oxide film (TiO_2) on the component's surface. This layer is detrimental because it reduces electrical conductivity and increases contact resistance.[88, 89] This TiO_2 layer is exceptionally stable and is resistant to attack by most substances, with the notable exception of F^- ions released during membrane degradation. To enhance corrosion resistance and prevent premature erosion, PGM and noble metal coatings are frequently applied; however, their high cost increases production expenses and has motivated research into alternative coatings for both fuel cells and electrolysers.[90, 91] It has also been shown

that using stainless steel for the BPPs does not resolve the issue, as oxide formation remains on the anode side under high-potential operation (Figure 8).[92] Furthermore, evidence indicates that under high potentials, corrosive species such as nickel and iron can migrate from the anode across the membrane to the cathode, causing membrane contamination, which in turn reduces the ECSA.[92]

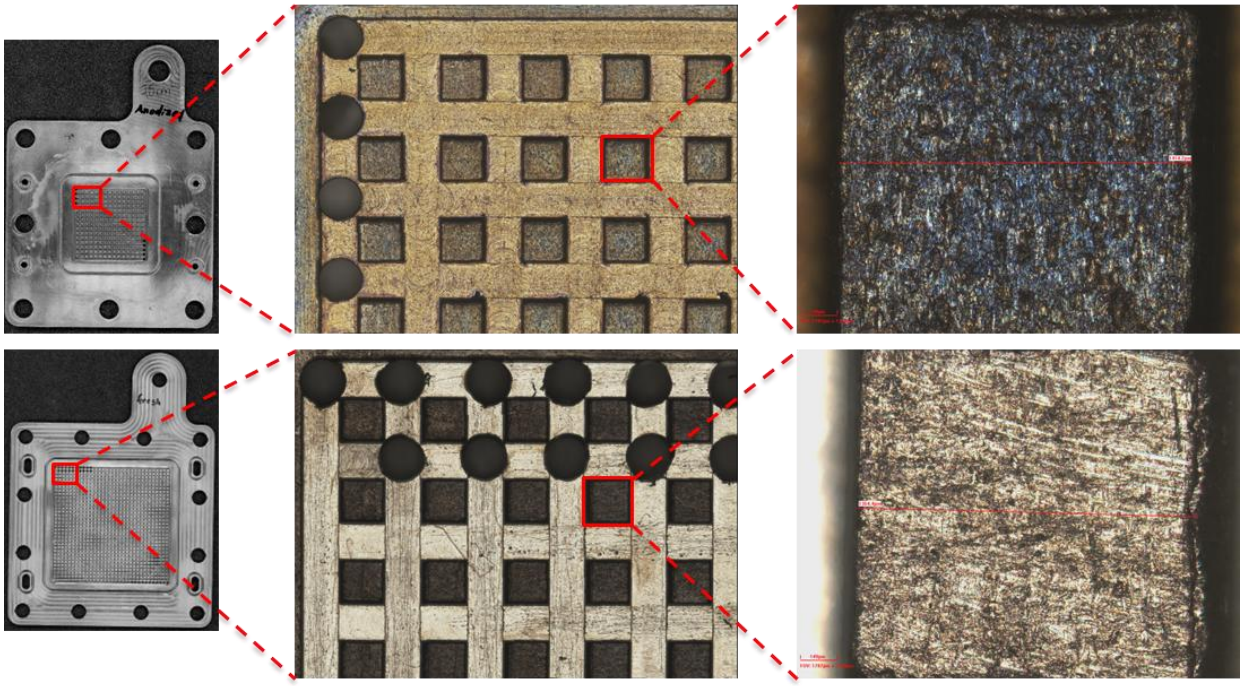


Figure 8: An in-house profilometric imaging of an oxidised (top) and fresh (bottom) bipolar plate/flow field, zoomed in sections indicated in red, magnifying the water inlet regions. Single pins from each are further magnified to illustrate the formation of suspected TiO_x. (source, HySA Infrastructure, NWU).

2.4.4 Porous Transport Layer (PTL)

Located between the BPPs and the CCM, the PTLs are critical for effective cell operation (Section 2.3.3). While PTL and GDL are often used interchangeably in the broader fuel cell literature, in PEMWE, a distinction is drawn based on the material constraints of the operating environment.

2.4.4.1 Chemical Degradation

As discussed in Section 2.3.1, carbon-based PTLs are typically employed on the cathode side as the PTL. These materials must efficiently facilitate electron transport and allow for the removal of the evolved H_2 gas. However, carbon is unsuitable for the anode because the high potentials (>1.5 V) required for OER would cause rapid carbon oxidation.[93] As previously mentioned in Section 2.4.3, the Ti PTL undergoes passivation, resulting in the formation of Ti-

oxides.[94]. This passivation layer increases the interfacial contact resistance (ICR) between the PTL and the BPP, contributing to significant voltage losses over time. Additionally, although rare under normal operating conditions, HE (Section 2.4.2) of titanium can occur if significant hydrogen crossover takes place.[95] The formation of oxides at the PTL can dissolve and contaminate the membrane, resulting in a decrease in ECSA, a mitigation strategy is to coat the titanium with PGMs, however this will further increase the manufacturing cost of a PEMWE.[96] Another viable mitigation strategy is the use of stainless steel, but corrosion still affects these components.[87]

2.4.4.2 Mechanical Degradation

The structural integrity and performance of the PEMWE stack are reliant on compression forces during assembly. Adequate compression between the various cell layers is essential to prevent the leakage of water and product gases (H_2 and O_2) and to minimise contact resistances, thereby ensuring efficient electrical, thermal, and mass transport.[97] However, the applied compression force significantly influences the physical properties of the PTLs. This mechanical stress can interfere with adjacent layers, including the catalyst layers and the BPPs. While increasing compression forces improves thermal and electrical conductivity by enhancing intercomponent contact, excessive compression can cause damaging alterations in the PTLs' microstructure.[98] Specifically, excessive compressive stress can cause mechanical damage to the carbon fibres (if used). This structural deformation alters the overall morphology of the porous medium, reducing fluid permeability and potentially impairing efficient mass transport of reactants and products.[98] Furthermore, alterations to the carbon fibre network can reduce effective current transport through the PTL, thereby increasing ohmic losses within the cell.

Maintaining a uniform pressure distribution during stack assembly is crucial for optimal operation of PEMWE. Non-uniform pressure has been correlated with an uneven distribution of electric current across the active area, resulting in localised degradation of both the PTL and the MEA.[99] These localised stresses and current densities (and concurrently, reaction heat localisation) can accelerate material degradation and shorten the lifespan of the electrolyser components.

Therefore, special attention to the assembly process is essential to ensure the application of appropriate and uniform compression forces, thereby minimising mechanical damage to the PTLs and promoting long-term stack durability and performance. Of particular importance, especially for larger PEMWE systems, is the precision manufacturing of BPPs, as slight deviations result in non-uniform contract distribution, regardless of compression.

2.4.5 Proton Exchange Membrane (PEM)

2.4.5.1 Thermal Degradation

Achieving high efficiency in electrochemical water splitting is a paramount focus of technological optimisation for the cost-effective production of green hydrogen.[52, 72, 100] Elevated operational temperatures (80-100˚C) have been demonstrated to significantly increase the ionic conductivity of PEM and accelerate electrochemical reaction kinetics.[101] However, the existing literature indicates that excessively high temperatures can lead to a reduction in membrane hydration and material degradation, ultimately resulting in membrane failure. Notably, some investigations have suggested that temperature constitutes a more significant stress factor for membrane durability than current density.[102]

Thermal and chemical degradation of PFSA membranes, such as Nafion®, shares mechanistic similarities, initiating with the deterioration of the sulfonic acid functional groups. Zhao *et al.*[103] reviewed membrane thermal degradation in vehicle fuel cell applications, while Chandesris *et al.*[104] presented both a model and experimental data demonstrating the significant influence of temperature on membrane thinning. Their research underscores the substantial impact of operating temperature on the dissolution of functional groups within the membrane, a process that is accelerated at temperatures exceeding 80 ˚C.

Membrane degradation is also associated with cold-start procedures. As demonstrated by Alink *et al.,*[105] water is forced out of the hydrophilic domains of the polymer chains, thereby increasing the probability of ice formation on the membrane surface. The polymer chains themselves will not freeze unless the membrane is fully saturated with water.[105] As a result, the membrane surface experiences stress from the volumetric expansion of ice, a process that can generate pinholes and cracks. This effect can be severe enough to cause the delamination of the catalyst layer.[72, 106].

2.4.5.2 Mechanical Degradation

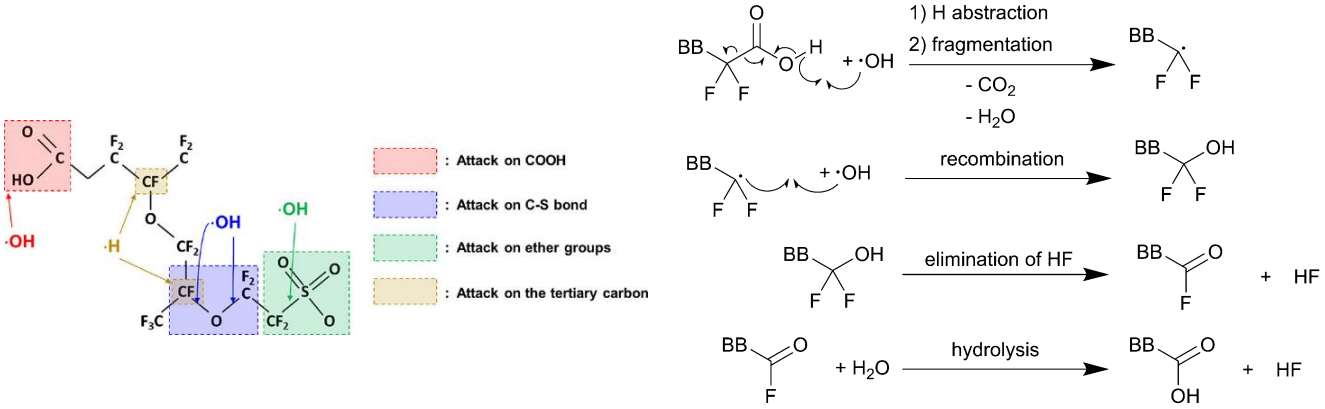
Early failure of the PEM has been predominantly attributed to mechanical degradation, which manifests as tears, cracks, punctures, mechanical stresses, and insufficient humidification of the system.[107, 108] Cracking of the membrane may result from excessive clamping force and non-uniform pressure distribution at the membrane contact areas with the BPPs flow channels and PTLs.[109] Membrane pinholes may develop due to temperature fluctuations, mechanical damage, and humidity cycling as the membrane undergoes swelling and shrinkage, leading to mechanical fatigue over extended periods.[110-112] The formation of pinholes poses a safety risk due to the potential mixing of combustible oxygen and hydrogen gases. Excessive water flow rates can lead to pressure accumulation, resulting in mechanical degradation.[113] In contrast, if the water

flow rate is too low, the BPP channels are unevenly distributed, resulting in a non-uniform electric current distribution.[114] This non-uniform distribution results in membrane swelling and the formation of hot spots due to the exothermic reaction, further degrading the membrane at high voltages. [113]

2.4.5.3 Chemical Degradation

During water electrolysis, the membrane and PFSA present in the CCM catalyst layers are susceptible to cationic impurities, such as Na^{+}, Ca^{2+}, Cu^{2+}, Ni^{2+}, Pb^{2+}, and $Fe^{2+,3+}$.[115] These species originate mainly from impurities in the feed water, corrosion of piping and stack component materials, e.g., stainless steel [116], and the fabrication process of the PEMWE system. [117-119]. Metal cation poisoning is a prevalent degradation mechanism in which cations migrate into the ionomer network and occupy the active sulfonic acid exchange sites. This proton displacement reduces ionic conductivity and diminishes kinetic efficiency in the catalyst layer.[120]

Cation poisoning increases overpotential and charge-transfer resistance, thereby raising the cell voltage.[121-125] These metal cationic species catalyse the formation of •OH and •OOH radicals via hydrogen gas crossover, thereby promoting further degradation of the PFSA ionomer (Section 2.6.1).[126-128] This degradation results in a permanent performance loss and can be measured by the FRR and the sulfur emission rate (SER)[38, 129-132]. The oxidative attack on the PFSA ionomer results in the dissolution of sulfur from the side chain and fluorine throughout the structure, as illustrated in the summarised mechanism of degradation in Figure 9 a). This process leads to membrane thinning, thereby increasing gas crossover. A thinner membrane permits greater gas crossover, thereby accelerating radical generation in the presence of cationic species.



a) b)

Figure 9: a) Summary of the radical attack mechanism of the Nafion® structure b) Main chain unzipping mechanism. BB represents the backbone of the PFSA membrane. (Reproduced from [133] and [134] with permission from ACS and RSC under CC BY-NC license: https://creativecommons.org/licenses/by-nc/3.0/)

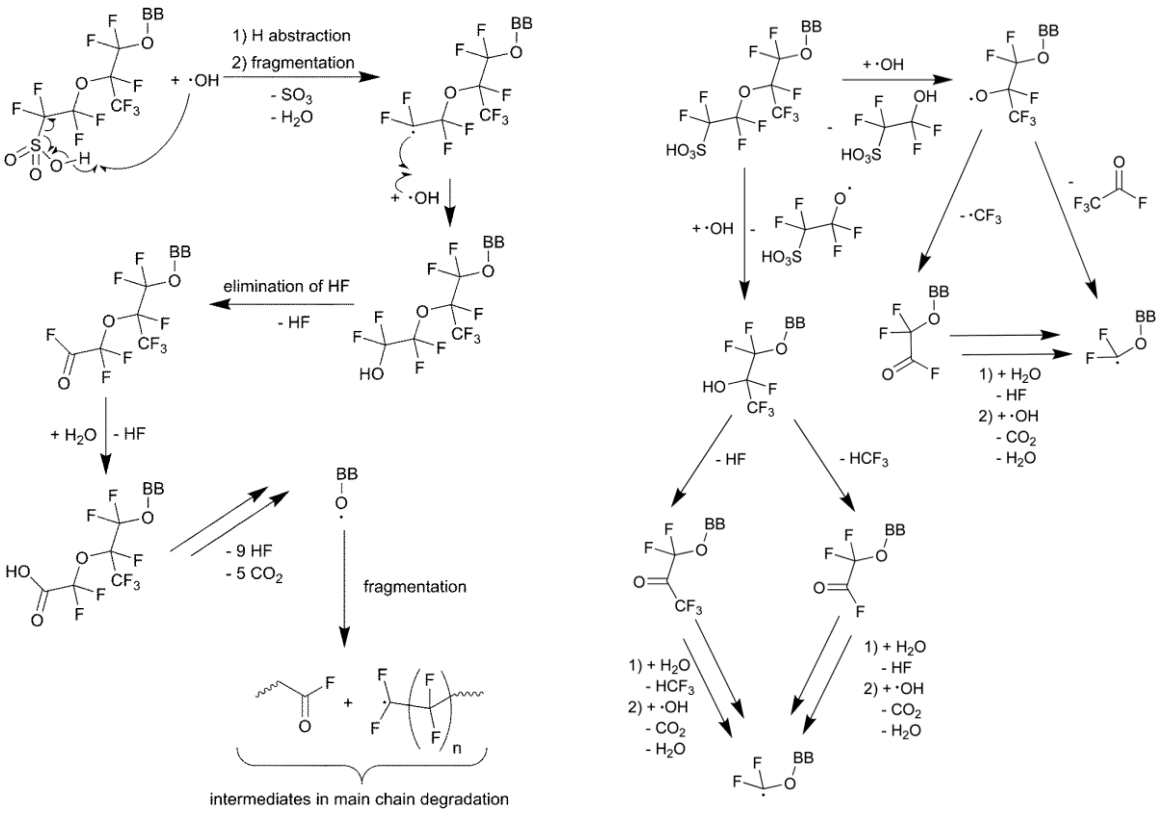
Among possible metallic cationic species in the feed water, Wang *et al.* have shown that $Fe^{2+, 3+}$ is the most membrane-degrading, as Fe^{x+} has a greater affinity for the active sulfonic acid sites than H^+, leading to greater loss of proton conductivity and SO_3H concentration.[118]

As represented in Figure 9, a) and b). The chemically induced degradation of PFSA ionomers has previously been characterised into four sub-categories: i) the unzipping reaction on the terminal carboxylic group, ii) side chain degradation on the C-S bond, iii) OH attack of the ether groups, and iv) finally •H radical attack on the tertiary carbon. [133-135]

The previously mentioned formation of •OH and •OOH radicals (Section 2.3.1) in the presence of Fe^{2+} and H_2O_2 leads to chemical degradation of the membrane structure. Lim, Kim, and Yun[133] proposed that the radical-induced chemical degradation mechanisms can be characterised into 4 categories, which are summarised in Figure 9 b). First, the unzipping reaction begins with •OH radicals attacking the terminal carboxylic group in the backbone, generating difluoroalkyl radicals(•CF_2-R) and releasing CO_2 and H_2O. The generated •CF_2-R radical reacts with an additional •OH radical, releasing Hydrofluoric Acid (HF), reforming the terminal carboxylic group. This mechanism repeats, removing a difluorocarbene (CF_2) unit from the backbone each time, thereby degrading the membrane. This mechanism, shown in Figure 9 b) is further supported by Curtin *et al.*[135] and Fruhwirt *et al.*[134]

The second proposed mechanism is the attack of the •OH radical on the C-S bond of the PFSA structure, resulting in •CF_2-R radicals, SO_3, and H_2O. The produced •CF_2-R radical results in the unzipping reaction mentioned above by reacting with additional •OH radicals present in solution. Fruhwirt *et al.*[134]proposed an alternative mechanism, suggesting that the •OH radical attacks the SO_3H group, producing the above-mentioned •CF_2-R radical.

Thirdly, the •OH radical attacks the difluoromethoxy group (β-OCF_2) of the side chain, close to the sulfonic acid group, followed by the α-OCF_2 close to the backbone, resulting in decomposition. This is further supported by Fruhwirt *et al.*[134] which can be seen in Figure 10 b).



a) b)

Figure 10: a) Side chain degradation mechanism. b) Mechanism of ether cleavage with subsequent fragmentation and side-chain unzipping. BB represents the backbone of the PFSA ionomer (Reproduced from [134] with permission from RSC under CC BY-NC license: https://creativecommons.org/licenses/by-nc/3.0/)

Lastly, the hydrogen radical (•H) attacks the tertiary carbon near the ether group, resulting in CF chain dissociation of both main and side chains.

PFSA Membrane degradation occurs through several mechanisms and complex chemical kinetics (discussed in section 2.6.1). However, the kinetics and details of degradation and how they are influenced by electrolysis conditions are not yet fully understood. *Ex-situ* degradation tests that expose membrane samples to controlled electrolysis-like environments can provide insights into degradation mechanisms and kinetics without the complexities of an operating electrolyser.

This study focuses solely on Nafion® PFSA membranes; however, extensive research and development are underway to create suitable non-fluorinated cation-exchange membranes for use in electrolysers, fuel cells, and redox flow batteries. An in-depth table comparing the physicochemical properties of fluorinated and hydrocarbon-based PEMs is provided in Annexure D: Recent developments in hydrocarbon-based PEMs.

2.5 PEMWE Accelerated Stress Testing (AST)

Evaluating the durability of a PEMWE traditionally involves monitoring voltage changes over the cell's operational life. With reported lifetimes reaching 20 000 h and degradation rates of 14 $\mu V.h^{-1}$ [33], this approach is prohibitively time-consuming. Consequently, the development of AST protocols is essential to facilitate efficient research and development in PEMWE technology. Compared with the numerous standardised protocols available for fuel cells, ASTs for electrolysers have been significantly less investigated.[136] A major issue is that most existing AST procedures for electrolysis yield results that cannot be compared, often because the specific test conditions are not clearly reported. To address this, the European Commission (EC) has recently proposed harmonised AST protocols for low-temperature electrolysis, which should facilitate future comparisons of results and technologies.[137]

The primary advantages of using ASTs for PEMWE are the significant reduction in time required to induce component degradation and the ability to simulate realistic operational stressors.[72] For fuel cells, the EC has already set clear definitions for ASTs, and methodologies have been proposed to fit these definitions.[138] For instance, Escribano *et al.*[139] suggested a two-step process: first, a baseline is established by measuring degradation from ageing tests that use realistic load profiles and conditions; second, modified load cycles are employed to intensify the degradation and induce voltage loss, thereby achieving a comparable level of performance decay in a much shorter timeframe. A comprehensive review of these AST methodologies as applied to PEMFCs has been presented by Petrone *et al.*[136]

For PEMWE ASTs, Kuhnert *et al.*[140] presents an approach to a review of methodologies proposed for AST of PEMWE systems and Tomic *et al.,* a review on the testing procedures post-degradation, and emphasises the need for standardisation to allow for comparable results.[141]

The following sections discuss PEMWE AST methodologies in accordance with the EC's definitions.[137]

2.5.1 Accelerated Stress Tests (ASTs) for Proton Exchange Membrane Water Electrolysis (PEMWE) Cell Components

Recent research has focused on enhancing electrolytic efficiency while simultaneously reducing material costs, particularly by lowering IrO_2 and Pt loadings to <0.3 and <0.2 $g.cm^{-2}$, respectively.[142] The development of suitable AST protocols is fundamental to achieving these targets by enabling rapid material development. This section reviews proposed AST procedures for the membrane, MEA, catalysts, GDL/PTL, and BPP.

The MEA is widely regarded as the least stable component, and numerous studies have focused on its specific degradation pathways. Grigoriev *et al.*[115] investigated MEAs with platinum at both electrodes, a setup intended to accelerate degradation, by applying galvanostatic pulses cycling from OCV to 1 $A.cm^{-2}$ for 25 h cycles until the electrolyser failed. They found that the electrolyser ceased functioning at 5 500 h of operation, with post-mortem analysis revealing that catalyst-layer corrosion and dissolution into the membrane were the initial failure modes, followed by severe membrane thinning (75% thickness loss).

For *ex-situ* membrane testing, Kundu *et al.*[143] compared two different Nafion® membranes using accelerated ageing tests lasting 3-5 days. They proposed two protocols based on the Fenton-type test: the first method involves submersing the membranes in a mixed solution of Fe^{2+} and H_2O_2, whereas the second is a cation-exchange method in which membranes are first soaked in an Fe^{2+} solution and then transferred to a H_2O_2 solution. The study concluded that although there was no significant chemical difference between the two methods, they produced distinct morphological changes.

Regarding catalysts, most reported ASTs focus on the iridium-based anode catalyst. To obtain stability data, Spöri *et al.*[144] proposed an AST involving voltage cycling between 1.75 V and OCV at 80 ˚C with a 3-second dwell interval for 15,000 cycles (simulating 25 hours of operation). This protocol resulted in a threefold increase in Ir dissolution and a fivefold increase in OER performance loss relative to baseline. Due to the observed excessive dissolution, they proposed a less aggressive protocol at 1.6 V. Similarly, Elia *et al.*[145] proposed a protocol cycling between 1.45 V and 2 V in 1-minute periods at 80 ˚C. Thomassen *et al.*[146] investigated catalyst dissolution using a square-wave current cycling approach between 0.1-1 $A.cm^{-2}$ over 10-minute intervals for 100 hours.

Rozain *et al.*[147] evaluated micro-sized Ti particles as a support for the IrO_2 anode catalyst, using an AST that applied 30-minute current steps between 0-2 $A.cm^{-2}$ at 80 ˚C, simulating a solar energy profile. They found that the micro-sized Ti support provided good cell stability, even with a low IrO_2 loading of 0.1 $mg.cm^{-2}$.

In the related field of fuel cells, Chun *et al.*[148] studied the mechanical degradation of the GDL over 28 days using a dummy cell. It is possible that findings from PEMFC GDL studies, which use tests like freeze/thaw cycles, electrochemical degradation, and immersion in carbon-peroxide solutions, could apply to the cathodic GDL in a PEMWE due to the technological similarities.[149-151] For the use of stainless steel GDLs, Mo *et al.*[92] utilised an AST that applied a high positive potential at the anode to investigate the corrosion and durability of different metals.

In short, the development of ASTs for PEMWE components spans a wide range of electrochemical, mechanical, and chemical testing environments tailored to specific component vulnerabilities. To facilitate a clear comparison between these varying approaches, Table 2 consolidates the baseline protocols discussed above, outlining the targeted cell components, specific testing parameters, durations, and primary degradation outcomes.

Table 2: Summary of cell components AST for PEMWE Reproduced from [72] with permission from Elsevier, under CC BY 4.0 license: https://creativecommons.org/licenses/by/4.0/)

Stressor	Methodology	Cell component
Current density	Galvanostatic pulses, OCV to 1 $A.cm^{-2}$ for 25 h periods until the electrolyser no longer works (5 500 h)	Anode catalyst
	Current steps: 30 min, from 0 to 2 $A.cm^{-2}$. Real solar energy profile applied. T= 80 ˚C	Anode catalyst
	Square-wave current cycle 0.1 − 1 $A.cm^{-2}$, 10 min cycling intervals, and total duration of 100 h.	MEA
Voltage	High positive voltages at the anode.	Stainless steel GDL
	Cycles between 1.45 − 2 V, 1 min periods. T= 80 ˚C	Anode catalyst
	cycling between 1.75 V and OCV. Dwell interval of 3 s for 15 000 cycles. T= 80 ˚C	Anode catalyst
Radical attack	Membrane attack with OH radicals by Fenton-type test	Membrane
Mechanical	Mechanical compression was applied for 28 days.	GDL

2.5.2 Accelerated Stress Tests (ASTs) for Single Cell

Although significant work exists on degradation modelling and ASTs for fuel cells, the development of ASTs for electrolysis cells remains limited. The two technologies are distinct: electrolysers employ Ir- and/or Ru-based anode catalysts and typically use much thicker

membranes, necessitating different analytical methods for studying their degradation. In literature, three groups have attempted to assess electrolyser behaviour under realistic operating conditions.

The first group, Weiß *et al.,*[127] proposed an AST that mimics a variable power profile and simulates inputs from renewable energy. This protocol involved powering the cell at high (3 $A.cm^{-2}$) and low (0.1 $A.cm^{-2}$) current densities, interspersed with periods of inactivity (OCV). Through detailed electrochemical and physical analyses of the MEA, they observed an initial 50 mV increase over the first 10 cycles. This was followed by a performance decrease during the OCV phases, which was attributed to a 1.6-fold increase in High-Frequency Resistance (HFR) over 718 cycles.

The second group, Aßmann *et al.*[152] proposed an AST protocol designed to examine new materials and components. They hypothesised that the primary degradation stressors are power supply fluctuations, high current densities, and periods of inactivity. Their resulting four-step protocol consists of: (i) operation at nominal current density, (ii) high current density cycling, which is believed to primarily degrade the anode catalyst binder, membrane, and any uncoated Ti components, (iii) load cycling, expected to deteriorate the cathode catalyst layer, and (iv) OCV periods, which are also thought to cause degradation on the cathode side.

Finally, Li *et al.*[153], conducted a comprehensive study comparing three single cells under different cycling profiles. The reference cell operated at a constant current density of 1 $A.cm^{-2}$; the second cell underwent variable current-density cycling between 1.2 and 2 $A.cm^{-2}$; and the final cell underwent low-load cycling between 0 and 0.5 $A.cm^{-2}$. The reference cell showed a degradation rate of -29.8 $\mu V.h^{-1}$. The low-load cycling cell showed an increased degradation rate of -51.4 $\mu V.h^{-1}$. However, in contrast to other investigations, the cell subjected to high-load cycling showed a performance gain, with a rate of +55.8 $\mu V.h^{-1}$.

Given the variations in cycling profiles, current densities, and observed degradation phenomena across these studies, a centralised comparison is essential to contextualise their findings. Table 3 summarises the core parameters and key degradation mechanisms of the single-cell AST protocols discussed, serving as a baseline for current PEMWE degradation benchmarks.

Table 3: Summary of single cell AST for PEMWE (Reproduced from [72] with permission from Elsevier, under CC BY 4.0 license: https://creativecommons.org/licenses/by/4.0/)

Stressor	Methodology
Current density	Cycling between 3 and 0.1 A.cm^{-2}, followed by OCV sections for 718 cycles
	Nominal current density, high current density cycling, load cycling, and finally OCV periods.
	3 Tests: Constant current density at 1 A.cm^{-2}, low load cycling between 0-0.5 A.cm^{-2} and high load cycling at 1.2-2 A.cm^{-2}

2.5.3 Accelerated Stress Tests (AST) for Electrolysis Stacks

When moving from single cell analysis to stack-level investigations, published AST protocols are exceptionally scarce. A notable exception is the research by Lee *et al.,*[149] who developed a protocol for a three-cell stack. Their primary goal was to assess the operational integrity of a new, integrated, and flexible micro-sensor. This sensor, fabricated using Micro-Electromechanical Systems (MEMS) technology, was designed to measure key parameters (current, voltage, flow, pressure, and temperature) within the harsh electrolyser environment. After establishing the electrolyser's performance at temperatures above 85 ˚C, Lee *et al.*[149] proposed an AST protocol that involved operating the stack at 95 ˚C and a high voltage of 3 V for 100 h. This voltage was selected as the upper limit because potentials exceeding 3 V would cause irreversible damage to the catalyst.

While *in-situ* ASTs provide system-level data, they are often obscured by mechanical and thermal noise. To isolate the chemical durability of the ionomer, specifically its resistance to the radical attacks identified in Section 2.4, a controlled *ex-situ* environment is required. This necessitates the use of Fenton's reagent.

2.6 Fenton-Based *Ex-situ* Degradation

As the focus of this study is on the use of Fenton-based degradation of PFSAs, the previously discussed (Sections 2.4.1 and 2.4.5.3) formation of •OH and •OOH radicals in the presence of Fe^{2+} and H_2O_2, arising from gas crossover, leads to chemical degradation of the membrane structure. This degradation phenomenon occurs over prolonged periods; therefore, a representative AST method is required to investigate the radical-induced chemical degradation of the PFSA ionomer.

In 1894, Fenton discovered that a mixture of H_2O_2 reacting with Fe^{2+} salts effectively reacts with tartaric acid.[154] Today, the Fenton test is utilised to generate •OH and •OOH radicals during conducting *ex-situ* PFSA degradation studies.[134] The mechanisms by which these radicals attack the PFSA structure, resulting in chemical degradation, are discussed in Section 2.4.5.3.

2.6.1 Generation and Kinetics of •OH, •OOH and H_2O_2

Table 4 presents the reactions involved in the Fenton test and includes the radical-generating (R_{1-2}, R_6), radical-consuming (R_{3-5}, R_{7-13}), and PFSA-related reactions (R_{14-23}).

In 2004, Panchenko *et al.* [155] provided experimental proof that •OH and •OOH radicals are produced while operating a miniature fuel cell within an Electron Paramagnetic Resonance (EPR) spectrometer. The reaction generating •OH and •OOH radicals can be seen in Reaction schemes R_1 and R_2 in Table 4.

Table 4: Summary of kinetic data of simultaneous reactions present during radical-induced PFSA degradation.

For each reaction (R_1–R_{23}), rate constant k at 298.15 K in L.mol^{-1}.s^{-1}, activation energy E_a in kJ. mol^{-1} and pre-exponential factor A in L.mol^{-1}.s^{-1}are given. (Reproduced from [134] with permission from RSC under CC BY-NC license: https://creativecommons.org/licenses/by-nc/3.0/)

	Reaction		k (L.mol^{-1}.s^{-1})	E_a (kJ.mol^{-1})	A (L.mol^{-1}.s^{-1})
R_1	$Fe^{2+} + H_2O_2 + H^+ \rightarrow Fe^{3+} + \bullet OH + H_2O$	$r_1 = k_1[Fe^{2+}][H_2O_2]$	66	35.4	1.05×10^8
R_2	$Fe^{3+} + H_2O_2 \rightarrow Fe^{2+} + \bullet OOH + H^+$	$r_2 = k_2[Fe^{3+}][H_2O_2]$	8.6×10^{-4}	126	8.43×10^{18}
R_3	$Fe^{2+} + \bullet OH + H^+ \rightarrow Fe^{3+} + H_2O$	$r_3 = k_3[Fe^{2+}][\bullet OH]$	3.6×10^8 [a]	9	1.37×10^{10}
R_4	$Fe^{2+} + \bullet OOH + H^+ \rightarrow Fe^{3+} + H_2O_2$	$r_4 = k_4[Fe^{2+}][\bullet OOH]$	1.2×10^6	42	2.74×10^{13}
R_5	$Fe^{3+} + \bullet OOH \rightarrow Fe^{2+} + H^+ + O_2$	$r_5 = k_5[Fe^{3+}][\bullet OOH]$	8.1×10^4	33	4.9×10^{10}
R_6	$H_2O_2 \rightarrow 2\bullet OH$	$r_6 = k_6[H_2O_2]$	6.5×10^{-23} [s^{-1}]	201	10^{13} [s^{-1}]
R_7	$\bullet OH + H_2O_2 \rightarrow \bullet OOH + H_2O$	$r_7 = k_7[\bullet OH][H_2O_2]$	3.0×10^7 [a]	14	8.43×10^9
R_8	$\bullet OOH + H_2O_2 \rightarrow \bullet OH + H_2O + O_2$	$r_8 = k_8[\bullet OOH][H_2O_2]$	3.7	33.5 [b]	2.71×10^6
R_9	$2\bullet OOH \rightarrow H_2O_2 + O_2$	$r_9 = k_9[\bullet OOH]^2$	9.1×10^5 [a]	20.6	3.70×10^9
R_{10}	$2\bullet OH \rightarrow H_2O_2$	$r_{10} = k_{10}[\bullet OH]^2$	5.3×10^9 [a]	8	1.33×10^{11}
R_{11}	$\bullet OOH + \bullet OH \rightarrow H_2O + O_2$	$r_{11} = k_{11}[\bullet OOH][\bullet OH]$	1.1×10^{10} [a]	14.2	3.39×10^{12}
R_{12}	$\bullet OH + H_2 \rightarrow H_2O + \bullet H$	$r_{12} = k_{12}[\bullet OH][H_2]$	3.9×10^7 [a]	19.2	9.14×10^{10}
R_{13}	$\bullet H + O_2 \rightarrow \bullet OOH$	$r_{13} = k_{13}[\bullet H][O_2]$	2.2×10^{10} [a]	10.3	1.37×10^{12}
R_{14}	$SC–SO_3H + \bullet OH \rightarrow SC–O\bullet + HOCF_2CF_2SO_3H$	$r_{14} = k_{14}[SC–SO_3H][\bullet OH]$	3.7×10^6	70 [c]	6.80×10^{18}
R_{15}	$SC–O\bullet + 3\bullet OH \rightarrow BB–O\bullet + 6HF + 3CO_2$	$r_{15} = k_{15}[SC–O\bullet][\bullet OH]$	3×10^7	70 [c]	5.51×10^{19}
R_{16}	$BB–O\bullet + \bullet OH \rightarrow 2–(CF_2)_n COOH + 3HF$	$r_{16} = k_{16}[BB–O\bullet][\bullet OH]$	8.5×10^7	70 [c]	1.56×10^{20}
R_{17}-R_{23}	$–(CF_2)_nCOOH + 2\bullet OH \rightarrow –(CF_2)_{n-1}COOH + CO_2 + 2HF$	$r_{unzip} = k_{unzip}[–(CF_2)_nCOOH][\bullet OH]$ ($7 \leq n \leq 1$)	1.0×10^6 [d]	70 [c]	1.84×10^{18}

[a] Rate constant calculated for T = 298.15 K.
[b] Activation energy is estimated between 6 and 10 kcal mol^{-1}.
[c] Average activation energy found in various degradation experiments.
[d] Upper limit for the attack of •OH on CF_3COOH.

Evidence for H_2O_2 formation was provided by Liu and Zuckerbrod, who detected micromolar concentrations of H_2O_2 during membrane operation under OCV conditions at 60 ˚C.[156] Additionally, they observed a relationship between H_2O_2 concentration and membrane thickness,

with higher H_2O_2 concentrations when thinner membranes were used. It is suggested that gas crossover increases with thinner membranes.[156]

Fruhwirt *et al.*[134] modelled, and predicted chemical membrane degradation using a holistic zero-dimensional kinetic framework with the use of the Fenton test conditions (3 wt% H_2O_2 and 13 ppm Fe^{2+}) and concluded the following: i) During the initial stages of the PFSA degradation via the Fenton test, the mechanical stability is unaffected as the first ether bridge and head group are decomposed. ii) Once the degradation continues, R_{16} is initiated, which leads to a fragmentation of the main chain at the anchor position, followed by shortening of the main chain (R_{17}–R_{23}). From this point on, the membrane's mechanical properties are affected.

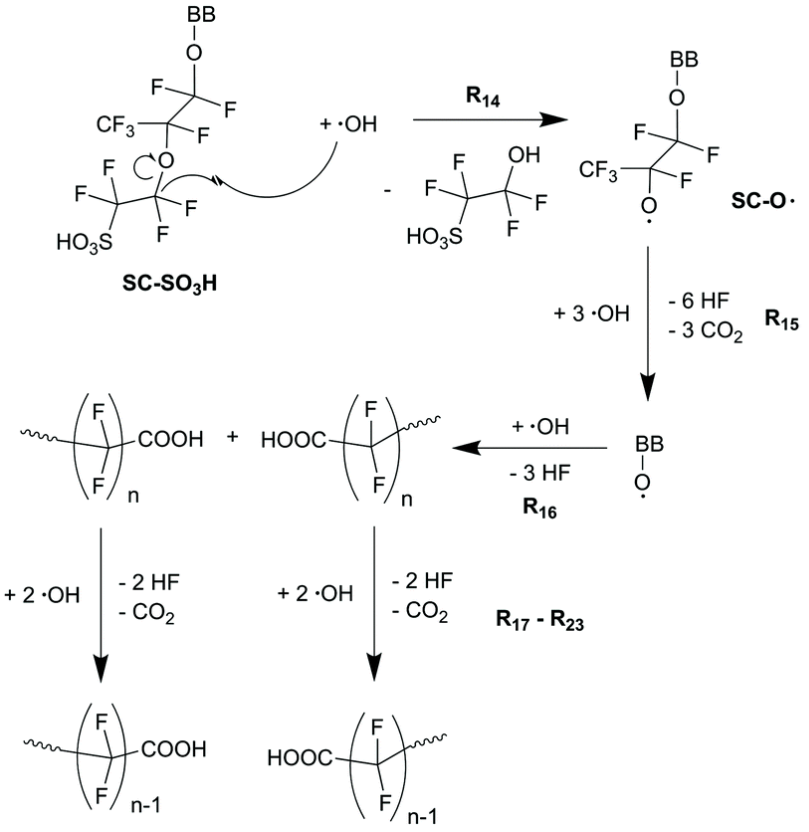


Figure 11: Sidechain degradation of PFSA via Fenton solution (Reproduced with permission from RSC under CC BY-NC license: https://creativecommons.org/licenses/by-nc/3.0/)

With examination of the kinetic data presented in Table 4 from Fruhwirt *et al.*[134] an insight into the relative rates and controlling factors of the various reactions occurring during a Fenton test is obtained. The rate constants (k) and activation energies (E_a) reveal a highly competitive environment where the degradation of the PFSA polymer is not the primary fate of the generated •OH radicals.

There is an appreciable difference in reaction rates (*r*) between the radical quenching ($R_{9\text{-}11}$, defined as self-elimination of radical species) and scavenging ($R_{3\text{-}5,7\text{-}8,12\text{-}13}$) pathways and the

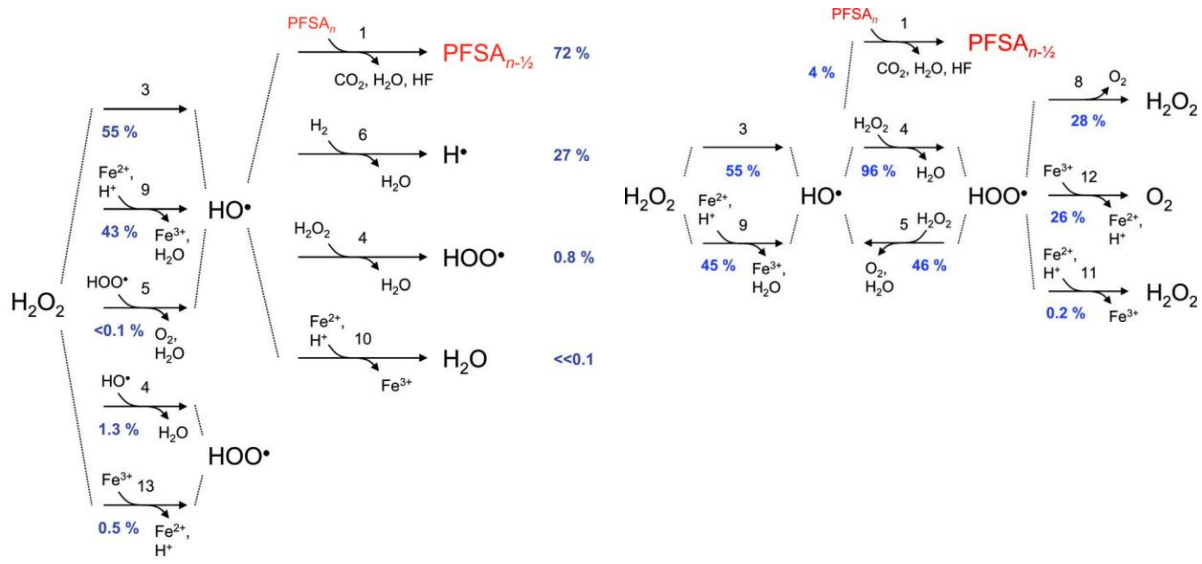
reactions leading to polymer degradation (R_{14-23}). The rate constants for radical-radical interactions, such as the self-quenching of two •OH radicals (R_{10}: k = 5.3 x 10^9 L.mol^{-1}.s^{-1}) and the reaction between •OH and •OOH radicals (R_{11}: k = 1.1 x 10^{10} L.mol^{-1}.s^{-1}), are exceptionally high. Similarly, the scavenging of •OH radicals by Fe^{2+} ions (R_3: k = 3.6 x 10^8 L.mol^{-1}.s^{-1}) and excess H_2O_2 (R_7: k = 3.0 x 10^7 L.mol^{-1}.s^{-1}) are also rapid processes.

In stark contrast, the initial, rate-determining attacks on the PFSA polymer structure exhibit significantly lower rate constants. The attack on the sulfonic acid side chain (R_{14}) and the main-chain unzipping reaction (R_{17-23}) have rate constants of 3.7 x 10^6 and 1.0 x 10^6 L.mol^{-1}.s^{-1}, respectively. This disparity, spanning two to four orders of magnitude, indicates that ionomer degradation is a kinetically slower process. Most •OH radicals generated via the Fenton reaction (R_1) are consumed by the much faster quenching and scavenging side reactions before they can diffuse and react with the polymer backbone or side chains. This kinetic competition provides a fundamental explanation for the experimental observation that only a small fraction of generated radicals ultimately contributes to membrane damage.

Furthermore, the E_a highlight the temperature sensitivity of these competing pathways. The polymer degradation reactions (R_{14}-R_{23}) are characterised by a high activation energy of approximately 70 kJ.mol^{-1}. Conversely, the dominant radical scavenging and quenching reactions (R_3, R_7, R_{10}) have significantly lower activation energies, typically in the range of 8-14 kJ.mol^{-1}. This indicates that the rate of polymer degradation is far more dependent on temperature than the rate of radical quenching. As the system temperature increases, the rate of degradation reactions increases exponentially more than that of competing quenching reactions, shifting the kinetic balance toward more aggressive polymer attack. This provides a clear kinetic basis for the empirically observed acceleration of membrane degradation and for the increase in FRR at elevated operating temperatures. This kinetic disparity also provides the fundamental rationale for conducting the present study's Fenton tests at an elevated temperature of 80 °C (as detailed in Chapter 3), as this preferentially accelerates the kinetically limited degradation pathways relative to the faster, less temperature-dependent scavenging reactions, thereby achieving a relevant and accelerated degradation profile.

Figure 12 from Lorenz *et. al.*[131] provides further supporting information for the rates of radical quenching and scavenging reactions. They investigated the rate of degradation caused by the Fenton test (1M H_2O_2 and 1 ppm Fe^{2+}) and found that only 4% of •OH radicals produced react with the ionomer, as the majority self-quenches by reacting with H_2O_2, forming water and •OOH radicals as depicted in Figure 12 b). These radicals can react via path 5 with water and oxygen to regenerate •OH radicals. This results in a highly dynamic equilibrium system in which •OH and •OOH radicals continuously interchange.

Additionally, they found that 54.2% of •OOH radicals are decomposed to H_2O_2 and O_2 via paths 8, 11 and 12 in Figure 12 b).



a) b)

Figure 12: a) Hydrogen peroxide reaction sequence in the presence of 1ppm Fe and PFSA. b) Dominant reactions of *ex-situ* Fenton test at 1M H_2O_2 and 1ppm Fe. (Reproduced from [131] with permission from IOP Publishing under CC BY-NC license: https://creativecommons.org/licenses/by-nc/3.0/)

The kinetic data reveal that PFSA degradation is governed by a series of relatively slow, high-activation-energy reactions that compete with rapid, low-activation-energy radical-quenching pathways. The initial attack on the polymer is the primary kinetic bottleneck, and the overall degradation rate is highly sensitive to temperature, which preferentially accelerates damaging reactions relative to quenching mechanisms.

2.6.2 Summary

This literature survey initially contextualises hydrogen as a critical energy carrier and a green chemical feedstock in the global transition away from fossil fuels, categorising production methods by their environmental impact and identifying water electrolysis as a sustainable pathway. Among available technologies, PEMWE is a leading candidate for integration with renewable energy sources due to its compact design and dynamic operational capabilities; however, it remains constrained by material costs and durability issues. The discussion then turns to the fundamental components of the PEMWE cell, specifically the MEA, and reviews the primary degradation modes that affect component longevity, including catalyst dissolution, bipolar plate passivation, and membrane thinning.

This literature survey has established that the chemical degradation of the PFSA membrane is a barrier to achieving the long-term durability required for the widespread commercialisation of PEMWE.

The urgency of addressing PEMWE degradation is highlighted by the ambitious key performance indicators set by global energy departments. According to the US Technical Targets for PEME stacks, the ultimate lifetime target is 80 kh of operation.[157] To reach this, the average degradation rate must decline to 2.0 $mV.kh^{-1}$ (or $0.13\%.kh^{-1}$), a significant reduction from the 2022 status of 4.8 $mV.kh^{-1}$. Similarly, European targets aim for a reduction in degradation from $0.19\%.kh^{-1}$ (2020 State of the Art) to 0.12% by 2030.[158]

Achieving these KPIs requires a move beyond incremental improvements toward a fundamental mitigation of the chemical stressors that govern the membrane's end-of-life.

The consensus in the literature is that the principal failure mode is initiated by a complex series of radical attacks (primarily by •OH and •OOH species) on the ionomer structure. A crucial finding is that this process is dramatically accelerated by metallic impurities, particularly ferrous ions (Fe^{2+}), which catalyse radical formation via Fenton-like chemistry, making them the most aggressive and relevant contaminant species to study.

A key takeaway from detailed kinetic studies is that PFSA polymer degradation is kinetically slower. The reactions leading to polymer chain scission are in direct competition with radical quenching and scavenging pathways that are several orders of magnitude faster. This kinetic competition explains why operational parameters, especially temperature, play such a significant role. The high activation energy of the polymer degradation reactions (~70 $kJ \cdot mol^{-1}$) compared to the low activation energy of the quenching reactions (8-14 $kJ \cdot mol^{-1}$) means that elevated temperatures disproportionately accelerate the destructive pathways. The take-home message from the existing body of work is therefore clear: while *ex-situ* Fenton-based ASTs are a valid and indispensable tool for probing these complex mechanisms, the results are highly sensitive to the specific conditions applied. More importantly, a direct quantitative link between the chemical markers measured in these tests (e.g., IEC loss or FRR) and the resulting functional decay of the membrane in an operating electrolyser remains an area of active investigation.

This survey, therefore, reveals a gap between the fundamental understanding of chemical degradation and its practical implications for electrolyser performance. While many studies have successfully used *ex-situ* methods to characterise chemical changes and others have documented *in-situ* performance decay, there is a lack of research that systematically and quantitatively links the two. The primary contribution of this work is to bridge this divide.

Bibliography

(1) Jain, R.; Panwar, N. L.; Chitranjan Agarwal; Gupta, T. A comprehensive review on unleashing the power of hydrogen: revolutionizing energy systems for a sustainable future. *Environmental Science and Pollution Research* **2025**, *32* (22), 13329-13359. DOI: 10.1007/s11356-024-33541-1.

(2) (IEA), I. E. A. *Global Hydrogen Review 2024*. 2024. https://www.iea.org/reports/global-hydrogen-review-2024 (accessed 2026 08-03).

(3) Birol, F. The future of hydrogen: seizing today's opportunities. *IEA Report prepared for the G* **2019**, *20*, 442.

(4) Energieagentur, I. *Towards hydrogen definitions based on their emissions intensity*; OECD Publishing, 2023.

(5) Gateway, W. The Western Gateway Hydrogen Ecosystem. In *Providing the nation with a testbed for developing the UK hydrogen economy.*, 2022; p 8.

(6) Arcos, J. M. M.; Santos, D. M. F. The Hydrogen Color Spectrum: Techno-Economic Analysis of the Available Technologies for Hydrogen Production. In *Gases*, 2023; Vol. 3, pp 25-46.

(7) Schneider, S.; Bajohr, S.; Graf, F.; Kolb, T. State of the Art of Hydrogen Production via Pyrolysis of Natural Gas. *ChemBioEng Reviews* **2020**, *7* (5), 150-158. DOI: https://doi.org/10.1002/cben.202000014.

(8) Chirosca, A.-M.; Rusu, E.; Minzu, V. Green Hydrogen—Production and Storage Methods: Current Status and Future Directions. In *Energies*, 2024; Vol. 17.

(9) Lollar, B. S.; Onstott, T. C.; Lacrampe-Couloume, G.; Ballentine, C. The contribution of the Precambrian continental lithosphere to global H2 production. *Nature* **2014**, *516* (7531), 379-382.

(10) Akhlaghi, N.; Najafpour-Darzi, G. A comprehensive review on biological hydrogen production. *International Journal of Hydrogen Energy* **2020**, *45* (43), 22492-22512. DOI: https://doi.org/10.1016/j.ijhydene.2020.06.182.

(11) Tamagnini, P.; Axelsson, R.; Lindberg, P.; Oxelfelt, F.; Wünschiers, R.; Lindblad, P. Hydrogenases and Hydrogen Metabolism of Cyanobacteria. *Microbiology and Molecular Biology Reviews* **2002**, *66* (1), 1-20. DOI: 10.1128/mmbr.66.1.1-20.2002 (acccessed 2025/04/16).

(12) Millet, P. Fundamentals of Water Electrolysis. In *Hydrogen Production*, 2015; pp 33-62.

(13) (IEA), I. E. A. *Comparison of the emissions intensity of different hydrogen production routes, 2021*. 2023. https://www.iea.org/data-and-statistics/charts/comparison-of-the-emissions-intensity-of-different-hydrogen-production-routes-2021 (accessed 2025 16 April).

(14) Sharma, S.; Ghoshal, S. K. Hydrogen the future transportation fuel: From production to applications. *Renewable and Sustainable Energy Reviews* **2015**, *43*, 1151-1158. DOI: https://doi.org/10.1016/j.rser.2014.11.093.

(15) Okunola A, A.; Kehinde I, O.; Oluwaseun, A.; Olufiropo E, A. Public and Environmental Health Effects of Plastic Wastes Disposal: A Review. *Journal of Toxicology and Risk Assessment* **2019**, *5* (2). DOI: 10.23937/2572-4061.1510021.

(16) Alka, D. K.; Vinod Kumar, S.; Prakash Dhondiram, C.; Vinod Atmaram, M. Co-gasification of coal and biomass an emerging clean energy technology: Status and prospects of development in Indian context. *International Journal of Mining Science and Technology* **2019**, *29* (2), 171-186. DOI: https://doi.org/10.1016/j.ijmst.2018.03.011.

(17) Shah, H. H.; Amin, M.; Iqbal, A.; Nadeem, I.; Kalin, M.; Soomar, A. M.; Galal, A. M. A review on gasification and pyrolysis of waste plastics. *Frontiers in Chemistry* **2023**, *Volume 10 - 2022*, Review. DOI: 10.3389/fchem.2022.960894.

(18) Argyle, M. D.; Bartholomew, C. H. Heterogeneous Catalyst Deactivation and Regeneration: A Review. In *Catalysts*, 2015; Vol. 5, pp 145-269.

(19) Han, J.; Kim, H. The reduction and control technology of tar during biomass gasification/pyrolysis: An overview. *Renewable and Sustainable Energy Reviews* **2008**, *12* (2), 397-416. DOI: https://doi.org/10.1016/j.rser.2006.07.015.

(20) Temitope, A. Optimization of Plastic Pyrolysis Conditions for High Syngas Yield. University of Lagos: 2025.

(21) Al-Qadri, A. A.; Ahmed, U.; Ahmad, N.; Abdul Jameel, A. G.; Zahid, U.; Naqvi, S. R. A review of hydrogen generation through gasification and pyrolysis of waste plastic and tires: Opportunities and challenges. *International Journal of Hydrogen Energy* **2024**, *77*, 1185-1204. DOI: https://doi.org/10.1016/j.ijhydene.2024.06.207.

(22) Maier, M.; Schulze-Netzer, C.; Adams, T. A., II. Chemical Recycling of Plastic Waste via Production of Ethylene from Gasification Syngas. *Industrial & Engineering Chemistry Research* **2025**, *64* (1), 575-589. DOI: 10.1021/acs.iecr.4c03441.

(23) Dou, X.; Veksha, A.; Chan, W. P.; Oh, W.-D.; Liang, Y. N.; Teoh, F.; Mohamed, D. K. B.; Giannis, A.; Lisak, G.; Lim, T.-T. Poisoning effects of H2S and HCl on the naphthalene steam reforming and water-gas shift activities of Ni and Fe catalysts. *Fuel* **2019**, *241*, 1008-1018.

(24) Ungureanu, N.; Vlăduț, N.-V.; Biriș, S.-Ș.; Ionescu, M.; Gheorghiță, N.-E. Municipal Solid Waste Gasification: Technologies, Process Parameters, and Sustainable Valorization of By-Products in a Circular Economy. In *Sustainability*, 2025; Vol. 17, p 6704.

(25) *Hydrogen Production Using Nuclear Energy*; INTERNATIONAL ATOMIC ENERGY AGENCY, 2013.

(26) Badwal, S. P. S.; Giddey, S. S.; Munnings, C.; Bhatt, A. I.; Hollenkamp, A. F. Emerging electrochemical energy conversion and storage technologies. *Frontiers in Chemistry* **2014**, *Volume 2 - 2014*, Review. DOI: 10.3389/fchem.2014.00079.

(27) Zhang, W.; Yu, B.; Xu, J. Efficiency evaluation of high-temperature steam electrolytic systems coupled with different nuclear reactors. *International Journal of Hydrogen Energy* **2012**, *37* (17), 12060-12068. DOI: https://doi.org/10.1016/j.ijhydene.2012.04.024.

(28) Demkowicz, P., Medvedev, P., DeWall, K., Lessing, P., & Sachdev, P. Materials degradation studies for high temperature steam electrolysis systems. In *2007 International Topical Meeting on Safety and Technology of Nuclear Hydrogen Production, Control, and Management*, 2007; pp 202-206.

(29) Iglesias, N.; Díaz, E. Influence of H2S and CO2 Partial Pressures and Temperature on the Corrosion of Superduplex S32750 Stainless Steel. In *Corrosion and Materials Degradation*, 2025; Vol. 6, p 20.

(30) Xu, D.; Dong, L.; Ren, J. Chapter 2 - Introduction of hydrogen routines. In *Hydrogen Economy (Second Edition)*, Scipioni, A., Manzardo, A., Ren, J. Eds.; Academic Press, 2023; pp 45-65.

(31) Mulk, W. U.; Aziz, A. R. A.; Ismael, M. A.; Ghoto, A. A.; Ali, S. A.; Younas, M.; Gallucci, F. Electrochemical hydrogen production through anion exchange membrane water electrolysis (AEMWE): Recent progress and associated challenges in hydrogen production. *International Journal of Hydrogen Energy* **2024**, *94*, 1174-1211. DOI: https://doi.org/10.1016/j.ijhydene.2024.11.143.

(32) Trasatti, S. Water electrolysis: who first? *Journal of Electroanalytical Chemistry* **1999**, *476* (1), 90-91. DOI: https://doi.org/10.1016/S0022-0728(99)00364-2.

(33) Carmo, M.; Fritz, D. L.; Mergel, J.; Stolten, D. A comprehensive review on PEM water electrolysis. *International Journal of Hydrogen Energy* **2013**, *38* (12), 4901-4934. DOI: https://doi.org/10.1016/j.ijhydene.2013.01.151.

(34) Grubb, W. T.; Niedrach, L. W. Batteries with Solid Ion-Exchange Membrane Electrolytes: II . Low-Temperature Hydrogen-Oxygen Fuel Cells. *Journal of The Electrochemical Society* **1960**, *107* (2), 131. DOI: 10.1149/1.2427622.

(35) Grubb, W. T. Batteries with Solid Ion Exchange Electrolytes: I . Secondary Cells Employing Metal Electrodes. *Journal of The Electrochemical Society* **1959**, *106* (4), 275. DOI: 10.1149/1.2427329.

(36) Thomassen, M. S.; Reksten, A. H.; Barnett, A. O.; Khoza, T.; Ayers, K. Chapter 6 - PEM water electrolysis. In *Electrochemical Power Sources: Fundamentals, Systems, and Applications*, Smolinka, T., Garche, J. Eds.; Elsevier, 2022; pp 199-228.

(37) Wolf, S. E.; Winterhalder, F. E.; Vibhu, V.; de Haart, L. G. J.; Guillon, O.; Eichel, R.-A.; Menzler, N. H. Solid oxide electrolysis cells – current material development and industrial application. *Journal of Materials Chemistry A* **2023**, *11* (34), 17977-18028, 10.1039/D3TA02161K. DOI: 10.1039/D3TA02161K.

(38) Kuhnert, E.; Heidinger, M.; Sandu, D.; Hacker, V.; Bodner, M. Analysis of PEM Water Electrolyzer Failure Due to Induced Hydrogen Crossover in Catalyst-Coated PFSA Membranes. *Membranes* **2023**, *13* (3), 348.

(39) Mandal, M. Novel Electrocatalyst for Alkaline Membrane Water Electrolysis. *ChemElectroChem* **2020**, *7* (21), 4303-4305. DOI: https://doi.org/10.1002/celc.202001074.

(40) Lee, S. A.; Kim, J.; Kwon, K. C.; Park, S. H.; Jang, H. W. Anion exchange membrane water electrolysis for sustainable large-scale hydrogen production. *Carbon Neutralization* **2022**, *1* (1), 26-48.

(41) Tang, D.; Tan, G.-L.; Li, G.-W.; Liang, J.-G.; Ahmad, S. M.; Bahadur, A.; Humayun, M.; Ullah, H.; Khan, A.; Bououdina, M. State-of-the-art hydrogen generation techniques and storage methods: A critical review. *Journal of Energy Storage* **2023**, *64*, 107196. DOI: https://doi.org/10.1016/j.est.2023.107196.

(42) Lee, J.; Jung, H.; Park, Y. S.; Woo, S.; Yang, J.; Jang, M. J.; Jeong, J.; Kwon, N.; Lim, B.; Han, J. W. High-efficiency anion-exchange membrane water electrolyzer enabled by ternary layered double hydroxide anode. *Small* **2021**, *17* (28), 2100639.

(43) Ji, M.; Wang, J. Review and comparison of various hydrogen production methods based on costs and life cycle impact assessment indicators. *International Journal of Hydrogen Energy* **2021**, *46* (78), 38612-38635. DOI: https://doi.org/10.1016/j.ijhydene.2021.09.142.

(44) Chen, Y.; Liu, C.; Xu, J.; Xia, C.; Wang, P.; Xia, B. Y.; Yan, Y.; Wang, X. Key Components and Design Strategy for a Proton Exchange Membrane Water Electrolyzer. *Small Structures* **2023**, *4* (6), 2200130. DOI: https://doi.org/10.1002/sstr.202200130 (acccessed 2025/04/15).

(45) Zeng, K.; Zhang, D. Recent progress in alkaline water electrolysis for hydrogen production and applications. *Progress in Energy and Combustion Science* **2010**, *36* (3), 307-326. DOI: https://doi.org/10.1016/j.pecs.2009.11.002.

(46) Wendt, H.; Hofmann, H. Ceramic diaphragms for advanced alkaline water electrolysis. *Journal of Applied Electrochemistry* **1989**, *19* (4), 605-610. DOI: 10.1007/BF01022121.

(47) Khouya, A. Levelized costs of energy and hydrogen of wind farms and concentrated photovoltaic thermal systems. A case study in Morocco. *International Journal of Hydrogen Energy* **2020**, *45* (56), 31632-31650. DOI: https://doi.org/10.1016/j.ijhydene.2020.08.240.

(48) Vincent, I.; Bessarabov, D. Low cost hydrogen production by anion exchange membrane electrolysis: A review. *Renewable and Sustainable Energy Reviews* **2018**, *81*, 1690-1704. DOI: https://doi.org/10.1016/j.rser.2017.05.258.

(49) Hu, K.; Fang, J.; Ai, X.; Huang, D.; Zhong, Z.; Yang, X.; Wang, L. Comparative study of alkaline water electrolysis, proton exchange membrane water electrolysis and solid oxide electrolysis through multiphysics modeling. *Applied Energy* **2022**, *312*, 118788. DOI: https://doi.org/10.1016/j.apenergy.2022.118788.

(50) Xu, Y.; Cai, S.; Chi, B.; Tu, Z. Technological limitations and recent developments in a solid oxide electrolyzer cell: A review. *International Journal of Hydrogen Energy* **2024**, *50*, 548-591. DOI: https://doi.org/10.1016/j.ijhydene.2023.08.314.

(51) Vinodh, R.; Kalanur, S. S.; Natarajan, S. K.; Pollet, B. G. Recent advancements of polymeric membranes in anion exchange membrane water electrolyzer (AEMWE): A critical review. *Polymers* **2023**, *15* (9), 2144.

(52) Ayers, K. E.; Anderson, E. B.; Capuano, C.; Carter, B.; Dalton, L.; Hanlon, G.; Manco, J.; Niedzwiecki, M. Research Advances towards Low Cost, High Efficiency PEM Electrolysis. *ECS Transactions* **2010**, *33* (1), 3. DOI: 10.1149/1.3484496.

(53) Yuan, X.-Z.; Shaigan, N.; Song, C.; Aujla, M.; Neburchilov, V.; Kwan, J. T. H.; Wilkinson, D. P.; Bazylak, A.; Fatih, K. The porous transport layer in proton exchange membrane water electrolysis: perspectives on a complex component. *Sustainable Energy & Fuels* **2022**, *6* (8), 1824-1853, 10.1039/D2SE00260D. DOI: 10.1039/D2SE00260D.

(54) Kıstı, M.; Hüner, B.; Albadwi, A.; Özdoğan, E.; Uzgören İ, N.; Uysal, S.; Conağası, M.; Süzen, Y. O.; Demir, N.; Kaya, M. F. Recent Advances in Polymer Electrolyte Membrane Water Electrolyzer Stack Development Studies: A Review. *ACS Omega* **2025**, *10* (10), 9824-9853. DOI: 10.1021/acsomega.4c10147 From NLM.

(55) Ito, H.; Maeda, T.; Nakano, A.; Takenaka, H. Properties of Nafion membranes under PEM water electrolysis conditions. *International Journal of Hydrogen Energy* **2011**, *36*, 10527-10540. DOI: 10.1016/j.ijhydene.2011.05.127.

(56) Dotan, H.; Landman, A.; Sheehan, S. W.; Malviya, K. D.; Shter, G. E.; Grave, D. A.; Arzi, Z.; Yehudai, N.; Halabi, M.; Gal, N.; et al. Decoupled hydrogen and oxygen evolution by a two-step electrochemical–chemical cycle for efficient overall water splitting. *Nature Energy* **2019**, *4* (9), 786-795. DOI: 10.1038/s41560-019-0462-7.

(57) Wang, C.; Feng, L. Recent advances and perspectives of Ir-based anode catalysts in PEM water electrolysis. *Energy Advances* **2024**, *3* (1), 14-29, 10.1039/D3YA00492A. DOI: 10.1039/D3YA00492A.

(58) METALS, T. P. *Electrocatalysts for Fuel Cell / Water Electrolysis (PEM type)*. https://tanaka-preciousmetals.com/en/products/detail/pefcs/ (accessed 2025.

(59) Wang, C. R.; Stansberry, J. M.; Mukundan, R.; Chang, H.-M. J.; Kulkarni, D.; Park, A. M.; Plymill, A. B.; Firas, N. M.; Liu, C. P.; Lang, J. T.; et al. Proton Exchange Membrane (PEM) Water Electrolysis: Cell-Level Considerations for Gigawatt-Scale Deployment. *Chemical Reviews* **2025**, *125* (3), 1257-1302. DOI: 10.1021/acs.chemrev.3c00904.

(60) Padgett, E.; Bender, G.; Haug, A.; Lewinski, K.; Sun, F.; Yu, H.; Cullen, D. A.; Steinbach, A. J.; Alia, S. M. Catalyst Layer Resistance and Utilization in PEM Electrolysis. *Journal of The Electrochemical Society* **2023**, *170* (8), 084512. DOI: 10.1149/1945-7111/acee25.

(61) Yuan, S.; Zhao, C.; Luo, L.; Fu, C.; Li, H.; An, L.; Cheng, X.; Shen, S.; Yin, J.; Yan, X.; et al. Revealing the Role of the Ionomer at the Triple-Phase Boundary in a Proton-Exchange Membrane Water Electrolyzer. *The Journal of Physical Chemistry Letters* **2024**, *15* (19), 5223-5230. DOI: 10.1021/acs.jpclett.4c00851.

(62) Bernt, M.; Gasteiger, H. A. Influence of Ionomer Content in IrO2/TiO2 Electrodes on PEM Water Electrolyzer Performance. *Journal of The Electrochemical Society* **2016**, *163* (11), F3179. DOI: 10.1149/2.0231611jes.

(63) Yuan, S.; Zhao, C.; Li, H.; Shen, S.; Yan, X.; Zhang, J. Rational electrode design for low-cost proton exchange membrane water electrolyzers. *Cell Reports Physical Science* **2024**, *5* (3), 101880. DOI: https://doi.org/10.1016/j.xcrp.2024.101880.

(64) Jang, Y.; Seol, C.; Kim, S. M.; Jang, S. Investigation of the correlation effects of catalyst loading and ionomer content in an anode electrode on the performance of polymer electrode membrane water electrolysis. *International Journal of Hydrogen Energy* **2022**, *47* (42), 18229-18239. DOI: https://doi.org/10.1016/j.ijhydene.2022.04.019.

(65) Lee, J. K.; Anderson, G.; Tricker, A. W.; Babbe, F.; Madan, A.; Cullen, D. A.; Arregui-Mena, J. D.; Danilovic, N.; Mukundan, R.; Weber, A. Z.; et al. Ionomer-free and recyclable porous-transport electrode for high-performing proton-exchange-membrane water electrolysis. *Nature Communications* **2023**, *14* (1), 4592. DOI: 10.1038/s41467-023-40375-x.

(66) Liu, H.; Wang, X.; Lao, K.; Wen, L.; Huang, M.; Liu, J.; Hu, T.; Hu, B.; Xie, S.; Li, S.; et al. Optimizing Ionomer Distribution in Anode Catalyst Layer for Stable Proton Exchange Membrane Water Electrolysis. *Advanced Materials* **2024**, *36* (28), 2402780. DOI: https://doi.org/10.1002/adma.202402780 (acccessed 2026/01/11).

(67) Jung, G.-B.; Chan, S.-H.; Lai, C.-J.; Yeh, C.-C.; Yu, J.-W. Innovative Membrane Electrode Assembly (MEA) Fabrication for Proton Exchange Membrane Water Electrolysis. *Energies* **2019**, *12* (21), 4218.

(68) Liu, J.; Liu, H.; Yang, Y.; Tao, Y.; Zhao, L.; Li, S.; Fang, X.; Lin, Z.; Wang, H.; Tao, H. B.; et al. Efficient and Stable Proton Exchange Membrane Water Electrolysis Enabled by Stress Optimization. *ACS Central Science* **2024**, *10* (4), 852-859. DOI: 10.1021/acscentsci.4c00037.

(69) Wang, Y.; Wang, Z.; Qiao, J.; Li, H.; Wang, X.; Cao, B.; Zhu, T.; Zhang, B.; Wang, M. Materials and flow fields of bipolar plates in polymer electrolyte membrane water electrolysis: A review. *Energy Reviews* **2025**, *4* (2), 100132. DOI: https://doi.org/10.1016/j.enrev.2025.100132.

(70) Zagoraiou, E.; Krishan, S.; Siriwardana, A.; Moschovi, A. M.; Yakoumis, I. Performance of Stainless-Steel Bipolar Plates (SS-BPPs) in Polymer Electrolyte Membrane Water Electrolyser (PEMWE): A Comprehensive Review. In *Compounds*, 2024; Vol. 4, pp 252-267.

(71) de Bruijn, F. A.; Dam, V. A. T.; Janssen, G. J. M. Review: Durability and Degradation Issues of PEM Fuel Cell Components. *Fuel Cells* **2008**, *8* (1), 3-22. DOI: https://doi.org/10.1002/fuce.200700053 (acccessed 2025/06/20).

(72) Urbano, E.; Pahon, E.; Yousfi-Steiner, N.; Guillou, M. Accelerated stress testing in proton exchange membrane water electrolysis - critical review. *Journal of Power Sources* **2024**, *623*, 235451. DOI: https://doi.org/10.1016/j.jpowsour.2024.235451.

(73) Hartig-Weiss, A.; Miller, M.; Beyer, H.; Schmitt, A.; Siebel, A.; Freiberg, A. T. S.; Gasteiger, H. A.; El-Sayed, H. A. Iridium Oxide Catalyst Supported on Antimony-Doped Tin Oxide for High Oxygen Evolution Reaction Activity in Acidic Media. *ACS Applied Nano Materials* **2020**, *3* (3), 2185-2196. DOI: 10.1021/acsanm.9b02230.

(74) Bernt, M.; Hartig-Weiß, A.; Tovini, M. F.; El-Sayed, H. A.; Schramm, C.; Schröter, J.; Gebauer, C.; Gasteiger, H. A. Current Challenges in Catalyst Development for PEM Water Electrolyzers. *Chemie Ingenieur Technik* **2020**, *92* (1-2), 31-39. DOI: https://doi.org/10.1002/cite.201900101 (acccessed 2025/04/08).

(75) Alia, S. M.; Stariha, S.; Borup, R. L. Electrolyzer Durability at Low Catalyst Loading and with Dynamic Operation. *Journal of The Electrochemical Society* **2019**, *166* (15), F1164. DOI: 10.1149/2.0231915jes.

(76) Cherevko, S.; Geiger, S.; Kasian, O.; Mingers, A.; Mayrhofer, K. J. J. Oxygen evolution activity and stability of iridium in acidic media. Part 2. – Electrochemically grown hydrous iridium oxide. *Journal of Electroanalytical Chemistry* **2016**, *774*, 102-110. DOI: https://doi.org/10.1016/j.jelechem.2016.05.015.

(77) Cherevko, S.; Geiger, S.; Kasian, O.; Mingers, A.; Mayrhofer, K. J. J. Oxygen evolution activity and stability of iridium in acidic media. Part 1. – Metallic iridium. *Journal of Electroanalytical Chemistry* **2016**, *773*, 69-78. DOI: https://doi.org/10.1016/j.jelechem.2016.04.033.

(78) Pourbaix, M. J. N. Atlas of Electrochemical Equilibria in Aqueous Solutions. In 1974.

(79) Dodwell, J.; Maier, M.; Majasan, J.; Jervis, R.; Castanheira, L.; Shearing, P.; Hinds, G.; Brett, D. J. L. Open-circuit dissolution of platinum from the cathode in polymer electrolyte

membrane water electrolysers. *Journal of Power Sources* **2021**, *498*, 229937. DOI: https://doi.org/10.1016/j.jpowsour.2021.229937.

(80) Liu, P.; Yang, D.; Li, B.; Qu, T.; Ming, P.; Zhang, C.; Pan, X. Agglomeration behavior of carbon-supported platinum nanoparticles in catalyst ink: modeling and experimental investigation. *Journal of Power Sources* **2024**, *602*, 234309. DOI: https://doi.org/10.1016/j.jpowsour.2024.234309.

(81) Feng, Q.; Yuan, X. Z.; Liu, G.; Wei, B.; Zhang, Z.; Li, H.; Wang, H. A review of proton exchange membrane water electrolysis on degradation mechanisms and mitigation strategies. *Journal of Power Sources* **2017**, *366*, 33-55. DOI: https://doi.org/10.1016/j.jpowsour.2017.09.006.

(82) Claudel, F.; Dubau, L.; Berthomé, G.; Sola-Hernandez, L.; Beauger, C.; Piccolo, L.; Maillard, F. Degradation Mechanisms of Oxygen Evolution Reaction Electrocatalysts: A Combined Identical-Location Transmission Electron Microscopy and X-ray Photoelectron Spectroscopy Study. *ACS Catalysis* **2019**, *9* (5), 4688-4698. DOI: 10.1021/acscatal.9b00280.

(83) Storage of Pure Hydrogen in Different States. In *Hydrogen Storage Technologies*, 2012; pp 97-170.

(84) Lu, P. W. T.; Srinivasan, S. Advances in water electrolysis technology with emphasis on use of the solid polymer electrolyte. *Journal of Applied Electrochemistry* **1979**, *9* (3), 269-283. DOI: 10.1007/BF01112480.

(85) Bessarabov, D.; wang, H.; Li, H.; Zhao, N. *PEM Electrolysis for Hydrogen Production: Principles and Applications*; 2015.

(86) Lettenmeier, P.; Wang, R.; Abouatallah, R.; Helmly, S.; Morawietz, T.; Hiesgen, R.; Kolb, S.; Burggraf, F.; Kallo, J.; Gago, A. S.; et al. Durable Membrane Electrode Assemblies for Proton Exchange Membrane Electrolyzer Systems Operating at High Current Densities. *Electrochimica Acta* **2016**, *210*, 502-511. DOI: https://doi.org/10.1016/j.electacta.2016.04.164.

(87) Gago, A. S.; Ansar, S. A.; Saruhan, B.; Schulz, U.; Lettenmeier, P.; Cañas, N. A.; Gazdzicki, P.; Morawietz, T.; Hiesgen, R.; Arnold, J.; et al. Protective coatings on stainless steel bipolar plates for proton exchange membrane (PEM) electrolysers. *Journal of Power Sources* **2016**, *307*, 815-825. DOI: https://doi.org/10.1016/j.jpowsour.2015.12.071.

(88) Dettke, T. Surface Engineering of Bipolar Plates for PEM-Water Electrolysis : Cost-Effective Corrosion Protection. Student thesis, 2021. http://urn.kb.se/resolve?urn=urn:nbn:se:liu:diva-183205 (accessed 2022-02-28t12:10:42.692+01:00).

(89) Dihrab, S. S.; Sopian, K.; Alghoul, M. A.; Sulaiman, M. Y. Review of the membrane and bipolar plates materials for conventional and unitized regenerative fuel cells. *Renewable and Sustainable Energy Reviews* **2009**, *13* (6), 1663-1668. DOI: https://doi.org/10.1016/j.rser.2008.09.029.

(90) Jung, H.-Y.; Huang, S.-Y.; Popov, B. N. High-durability titanium bipolar plate modified by electrochemical deposition of platinum for unitized regenerative fuel cell (URFC). *Journal of Power Sources* **2010**, *195* (7), 1950-1956. DOI: https://doi.org/10.1016/j.jpowsour.2009.10.002.

(91) Zhang, M.; Hu, L.; Lin, G.; Shao, Z. Honeycomb-like nanocomposite Ti-Ag-N films prepared by pulsed bias arc ion plating on titanium as bipolar plates for unitized regenerative fuel cells. *Journal of Power Sources* **2012**, *198*, 196-202. DOI: https://doi.org/10.1016/j.jpowsour.2011.10.022.

(92) Mo, J.; Steen, S. M.; Zhang, F.-Y.; Toops, T. J.; Brady, M. P.; Green, J. B. Electrochemical investigation of stainless steel corrosion in a proton exchange membrane electrolyzer cell. *International Journal of Hydrogen Energy* **2015**, *40* (36), 12506-12511. DOI: https://doi.org/10.1016/j.ijhydene.2015.07.061.

(93) Prestat, M. Corrosion of structural components of proton exchange membrane water electrolyzer anodes: A review. *Journal of Power Sources* **2023**, *556*, 232469. DOI: https://doi.org/10.1016/j.jpowsour.2022.232469.

(94) Rakousky, C.; Reimer, U.; Wippermann, K.; Kuhri, S.; Carmo, M.; Lueke, W.; Stolten, D. Polymer electrolyte membrane water electrolysis: Restraining degradation in the presence of fluctuating power. *Journal of Power Sources* **2017**, *342*, 38-47. DOI: https://doi.org/10.1016/j.jpowsour.2016.11.118.

(95) Liu, C.; Shviro, M.; Bender, G.; Gago, A. S.; Morawietz, T.; Dzara, M. J.; Biswas, I.; Gazdzicki, P.; Kang, Z.; Zaccarine, S. F.; et al. Degradation Effects at the Porous Transport Layer/Catalyst Layer Interface in Polymer Electrolyte Membrane Water Electrolyzer. *Journal of The Electrochemical Society* **2023**, *170* (3), 034508. DOI: 10.1149/1945-7111/acc1a5.

(96) Bystron, T.; Vesely, M.; Paidar, M.; Papakonstantinou, G.; Sundmacher, K.; Bensmann, B.; Hanke-Rauschenbach, R.; Bouzek, K. Enhancing PEM water electrolysis efficiency by reducing the extent of Ti gas diffusion layer passivation. *Journal of Applied Electrochemistry* **2018**, *48* (6), 713-723. DOI: 10.1007/s10800-018-1174-6.

(97) Shiva Kumar, S.; Himabindu, V. Hydrogen production by PEM water electrolysis – A review. *Materials Science for Energy Technologies* **2019**, *2* (3), 442-454. DOI: https://doi.org/10.1016/j.mset.2019.03.002.

(98) Lapicque, F.; Belhadj, M.; Bonnet, C.; Pauchet, J.; Thomas, Y. A critical review on gas diffusion micro and macroporous layers degradations for improved membrane fuel cell durability. *Journal of Power Sources* **2016**, *336*, 40-53. DOI: https://doi.org/10.1016/j.jpowsour.2016.10.037.

(99) Verdin, B.; Fouda-Onana, F.; Germe, S.; Serre, G.; Jacques, P. A.; Millet, P. Operando current mapping on PEM water electrolysis cells. Influence of mechanical stress. *International Journal of Hydrogen Energy* **2017**, *42* (41), 25848-25859. DOI: https://doi.org/10.1016/j.ijhydene.2017.08.189.

(100) Ayers, K. High efficiency PEM water electrolysis: enabled by advanced catalysts, membranes, and processes. *Current Opinion in Chemical Engineering* **2021**, *33*, 100719. DOI: https://doi.org/10.1016/j.coche.2021.100719.

(101) Noor Azam, A. M.; Li, N. K.; Zulkefli, N. N.; Masdar, M. S.; Majlan, E. H.; Baharuddin, N. A.; Mohd Zainoodin, A.; Mohamad Yunus, R.; Shamsul, N. S.; Husaini, T.; et al. Parametric Study and Electrocatalyst of Polymer Electrolyte Membrane (PEM) Electrolysis Performance. In *Polymers*, 2023; Vol. 15.

(102) Fouda-Onana, F.; Chandesris, M.; Médeau, V.; Chelghoum, S.; Thoby, D.; Guillet, N. Investigation on the degradation of MEAs for PEM water electrolysers part I: Effects of testing conditions on MEA performances and membrane properties. *International Journal of Hydrogen Energy* **2016**, *41* (38), 16627-16636. DOI: https://doi.org/10.1016/j.ijhydene.2016.07.125.

(103) Zhao, J.; Li, X. A review of polymer electrolyte membrane fuel cell durability for vehicular applications: Degradation modes and experimental techniques. *Energy Conversion and Management* **2019**, *199*, 112022. DOI: https://doi.org/10.1016/j.enconman.2019.112022.

(104) Chandesris, M.; Médeau, V.; Guillet, N.; Chelghoum, S.; Thoby, D.; Fouda-Onana, F. Numerical modelling of membrane degradation in PEM water electrolyzer: Influence of the temperature and current density. *International Journal of Hydrogen Energy* **2015**, *40*, 1-8.

(105) Alink, R.; Gerteisen, D.; Oszcipok, M. Degradation effects in polymer electrolyte membrane fuel cell stacks by sub-zero operation—An in situ and ex situ analysis. *Journal of Power Sources* **2008**, *182* (1), 175-187. DOI: https://doi.org/10.1016/j.jpowsour.2008.03.074.

(106) Yan, Q.; Toghiani, H.; Lee, Y.-W.; Liang, K.; Causey, H. Effect of sub-freezing temperatures on a PEM fuel cell performance, startup and fuel cell components. *Journal of Power Sources* **2006**, *160* (2), 1242-1250. DOI: https://doi.org/10.1016/j.jpowsour.2006.02.075.

(107) Sun, S.; Shao, Z.; Yu, H.; Li, G.; Yi, B. Investigations on degradation of the long-term proton exchange membrane water electrolysis stack. *Journal of Power Sources* **2014**, *267*, 515-520. DOI: https://doi.org/10.1016/j.jpowsour.2014.05.117.

(108) Kobayashi, Y.; Kosaka, K.; Yamamoto, T.; Tachikawa, Y.; Ito, K.; Sasaki, K. A solid polymer water electrolysis system utilizing natural circulation. *International Journal of Hydrogen Energy* **2014**, *39* (29), 16263-16274. DOI: https://doi.org/10.1016/j.ijhydene.2014.07.153.

(109) Millet, P.; Ranjbari, A.; de Guglielmo, F.; Grigoriev, S. A.; Auprêtre, F. Cell failure mechanisms in PEM water electrolyzers. *International Journal of Hydrogen Energy* **2012**, *37* (22), 17478-17487. DOI: https://doi.org/10.1016/j.ijhydene.2012.06.017.

(110) Lee, H.; Kim, T.; Sim, W.; Kim, S.; Ahn, B.; Lim, T.; Park, K. Pinhole formation in PEMFC membrane after electrochemical degradation and wet/dry cycling test. *Korean Journal of Chemical Engineering* **2011**, *28* (2), 487-491. DOI: 10.1007/s11814-010-0381-6.

(111) Silberstein, M. N.; Boyce, M. C. Hygro-thermal mechanical behavior of Nafion during constrained swelling. *Journal of Power Sources* **2011**, *196* (7), 3452-3460. DOI: https://doi.org/10.1016/j.jpowsour.2010.11.116.

(112) Xing, Y.; Li, H.; Avgouropoulos, G. Research Progress of Proton Exchange Membrane Failure and Mitigation Strategies. In *Materials*, 2021; Vol. 14.

(113) Ito, H.; Maeda, T.; Nakano, A.; Hasegawa, Y.; Yokoi, N.; Hwang, C. M.; Ishida, M.; Kato, A.; Yoshida, T. Effect of flow regime of circulating water on a proton exchange membrane electrolyzer. *International Journal of Hydrogen Energy* **2010**, *35* (18), 9550-9560. DOI: https://doi.org/10.1016/j.ijhydene.2010.06.103.

(114) Grigoriev, S. A.; Millet, P.; Korobtsev, S. V.; Porembskiy, V. I.; Pepic, M.; Etievant, C.; Puyenchet, C.; Fateev, V. N. Hydrogen safety aspects related to high-pressure polymer electrolyte membrane water electrolysis. *International Journal of Hydrogen Energy* **2009**, *34* (14), 5986-5991. DOI: https://doi.org/10.1016/j.ijhydene.2009.01.047.

(115) Grigoriev, S. A.; Dzhus, K. A.; Bessarabov, D. G.; Millet, P. Failure of PEM water electrolysis cells: Case study involving anode dissolution and membrane thinning. *International Journal of Hydrogen Energy* **2014**, *39* (35), 20440-20446. DOI: https://doi.org/10.1016/j.ijhydene.2014.05.043.

(116) Pozio, A.; Silva, R. F.; De Francesco, M.; Giorgi, L. Nafion degradation in PEFCs from end plate iron contamination. *Electrochimica Acta* **2003**, *48* (11), 1543-1549. DOI: https://doi.org/10.1016/S0013-4686(03)00026-4.

(117) Qi, F.; Xiao−Zi, Y.; Gaoyang, L.; Bing, W.; Zhen, Z.; Hui, L.; Haijiang, W. A review of proton exchange membrane water electrolysis on degradation mechanisms and mitigation strategies. *Journal of Power Sources* **2017**, *366*, 33-55. DOI: https://doi.org/10.1016/j.jpowsour.2017.09.006.

(118) Xunying, W.; Linsong, Z.; Guangfu, L.; Geng, Z.; Zhi-Gang, S.; Baolian, Y. The influence of Ferric ion contamination on the solid polymer electrolyte water electrolysis performance.

Electrochimica Acta **2015**, *158*, 253-257. DOI: https://doi.org/10.1016/j.electacta.2015.01.140.

(119) Shwe Sin, P.; Wai, S.; Ota, Y.; Nishioka, K.; Suzuki, Y. Performance recovery of proton exchange membrane electrolyzer degraded by metal cations contamination. *International Journal of Hydrogen Energy* **2024**, *53*, 86-92. DOI: https://doi.org/10.1016/j.ijhydene.2023.12.049.

(120) Li, N.; Araya, S. S.; Cui, X.; Kær, S. K. The effects of cationic impurities on the performance of proton exchange membrane water electrolyzer. *Journal of Power Sources* **2020**, *473*, 228617. DOI: https://doi.org/10.1016/j.jpowsour.2020.228617.

(121) Coms, F. D.; Fuller, T. J.; Schaffer, C. P. A Mechanistic Study of Perfluorosulfonic Acid Membrane Water Permeance Degradation in Air. *ECS Transactions* **2015**, *69* (17), 189. DOI: 10.1149/06917.0189ecst.

(122) Kelly, M. J.; Fafilek, G.; Besenhard, J. O.; Kronberger, H.; Nauer, G. E. Contaminant absorption and conductivity in polymer electrolyte membranes. *Journal of Power Sources* **2005**, *145* (2), 249-252. DOI: https://doi.org/10.1016/j.jpowsour.2005.01.064.

(123) Kelly, M. J.; Egger, B.; Fafilek, G.; Besenhard, J. O.; Kronberger, H.; Nauer, G. E. Conductivity of polymer electrolyte membranes by impedance spectroscopy with microelectrodes. *Solid State Ionics* **2005**, *176* (25), 2111-2114. DOI: https://doi.org/10.1016/j.ssi.2004.07.071.

(124) Okada, T. Effect of ionic contaminants. In *Handbook of Fuel Cells*.

(125) Weber, A. Z.; Delacourt, C. Mathematical Modelling of Cation Contamination in a Proton-exchange Membrane. *Fuel Cells* **2008**, *8* (6), 459-465. DOI: https://doi.org/10.1002/fuce.200800044.

(126) Frensch, S. H.; Fouda-Onana, F.; Serre, G.; Thoby, D.; Araya, S. S.; Kær, S. K. Influence of the operation mode on PEM water electrolysis degradation. *International Journal of Hydrogen Energy* **2019**, *44* (57), 29889-29898. DOI: https://doi.org/10.1016/j.ijhydene.2019.09.169.

(127) Weiß, A.; Siebel, A.; Bernt, M.; Shen, T. H.; Tileli, V.; Gasteiger, H. A. Impact of Intermittent Operation on Lifetime and Performance of a PEM Water Electrolyzer. *Journal of The Electrochemical Society* **2019**, *166* (8), F487. DOI: 10.1149/2.0421908jes.

(128) Majumdar, A.; Haas, M.; Elliot, I.; Nazari, S. Control and control-oriented modeling of PEM water electrolyzers: A review. *International Journal of Hydrogen Energy* **2023**, *48* (79), 30621-30641. DOI: https://doi.org/10.1016/j.ijhydene.2023.04.204.

(129) Frensch, S. H.; Serre, G.; Fouda-Onana, F.; Jensen, H. C.; Christensen, M. L.; Araya, S. S.; Kær, S. K. Impact of iron and hydrogen peroxide on membrane degradation for polymer electrolyte membrane water electrolysis: Computational and experimental investigation on

fluoride emission. *Journal of Power Sources* **2019**, *420*, 54-62. DOI: https://doi.org/10.1016/j.jpowsour.2019.02.076.

(130) Marocco, P.; Sundseth, K.; Aarhaug, T.; Lanzini, A.; Santarelli, M.; Barnett, A. O.; Thomassen, M. Online measurements of fluoride ions in proton exchange membrane water electrolysis through ion chromatography. *Journal of Power Sources* **2021**, *483*, 229179. DOI: https://doi.org/10.1016/j.jpowsour.2020.229179.

(131) Lorenz, G.; Sindy, M. D.; Willem, H. K. Radical (HO•, H• and HOO•) Formation and Ionomer Degradation in Polymer Electrolyte Fuel Cells. *Journal of The Electrochemical Society* **2011**, *158* (7), B755. DOI: 10.1149/1.3581040.

(132) Rodgers, M. P.; Bonville, L. J.; Kunz, H. R.; Slattery, D. K.; Fenton, J. M. Fuel Cell Perfluorinated Sulfonic Acid Membrane Degradation Correlating Accelerated Stress Testing and Lifetime. *Chemical Reviews* **2012**, *112* (11), 6075-6103. DOI: 10.1021/cr200424d.

(133) Lim, H. J.; Kim, G.; Yun, G. J. Durability and Performance Analysis of Polymer Electrolyte Membranes for Hydrogen Fuel Cells by a Coupled Chemo-mechanical Constitutive Model and Experimental Validation. *ACS Applied Materials \& Interfaces* **2023**, *15* (20), 24257-24270. DOI: 10.1021/acsami.2c15451 , note = PMID: 37179493.

(134) Frühwirt, P.; Kregar, A.; Törring, J. T.; Katrašnik, T.; Gescheidt, G. Holistic approach to chemical degradation of Nafion membranes in fuel cells: modelling and predictions. *Physical Chemistry Chemical Physics* **2020**, *22* (10), 5647-5666, 10.1039/C9CP04986J. DOI: 10.1039/C9CP04986J.

(135) Dennis, E. C.; Robert, D. L.; Timothy, J. H.; Paul, C. T.; Monica, E. T. Advanced materials for improved PEMFC performance and life. *Journal of Power Sources* **2004**, *131* (1), 41-48. DOI: https://doi.org/10.1016/j.jpowsour.2004.01.023.

(136) Petrone, R.; Hissel, D.; Péra, M. C.; Chamagne, D.; Gouriveau, R. Accelerated stress test procedures for PEM fuel cells under actual load constraints: State-of-art and proposals. *International Journal of Hydrogen Energy* **2015**, *40* (36), 12489-12505. DOI: https://doi.org/10.1016/j.ijhydene.2015.07.026.

(137) Malkow, T.; Pilenga, A. EU harmonised accelerated stress testing protocols for low-temperature water electrolyser: A proposal with testing guidance for assessing performance degradation in water electrolyser stacks. **2024**.

(138) Union, E. Definition of Accelerated Stress Testing (AST) protocols deduced from understanding of degradation mechanisms of aged stack components in Fuel Cell systems. 2025.

(139) Escribano, S.; Micoud, F.; Guetaz, L. Development of exacerbated load cycles as AST for PEMFC stacks and validation by in-situ and ex-situ characterizations. In *EHEC 2022* -

European Hydrogen Energy Conference 2022, Madrid, Spain, 2022-05-18, 2022; https://cea.hal.science/cea-03727248v1/document

https://cea.hal.science/cea-03727248v1/file/EHEC2022_Abstract_EscribanoSylvie1_Exacerbated-Load-Cycles-AST-PEMFC-stack.pdf.

(140) Kuhnert, E.; Hacker, V.; Bodner, M. A Review of Accelerated Stress Tests for Enhancing MEA Durability in PEM Water Electrolysis Cells. *International Journal of Energy Research* **2023**, *2023*, 3183108. DOI: 10.1155/2023/3183108.

(141) Tomić, A. Z.; Pivac, I.; Barbir, F. A review of testing procedures for proton exchange membrane electrolyzer degradation. *Journal of Power Sources* **2023**, *557*, 232569. DOI: https://doi.org/10.1016/j.jpowsour.2022.232569.

(142) Zhang, K.; Liang, X.; Wang, L.; Sun, K.; Wang, Y.; Xie, Z.; Wu, Q.; Bai, X.; Hamdy, M. S.; Chen, H.; et al. Status and perspectives of key materials for PEM electrolyzer. *Nano Research Energy* **2022**, *1*, 9120032. DOI: 10.26599/NRE.2022.9120032.

(143) Kundu, S.; Simon, L. C.; Fowler, M. W. Comparison of two accelerated Nafion™ degradation experiments. *Polymer Degradation and Stability* **2008**, *93* (1), 214-224. DOI: https://doi.org/10.1016/j.polymdegradstab.2007.10.001.

(144) Spöri, C.; Brand, C.; Kroschel, M.; Strasser, P. Accelerated Degradation Protocols for Iridium-Based Oxygen Evolving Catalysts in Water Splitting Devices. *Journal of The Electrochemical Society* **2021**, *168* (3), 034508. DOI: 10.1149/1945-7111/abeb61.

(145) Alia, S. M.; Rasimick, B.; Ngo, C.; Neyerlin, K. C.; Kocha, S. S.; Pylypenko, S.; Xu, H.; Pivovar, B. S. Activity and Durability of Iridium Nanoparticles in the Oxygen Evolution Reaction. *Journal of The Electrochemical Society* **2016**, *163* (11), F3105. DOI: 10.1149/2.0151611jes.

(146) Thomassen, M. S.; Mokkelbost, T.; Sheridan, E.; Lind, A. Supported Nanostructured Ir and IrRu Electrocatalysts for Oxygen Evolution in PEM Electrolysers. *ECS Transactions* **2011**, *35* (34), 271. DOI: 10.1149/1.3654225.

(147) Rozain, C.; Mayousse, E.; Guillet, N.; Millet, P. Influence of iridium oxide loadings on the performance of PEM water electrolysis cells: Part II – Advanced oxygen electrodes. *Applied Catalysis B: Environmental* **2016**, *182*, 123-131. DOI: https://doi.org/10.1016/j.apcatb.2015.09.011.

(148) Chun, J. H.; Jo, D. H.; Kim, S. G.; Park, S. H.; Lee, C. H.; Kim, S. H. Improvement of the mechanical durability of micro porous layer in a proton exchange membrane fuel cell by elimination of surface cracks. *Renewable Energy* **2012**, *48*, 35-41. DOI: https://doi.org/10.1016/j.renene.2012.04.011.

(149) Lee, C.-Y.; Chen, C.-H.; Jung, G.-B.; Li, S.-C.; Zeng, Y.-Z. Internal Microscopic Diagnosis of Accelerated Aging of Proton Exchange Membrane Water Electrolysis Cell Stack. In *Micromachines*, 2020; Vol. 11.

(150) Chen, G.; Zhang, H.; Ma, H.; Zhong, H. Electrochemical durability of gas diffusion layer under simulated proton exchange membrane fuel cell conditions. *International Journal of Hydrogen Energy* **2009**, *34* (19), 8185-8192. DOI: https://doi.org/10.1016/j.ijhydene.2009.07.085.

(151) Wu, J.; Martin, J. J.; Orfino, F. P.; Wang, H.; Legzdins, C.; Yuan, X.-Z.; Sun, C. In situ accelerated degradation of gas diffusion layer in proton exchange membrane fuel cell: Part I: Effect of elevated temperature and flow rate. *Journal of Power Sources* **2010**, *195* (7), 1888-1894. DOI: https://doi.org/10.1016/j.jpowsour.2009.10.022.

(152) Aßmann, P.; Gago, A. S.; Gazdzicki, P.; Friedrich, K. A.; Wark, M. Toward developing accelerated stress tests for proton exchange membrane electrolyzers. *Current Opinion in Electrochemistry* **2020**, *21*, 225-233. DOI: https://doi.org/10.1016/j.coelec.2020.02.024.

(153) Li, N.; Araya, S. S.; Kær, S. K. Investigating low and high load cycling tests as accelerated stress tests for proton exchange membrane water electrolysis. *Electrochimica Acta* **2021**, *370*, 137748. DOI: https://doi.org/10.1016/j.electacta.2021.137748.

(154) Fenton, H. J. H. LXXIII.—Oxidation of tartaric acid in presence of iron. *Journal of the Chemical Society, Transactions* **1894**, *65* (0), 899-910, 10.1039/CT8946500899. DOI: 10.1039/CT8946500899.

(155) Panchenko, A.; Dilger, H.; Möller, E.; Sixt, T.; Roduner, E. In situ EPR investigation of polymer electrolyte membrane degradation in fuel cell applications. *Journal of Power Sources* **2004**, *127* (1), 325-330. DOI: https://doi.org/10.1016/j.jpowsour.2003.09.047.

(156) Liu, W.; Zuckerbrod, D. In Situ Detection of Hydrogen Peroxide in PEM Fuel Cells. *Journal of The Electrochemical Society* **2005**, *152* (6), A1165. DOI: 10.1149/1.1904988.

(157) U.S. Department of Energy. *Technical Targets for Proton Exchange Membrane Electrolysis*. 2026. https://www.energy.gov/eere/fuelcells/technical-targets-proton-exchange-membrane-electrolysis (accessed 2026 3 March).

(158) Clean Hydrogen Joint Undertaking. *Strategic Research and Innovation Agenda 2021 – 2027*; Annex to GB decision no. CleanHydrogen-GB-2022-02; Clean Hydrogen Joint Undertaking, Brussels, 2022. https://www.clean-hydrogen.europa.eu/system/files/2022-02/Clean%20Hydrogen%20JU%20SRIA%20-%20approved%20by%20GB%20-%20clean%20for%20publication%20%28ID%2013246486%29.pdf (accessed March 8, 2026).

CHAPTER 3: METHODOLOGY

This chapter describes the experimental framework used to investigate the degradation mechanisms of Nafion® membranes under Fenton AST conditions. The experimental design was structured to establish correlations among molecular-level chemical degradation, macroscopic morphological failure, and the resulting loss in electrochemical performance.

The methodology is systematised into four distinct phases:

Membrane Preparation: The selection and pre-treatment of commercial Nafion® membranes, with a specific focus on comparing mechanical (scalpel) versus thermal (laser) cutting techniques to evaluate the influence of edge defects on degradation initiation.

Accelerated Stress Testing (AST): The implementation of an *ex-situ* Fenton's reagent protocol, controlled for Fe^{2+} concentration and exposure duration.

Physicochemical Characterisation: A multi-modal analytical approach utilising chemical titrations (IEC), effluent analysis (FRR), spectroscopy (Fourier Transform Infrared Spectroscopy (FT-IR), Raman, Nuclear Magnetic Resonance (NMR)), and surface imaging (Scanning Electron Microscopy (SEM), Profilometry) to quantify the extent and nature of the degradation.

***In-Situ* Performance Evaluation:** The fabrication of CCMs from degraded samples and their subsequent electrochemical testing in a PEMWE single cell to validate the impact of *ex-situ* material damage on operational efficiency.

The following sections describe the specific equipment, protocols, and standard operating procedures utilised in each phase.

3.1 Materials

3.1.1 Membranes

Sheets of 30.5 x 30.5 cm Nafion® 115 and Nafion® 117 were obtained from Ion Power Inc. (DuPont, USA) and used throughout this study.

3.1.2 Chemicals

Below is a representative table of chemicals used, their suppliers, and the purity, concentration, and ppm contaminants, as stated in the certificates of analysis received from the suppliers.

Table 5: Chemicals, suppliers, concentration, purity, and % contaminants of chemicals used.

Chemical	Chemical symbol	Supplier	Concentration / Purity (%)	Contaminants (ppm)
Hydrogen peroxide (vol.%)	H_2O_2	Associated Chemical Enterprises	50	Fe: 1 Pb: 1 PO_4: 500 SO_4: 50 Cl: 5
Iron (II) chloride tetrahydrate	$FeCl_2.4H_2O$	Sigma Aldrich	99	undisclosed
Sodium chloride	NaCl	Associated Chemical Enterprises	99	Fe: 5 Pb: 5 PO_4: 10 SO_4: 1000
Hydrochloric acid	HCl	Associated Chemical Enterprises	37	Cl: 2 SO_4:5 SO_3: 1
Deionized water	H_2O	In-House	-	F^-: 0.48[a] S^{2-}: 4.65[a]

a: Measured with the use of Dionex ion chromatograph

3.2 Membrane Pre-treatment

The following pre-treatment procedure was employed to establish a consistent baseline for all membrane samples, effectively mitigating the influence of prior thermal history and ensuring uniformity in key physicochemical properties. This procedure is critical for achieving reproducible and reliable results in subsequent degradation studies and PEMWE performance evaluations. The protocol integrates elements of established methodologies reported in the literature, with adaptations tailored to the requirements of this investigation.[1-8] The pre-treatment aims to ensure consistent water uptake, surface topology, and mechanical properties[9], transport coefficients[5], density[10], permeability[6], ionic conductivity[7], selectivity[6], thermal stability, and crystallinity[8] across all membrane samples.

3.2.1 Membrane Preparation

To remove residual organic contaminants from the manufacturing process, the as-received membrane sheets (Nafion® 115 and Nafion® 117) were initially immersed in a 3 v/v% H_2O_2 solution. This step was performed at 80 °C for 2 hours. Following the H_2O_2 treatment, the membranes were sequentially washed with deionised water. Specifically, the membranes were washed in deionised (DI) water (80 °C) for a total of 2 hours, with the DI water being replaced every hour to ensure effective removal of any remaining contaminants. The use of elevated temperature in both the H_2O_2 treatment and the washing steps enhances contaminant removal efficiency and promotes thorough membrane hydration.[11-13]

3.2.2 Protonation

To ensure that all membrane samples were fully protonated (H^+), the cleaned membrane sheets were immersed in 2 M hydrochloric acid (HCl). The protonation was conducted at 80 °C for 2 h. This elevated temperature facilitates ion exchange, ensuring complete conversion of the membrane's ionic form to the desired protonated state.[14, 15] After the acid treatment, the membranes were washed in DI water using the same procedure described in the cleaning step (Section 3.2.1) to remove any residual acid and restore the membranes to a nominal pH.

3.2.3 Cutting

After cleaning and protonation, the membrane sheets were carefully removed from DI water and dried with a paper towel to remove excess surface water. The partially dried sheets were then left under ambient conditions to equilibrate and further remove any remaining surface moisture before cutting.

Once sufficiently dry, the membrane sheets were cut to the required dimensions using a Trotec Speedy100 flexx laser cutter. The laser cutter was selected for its precision and ability to produce clean, consistent cuts without introducing mechanical stress or contamination to the membrane. The membrane samples were cut to size. The specific laser cutting parameters employed were a cutting speed of 5 $cm.s^{-1}$ at 1000 Hz with a 20 W CO_2 laser. These parameters were optimised to ensure complete, clean membrane cutting while minimising thermal damage to the material.

3.2.4 Storage

To preserve the pre-treated membrane samples in a hydrated and contamination-free state, the cut membrane samples were stored in Low-Density Polyethene (LDPE) zip-lock bags. Each bag contained 20 mL of DI water to maintain membrane hydration. The bags were sealed to prevent evaporation and contamination and were stored in a dark area at ambient temperature until required for experiments. This storage protocol ensures that the membranes retain their desired properties and minimises any potential changes in their characteristics over time.[16-18]

3.3 Fenton degradation

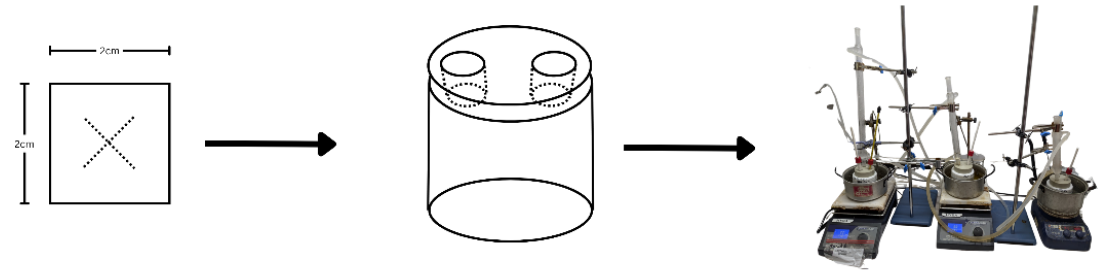
Membrane samples were subjected to accelerated chemical degradation using Fenton's reagent, i.e., ferrous (Fe^{2+}) chloride (5-30ppm), $FeCl_2.4H_2O$, in 30 wt% H_2O_2 at 80 °C. This notably deviates from ferrous sulfate ($FeSO_4.xH_2O$) used in previous studies[19-27]. This change in the Fe^{2+} source was made to enable subsequent SER analyses, as discussed in Section 2.4.5.

The degradation process was conducted at varying Fe^{2+} concentrations and membrane exposure durations. The Fe^{2+} concentration range was selected to represent a spectrum of

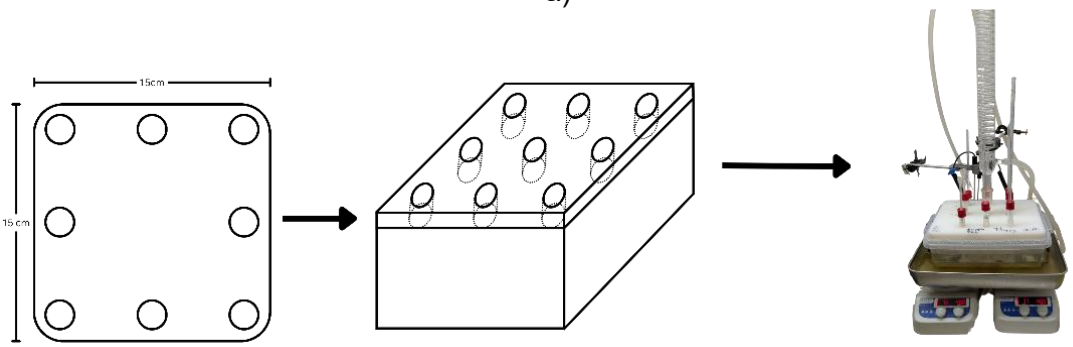
degradation levels that may occur in PEMWE systems. Two distinct experimental methodologies were employed; these are detailed in the following subsections as small- and large-scale degradation procedures. Unless stated otherwise, the methodology is identical for both small- and large-scale degradations.

3.3.1 Degradation Procedure

In this study, two relatively similar approaches were undertaken: i) small-scale degradations, which were done for rapid investigations. This method enabled initial screening of the degradation parameters, i.e., duration and initial Fe^{2+} concentration. ii) Once the degradation parameters were identified using the small-scale approach, large-scale degradations were done to generate the required degraded membranes for proceeding with CCM fabrication. Figure 13 presents the small- and large-scale degradation setups.



a)



b)

Figure 13: Membrane size and experimental setup for a) small-scale degradations, with the dotted line on the membrane representing the region that was cut and b) experimental setup for large-scale degradations. Images of the experimental setups are provided in which the membrane is submerged in Fenton solution with use of the PTFE rods, and a condenser is connected to limit evaporation.

Small-scale was for rapid screening/chemical analysis; large-scale was necessary to produce enough material for CCM fabrication. For small-scale Fenton degradation experiments, membrane samples were prepared by making a central x-shaped cut with a scalpel. The cut membrane was then secured between two polytetrafluoroethylene (PTFE) washers on a PP rod

with a 2 cm threaded section, as shown in Figure 13 a). Each degradation was carried out in a 300 mL HDPE container, using 250 mL of Fenton's reagent solution. The Fe^{2+} concentration in the Fenton reagent solution was varied according to the experimental design.

Large-scale degradations differed primarily in the method of membrane mounting and in the volume of Fenton reagent solution. The laser-cutting procedure used to prepare these samples produced regions for bolt fittings (as shown in Figure 13 b, outer edges of the membrane).

Instead of making use of the aforementioned x-shaped cut, each membrane section was secured with 8 PP rods and 16 PTFE washers, maintaining a configuration similar to that of the small-scale setup. Each degradation was carried out in a 3200 mL HDPE container, using 3000 mL of Fenton's reagent solution. The membrane was submerged at a 50° angle to prevent air pockets from forming on its bottom surface. The degradation of both the small- and large-scale samples was conducted under reflux. The reaction mixture was heated at 80 °C in a silicone oil bath, and the solution was stirred at 400 rpm with a PTFE-coated magnetic stirrer to maintain homogeneity.

3.3.2 Post-Degradation Treatment

Following Fenton degradation, membrane samples were treated to remove residual reagents and prepared for subsequent analysis. First, to ensure complete removal of residual Fe^{2+} from the membrane, the degraded membranes were subjected to acidic washing by immersion in 2 M HCl at 80 °C for 2 h. This acidic washing was followed by DI rinsing to remove any residual HCl. Specifically, the membranes were rinsed in DI water at 80 °C for a total of 2 h, with the water being replaced every hour. Finally, the treated membrane samples were stored in DI water until required for further characterisation.

3.4 Membrane Characterisation

3.4.1 Ion Exchange Capacity (IEC) Measurement

The IEC of each membrane sample was determined by titration. Samples were immersed in 2 M NaCl for 12 h at ambient temperature to ensure complete cation exchange between sodium ions and the sulfonic acid functional groups in the membrane sample.[28] Titrations were done using an SI Analytics Titrator TitroLine® 7000 automatic titrator. Before titration, the instrument was calibrated weekly with standardised pH buffer solutions (Hanna Instruments®) at pH 4, 7, and 10, yielding a calibration slope of -57.6 mV/pH. The resulting solutions were then titrated with 0.05 M NaOH for small-scale samples and 1 M NaOH for large-scale samples. Following the IEC

determination, membrane samples were re-protonated and washed according to the procedure detailed in Section 3.3.2 (Post-Degradation Treatment).

3.4.2 Water Uptake Measurement

PFSA membranes are inherently hygroscopic, a property fundamental to their operation but that also entails a trade-off in stability. Water uptake is a critical parameter to quantify because it directly governs proton conductivity; sufficient hydration is required to form the hydrophilic channels necessary for proton transport. However, excessive water uptake can lead to severe dimensional swelling and mechanical stress, potentially compromising the membrane's structural integrity.

To evaluate this property, membrane water uptake was measured gravimetrically. First, the wet mass was recorded after removing the samples from their storage containers and carefully blotting them with paper towels to eliminate excess surface water. Subsequently, the dry mass was obtained by oven-drying the samples for 12 h at 75 °C. While this drying protocol was successful for small-scale samples, it proved unsuitable for the degraded large-scale membranes. These larger samples experienced mechanical failure and tearing during the drying phase due to excessive tensile forces generated by shrinkage.

3.4.3 Fourier Transform Infrared Spectroscopy (FT-IR) Analysis

FT-IR spectroscopy was performed using a PerkinElmer Spectrum 3 FT-IR/NIR Spectrometer, covering the spectral range 4000-550 cm^{-1}, with a resolution of 4 cm^{-1} and 32 scans accumulated. This was done by placing membrane samples on the universal Attenuated Total Reflectance (ATR) mounting plate and securing it on the Diamond-ZnSe focusing element with 80 Newtons of force to ensure reproducibility between samples.



Figure 14: Perkin Elmer Spectrum 3 FT-IR/NIR Spectrometer (source, HySA Infrastructure, NWU).

3.4.4 Raman Spectroscopy

The Raman data presented in this study focus on the spectral range of 0-1340 cm^{-1}, as this is the region where Nafion® chemical degradation is visible.[29-32] To enhance signal clarity and remove noise without distorting peak features, the raw Raman data were processed using a Savitzky-Golay smoothing filter. A polynomial order of 8 and a frame length of 21 points were selected to preserve the integrity of the spectral peaks while effectively minimising high-frequency noise.

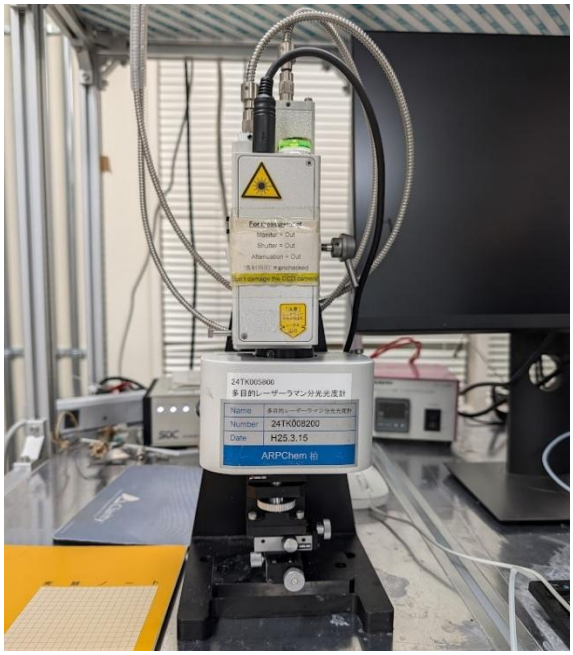


Figure 15: ARPChem Raman spectrophotometer used for Raman spectral acquisition. (source, CatEC research group, University of Tokyo).

3.4.5 CP-MAS NMR Spectroscopy Measurement

Cross-Polarisation Magic-Angle-Spinning Nuclear Magnetic Resonance (CP-MAS NMR) spectroscopy was performed with the use of a Bruker Ultrashield Plus Avance III 500 Hz spectrometer. Analysis was conducted at 62.5 kHz with a 4 mm MAS rotor with NaCl used as a filler. Samples were homogenised using a mortar and pestle under liquid nitrogen until a fine powder was obtained.

3.4.6 Profilometry

Surface topography was analysed using a KLA Zeta-20 optical Profilometer, with each membrane being analysed in 4 different regions with an analysed surface area of 1787 x 1340 μm per image. Each analysis was done on dried membranes at a 5 μm vertical resolution.

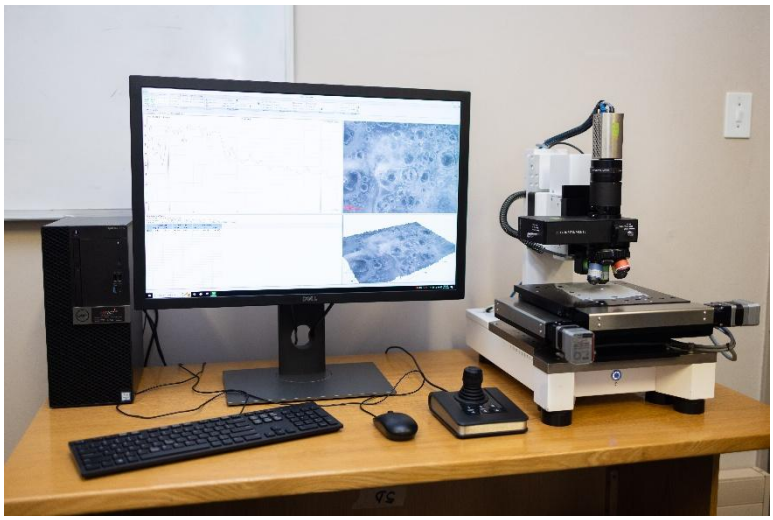


Figure 16: KLA Zeta-20 optical profilometer used for topographical analysis. (source, HySA Infrastructure, NWU).

3.4.7 Effluent Analysis

Before analysis, the effluent collected after Fenton degradation is filtered through a 0.45 µm syringe filter, then diluted 10x with DI water. Samples were analysed using a Dionex ICS-3000. A Dionex IonPac AS15 4 x 250mm column was used, with potassium hydroxide as the eluent, provided by the Dionex EGC 500 KOH Eluent Generator.



Figure 17 Dionex ICS-3000 used for IC (from left to right in the image: computer, autosampler carousel, Dionex ICS-3000, Dionex EGC 500 KOH eluent generator). (source, CRB, NWU).

3.5 PEMWE Single Cell *In-situ* Testing

As stated in Section 3.1, degraded large-scale membranes were used to fabricate CCMs. These CCMs were subsequently tested in a single cell. The relevant procedures are described in the proceeding section.

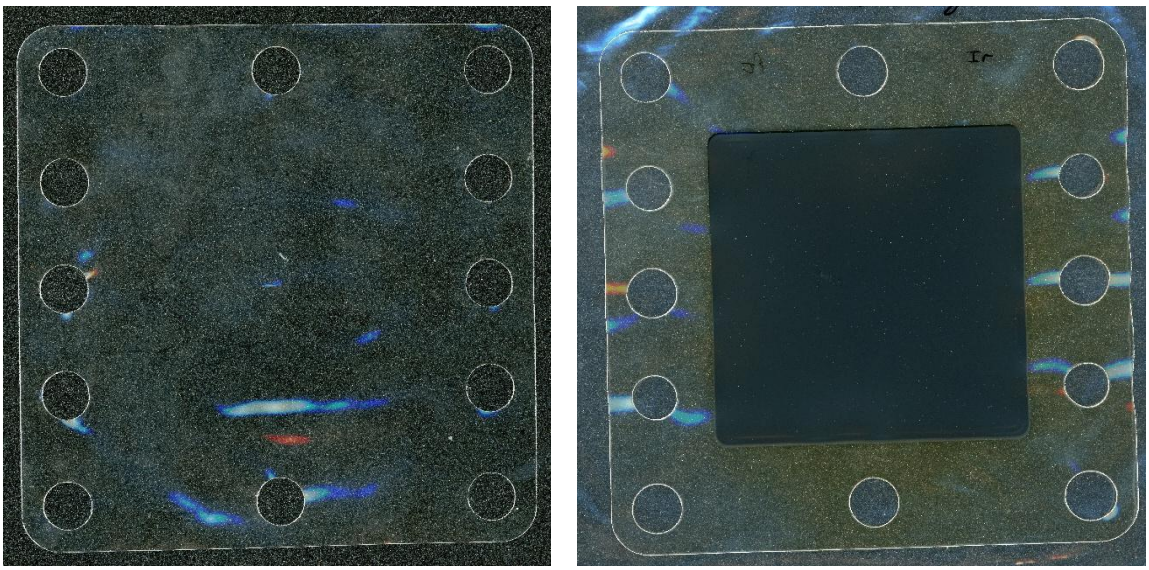
3.5.1 Catalyst Coated Membrane (CCM) Fabrication

CCMs with active areas of 56 cm^2 were prepared using a Sono ExactaCoat (Figure 18).



Figure 18: SonoTek Exacta coat used for CCM fabrication. (source, HySA Infrastructure, NWU).

The prepared CCMs, as shown in Figure 19, comprised a 2.5 $mg.cm^{-2}$ Ir-black anode catalyst layer (synthesised) and a 0.17 $mg.cm^{-2}$ Pt catalyst supported on high-surface-area carbon (Pt/C) from Tanaka Kikinzoku Kogyo, Japan.



a) b)

Figure 19: a) Post-degradation (5 ppm Fe^{2+} 24h), uncoated Nafion® 115 membrane, and b) a fabricated CCM prepared using the degraded membrane shown in a) (source, HySA Infrastructure, NWU).

3.5.2 Porous Transport Layer (PTL) Preparation and Flow Fields

Sintered Ti sheets (500 µm thickness, ~60% porosity) were obtained from an original equipment manufacturer. The anode and cathode PTLs were coated with a 70 nm Pt layer to promote corrosion resistance and electrical conductivity. Pt coatings were done by magnetron sputter deposition, using a Q150T S coater (Quorum, UK) at a coating current of 30 mA.

The flow fields used are shown in Figure 20, where the pin-type flow-field channels facilitate water transport, and the outlet gases are visible.

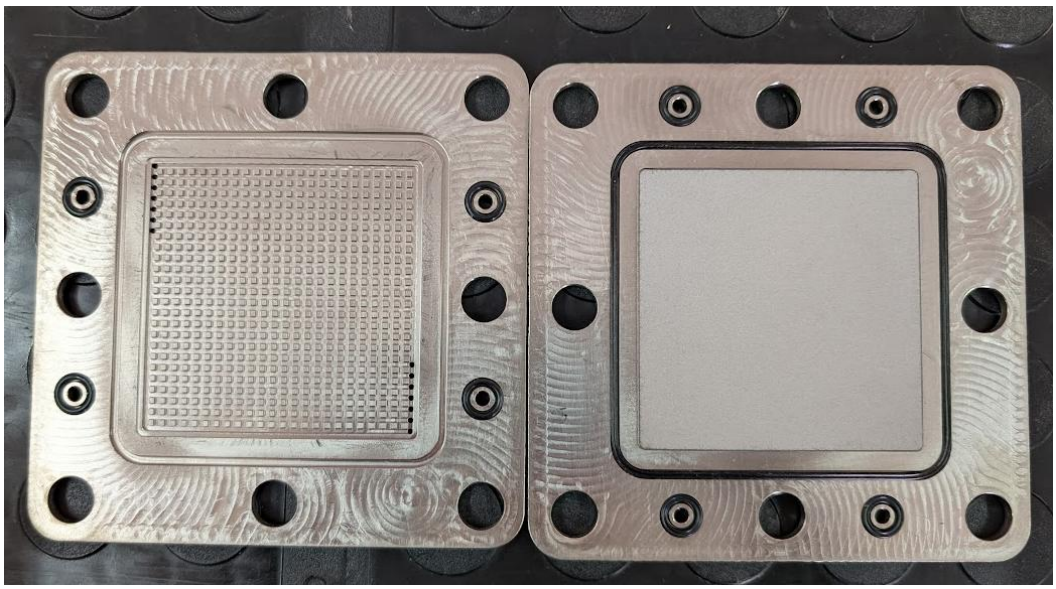


Figure 20: Image of sintered passivated PTL utilised in this study, placed on the flow field (right) and bipolar plate with the flow field visible (left). (source, HySA Infrastructure, NWU).

3.5.3 Single Cell Assembly

As described in Section 2.3, Figure 4, the cell is assembled in order of CCM, PTL, BPP (which also served as the current collectors), and end plates. The cell was assembled by torquing 8 bolts to 30 Nm.[33] The fully assembled cell is represented in Figure 21. The same BPPs were used throughout the study and were washed with DI water and cleaned with a wire brush between tests.



Figure 21: Assembled PEMWE cell (source, HySA Infrastructure, NWU).

3.6 Electrochemical Conditioning and Testing Protocol:

A multi-step conditioning and break-in protocol was implemented for each assembled cell to ensure stable and reproducible electrochemical performance before data acquisition. This was done by performing the following steps: i) *in-situ* hydration and heating, DI water was circulated through the anodic compartment to ensure full *in-situ* hydration of the CCM. Concurrently, the cell was heated to a target operating temperature of 60 ˚C. ii) Voltage-mode condition: once thermal equilibrium at 60 ˚C was reached, the power supply was engaged in constant voltage mode. An initial potential of 1.5 V was applied (corresponding to the minimum current density of 0.05 $A.cm^{-2}$). These conditions were maintained for 10 minutes to monitor stability. The cell voltage was then increased to 1.6 V and held for an additional 10 minutes. iii) Current-mode break-in: After the initial voltage conditioning, the power supply was switched to constant current mode. The current density was increased in 0.1 $A.cm^{-2}$ increments until a cell voltage of 1.85 V was achieved. iv) Performance stabilisation: the cell was operated at a constant 1.85 V for a minimum duration of 12 hours to complete the membrane break-in and ensure stable performance. For severely degraded samples, the stabilisation duration was increased to a minimum of 40 h. With this increase in duration, an automated script (Annexure 6.2.1) was developed to continuously adjust

the current to maintain a constant potential of 1.85 V. v) Electrochemical testing: upon successful completion of the conditioning protocol, the cell was prepared for subsequent electrochemical analyses. Polarisation curves and other diagnostic tests were conducted on the following day.



Figure 22: Greenlight Innovations® PEMWE/FC testing station (source, HySA Infrastructure, NWU).

A summative table of test CCM fabrication, assembly, and testing parameters is presented in Table 6.

Table 6: Summative table of CCM fabrication, cell assembly and pre-conditioning parameters

	Anode	Cathode
Membrane type	Nafion® 115	
CCM active surface area (cm^2)	56	
Catalyst type	Ir Black	Pt on HSAC
Particle size (nm)	1.5-2.0	1.1-5[34]
Loading ($mg.cm^{-2}$)	2.5	0.17
Ionomer type	Fumatec	
Ionomer loading (wt%)	21	40
PTL type	Titanium	
PTL coating type	Platinum	
PTL coating thickness (nm)	70	
Assembly Parameters		
Torque (N.m)	30	
Testing parameters		
Pre-conditioning	*In-situ* hydration, heating until 60˚C.	
	In voltage mode, run the cell at 0.05 $A.cm^{-2}$ and 1.5 V and wait for 10min of stability. Potential is increased to 1.6 V, and once stability is reached, it is run for 10 min.	
	In constant current mode, current density is increased stepwise (0.1 $A.cm^{-2}$ steps) until a potential of 1.85V is achieved. The cell is held at 1.85V for at least 12 hours to assess stability.	

3.6.1 Gas-Crossover Testing

The test bench was connected in-line with an SRI 8610C gas chromatograph (GC), set to 50 °C, coupled with a Hidden Analytica HPR-20 mass spectrometer (MS) (1.2×10^{-9} bar internal pressure). Calibration was done with the use of 1.08, 3.07 and 5.05 vol% hydrogen in argon (Ar) calibration gases at a flow rate of 1.8 $L.h^{-1}$ and a pressure of 1.2 kPa, yielding an uncertainty of 0.04 vol% when compared to previous calibration gases.

Each cell was tested at 0.35, 0.5 and 0.7 $A.cm^{-2}$ at 40 °C, followed by 0.7 $A.cm^{-2}$ at 60 and 75 °C. Each set was repeated in triplicate. The Anode flow was continuously regulated to ~1.8 $L.h^{-1}$, and each test was allowed to stabilise for 120 min after a change in current density.

3.6.2 Electrochemical Impedance Spectroscopy (EIS)

EIS was conducted at 40, 60, and 75 °C using a Gamry 3000 Potentiostat connected to a Gamry 30K Booster. Galvanostatic EIS was conducted at current densities of 0.1, 0.2, 0.3, 0.4, and 0.5 $A.cm^{-2}$ in the frequency range from 20 000 and 0.1 Hz with 10 points per decade. Each scan was separated by a galvanostatic stabilisation of 330 s. Processing of EIS data was done using an I-R-(R)(P)-(R)(P) Equivalent Circuit Model (ECM) as shown in Figure 23

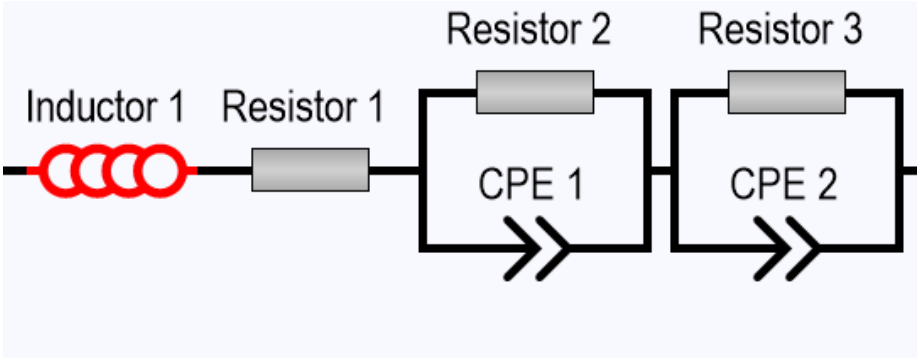


Figure 23: Equivalent circuit diagram used for EIS processing of PEMWE cells with use of two Constant Phase Elements (CPE).

Bibliography

(1) Kinumoto, T.; Inaba, M.; Nakayama, Y.; Ogata, K.; Umebayashi, R.; Tasaka, A.; Iriyama, Y.; Abe, T.; Ogumi, Z. Durability of perfluorinated ionomer membrane against hydrogen peroxide. *Journal of Power Sources* **2006**, *158* (2), 1222-1228. DOI: https://doi.org/10.1016/j.jpowsour.2005.10.043.

(2) Ghassemzadeh, L. Polymer electrolyte membrane degradation and mobility in fuel cells. **2010**.

(3) Ghassemzadeh, L.; Kreuer, K. D.; Maier, J.; Müller, K. Evaluating chemical degradation of proton conducting perfluorosulfonic acid ionomers in a Fenton test by solid-state 19F NMR spectroscopy. *Journal of Power Sources* **2011**, *196* (5), 2490-2497. DOI: https://doi.org/10.1016/j.jpowsour.2010.11.053.

(4) Lim, H. J.; Kim, G.; Yun, G. J. Durability and Performance Analysis of Polymer Electrolyte Membranes for Hydrogen Fuel Cells by a Coupled Chemo-mechanical Constitutive Model and Experimental Validation. *ACS Applied Materials \& Interfaces* **2023**, *15* (20), 24257-24270. DOI: 10.1021/acsami.2c15451 , note = PMID: 37179493.

(5) Libeth, M.; Jean-Christophe, P.; Jérôme, D.; Olivier, L. Characterization of polymer electrolyte Nafion membranes: Influence of temperature, heat treatment and drying protocol on sorption and transport properties. *Journal of Membrane Science* **2012**, *389*, 43-56. DOI: https://doi.org/10.1016/j.memsci.2011.10.014.

(6) Wei, X.; Robert, M. D.; Mike, L. P. Processing and Pretreatment Effects on Vanadium Transport in Nafion Membranes. *Journal of The Electrochemical Society* **2015**, *163* (1), A5084. DOI: 10.1149/2.0111601jes.

(7) Shi, S.; Dursch, T. J.; Blake, C.; Mukundan, R.; Borup, R. L.; Weber, A. Z.; Kusoglu, A. Impact of hygrothermal aging on structure/function relationship of perfluorosulfonic-acid membrane. *Journal of Polymer Science Part B: Polymer Physics* **2016**, *54* (5), 570-581. DOI: https://doi.org/10.1002/polb.23946.

(8) Feng, K.; Hou, L.; Tang, B.; Wu, P. Does thermal treatment merely make a H2O-saturated Nafion membrane lose its absorbed water at high temperature? *Physical Chemistry Chemical Physics* **2015**, *17* (14), 9106-9115, 10.1039/C5CP00203F. DOI: 10.1039/C5CP00203F.

(9) Wang, J.; Yang, M.-m.; Dou, P. C.; Wang, X.; Zhang, H. Influences of Annealing on the Perfluorosulfonate Ion-Exchanged Membranes Prepared by Melt Extrusion. *Industrial & Engineering Chemistry Research* **2014**, *53*, 14175-14182.

(10) Takamatsu, T.; Eisenberg, A. Densities and expansion coefficients of nafion polymers. *Journal of Applied Polymer Science* **1979**, *24* (11), 2221-2235. DOI: https://doi.org/10.1002/app.1979.070241102.

(11) Karelin, A. I.; Kayumov, R. R.; Dobrovolsky, Y. A. FTIR spectroscopic study of the interaction between NH4+ and DMSO in Nafion. *Spectrochimica Acta Part A: Molecular and Biomolecular Spectroscopy* **2019**, *215*, 381-388. DOI: https://doi.org/10.1016/j.saa.2019.03.007.

(12) Karelin, A. I.; Kayumov, R. R.; Sanginov, E. A.; Dobrovolsky, Y. A. FTIR spectroscopic study of the complex formation between H+ and DMSO in Nafion. *Spectrochimica Acta Part A: Molecular and Biomolecular Spectroscopy* **2017**, *178*, 94-104. DOI: https://doi.org/10.1016/j.saa.2017.01.062.

(13) Lue, S. J.; Pai, Y.-L.; Shih, C.-M.; Wu, M.-C.; Lai, S.-M. Novel bilayer well-aligned Nafion/graphene oxide composite membranes prepared using spin coating method for direct liquid fuel cells. *Journal of Membrane Science* **2015**, *493*, 212-223. DOI: https://doi.org/10.1016/j.memsci.2015.07.007.

(14) Karimi, M. B.; Mohammadi, F.; Hooshyari, K. Recent approaches to improve Nafion performance for fuel cell applications: A review. *International Journal of Hydrogen Energy* **2019**, *44* (54), 28919-28938. DOI: https://doi.org/10.1016/j.ijhydene.2019.09.096.

(15) Suzuki, S.; Shoji, N.; Tsuru, T. Performance evaluation of water vapor permeation through perfluorosulfonic acid capillary membranes. *Separation and Purification Technology* **2021**, *266*, 118508. DOI: https://doi.org/10.1016/j.seppur.2021.118508.

(16) Elgammal, R. A.; Tang, Z.; Sun, C.-N.; Lawton, J.; Zawodzinski, T. A. Species Uptake and Mass Transport in Membranes for Vanadium Redox Flow Batteries. *Electrochimica Acta* **2017**, *237*, 1-11. DOI: https://doi.org/10.1016/j.electacta.2017.03.131.

(17) Collette, F. M.; Thominette, F.; Mendil-Jakani, H.; Gebel, G. Structure and transport properties of solution-cast Nafion® membranes subjected to hygrothermal aging. *Journal of Membrane Science* **2013**, *435*, 242-252. DOI: https://doi.org/10.1016/j.memsci.2013.02.002.

(18) Shi, S.; Weber, A. Z.; Kusoglu, A. Structure/property relationship of Nafion XL composite membranes. *Journal of Membrane Science* **2016**, *516*, 123-134. DOI: https://doi.org/10.1016/j.memsci.2016.06.004.

(19) Lim, H. J.; Kim, G.; Yun, G. J. Durability and Performance Analysis of Polymer Electrolyte Membranes for Hydrogen Fuel Cells by a Coupled Chemo-mechanical Constitutive Model and Experimental Validation. *ACS Appl Mater Interfaces* **2023**, *15* (20), 24257-24270. DOI: 10.1021/acsami.2c15451 From NLM.

(20) Tsuneda, T.; Singh, R. K.; Iiyama, A.; Miyatake, K. Theoretical Investigation of the H2O2-Induced Degradation Mechanism of Hydrated Nafion Membrane via Ether-Linkage Dissociation. *ACS Omega* **2017**, *2* (7), 4053-4064. DOI: 10.1021/acsomega.7b00594.

(21) Robert, M.; El Kaddouri, A.; Perrin, J.-C.; Raya, J.; Lottin, O. Time-resolved monitoring of composite Nafion™ XL membrane degradation induced by Fenton's reaction. *Journal of Membrane Science* **2021**, *621*, 118977. DOI: https://doi.org/10.1016/j.memsci.2020.118977.

(22) Frensch, S. H.; Serre, G.; Fouda-Onana, F.; Jensen, H. C.; Christensen, M. L.; Araya, S. S.; Kær, S. K. Impact of iron and hydrogen peroxide on membrane degradation for polymer electrolyte membrane water electrolysis: Computational and experimental investigation on fluoride emission. *Journal of Power Sources* **2019**, *420*, 54-62. DOI: https://doi.org/10.1016/j.jpowsour.2019.02.076.

(23) Halalay, I. C.; Merzougui, B.; Mance, A. Three Mechanisms for Protecting the Fuel Cell Membrane, Plates and Catalysts. *ECS Transactions* **2008**, *16* (2), 969. DOI: 10.1149/1.2981937.

(24) Bosnjakovic, A.; Kadirov, M. K.; Schlick, S. Using ESR spectroscopy to study radical intermediates in proton-exchange membranes exposed to oxygen radicals. *Research on Chemical Intermediates* **2007**, *33* (8), 677-687. DOI: 10.1163/156856707782169372.

(25) Liu, H.; Coms, F. D.; Zhang, J.; Gasteiger, H. A.; LaConti, A. B. Chemical degradation: correlations between electrolyzer and fuel cell findings. Springer: 2009; Vol. 1.

(26) Gao, Y.; Salako, E.; Thompson, M. Synthesis of New Perfluorosulfonic Acids Against H2o2 Degradations. *Available at SSRN 4645297*.

(27) Hassan, M. K.; Nalawade, A.; Abukmail, A.; Patil, Y.; Mauritz, K. A. Analysis of Nafion Fuel Cell Membrane Chemical Durability Using Broadband Dielectric Spectroscopy. *ECS Transactions* **2011**, *41* (1), 1359.

(28) Rajabalizadeh Mojarrad, N.; Kırlıoğlu, A. C.; Yarar Kaplan, B. P(VDF-TrFE) reinforced composite membranes fabricated via sol-gel and dual-fiber electrospinning for reduced relative humidity operation of PEM fuel cells. *Solid State Ionics* **2023**, *392*, 116152. DOI: https://doi.org/10.1016/j.ssi.2023.116152.

(29) Maximilian, M.; Dunia, A.; Miriam, K.; Muhammad Solihul, M. m.; Simon, T.; Thomas, B. A comprehensive study on the ionomer properties of PFSA membranes with confocal Raman microscopy. *Journal of Membrane Science* **2023**, *669*, 121244. DOI: https://doi.org/10.1016/j.memsci.2022.121244.

(30) Böhm, T.; Moroni, R.; Breitwieser, M.; Thiele, S.; Vierrath, S. Spatially Resolved Quantification of Ionomer Degradation in Fuel Cells by Confocal Raman Microscopy. *Journal of The Electrochemical Society* **2019**, *166* (7), F3044. DOI: 10.1149/2.0051907jes.

(31) Gruger, A.; Régis, A.; Schmatko, T.; Colomban, P. Nanostructure of Nafion® membranes at different states of hydration: An IR and Raman study. *Vibrational Spectroscopy* **2001**, *26* (2), 215-225. DOI: https://doi.org/10.1016/S0924-2031(01)00116-3.

(32) Nechitailov, A. A.; Volovitch, P.; Glebova, N. V.; Krasnova, A. Features of the Degradation of the Proton-Conducting Polymer Nafion in Highly Porous Electrodes of PEM Fuel Cells. In *Membranes*, 2023; Vol. 13, p 342.

(33) Bornman, M.; Pushkarev, A.; Martinson, C.; du Preez, S. P.; Bessarabov, D. G.; Kruger, G.; Gouws, R. A novel current switching device for proton exchange membrane electrolyser characterisation and monitoring. *International Journal of Hydrogen Energy* **2025**, *168*, 151091. DOI: https://doi.org/10.1016/j.ijhydene.2025.151091.

(34) Tanaka precious metals. *Electrocatalysts for Fuel Cell / Water Electrolysis (PEM type)*. https://tanaka-preciousmetals.com/en/products/detail/pefcs/ (accessed 2026 9 March).

CHAPTER 4: RESULTS AND DISCUSSION

The chapter begins by establishing the physicochemical baseline of virgin Nafion® in Section 4.1, thereby ensuring that subsequent variations can be accurately attributed to the degradation protocol rather than manufacturing variability. Section 4.2 details the *ex-situ* degradation phenomena, correlating chemical decomposition (quantified by IEC, FRR, and SER) with structural and morphological changes (observed via spectroscopy and microscopy). Finally, Section 4.3 translates these material-level degradation modes into performance losses and evaluates the electrochemical behaviour of the degraded membranes in a single PEMWE cell. This structured approach aims to elucidate the critical structure-property-performance relationships governing membrane durability following Fenton AST.

4.1 Virgin Membrane Characterisation

The initial characterisation of virgin Nafion® membranes (defined here as pre-treated membranes) was conducted to establish a baseline for subsequent degradation studies. Table 7 summarises the properties of 60 individual samples, categorised by membrane type.

Table 7: Virgin Nafion® samples including IEC, EW, Water uptake (%) and Hydration number (λ). Based on 60 analyses, with averages and deviations shown.

	Nafion® 117	**Nafion® 115**
IEC (meq.g^{-1})	0.909 (±0.05)	0,914 (±0.01)
EW(g.eq^{-1})	1104.60 (±57.15)	1096,460 (±15.66)
Water Uptake (%)	17.33 (± 5.47)	25.002 (±1.02)
Hydration Number (λ)	8.844 (±4.87)	15.001 (± 0.59)

The IEC and EW values remained consistent across both sample sets, falling within a narrow range (IEC ≈ 0.90-0.91 meq.g^{-1}; EW ≈ 1096-1104 g.eq^{-1}). These results align closely with the theoretical specifications for Nafion® (nominal EW ≈ 1100 g.eq^{-1})[1], indicating that the density of sulfonic acid functional groups is uniform across the various membrane types.[2]

In contrast to the stability of the IEC, the data in Table 7 reveal significant deviations in WU and the corresponding hydration number (λ). These fluctuations are likely attributable to two primary factors: environmental sensitivity and intrinsic physical properties. First, the hygroscopic nature of PFSA membranes makes them highly sensitive to ambient temperature and humidity fluctuations during weighing, leading to a variance in WU of up to 11.19% as measurements were done over multiple days. Second, a distinct trend related to membrane thickness was observed. The thinner Nafion® 115 membrane consistently exhibited a higher water uptake (~25.0%) and

hydration number(λ~15) compared to the thicker Nafion® 117 (e.g., 17.33% and λ~8.8). This is consistent with the mechanical behaviour of the ionomer; thinner membranes typically experience fewer morphological constraints throughout the bulk polymer, permitting greater swelling upon hydration.[3, 4] This enhanced swelling capacity directly increases the total water volume fraction per unit mass of dry polymer.

The measured λ in this study (8.8-15.0) falls well within the broad range reported in the literature, which typically spans 3.8 to 20.1 ± 1.2 depending on the specific thermal history and pre-treatment protocols employed. The values obtained here suggest that the pre-treatment protocol successfully achieved a moderate-to-high state of hydration, providing a representative baseline for a functional PEM water electrolyser environment.[5-8]

- **ATR FT-IR spectroscopy**

The chemical structure of the virgin PFSA ionomer was confirmed via ATR FT-IR spectroscopy, as shown in Figure 24. Here, Nafion® 117 was analysed, as it is assumed that the spectra for Nafion® 115 and Nafion® 117 are identical. The spectrum is presented in the 1800-550 cm^{-1} range, which encompasses the primary vibrational modes characteristic of PFSA materials.[9] The observed bands align with established literature assignments.[10-15] Strong absorption features between 1100 and 1300 cm^{-1} correspond to the symmetric and asymmetric stretching vibrations of the C-F bonds within the PTFE backbone. Key side-chain functional groups are also clearly resolved: the symmetric S-O stretch of the sulfonate group (SO_3^-) appears at 1056 cm^{-1}, while the C-O-C ether linkages are identified by the doublet at 968 cm^{-1} and 982 cm^{-1}. Finally, the broad band at 1723 cm^{-1} is attributed to the H-O-H bending vibrations of water molecules and hydronium ions (H_3O^+), within the hydrophilic clusters, confirming the hydrated state of the membrane baseline.

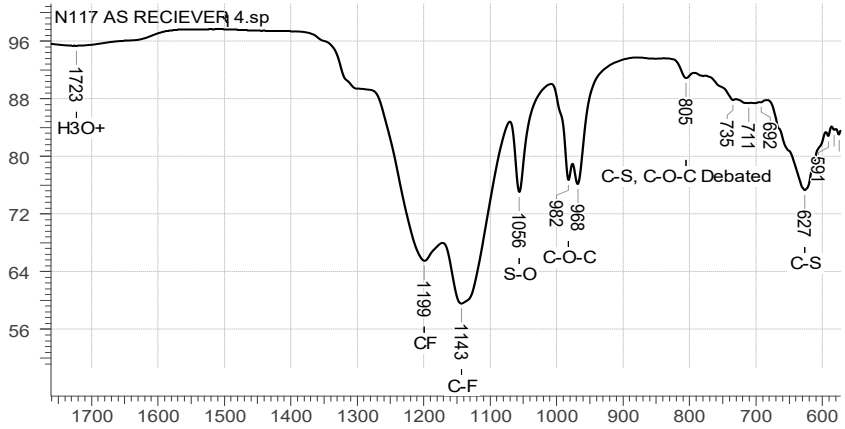


Figure 24: ATR FT-IR transmittance spectrum of as-received Nafion® 117 in the spectral range of 1800-550 cm^{-1}.

Raman spectroscopy

Figure 25 presents the full-range Raman spectrum (0-3750 cm^{-1}) of the virgin Nafion® 117 membrane, serving as a complete so-called fingerprint of the material before degradation. To facilitate structural elucidation. The Raman signature of Nafion® is well established in the literature, enabling the precise assignment of vibrational modes to the polymer backbone and side chains.[9, 16-20]

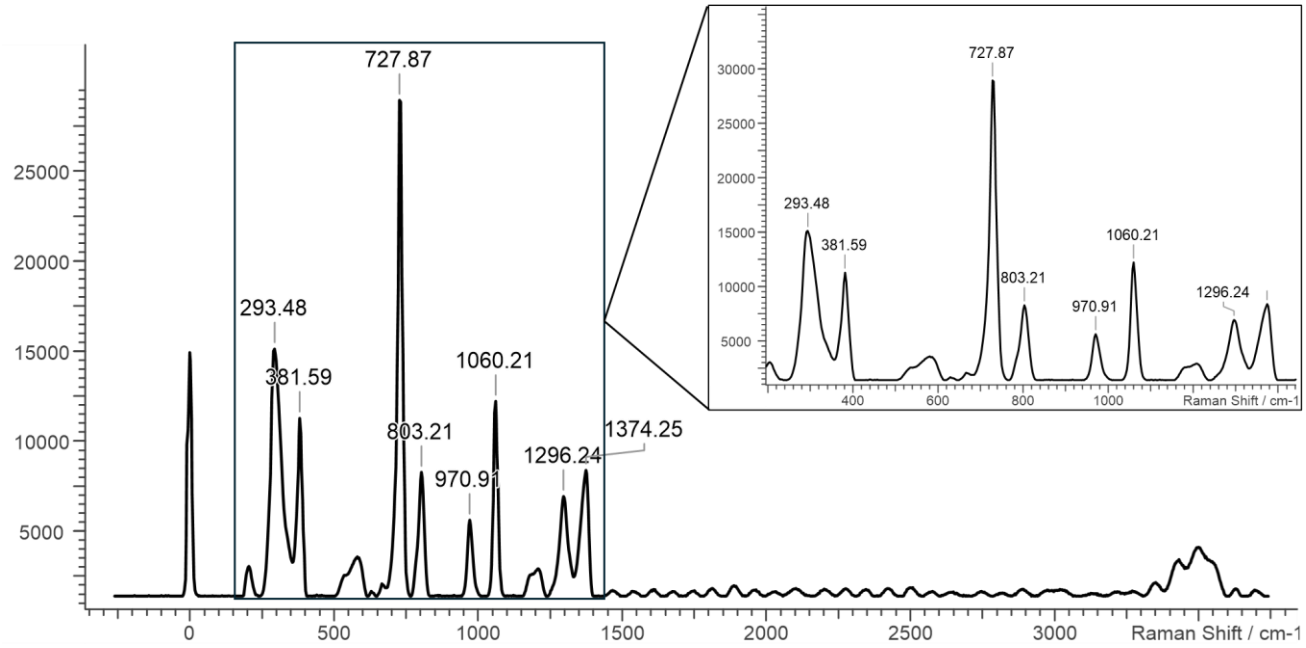


Figure 25: Raman spectrum of as-received Nafion® 117

In Figure 25, the most prominent response, observed at 727.87 cm^{-1}, corresponds to the symmetric stretching of the C-F bonds within the PTFE backbone (CF_{bb}). Additional modes associated with the backbone are also identified at 293, 382, 1296, and 1374 cm^{-1}.

Conversely, Raman peaks observed at 803, 971, and 1060 are attributed to vibrations within the perfluoroether side chain. Specifically, the peak at 1060 cm^{-1} is assigned to the S-O stretching vibration of the terminal sulfonyl group. The response at 971 cm^{-1} is attributed to the symmetric C-O-C stretching of the ether linkages within the side chain.[9, 16] The assignment of the peak at 803 cm^{-1} remains inconclusive in the literature; some studies attribute this response to the symmetric C-S stretching vibration stretching[21] while others assign it to the symmetric stretching of C-F bonds located within the side chain (CF_{sc}).[16, 17]

NMR spectroscopy

NMR spectroscopy provides complementary insight into the molecular environment of the virgin membrane. Figure 26 shows the ^{1}H and ^{19}F Liquid NMR of a virgin Nafion® 117 membrane. Figure 26 a) shows a prominent peak at 3.99 ppm, which corresponds to the protons in water,

confirming the presence of residual hydration within the membrane. The rest of the spectrum represents the solvent peaks.

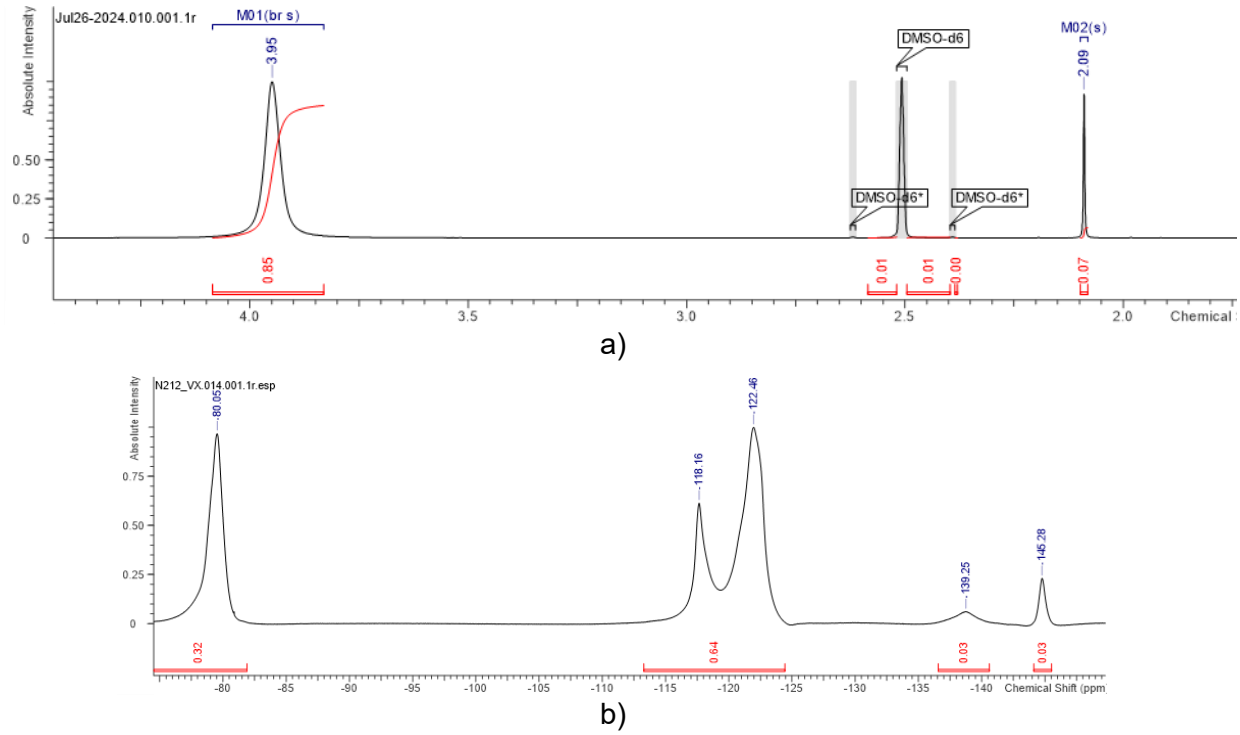


Figure 26: Virgin a) ^{1}H Liquid NMR spectrum and b)^{19}F liquid NMR spectrum of a virgin Nafion® 117 membrane

The liquid-state ^{19}F NMR spectrum of virgin Nafion® 115 (Figure 26 b)) shows multiple signals characteristic of the distinct fluorine environments expected within the PFSA structure. These include resonances assigned to the backbone (CF_{bb}) groups at 121 ppm, the side-chain -OCF_2- groups at 188 ppm, and the terminal trifluoromethyl (-CF_3) groups at 80 ppm.

These assignments are corroborated by the solid-state ^{13}C CP-MAS NMR spectrum (Figure 27), which shows distinct resonances for the carbon atoms in both the PTFE backbone and the perfluoroether side chain.

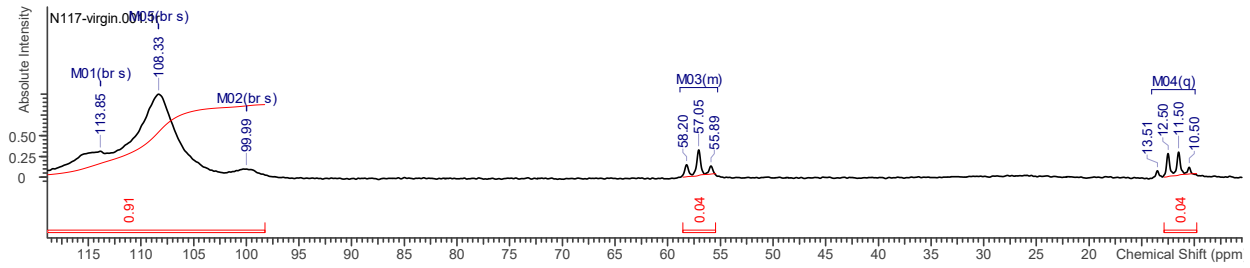


Figure 27: Virgin ^{13}C CP-MAS NMR spectrum

Summary of Structural Verification

Collectively, the FT-IR, Raman, and multinuclear NMR analyses provide comprehensive structural verification of the virgin, pretreated Nafion® 117 membrane. These complementary techniques confirm the expected chemical structure, ranging from the vibrational modes of the fluorocarbon backbone and ether linkages to the specific nuclear environments of the side-chain functionalities. This multi-technique characterisation establishes a robust baseline against which the effects of chemical degradation can be assessed. Table 8 provides a consolidated summary of the characteristic chemical shifts and vibrational frequencies identified in this section.

Table 8: Table of identification for characteristic chemical shift present in PFSA structure in NMR, FT-IR and Raman spectroscopy.

	^{13}C NMR (ppm)	**^{19}F NMR (ppm)[22]**	**ATR FT-IR (cm^{-1})**	**Raman (cm^{-1})[23]**
CF_{sc}	103.4	-144	-	803
CF_{bb}	108.2	-138	-	728, 293, 382, 1296
$(CF_2)_n$	111.4	-121	1143, 1199	
SCF_2	113	-117	-	
OCF_2	116.7	-80.1	-	
CF_3	118	-80	-	
SO_3^-	-	-	1056	1060
COC	-	-	982, 968	971

4.2 Ex-Situ Degradation: Impact on Physicochemical Properties

4.2.1 Ion Exchange Capacity (IEC) Loss

Figure 28 a-d shows the IEC loss of Nafion® 117 and 115, which provides the foundational quantitative measure of chemical degradation. The raw data is presented in Annexure A, 6.1.1.

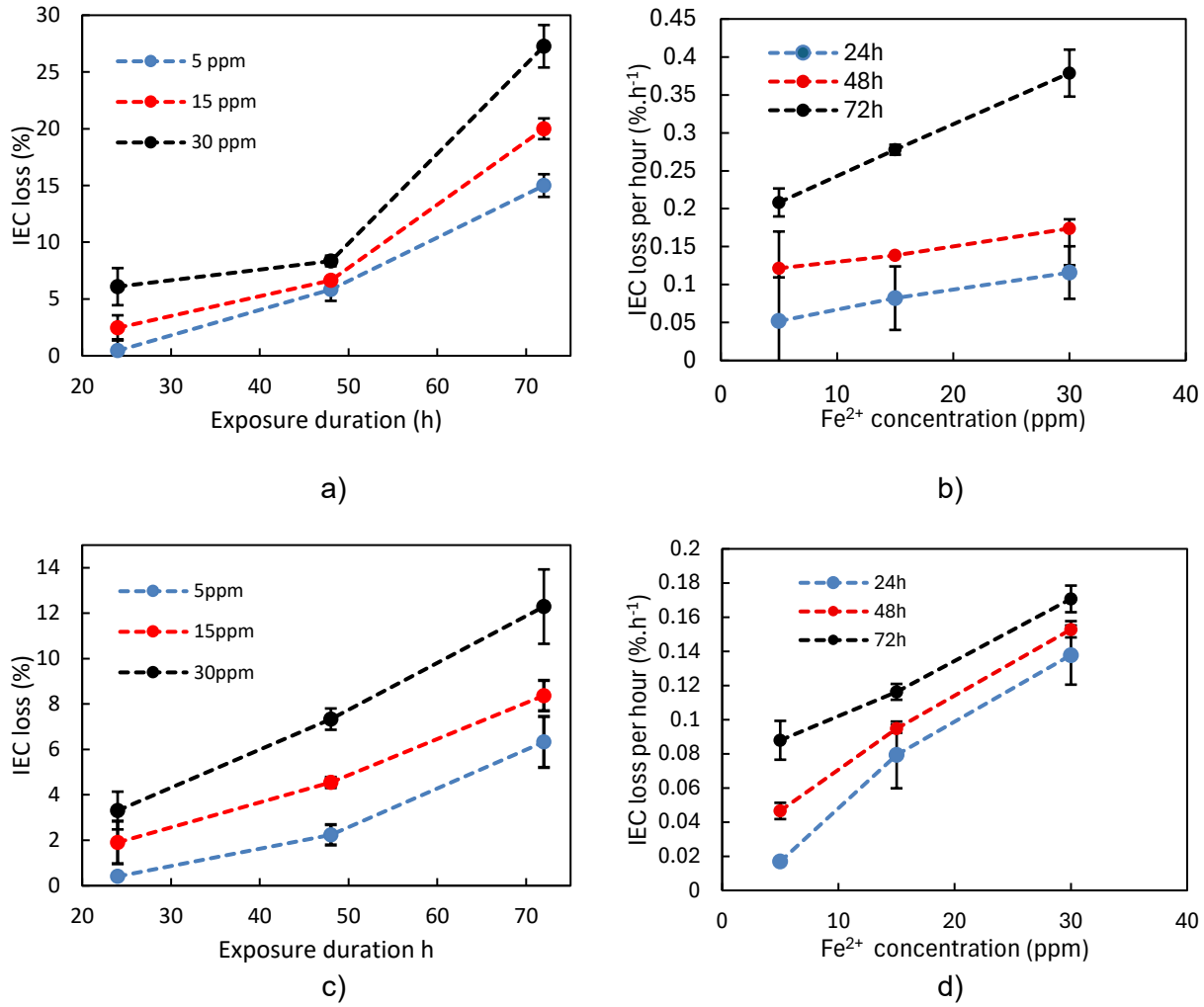


Figure 28: a) IEC loss of small-scale Nafion® 117 as a) function of exposure duration, and b) percentage IEC loss per hour as a function of Fe^{2+} concentration. IEC loss of large-scale Nafion® 115 as c) function of exposure duration, and d) percentage IEC loss per hour as a function of Fe^{2+} concentration.

With examination of the IEC loss, two interrelated trends emerge from Figure 28. First, a clear dose-response relationship is evident. Both Figures 28 a) (small-scale) and c) (large-scale) illustrate a positive correlation between the severity of the degradation conditions and the resulting loss in IEC.

The IEC loss scaled with the Fe^{2+} concentration, with small-scale increasing from 15% to 27.27% and large-scale from 0.4% to 12.29% across the mildest (5 ppm, 24 h) to the most severe (30 ppm, 72 h) conditions, respectively. This confirms that the degradation is not merely a function of time in hydrogen peroxide but is catalytically driven by Fe^{2+}.

Second, a more nuanced analysis, particularly of Figure 28 b) and d) (both scales), indicates that the degradation rate (%IEC loss.h^{-1}) accelerates over time. For any given Fe^{2+} concentration, the rate of IEC loss calculated at the 72 h mark is significantly higher than the rate

at 24 h. This suggests the degradation process may be autocatalytic, or that the initial chemical attacks create more vulnerable sites on the polymer, leading to a cascade of subsequent scission events. This observation suggests that linearly extrapolating degradation data from short-term tests would underestimate the membrane's long-term damage and lifetime.

These experimental findings validate the degradation mechanisms and kinetic models detailed in Chapter 2. As described in Section 2.4.5.3, the primary mechanism of chemical degradation is a radical-induced attack on the ionomer side chain, specifically targeting the C-S bond (Table 4; R_{14}: $SC–SO_3H + •OH \rightarrow SC–O• + HOCF_2CF_2SO_3H$).[24, 25] The loss of IEC measured in this section is the quantitative consequence of the C-S bond scission, which results in the complete cleavage and loss of the sulfonyl functional groups.[26] Figure 28, therefore, provides experimental evidence, i.e., the reported IEC losses, that side-chain scission is a dominant degradation mode under Fenton-like conditions.

Furthermore, the results experimentally validate the kinetic competition framework established in the literature. As discussed by Frühwirt *et al.*[25] (Section 2.6.1, Table 4) and Lorenz *et al.*[27] (Section 2.6.1, Figure 12), the Fe^{2+} ion is the catalyst for the primary •OH radical generation step (R_1, Table 4; $Fe^{2+} + H_2O_2 + H^+ \rightarrow Fe^{3+} + •OH + H_2O$). By increasing the Fe^{2+} concentration from 5 to 30 ppm, the IEC loss rate increases, effectively flooding the system with •OH radicals and thereby increasing the statistical probability of the kinetically slower polymer attack. [25] The result is the higher rate of IEC loss observed in Figures 28 b and c, confirming that the Fe^{2+} concentration is a primary controlling factor in the degradation rate, as predicted by the kinetic model presented in Section 2.6.1.

In summary, the IEC loss presented in this section provides the quantitative basis for the degradation method used in this study. It validates the side-chain scission mechanisms and kinetic competition models proposed in Sections 2.4.5 and 2.6.1. The data show a correlation: conditions that produce the highest IEC loss (i.e., high Fe^{2+} concentration) also produce the highest SER (Figure 29), as these two measurements quantify the same chemical event from two different perspectives. This correlation suggests that the mechanism of IEC loss is C-S bond scission and subsequent dissolution of the sulfonic acid group.

4.2.2 Effluent Analysis: Fluoride Release Rate (FRR) and Sulfur Emission Rate (SER)

Analysis of the Fenton test effluent provides a measure of the rate of polymer degradation. FRR quantifies the scission of C-F bonds from both the polymer backbone and side chains, while the SER specifically measures the loss of the terminal sulfonic acid groups from the side chains. For FRR and SER, only the large-scale degradation results were reported, as the small-scale samples were primarily used for method development.

The fluoride release and sulfur emissions of the degradation effluent are shown in Figure 29. The analysis of the degradation effluent, presented in Figure 29 a), provides a quantification of the ionomer's chemical decomposition and offers mechanistic insights. Figure 29 a) and b) shows the cumulative F^- and S^{2-} emission, normalised per exposed membrane area, as a function of the initial Fe^{2+} ion concentration.

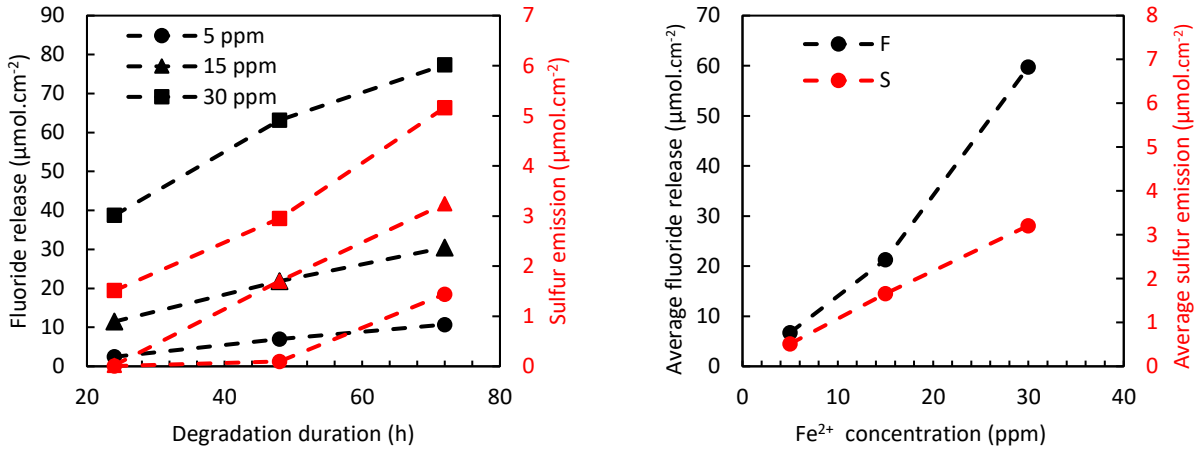


Figure 29: Fluoride release and sulfur emission per exposed surface area of the degraded membranes, as a) a function of degradation duration and b) average, normalised for degradation duration, release as a function of Fe^{2+} concentration.

From Figure 29 b), a strong, positive correlation is evident for F and S species. An increase in the Fe^{2+} concentration from 5 to 30 ppm results in an increase in the total emission of both fluoride (6.73 µmol.cm^{-2} to 59.76 µmol.cm^{-2}) and sulfur (from 0.51 µmol.cm^{-2} to 3.21 µmol.cm^{-2}). This trend is consistent with the Fenton degradation mechanism, wherein Fe^{+2} catalyses the decomposition of H_2O_2 to generate •OH radicals (Section 2.6.1, Table 4, R_1; $Fe^{2+} + H_2O_2 + H^+ \rightarrow Fe^{3+} + \bullet OH + H_2O$) which react with the side chain to release sulfonic acid and HF groups ($R_{14\text{-}15}$; $SC\text{–}SO_3H + \bullet OH \rightarrow SC\text{–}O\bullet + HOCF_2CF_2SO_3H$ and $SC\text{–}O\bullet + 3\bullet OH \rightarrow BB\text{–}O\bullet + 6HF + 3CO_2$) and the CF_{bb} releasing HF and ultimately undergoing the unzipping mechanism ($R_{16\text{-}23}$; $BB\text{–}O\bullet + \bullet OH \rightarrow 2\text{–}(CF_2)_n COOH + 3HF$ and $\text{–}(CF_2)_nCOOH + 2\bullet OH \rightarrow \text{–}(CF_2)_{n-1}COOH + CO_2 + 2H$).[25]

A deeper mechanistic insight is obtained by decoupling these two emission signals. Because the sulfur atom is present exclusively in the terminal sulfonic acid (-SO_3H) group of the ionomer side chain, the SER serves as a quantification of side-chain scission (C-S bond cleavage).[28, 29] Accordingly, this pathway represents the dominant chemical degradation mechanism responsible for IEC loss.

In contrast, fluorine is abundant, occurring in both the perfluoroether side chain and, more significantly, in the PTFE backbone. The FRR is therefore a composite metric that represents the

combined degradation of both the side and main chains.[30-32] By analysing the molar F:S ratio, it is possible to distinguish these two degradation pathways. Based on the known monomeric structure of the Nafion® side chain (-$OCF_2CF(CF_3)OCF_2CF_2SO_3H$), there are 10 fluorine atoms for every 1 sulfur atom. Therefore, if degradation proceeded exclusively via the scission and dissolution of the entire side chain, a theoretical F:S molar ratio of approximately 10:1 would be expected in the effluent. The experimental data from Figure 29 reveal an F:S molar ratio of 18.62:1 (calculated from 59.76 µmol.cm^{-2} F^- and 3.21 µmol.cm^{-2} S^{2-} at 30 ppm Fe^{2+}). This experimental ratio is 1.8 times greater than the theoretical value for side-chain-only degradation, which is supported by Curtin *et al.*,[33] who noted an increased FRR compared to SER. This discrepancy supports that the backbone and sidechain degradation mechanisms occur simultaneously.[30-32] As mentioned, the excess of released F^- can only originate from the C-F bonds of the ionomer's PTFE main chain. This confirms that the aggressive radical attack generated under these *ex-situ* AST conditions initiates main-chain degradation, or so-called unzipping, in addition to side-chain scission.

The molar F:S ratio suggests that while side-chain scission (measured by SER and correlated with IEC loss) represents chemical degradation of the membrane's functionality, the concurrent backbone degradation (excess FRR, defined as a molar F:S ratio > 10:1) signifies a loss of polymer mass and thickness.[34] This backbone degradation directly accounts for the physical membrane breakdown, reported in Section 4.2.4.

To situate the FRR findings from this study within the existing literature, the FRR is benchmarked against other *ex-situ* and *in-situ* degradation studies. Figure 30 compares the total FRR from this study with those reported by Shi *et al.*, Lim *et al.*, and Madhav *et al*.[35-37] SER has been omitted because $FeCl_2.4H_2O$ was used as a Fe^{2+} source, whereas other groups have used $FeSO_4.xH_2O$ in the past, making SER measurements difficult.[15, 38-45] This figure illustrates that the observed degradation rates fall within the range of other Fenton-based ASTs and are comparable to them. Here, the FRRs from the 30 ppm degradation tests were not included, as they overshadow the presented results; they are presented in Annexure 6.1.2.

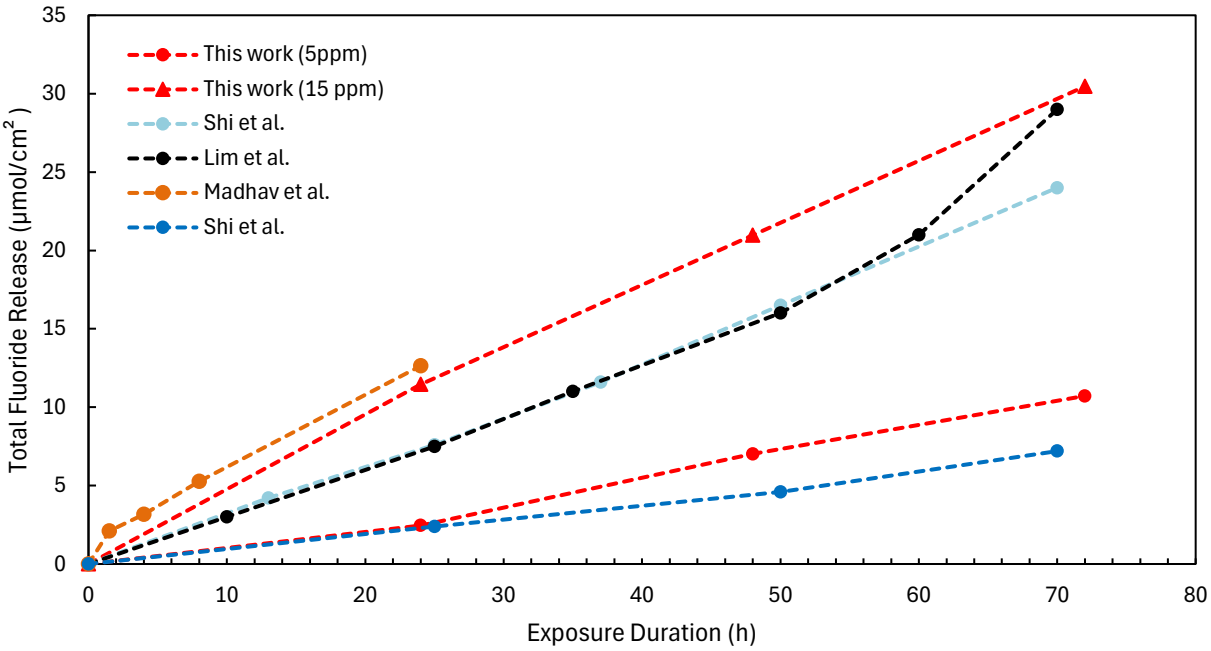


Figure 30: Comparative Figure of previous studies of total fluoride release in terms of *ex-situ* Fenton test duration**.** This line graph compares the total fluoride release (µmol.cm^{-2}) for the 5 and 15 ppm F^{2+} samples in this study with that reported in previous studies.

Table 9 provides a more detailed breakdown of these comparative studies, summarising the specific test conditions, membrane types, and reported FRR. This comparative analysis confirms that the *ex-situ* protocol employed in this study is a valid and effective method for accelerating degradation, producing quantifiable material loss consistent with similar methodologies in the field. Notably, the FRR in this work is comparable to that observed in other Fenton tests on Nafion®, further validating the AST conditions used in this study.

Table 9: Comparative table of previous degradation studies on Nafion® membranes

Degradation type	Fe^{2+} concentration (ppm)	Membrane type	FRR ($\mu mol.cm^{-2}.h^{-1}$)	Ref
Fenton test	5	Nafion® 115	0.132	This work
Fenton test	15	Nafion® 115	0.453	This work
Fenton test	30	Nafion® 115	1.335	This work
Fenton test	15	Nafion® 212	0.352	Lim *et al.* (2023)[36]
Fenton test	55.85	Nafion® 212	0.335	Shi *et al.* (2020)[35]
Fenton test	55.85	Nafion® XL	0.095	Shi *et al.* (2020)[35]
Fenton test	15	Nafion® 212	0.844	Madhav *et al.* (2023)[37]
Fenton test	13	Nafion® 112	~0.45	Sethuraman *et al.* (2008)[46]
Fenton test modelling	10	Nafion® 112	0.37	Fruhwirt *et al.* (2020)[25]
Open-circuit voltage	-	Nafion® 212	0.2-0.6	Patil *et al.*(2010)[47]
Open-circuit voltage	-	GORE-SELECT	0.21	Liu *et al.*(2006)[48]
Bilayer-membrane cell	-	Nafion®	0.13-0.86	Mittal *et al.*(2007)[49]

4.2.3 Spectroscopic Results

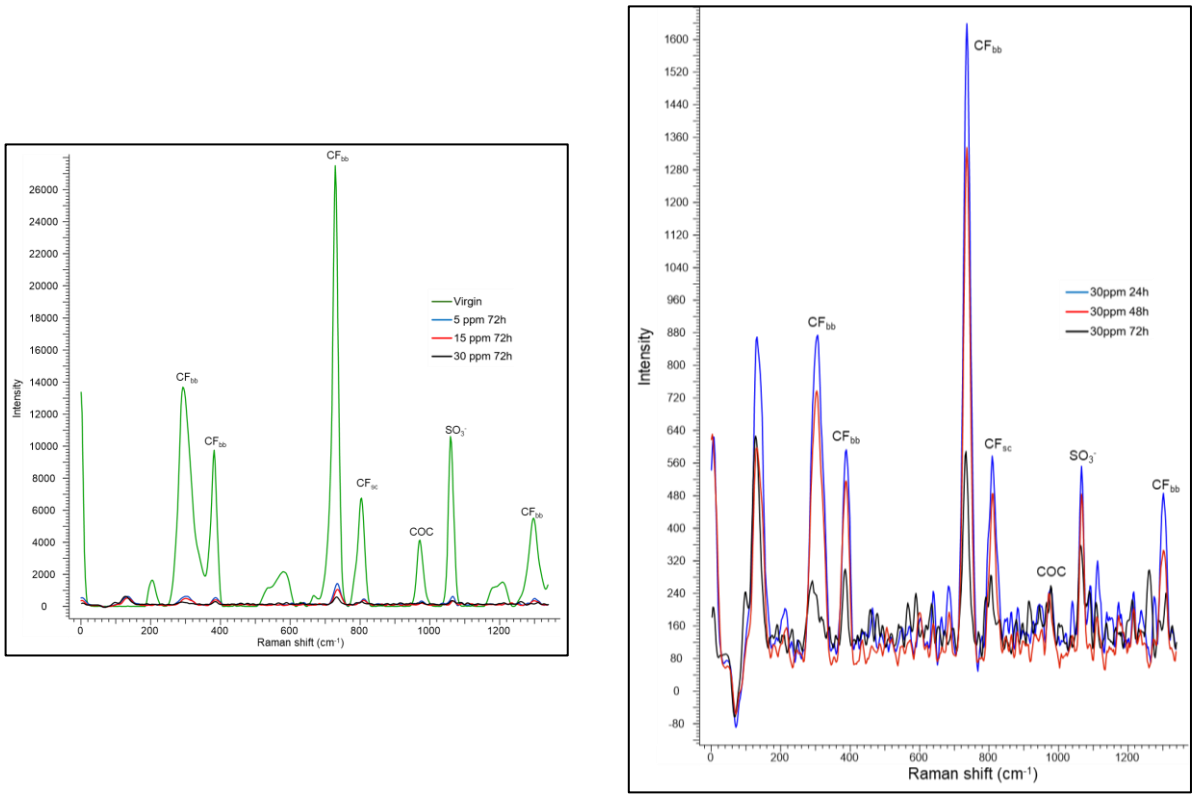
To complement the quantitative functional degradation measured by IEC loss (Section 4.2.1) and effluent analysis (Section 4.2.2), this section employs spectroscopic methods to characterise chemical changes in the PFSA ionomer structure induced by *ex-situ* Fenton degradation. As outlined in the methodology, Raman spectroscopy, ATR FT-IR spectroscopy, and ^{13}C CP-MAS NMR spectroscopy were selected for this purpose. The primary goal is to identify the specific bonds and functional groups attacked during Fenton-based AST and to correlate the extent of this structural damage with AST severity.

4.2.3.1 Raman Spectroscopy Results

Raman spectroscopy is a powerful tool for analysing the chemical environment, as it is highly sensitive to vibrations of key structural bonds within the Nafion® ionomer, including the C-

F backbone (CF_{bb}) and side-chain-specific functional groups, i.e., C-O-C ether linkages and S-O sulfone groups.

Figure 31 a) presents an overlay of Raman spectra for the virgin Nafion® 117 membrane against samples degraded for 72 h at varying Fe^{2+} concentrations. The virgin (green) line overshadows the degraded samples and provides evidence of degradation as signal intensity is proportional to sample concentration.[50] For this reason, Figure 31 b) presents a similar spectrum but excludes the virgin spectrum.



a) b)

Figure 31: Raman spectrum of the dose-response effect of Fe^{2+} concentration on Nafion®117 in the spectral range of 0-1340(cm^{-1}) for the a) 72 h degraded and the b) 30 ppm membranes.

Figure 31 b) examines the degradation progression over the invested degradation duration of 24, 48, and 72 h at the most aggressive degradation Fe^{2+} concentration of 30 ppm. The virgin sample has been omitted to facilitate visual comparison of the degraded samples. This further confirms the duration dependence of the ionomers' degradation, as peak intensity decreases with increasing duration.

The Raman data provide chemical-level evidence regarding the degradation mechanisms quantified in the preceding sections. While Section 4.2.1 demonstrated a dose-dependent IEC loss, indicative of C-S bond scission and the loss of the sulfonic acid groups, the Raman spectra

in Figure 31 visually corroborate this. The attenuation of the S-O stretching intensity at 1060 cm^{-1} across the 5, 15, and 30 ppm samples serves as direct spectroscopic verification of this cleavage (as shown in Figure 31 a)), whereas a similar attenuation is observed as a function of degradation duration (Figure 31 b)).

Furthermore, Section 4.2.2 reported an F:S molar ratio of 18.62:1 in the Fenton effluent, implying that main-chain scission (backbone unzipping) occurs concurrently with side-chain attack. The Raman analysis substantiates this dual mechanism. If degradation were limited to the side chain, the C-F backbone peak (728 cm^{-1}) would be expected to remain stable despite the loss of the S-O peak. Instead, a reduction in intensity is observed across all peaks in the 72 h samples, including the dominant C-F band.

In summary, the Raman analysis demonstrates that Fenton degradation, particularly at high Fe^{2+} concentrations, is not limited to side-chain scission (which is linked to IEC loss due to loss of C-S groups) but also induces significant structural degradation of the ionomers' C-F backbone. This supports the quantitative findings of Sections 4.2.1 (IEC loss) and 4.2.2 (FRR and SER).

4.2.3.2 ATR FT-IR spectroscopy Results

Unlike Raman analysis, ATR FT-IR spectroscopy did not reveal a clear correlation between the degree of degradation and spectral changes. Figure 32 overlays the spectra of the virgin membrane with those of samples degraded for 72 hours at varying Fe^{2+} concentrations.

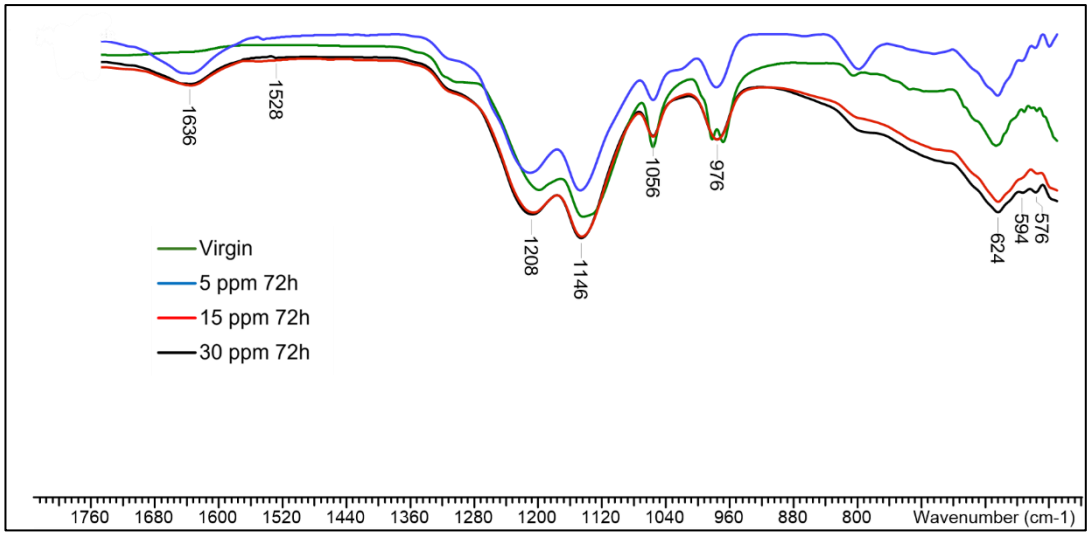


Figure 32: ATR FT-IR spectrum of the dose-response effect of Fe^{2+} concentration on Nafion® 117 in the spectral range of 550-1800(cm^{-1})

Despite the aggressive degradation conditions, the fundamental vibrational bands (C-F_{bb} at 1146–1208 cm^{-1}, S-O stretch at 1056 cm^{-1}, and C-O-C linkage at 976 cm^{-1}) remained largely stable. This insensitivity is likely attributable to the bulk nature of ATR FT-IR characterisation.

Although IEC and effluent analysis confirmed significant material loss, the remaining polymer fragments retained their original chemical structure and high dipole moments. These surviving bonds generate strong absorption signals that obscure the subtle reduction in peak intensity caused by chain scission. Consequently, for the specific degradation mechanisms investigated in this study, techniques sensitive to structural order (Raman) or functional group quantification (IEC) proved to be more effective diagnostic tools. However, this finding reflects a limitation of the specific methodology employed here rather than the technique itself; numerous research groups have successfully utilised FT-IR to investigate post-degradation in PFSA ionomers.[51-54]

4.2.3.3 CP-MAS NMR Analysis

While Raman spectroscopy provided a vibrational fingerprint of the degradation, Solid-State ^{13}C CP-MAS NMR was employed to probe specific changes in the ionomer's carbon skeleton. Unlike FT-IR, which proved insensitive to the bulk morphological changes, and Raman, which is sensitive to crystalline order, ^{13}C NMR provides a direct atomic-level probe of the C environments within the polymer backbone and side chains.[55] The spectra for samples degraded for 24 h at 5, 15, and 30 ppm Fe^{2+} are presented in Figure 33 a), compared against the virgin baseline. To elucidate the temporal evolution of degradation, Figure 33(b) displays the spectra for samples degraded for 24, 48, and 72 h at 30 ppm.

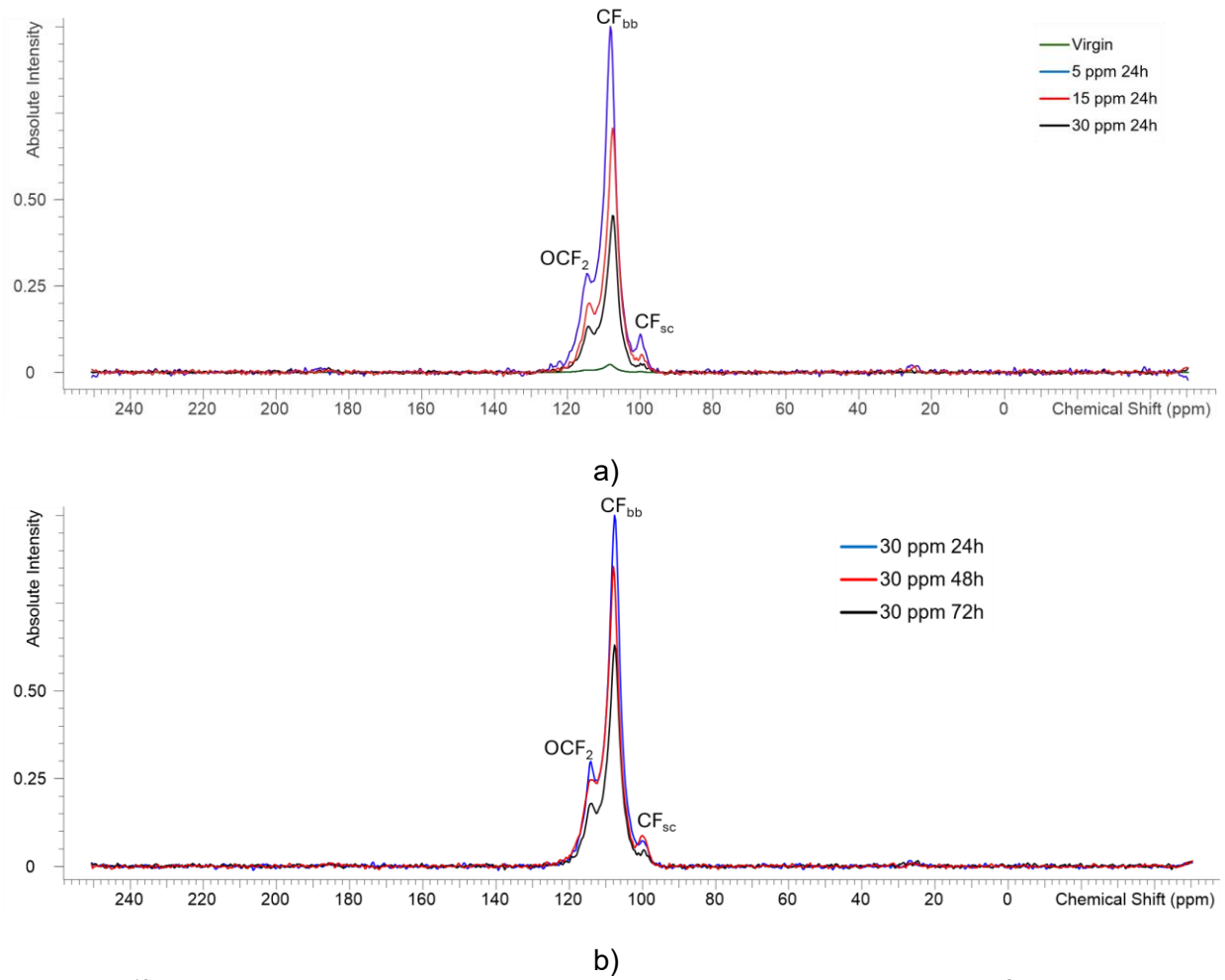


Figure 33: ^{13}C CP-MAS NMR spectrum of samples degraded for a) 24 h at Fe^{2+} concentrations of 5, 15, 30 ppm and b) for 24, 48 and 72h at 30 ppm Fe^{2+} concentration.

Analysis of the spectra reveals a dose- and duration-dependent trend that strongly corroborates the mechanistic findings from the Fenton test effluent analysis, specifically regarding the behaviour of the backbone (CF_{bb}) and the sidechain (CF_{sc}). The data exhibit a trajectory of signal attenuation consistent with the Raman results of the degraded membrane.

The peak intensity of CF_{bb}, which occurs at ~108.2 ppm, decreased with increasing Fe^{2+} concentration. Moreover, the spectral resolution required to distinguish the side-chain CF_{sc} carbons (103.4 ppm) from the backbone CF_{bb} is progressively lost as degradation severity increases.[56]

Despite this loss of resolution, the fundamental peak profile for CF_{bb} (~108.2 ppm) remains qualitatively consistent across the 6 spectra in Figure 33, exhibiting a primary signal with associated shoulders. This suggests that although the total quantity of the material is changing, the fundamental local chemical environment of the remaining polymer segments has not undergone a qualitative shift (i.e., there is no emergence of distinct new functional-group peaks).

This concurrent attenuation of peak intensity is a critical mechanistic finding. If degradation were limited strictly to side-chain scission (cleavage of the C-S bond), one would theoretically expect the disappearance of the side-chain resonances while the PTFE backbone signal remained largely intact.[25] However, Figure 33 demonstrates a simultaneous depletion of the CF_{bb} and CF_{sc} signals.

This loss of the CF_{bb} and CF_{sc} signal provides evidence confirming the dual-degradation mechanism. It further confirms that the FRR measured in Section 4.2.2 is not solely from side-chain degradation but results from the degradation of the carbon backbone. The disappearance of the CF_{bb} resonances supports the unzipping mechanism discussed in the literature review, where radical attack on carboxylic end-groups leads to the rapid depolymerisation of the PTFE main chain (Section 2.6.1, Table 4, $R_{16\text{-}23}$; BB–O• + •OH → 2–$(CF_2)_n$ COOH + 3HF and –$(CF_2)_n$COOH + 2•OH → –$(CF_2)_{n-1}$COOH + CO_2+ 2H.[25, 33]

Ultimately, the progressive attenuation of the ^{13}C signal intensity confirms that degradation is both concentration and duration-dependent. Since CP-MAS NMR signal intensity is generally proportional to the number of nuclei in the sample volume (assuming consistent cross-polarisation dynamics and relaxation dynamics), the reduction in peak area directly correlates to a loss of bulk material or the excision of carbon-containing segments from the polymer matrix.[57] This trend further corroborates the idea that the radical attack is cumulative, stripping away the polymer matrix over time and with increasing Fe^{2+} concentration.

4.2.4 Morphological Analyses

Macroscopic dimensional changes in the membrane were observed following degradation, disrupting downstream CCM fabrication. Specifically, pre-cut bolt holes are no longer aligned with the template, consistent with irreversible deformation resulting from polymer backbone damage. Hydration of an undegraded membrane caused reversible swelling of ~10.03% (14.25 × 13.87 cm to 15.00 × 14.69 cm). After degradation, the hydrated membrane expanded to 17.81 × 15.69 cm, a 29.27% increase relative to the original dry dimensions. Although drying reduced the degraded membrane to 15.13 × 14.13 cm (23.49% shrinkage from its hydrated state), it remained 7.55% larger than the initial cut size, confirming permanent dimensional change

These dimensional changes are illustrated in the flow diagram in Figure 34.

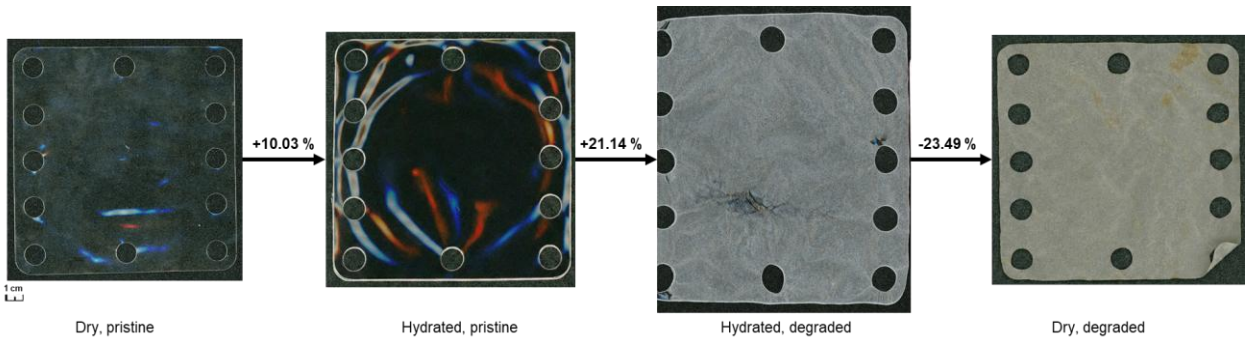


Figure 34: Flow diagram of membrane swelling and shrinkage during hydration and degradation. This Figure is a visual flow diagram showing the dimensional changes of the large-scale Nafion® 115 membrane. It uses four photographs to illustrate the irreversible swelling (source, HySA Infrastructure, NWU).

The observed irreversible swelling is attributed to chemically-accelerated creep and plasticization of the polymer matrix.[58] The unzipping degradation mechanism (driven by •OH) significantly reduces the average molecular weight and entanglement density of PFSAs, leading to a decrease in their Young's modulus.[59] This weakened, less elastic matrix is unable to effectively counterbalance the internal osmotic pressure of the water domains, resulting in excessive water uptake and plastic deformation (creep) that is structurally unrecoverable upon drying.[60]

Despite the evidence of macroscopic expansion, the degradation manifested differently in the cross-sectional dimension. While membrane thinning is a well-documented phenomenon in Fenton-exposed Nafion® resulting from polymer chain scission,[15, 61, 62] No statistically significant correlation between thickness reduction and exposure severity or duration was observed in this study. It is crucial to note that the absence of observable thinning does not imply the absence of degradation. On the contrary, the irreversible increase in swelling discussed above, together with corroborating spectroscopic data, demonstrates that the polymer backbone has degraded. Consequently, the degradation in this experimental setup manifested primarily as plastic deformation and mass loss via elution, rather than as a uniform, measurable reduction in thickness.

To evaluate the visible effects of chemical degradation on Nafion® 117 during method development, a series of small-scale membranes was exposed to Fenton conditions over 24, 48, and 72 h at Fe^{2+} concentrations spanning 5-30 ppm (including the intermediate 10 ppm condition). Figure 35 provides a photographic overview of the post-exposure appearance, capturing changes such as increased opacity, surface roughening, and localised pitting/blemishing across the matrix of conditions. Overall, the severity of the macroscopic surface features increases more consistently with Fe^{2+} concentration than with exposure duration, with the most pronounced

roughening/pitting observed in the higher-catalyst cases. These small-scale observations were used primarily to inform the selection of conditions for the subsequent large-scale membrane experiments; accordingly, the small-scale samples are presented here for contextualisation and are not treated as the primary dataset in the study.

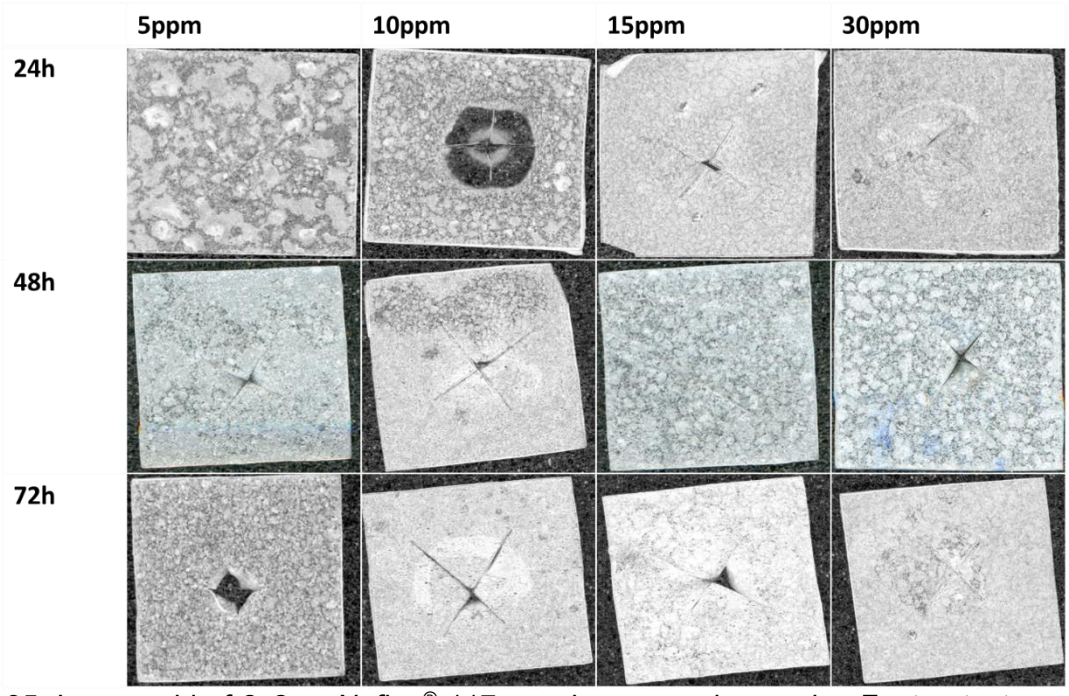
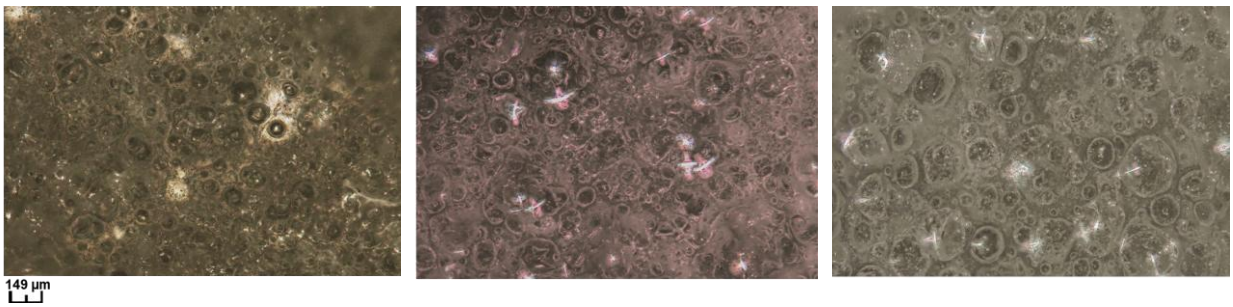


Figure 35: Image grid of 2x2cm Nafion® 117 membranes under varying Fenton test conditions. This is a 3x4 grid of photographs showing the macroscopic appearance of the small-scale Nafion® 117 membranes after degradation. The rows represent exposure duration (24, 48, 72 h) and the columns represent Fe^{2+} concentration (5, 10, 15, 30 ppm) (source, HySA Infrastructure, NWU).

In contrast to the clear cumulative trends observed in the chemical analyses (IEC and FRR), the profilometric analysis reveals that surface morphology does not exhibit a linear correlation with degradation duration. Instead, the Fe^{2+} concentration emerges as the governing variable determining the severity of surface defects.

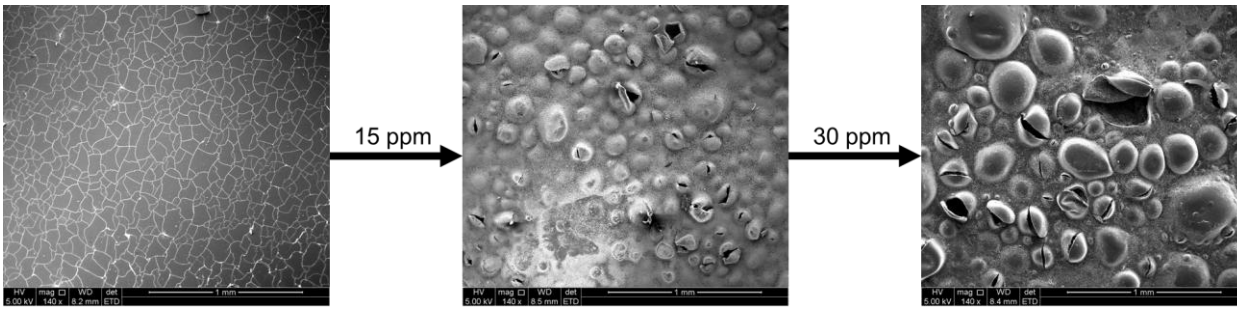
Figure 36 presents the surface topography of samples degraded for 24 h at 5, 15, and 30 ppm Fe^{2+} concentrations.



a) b) c)

Figure 36: Profilometric imaging of Fenton degraded membranes at a) 5 ppm, b) 15 ppm and c) 30 ppm for 24 hours (source, HySA Infrastructure, NWU).

Comparing these concentration intervals reveals that the characteristic surface damage, manifested as blistering, pitting, and texture roughening, develops rapidly. The widespread pitting and nascent blister formation observed at 5 ppm in the 24-hour samples (Figure 36 a) are notably less severe than the deep textural trenching observed at 30 ppm(Figure 36 c). This is further supported by the examination of Figure 37, which provides SEM imaging for a virgin sample and degraded samples at 15 and 30 ppm Fe^{2+} for 72h.



a) b) c)

Figure 37: SEM imaging of a) Virgin, non-degraded, b) 15 and c) 30 ppm Fe^{2+} degraded membranes for 72h (source, CRB, NWU).

The SEM images reveal a distinct loss of surface integrity commensurate with the increase in Fe^{2+} concentration. While the virgin membrane (Figure 37 a) exhibits a characteristically crack-like, dense topography, the degraded samples exhibit significant morphological restructuring. Specifically, the 15 ppm and 30 ppm samples (Figure 37 b and c) exhibit a network of micro-fissure patterns. These features suggest that the chemical attack has compromised the polymer's elasticity, rendering the surface brittle and susceptible to fracture upon dehydration.

These observed micro-fissures are critical because they serve as physical initiation sites for mechanical failure. Figure 38 provides a schematic for interpreting these failure modes, reproduced from Shi et al.,[35] which correlates these surface irregularities with fatigue propagation.

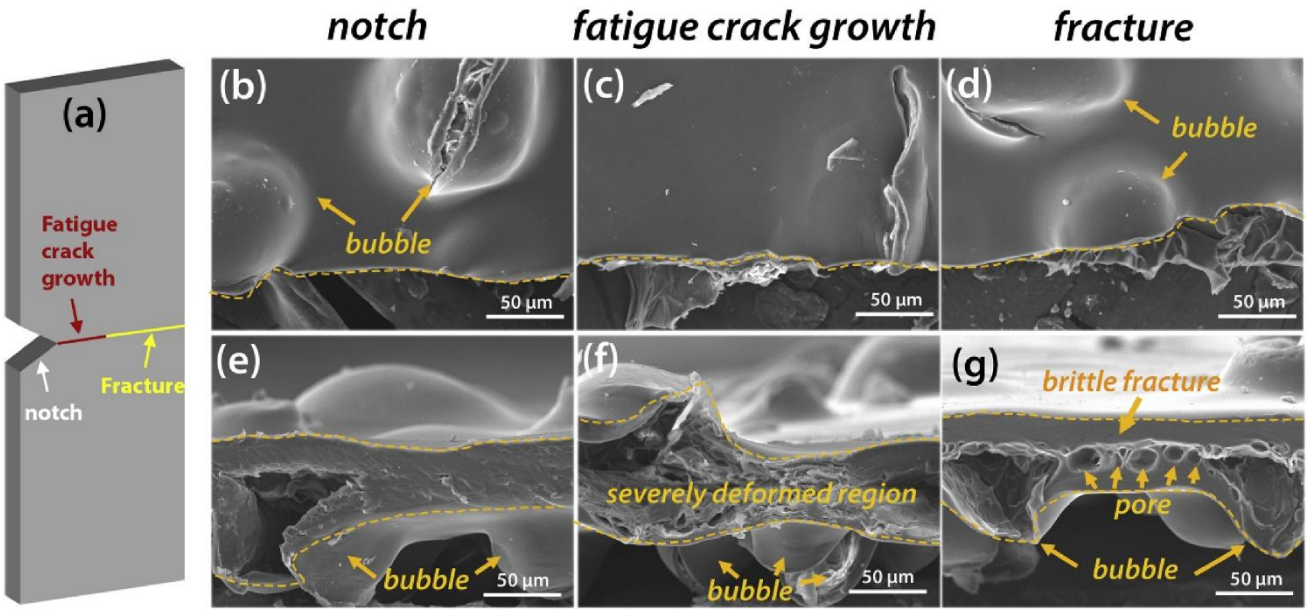


Figure 38: (a) Schematic illustration of notch area, fatigue crack growth area and fracture area. (b)–(d) are surface morphologies of notch area, fatigue crack growth area and fracture area of 48 h chemically-degraded Nafion® 212 membrane, respectively; (e)–(g) are corresponding cross-section morphologies. The contours of each part are indicated with dashed lines. (Reproduced from [35] with permission from Copyright 2020 Elsevier, License ID: 6070250077641)

Shi *et al.* identified the coalescence of surface bubbles and notch formation as key mechanisms that accelerate fatigue crack propagation.[35] The profilometry and SEM images in this study confirm the presence of these specific defect types, particularly at high Fe^{2+} concentrations. Although the dynamic growth of these bubbles over time was not discernible by profilometry in this study, their presence is critical. These crater-like defects (as seen in Figure 38 c) act as stress concentrators, serving as precursors to mechanical failure and pinhole formation. In the most severe cases (30 ppm), ruptures resembling the fracture zones described by Shi *et al.* were identified, indicating that the chemical attack had sufficiently weakened the polymer matrix to induce localised mechanical collapse.

This progression from highly localised surface defects to, full-thickness failure is well-documented in the literature.[63] A combination of chemical and electrochemical processes, coupled with operational stressors such as mechanical strain, temperature fluctuations, and changes in membrane water content, actively accelerates polymer degradation. Ultimately, these synergistic stressors result in severe membrane thinning, a critical loss of tensile strength, and the formation of pinholes.[63]

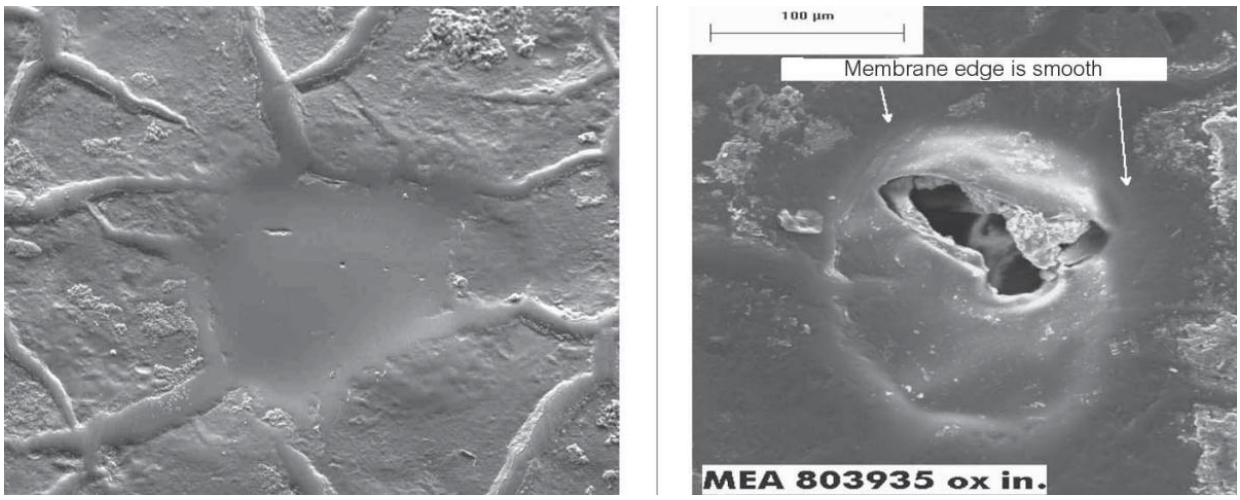


Figure 39: Thinning of an SPE membrane caused by various stressors, resulting in pinhole formation (Reproduced from [63, 64] with permission from Elsevier, licence ID: 6224691261966)

The SEM imaging provided by Bessarabov and Kozak (Figure 39) visually captures this end-stage failure, illustrating an area of severe, localised thinning that has ruptured to form a pinhole.[64] Notably, the ruptured membrane edge is smooth. This smooth morphology is indicative of chemical erosion and plastic yielding rather than purely brittle, mechanical tearing. This literature precedent strongly corroborates the mechanistic findings in this study; the initial craters and blisters act as high-energy stress concentrators that, upon continued chemical attack by radical species and internal osmotic pressure, yield the macroscopic ruptures seen in the severely degraded samples.

The macroscopic ruptures observed in the large-scale Nafion® 115 samples, commonly occurring at 30 ppm Fe^{2+} after 72 h, as shown in Figure 40, represent the ultimate endpoint of this chemo-mechanical failure pathway. However, an essential finding of this study is that the progression from the localized, stress-induced pinholes described by Bessarabov and Kozak to these widespread macroscopic ruptures does not occur homogeneously across the polymer matrix.[64]

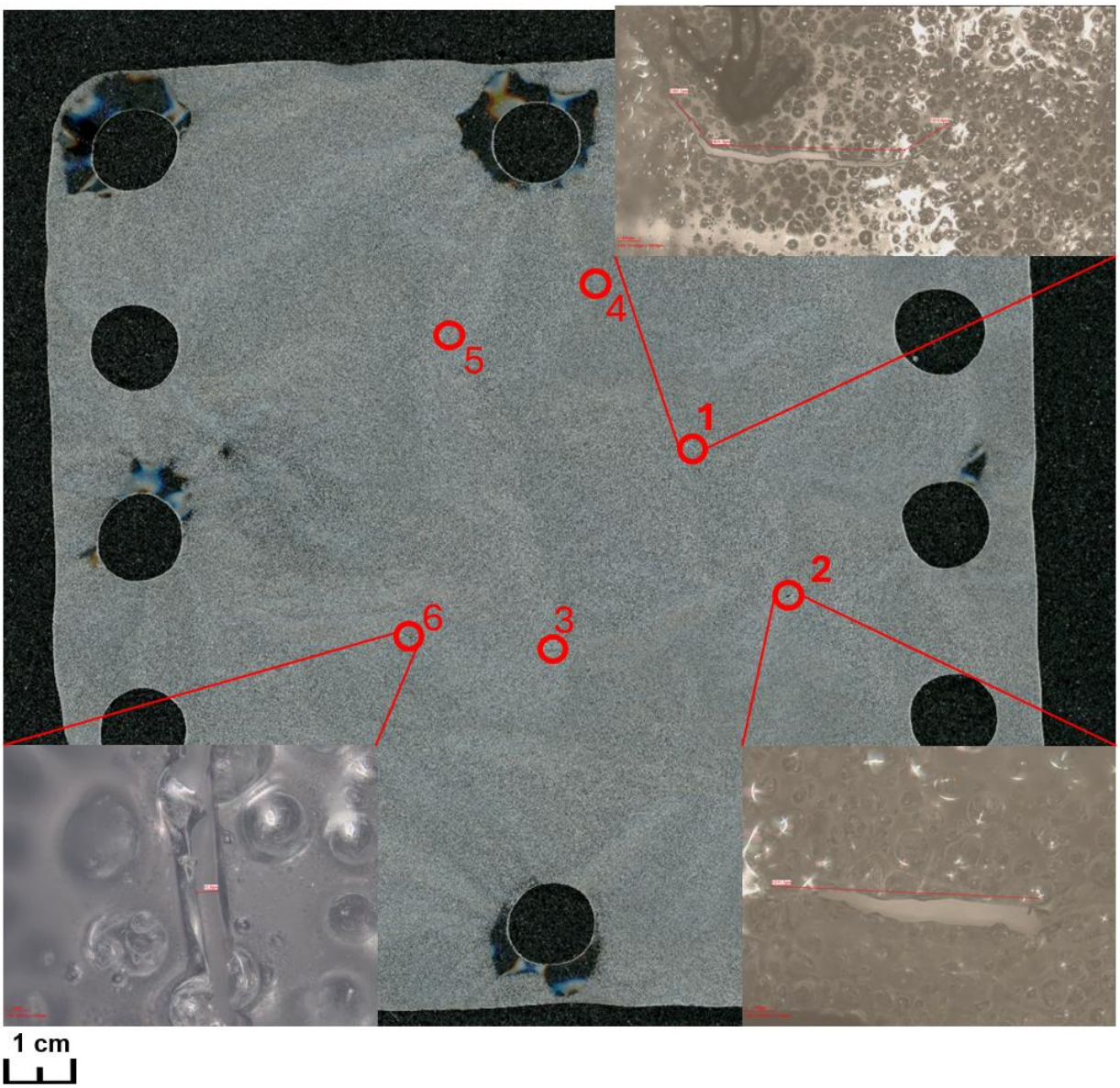


Figure 40: Post-degradation (30 ppm 72h) Nafion® 115 with indicated regions 1-6 in which rupturing can be seen. This figure is a photograph of the large-scale Nafion® 115 membrane after the most severe degradation test. It highlights six specific regions (labelled 1-6) where rupturing and pinholes have occurred. This sample was repeated to enable *in-situ* analysis. The sample used is shown in Annexure B-6.2.5 (Post-mortem imaging) (source, HySA Infrastructure, NWU).

A key morphological observation from the profilometry analysis is that the degradation, particularly the formation of bubbles and blisters, does not proceed homogeneously across the membrane surface. As illustrated in Figure 41 for the large-scale Nafion® 115 samples, the damage manifests as localised clusters rather than as a uniform erosion.

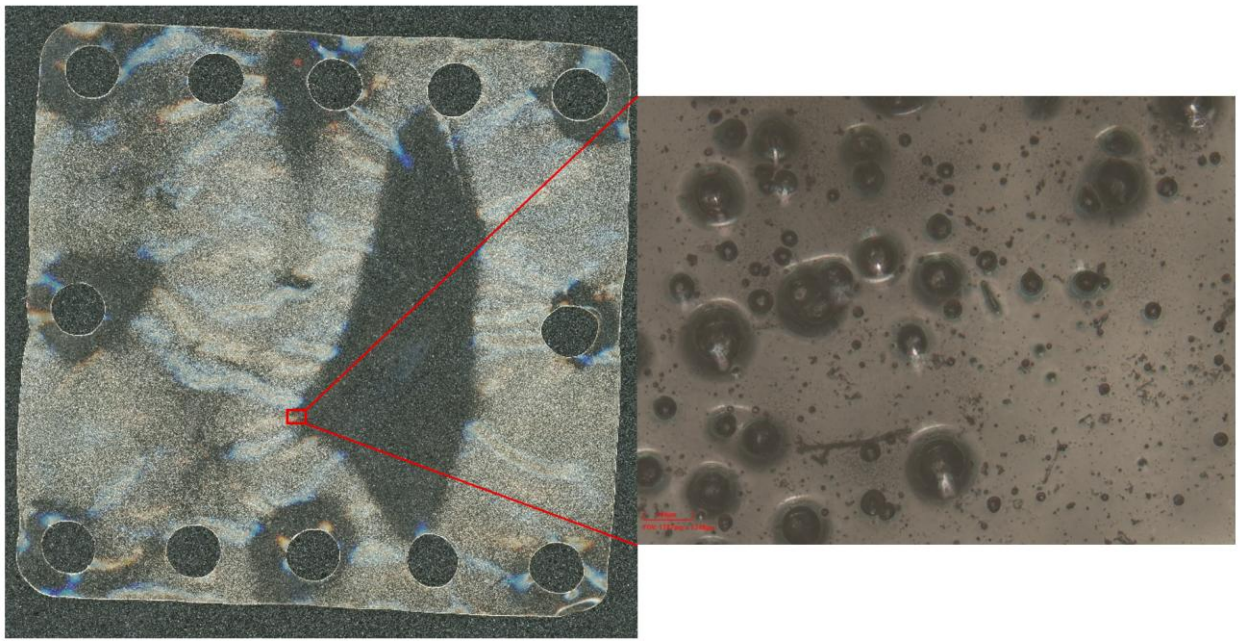


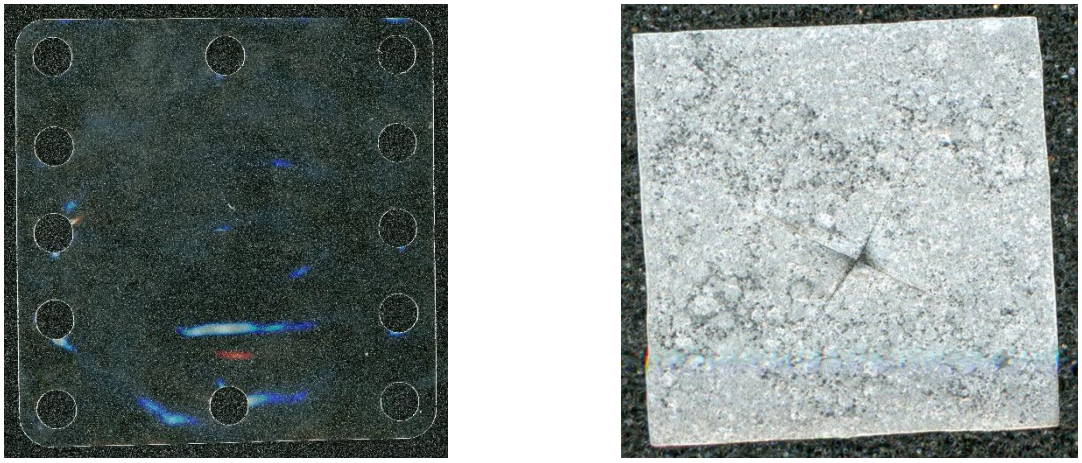
Figure 41: Post-degradation (15 ppm 72h) of 168.2 cm2 Nafion® 115 with visible bubble formation and the corresponding magnified region of 1787µm x 1340 µm showing bubble development from left to right (source, HySA Infrastructure, NWU).

This localisation is governed by the requirement for initiation sites, which act as focal points for an accelerated, localised chemo-mechanical degradation cascade.[65] This phenomenon supports the synergistic relationship between chemical attack by •OH radicals and the polymer's pre-existing mechanical state, as introduced in Section 2.4.5. Any microscopic or macroscopic flaw, such as a surface scratch, a microcrack, a manufacturing-induced void, or a point of high residual stress, constitutes an initiation site. At these high-energy sites, the polymer chains are under tensile strain, significantly increasing their susceptibility to chemical scission by the highly reactive radical species generated during the Fenton test.

Compelling experimental evidence for this defect-driven propagation is found in the contrast between the small-scale (4 cm^2) and large-scale (336.44 cm^2) degradation experiments.

As previously mentioned, the combined chemical and mechanical stressors actively drive tensile strength loss and membrane thinning; catastrophic structural collapse is highly dependent on pre-existing topographical focal points. The polymer requires localised high-energy initiation sites to catalyse the unzipping and yielding. This requirement explains the substantial deviation observed between the large (168.2 cm^2) and small-scale (4 cm^2) samples pertaining to visible bubble, notch, and rupture formation. During small-scale experimentation, visible signs of degradation are observed under the mildest conditions (24 h at 5 ppm Fe^{2+}), whereas in the large-scale counterpart, notch formation is delayed, only observed at 15 ppm Fe^{2+} after 48 hours.

The small-scale Nafion® 117 membranes were prepared using a scalpel (Section 3.3.1), a manual process that inherently introduces significant edge stress, micro-tears, and roughness. As shown in Figure 42 b), these samples exhibited severe, widespread bubble formation even under mild degradation conditions (5 ppm Fe^{2+}, 48 h). Conversely, the large-scale membranes were prepared using a precision laser cutter (Section 3.2.3), a technique that minimises mechanical stress and produces a clean, thermally sealed edge. These samples (Figure 42 a) demonstrated significantly higher resistance to morphological damage under the same experimental conditions



a) b)

Figure 42: Post-degradation (5 ppm 48h) a) of 168.2 cm^2 Nafion® 115 with no visible notch or rupture formation, and the corresponding counterpart b) of 4 cm^2 Nafion® 117 with severe bubble formation present (source, HySA Infrastructure, NWU).

The profilometry and visual analysis demonstrate that PFSA membrane degradation is a synergistic chemo-mechanical process that proceeds non-homogeneously, originating from localised mechanical initiation sites. While the chemical data (IEC/FRR) indicate cumulative degradation over time, the morphological evidence suggests that the location and severity of physical damage are influenced by surface flaws.

The stark difference in degradation resistance between the scalpel-cut and laser-cut membranes confirms that pre-existing mechanical flaws act as focal points for accelerating radical attack. This finding highlights that long-term durability depends on both chemical robustness and manufacturing integrity, suggesting that mitigating mechanical stress during assembly is as crucial as chemical stability for preventing localised component failure.

4.2.5 Summary

The multimodal characterisation employed in this section provides insight into the degradation pathways induced by the Fenton-based AST. Collectively, the data confirm that

radical attack is not limited to localised functional loss but also drives catastrophic, multi-scale failure of the ionomer.

Firstly, the chemical quantification presented in Sections 4.2.1 and 4.2.2 established that degradation is dose and duration-dependent. The loss of IEC confirmed the scission of sulfonic acid groups, directly compromising the membrane's proton-conducting ability. The effluent analysis revealed an F:S ratio exceeding 18:1, well above the theoretical value for exclusive side-chain attack. This provides quantitative evidence that the degradation mechanism involves concurrent side-chain scission and main-chain unzipping of the PTFE backbone.

This dual-degradation mechanism was corroborated spectroscopically in Section 4.2.3. While ATR FT-IR proved insensitive to bulk material loss, Raman and ^{13}C CP-MAS NMR spectroscopy identified a simultaneous depletion of side-chain ether/sulfone linkages and CF_{bb} bonds. This structural unravelling manifests macroscopically as the irreversible dimensional swelling and creep observed in Section 4.2.4.

Finally, the profilometric and SEM analysis highlighted the chemo-mechanical nature of this failure. The degradation does not proceed homogeneously; rather, it exploits pre-existing mechanical defects, such as manufacturing stresses (cutting method), which serve as initiation sites for accelerated radical attack. This results in blister formation and rupture, compromising the membrane's structural integrity. Consequently, the chemically degraded membranes characterised here exhibit both a loss of electrochemical functionality (lower IEC) and severe physical degradation, setting the stage for the loss of *in-situ* electrical performance discussed in the following section.

4.3 *In-Situ* Electrochemical Performance

To bridge the gap between *ex-situ* characterisation and real-world application, CCMs were fabricated using degraded Nafion® 115 membranes and their performance were evaluated in a PEMWE single cell. For ease of data representation and discussion, the nomenclature system defined in Table 10 will be followed in Section 4.3.

Table 10: Nomenclature for membranes exposed to different experimental conditions

Fe^{2+} concentration (ppm)	Exposure duration (h)	Nomenclature
0	0	0-0
5	24	5-24
	48	5-48
	72	5-72
15	24	15-24
	48	15-48
	72	15-72
30	24	30-24
	48	30-48
	72	30-72

4.3.1 Baseline Characterisation

4.3.1.1 Polarisation Behaviour of Non-Degraded CCMs

The polarisation curve, which plots cell voltage against current density, is a popular indicator of PEMWE's overall electrochemical performance.[66-69] In the context of this study, measuring the polarisation behaviour is essential for several reasons: i) While *ex-situ* characterisation (such as IEC and Raman spectroscopy) identifies chemical and structural changes, the polarisation curve provides a functional validation of how those changes translate into real-world performance decay in an operating electrolyser. ii) A primary focus of this dissertation is the impact of Fenton-induced degradation on the membrane's ionic conductivity. The slope of the linear region of the polarisation curve provides a macroscopic measure of the cell's total resistance and enables the determination of the ohmic resistance.[70] iii) Measuring the polarisation behaviour is a prerequisite for achieving Objective 4 of this study: establishing a quantitative correlation between *ex-situ* chemical markers (e.g., % IEC loss or FRR) and the resulting increase in cell voltage at specific current densities.

Figure 43 presents the polarisation curves for two CCMs assembled with virgin membranes, 3 polarisation curves were obtained for each cell, resulting in an average baseline of 6

measurements. The averaged data is presented in Annexure 6.2.2**.** The results obtained are consistent with literature results of 1.05, 1.35, and 1.70 A.cm^{-2} at 1.85V for 40, 60, and 75 ˚C, respectively, and will be used as the baseline for comparing results from degraded membrane samples.[71-73]

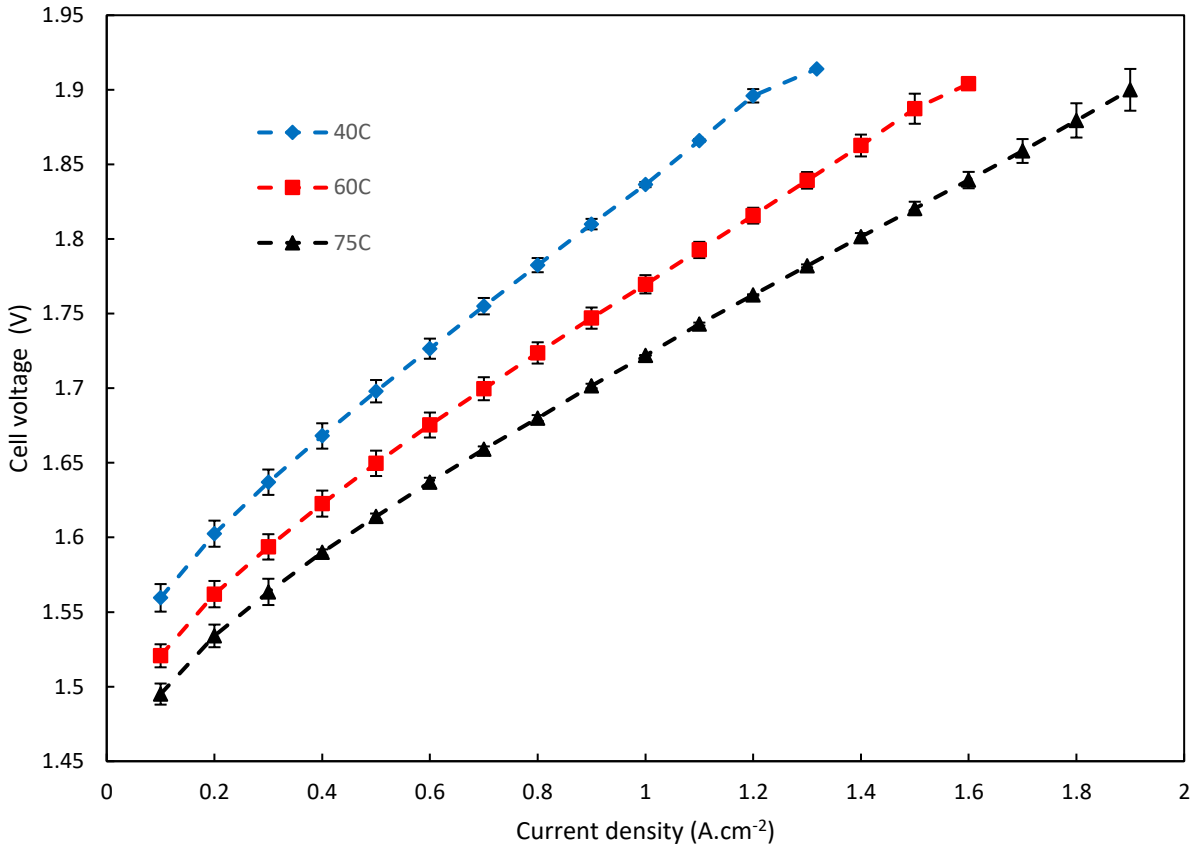
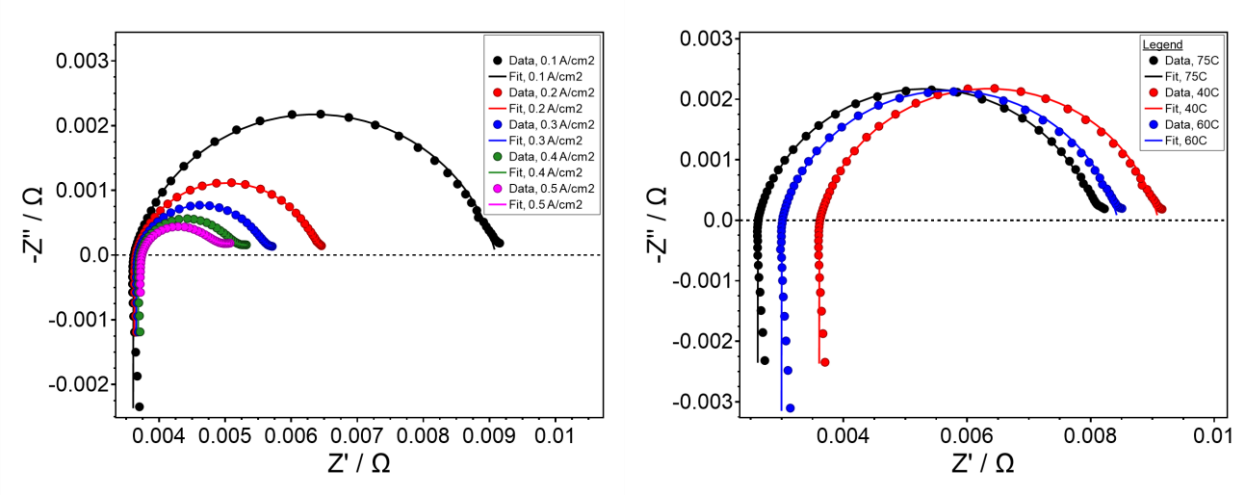


Figure 43: Polarisation curve for reference cells at 40, 60 and 75 °C. Curves and standard deviations are presented as averages based on six repeats.**4.3.1.2 Electrochemical Impedance Spectroscopy (EIS) Analysis of Non-Degraded CCMs**

The EIS analysis of the fresh, non-degraded CCMs establishes a baseline for quantifying subsequent degradation phenomena. The data presented in Figure 44 and Table 11 reveal two primary trends: a temperature-dependent reduction in ohmic resistance (R_Ω) and a current-density-dependent (j) reduction in charge-transfer resistance (R_{ct}). Additionally, a notable feature in the collected spectra at current densities of 0.5 A cm^{-2}, is the emergence of a low-frequency inductive loop or second semi-circle. This feature indicates the onset of mass-transport limitations, possibly induced by bubble formation at the anode.



a) b)

Figure 44: Nyquist plot for reference cell a) variable current density at 40 °C and b) variable temperature at 0.1 A.cm^{-2}

Table 11: Processed EIS data from non-degraded CCM at 0.1 and 0.5 A.cm^{-2} at 40, 60 and 75 °C

		40 (°C)	**60 (°C)**	**75 (°C)**
0.1 A.cm^{-2}	**Capacitance1, (F)**	2.79	2.85	2.81
	τ_1 (s)	0.015	0.015	0.015
	f_1 (Hz)	10.43	10.27	10.24
	R_Ω (mΩ.cm^2)	201.47	167.03	145.24
	R_{ct} (mΩ.cm^2)	306.32	304.87	309.53
0.5 A.cm^{-2}	**Capacitance 1 (F)**	2.95	2.83	2.69
	Capacitance 2 (F)	1040.63	1361.8	1587.41
	τ_1 (s)	0.003	0.003	0.003
	τ_2 (s)	0.97	0.78	0.76
	f_1 (Hz)	51.51	51.75	53.09
	f_2 (Hz)	0.16	0.20	0.21
	R_Ω (mΩ.cm^2)	207.28	149.69	129.35
	R_{ct} (mΩ.cm^2)	58.61	53.25	54.69
	R_{mt} (mΩ.cm^2)	52.45	28.29	23.52

Ohmic Resistance (R_Ω) and Proton Conductivity

The ohmic resistance (R_Ω), which represents the summation of the membrane ionic resistance, electronic contact resistances, and interfacial resistances, exhibited a significant inverse relationship with temperature. Specifically, at a current density (j) of 0.1 A.cm^{-2}, R_Ω decreased from 201.47 mΩ.cm^2 at 40 °C to 145.24 mΩ.cm^2 at 80 °C. These results align well with reported literature values, which typically range from 150 to 170 mΩ.cm^2. [74, 75]

This behaviour is consistent with the Arrhenius-type temperature dependence of proton conductivity in PFSA membranes.[76] As temperature increases, the activation energy required for

the Grotthuss mechanism (proton hopping) is more easily overcome, thereby enhancing ionic conductivity.

When analysing the dataset at a higher current density (j= 0.5 A.cm^{-2}, see Table 11) R_Ω decreased from 207.28 mΩ.cm^2 at 40 °C to 129.35 mΩ.cm^2 at 80 °C. Comparing the results at 0.1 and 0.5 A.cm^{-2} reveals distinct, temperature-dependent phenomenological differences:

At 40 °C, a 2.9% increase in R_Ω was observed when increasing current density. This increase is consistent with the "bubble masking" effect, where increased gas evolution at higher currents reduces the effective active area of the MEA.[77]

At 80 °C, an 11% decrease in R_Ω was observed between 0.1 and 0.5 A.cm^{-2}. This contradicts the bubble masking effect; the most plausible explanation is the dominance of Joule self-heating at higher currents. The increased local heat generation further reduces the ohmic resistance, thereby outweighing the effect of bubble formation.[78]

Despite these deviations, the obtained data remain within the range of previous studies. For instance, Liu *et al*., reported an average R_Ω of 126 mΩ.cm^2.[79] While the current experimental setup yielded slightly higher values than the highly optimised laboratory standard of 108 mΩ.cm^2, the results confirm that the cell is performing within acceptable standard parameters.[79]

Mass Transfer Resistance (R_{ct}) and Kinetics

The polarisation resistance, dominated by the R_{ct} of the OER, showed a strong inverse relationship with current density. At 40 °C, R_{ct} decreased from 306.32 mΩ.cm^2 at low current density to 112.33 mΩ.cm^2 as current density increased.

This trend follows the Butler-Volmer kinetic model. At higher current densities, the system operates at higher overpotentials, effectively lowering the activation barrier for the electrochemical reaction. This results in faster reaction kinetics and, consequently, a lower apparent charge-transfer resistance.

Summary

The baseline EIS analysis confirms that the non-degraded CCMs exhibit the standard ohmic and kinetic behaviours expected of commercial PFSA membranes. Both R_Ω and R_{ct} values fall within the established ranges for functional PEMWE cells reported in the literature, validating the experimental setup for the subsequent degradation study. Furthermore, the appearance of mass-transport features at 0.5 A cm^{-2} indicates that subsequent degradation analysis must

carefully distinguish between kinetic losses (attributable to catalyst degradation) and mass transport losses (attributable to PTL/interface passivation).

4.3.1.3 Hydrogen Crossover

Hydrogen crossover from the cathode to the anode is a critical parameter that compromises PEMWE performance across three dimensions: efficiency (reduction of Faradaic yield due to parasitic recombination), safety (risk of forming explosive H_2/O_2 mixtures), and membrane durability (formation of radical species via H_2O_2 generation).[80, 81]. Figure 45 presents the anodic hydrogen content measured for two non-degraded CCM, reference PEMWE cells as a function of temperature, a) and current density, b).

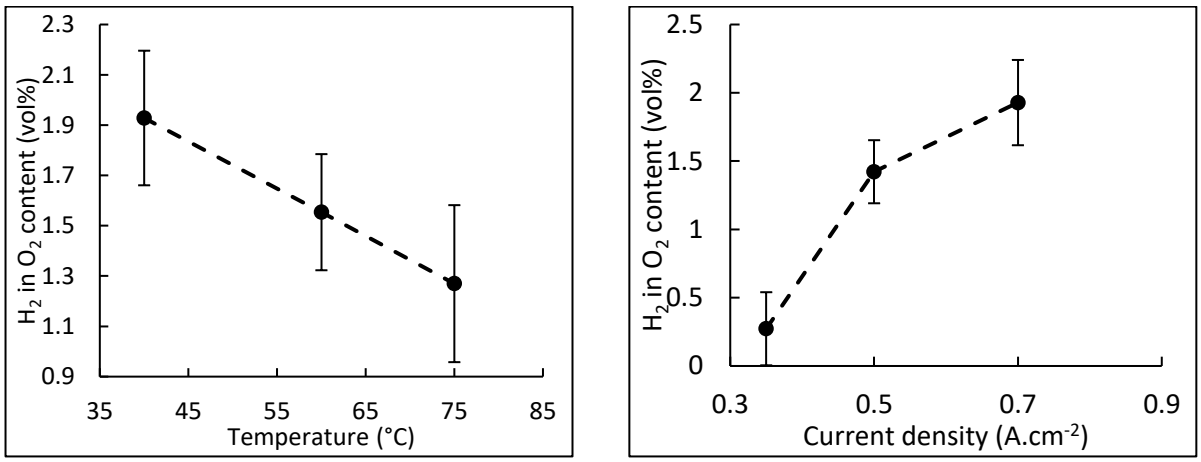


Figure 45: Hydrogen gas crossover of 2 reference cells from cathode to anode (H_2 in O_2) at a) variable temperature and b) variable current density Based on 6 repeats with standard deviations shown.

Figure 45 a) indicates that the anodic hydrogen content decreases linearly as the temperature rises. This trend initially appears counterintuitive to standard Fickian diffusion mechanics.[82] The permeability coefficient is defined as the product of solubility and diffusivity. While gas solubility typically decreases with temperature (following Henry's Law), diffusivity increases exponentially according to the Arrhenius relationship. In hydrated PFSA membranes, such as Nafion®, the increase in diffusivity typically dominates, resulting in a net increase in molar crossover flux at higher temperatures.[83]

Therefore, the observed decrease in anodic H_2 content is likely an artefact of two concurrent phenomena masking the true crossover flux; i) The partial pressure of water in the anode stream increases with temperature, as governed by the Antoine equation. This increased water vapour volume dilutes the gas stream, reducing the measured volumetric fraction of H_2 despite the higher molar flux. ii) The kinetics of the hydrogen oxidation reaction ($H_2 + \frac{1}{2}O_2 \rightarrow H_2O$) at the anode

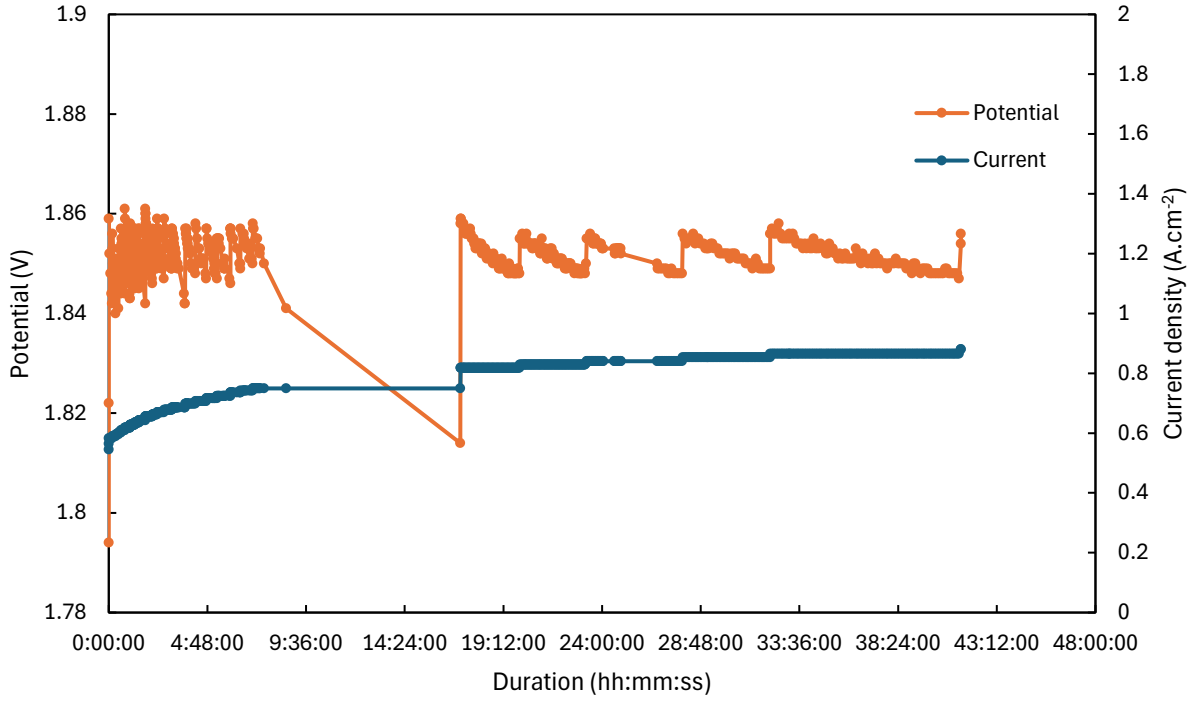
catalyst layer are thermally activated. As the temperature increases, a larger fraction of the crossing hydrogen is oxidised before the GC-MS can detect it. Recent literature confirms that neglecting this parasitic anodic current can lead to a significant underestimation of the true H_2 crossover flux.[84 85]

Figure 45 b) demonstrates that the anodic H_2 content increases with rising current density. According to standard dilution theory, increasing the current density should theoretically decrease the anodic hydrogen concentration, as the rate of oxygen evolution (the diluent) increases linearly with current. The increase in H_2 vol% indicates that the hydrogen crossover flux increases superlinearly. This behaviour is the signature of dissolved hydrogen supersaturation.[85, 86] At high current densities, hydrogen is generated at the cathode catalyst layer faster than it can be removed via the GDL and flow channels. This mass transport limitation creates a local concentration of dissolved hydrogen that significantly exceeds the Henry's Law saturation limit, thereby increasing the concentration gradient driving the crossover flux.

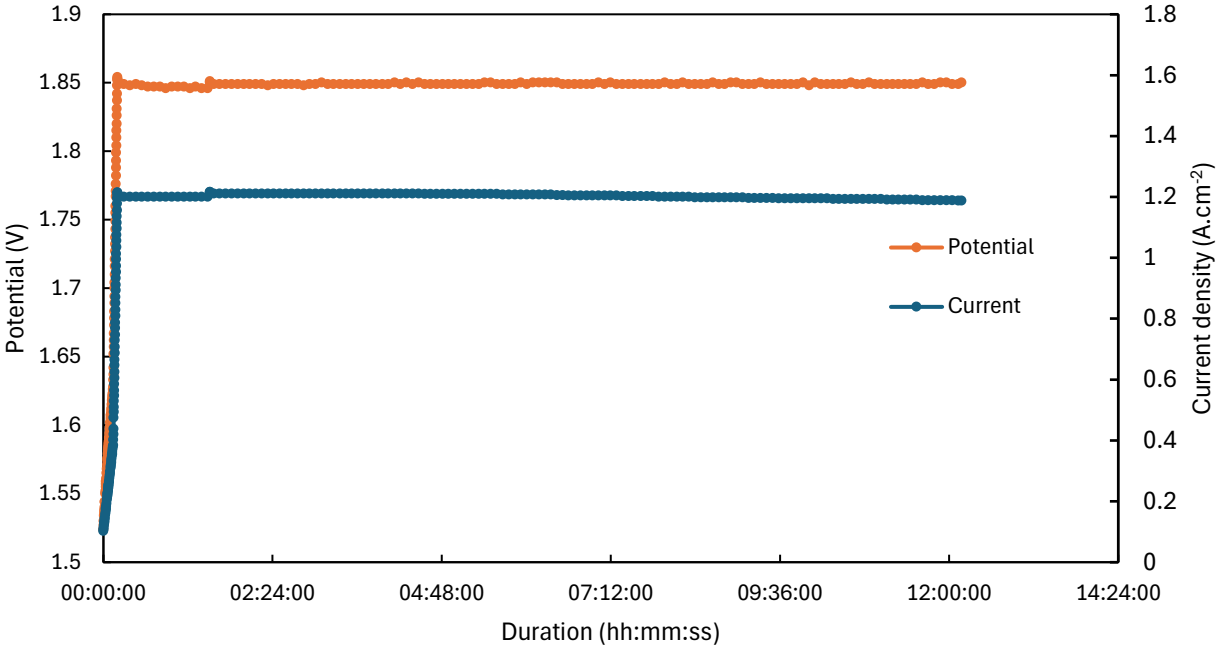
4.3.2 Degraded CCM Characterisation

4.3.2.1 CCM Break-In Procedure

At the onset of this work, the CCM break-in was performed manually, as described in Section 3.6 (target potential ~1.85 V). Figure 46 a) illustrates the progression of this manual extended break-in procedure for cell 30-48, and Figure 46 b) represents the normally observed break-in curve (represented by cell 15-48) once the automation script (Annexure 6.2.1) has been implemented. These break-in curves (Figures 46 and 47) have been included as a means to validate the break-in procedure



a)



b)

Figure 46: Potential and applied current as a function of time for cell a) 30-48, with automation script absent, and b) 15-48, with automation script present

The procedure was successful, resulting in a continual increase in current density at a constant voltage, indicative of improved cell efficiency (conditioning). The cell in Figure 46 a) exhibited significant initial conditioning, characterised by a potential decrease of 56.67 $mV.min^{-1}$. As the process extended (32–40 h), the system approached stability, with the rate of potential

change decreasing to 16.98 μV.min^{-1}. It should be noted that the data discontinuities observed between 08:37:00 and 17:06:00 are artefacts of the manual adjustment method and represent overnight periods when human intervention was not possible.

With the creation of the automation script presented in Annexure 6.2.1, the limitations of manual intervention were eliminated, allowing for continuous, precise data acquisition.

By maintaining a constant potential of 1.85 V, as shown in Figure 46(b), the system exhibited a stabilising trend in current density. The current initially increased at a rate of 0.267mA.min^{-1}. As the break-in procedure neared completion, the rate slowed significantly to 66.67 μA.min^{-1} indicating that the electrochemical environment within the cell was approaching a steady state. This was the common trend observed for all of the degraded CCM generated in this study, except for the severely degraded CCM (30-72). The 30-72 CCM yielded a non-standard break-in curve, as shown in Figure 47.

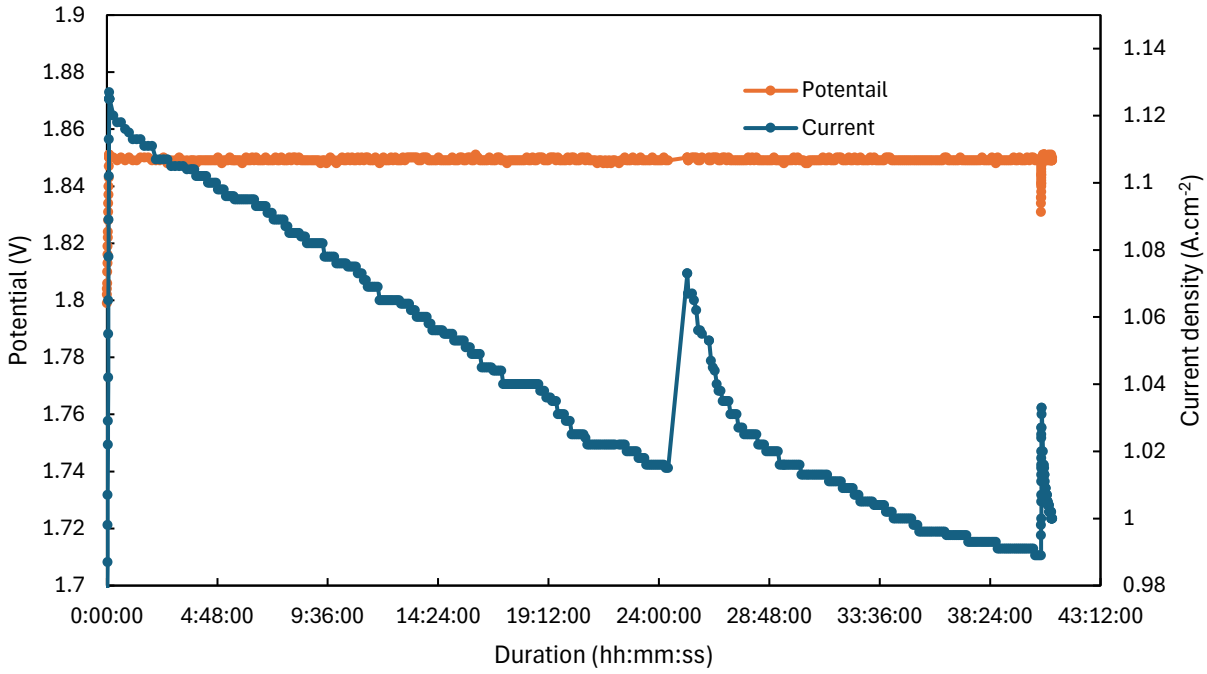


Figure 47: Potential and applied current as a function of time for cell 30-72, with automation script present

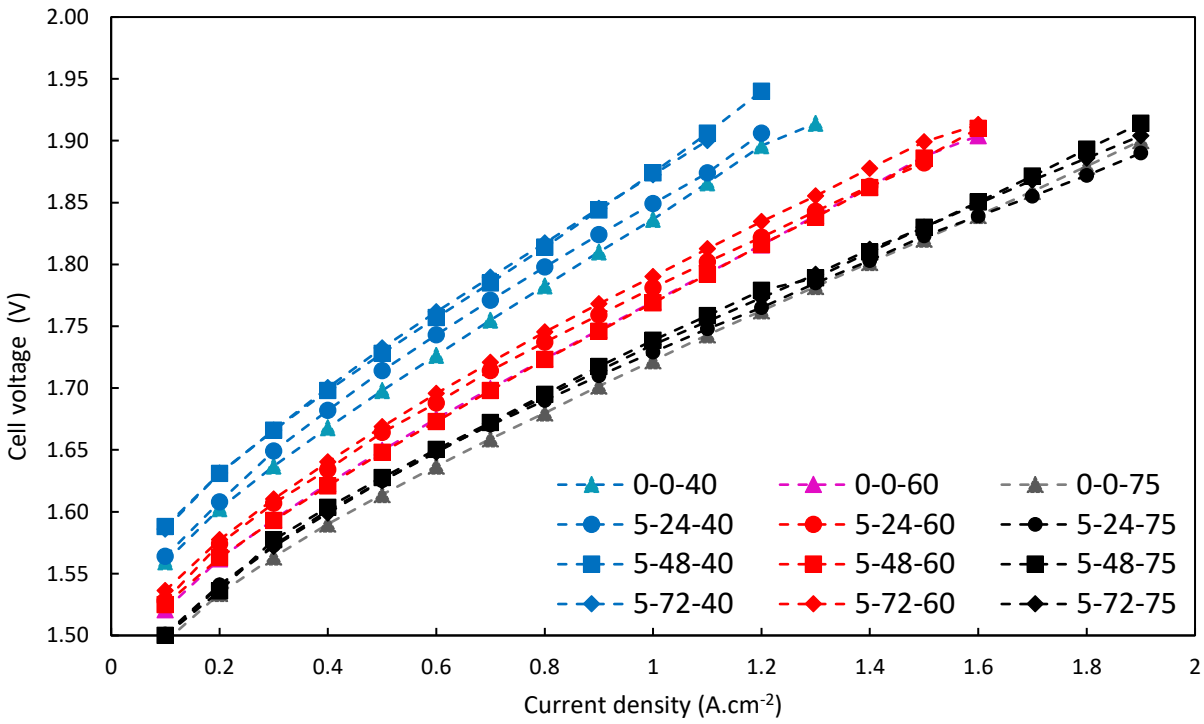
Figure 47 shows that despite utilising the same automation script to maintain 1.85 V, cell 30-72 (most severe degradation condition) exhibited a continuous, significant decline in current density, indicating a decrease in cell efficiency rather than stabilisation. The decay rates reveals an initial decline of -96.67 μA.min^{-1} over the first 5 hours. By the final 5 hours, this rate had slowed to -30.00 nA.min^{-1}, suggesting that the degradation or resistance increase was stabilising. Additionally, the transient spikes observed in regions (hh:mm:ss) 24:23:48 to 25:14:22 and 40:16:34 to 40:21:40 were identified as external anomalies resulting from power-supply failures,

which caused temporary increases in the recorded potential. Nevertheless, after 41h of break-in procedure, it was decided to stop the procedure and use the CCM as is, as described in Section 3.6.

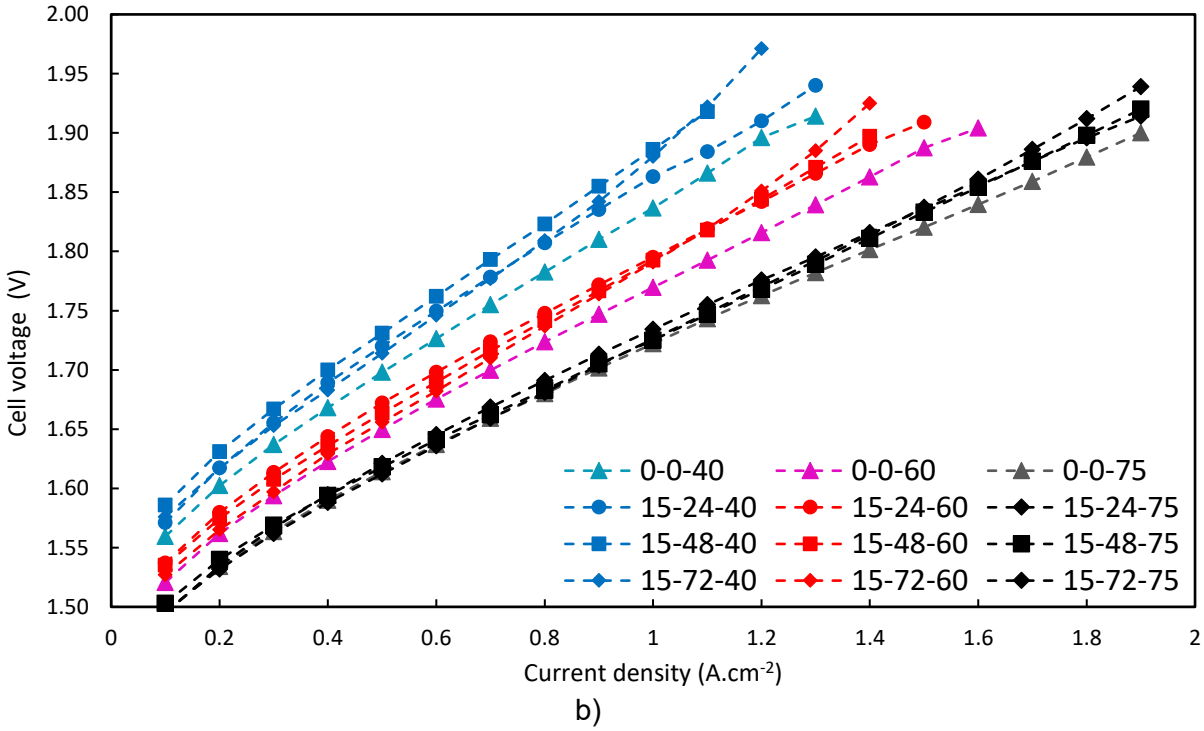
4.3.2.2 Polarisation Behaviour

The polarisation curves serve as the definitive functional validation of the CCM, integrating the thermodynamic, kinetic, and ohmic consequences of the *ex-situ* degradation into a single macroscopic performance metric. While *ex-situ* analyses (IEC, Raman, Profilometry) quantified discrete material damage, the polarisation behaviour reveals how these damages manifest under dynamic operating conditions.

A consistent trend is observed across most membrane samples, both virgin, as characterised in Section 4.3.1.1, and degraded: an increase in cell operating temperature correlates directly with improved electrochemical performance (i.e., reduced cell voltage at a given current density). As illustrated in Figure 48, the polarisation curves shift to lower potentials as the temperature increases from 40 to 75 °C. This behaviour is consistent with standard theoretical predictions and widely reported literature.[87, 88] The reduction in cell potential is driven by enhanced reaction kinetics, improved mass transport, higher membrane proton conductivity, and reduced ohmic losses.[89-92]



a)



b)

Figure 48: Polarisation curve for a) 5-ppm degraded and b)15 ppm degraded CCMs at 40, 60, and 75 °C. Sample labelling as Fenton concentration (ppm)-Degradation duration (h)-Polarisation testing temperature (°C)

The 5 ppm samples, presented in Figure 48 a), exhibit a distinct but mild performance decay. At 40 °C, the voltage penalty (the increase in potential relative to the virgin baseline) increases from 12.67 mV at 24 h to a plateau of approximately 32.80 mV at 72 h.

However, the voltage penalty trajectory shifts as the Fe^{2+} concentration increases. The 15 ppm degraded samples at 40 °C show a voltage penalty of 20.77 mV at 24h and 25.23 mV at 72 h. This suggests that mild radical attack primarily affects the surface or interface kinetics early on, potentially stabilising as the rate of defect creation equilibrates with the limited catalyst supply.

In stark contrast, the 30 ppm-degraded CCMs (Figure 49) exhibit a catastrophic loss of performance. The voltage penalty escalates non-linearly, reaching 13.08 mV at 24 h of degradation and peaking at 82.50 mV at 72 h of degradation (at 40 °C). This increase in potential aligns with the *ex-situ* findings of IEC loss (Section 4.2.1) and structural rupturing (Section 4.2.4). The loss of sulfonic acid groups (IEC) drastically reduces proton conductivity, thereby increasing the ohmic resistance. Simultaneously, the cratered surface morphology likely disrupts the catalyst layer-membrane interface, increasing contact resistance and disrupting the TPB.

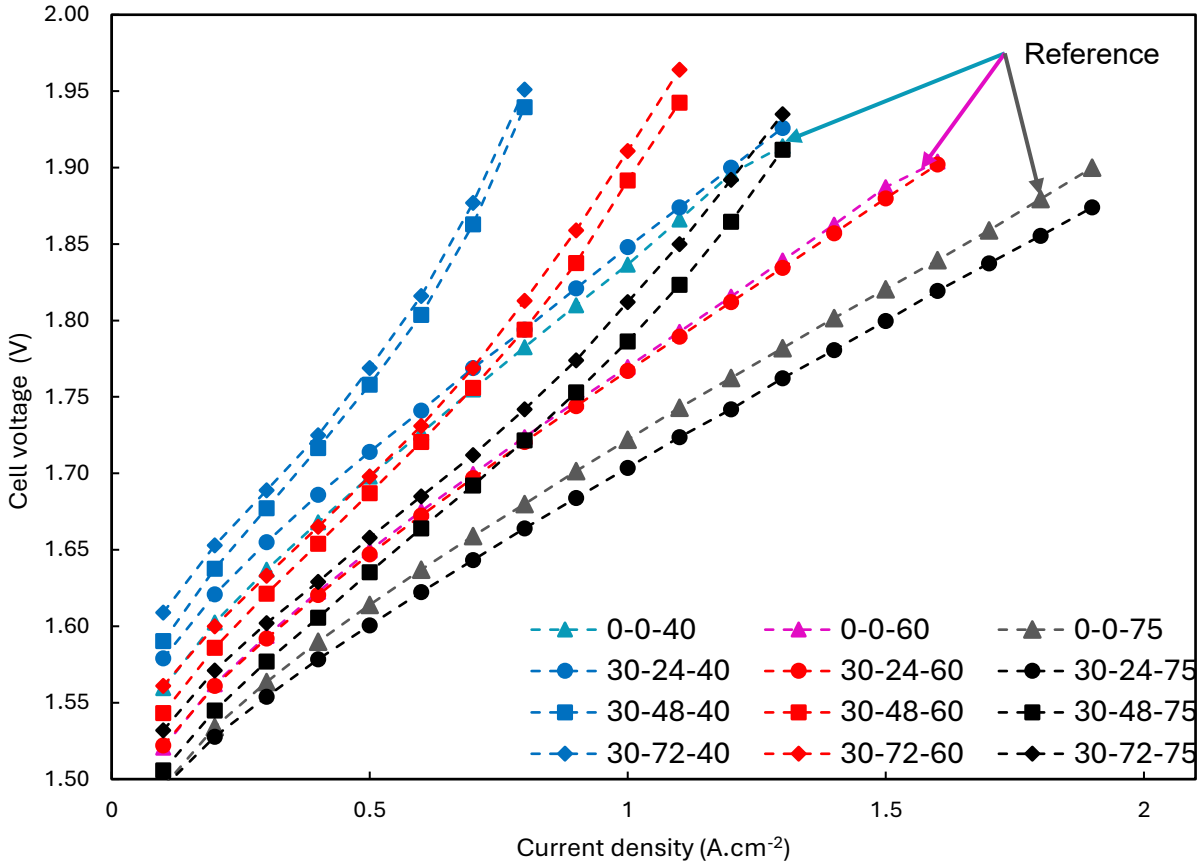


Figure 49: Polarisation curve for 30-ppm degraded CCMs at 40, 60, and 75 °C Sample labelling as Fenton concentration (ppm)-Degradation duration (h)-Polarisation testing temperature (°C)

Notably, the 30-24 sample, at all tested temperatures (40, 60, and 75°C), exhibited an anomalous improvement relative to the reference cell, showing a marginally lower cell voltage across the polarisation curve. This apparent performance enhancement is difficult to explain, but possibly could be attributed to thinning of membranes due to degradation. The thinning of membrane sections due to near-pinhole formation would effectively reduce the ionic transport path length locally, lowering the measured HFR and artificially decreasing the cell voltage. However, such a defect represents a critical mechanical failure and compromises membrane integrity. The improved apparent performance must therefore be interpreted as an artefact of structural damage rather than genuine material optimisation and will therefore be seen as an outlier.

Table 20, presented in Annexure 6.2.3, shows the deviation of each degraded CCM tested against the reference cell baseline over the entire polarisation curve. An observation from Table 20 is the decreasing magnitude of the voltage penalty at higher temperatures. For instance, the severe 30 ppm (72 h) sample shows an 82.50 mV penalty at 40 °C, which decreases to 70.04 mV at 75 °C.

It was found that there is a decrease in voltage penalty at increased testing temperatures. For instance, the severe 30 ppm (72 h) sample shows an 82.50 mV penalty at 40 °C, which decreases to 70.04 mV at 75 °C. This indicates that high-temperature operation can partially hide the effects of membrane degradation. As thermal energy drives faster kinetics and proton transport, the relative contribution of the degradation-induced resistance to the total cell voltage diminishes. However, this is a dangerous operational regime: although the voltage may appear acceptable, the underlying material is structurally compromised, and the higher temperature may accelerate the propagation of the ruptures identified in Section 4.2.4 via profilometry analysis.

Interestingly, the 15-ppm dataset reveals a counterintuitive, non-monotonic trend: the voltage penalty peaks at 48 h (37.32 mV) and subsequently decreases at 72 h (25.23 mV). This recovery is likely a signature of the competing chemo-mechanical trade-off; loss of IEC increases resistivity, and the concurrent radical-induced chain scission causes physical thinning of the membrane. At the 72 h mark, the membrane may have thinned sufficiently to reduce the path length for proton transport, thereby lowering the total HFR despite the lower intrinsic conductivity. This thinning effect temporarily lowers the cell voltage but represents a state of near-failure.

For comparative analysis, Table 21 is also presented in Annexure 6.2.3. While Table 20 represents the average deviation across the entire polarisation curve, Table 21 expresses the potential difference of each cell at a singular operational point of 1.85 V.

The polarisation data confirm that the chemical and structural damage quantified *ex-situ* translates directly into varying degrees of electrochemical efficiency loss. The degradation manifests primarily as an increase in cell voltage, driven by the loss of functional groups (IEC) and interfacial integrity. The data suggests that relying solely on voltage monitoring at high temperatures may obscure the onset of severe degradation, as thermal acceleration can mask the resistive penalties of a damaged membrane.

4.3.2.3 Electrochemical Impedance Spectroscopy (EIS) Analysis of Degraded Catalyst Coated Membranes (CCMs)

EIS was employed to deconvolute the electrochemical losses in the PEMWE single cell, specifically targeting changes in ohmic, charge-transfer, and mass-transport resistances following Fenton degradation. The complete ECM processed data is presented in Annexure 6.2.4.

Ohmic Resistance (R_Ω)

The ohmic resistance(R_Ω) showed significant dependence on both temperature and degradation severity. At a current density of 0.5 $A.cm^{-2}$, a clear inverse relationship between temperature and R_Ω was observed across all samples (Table 12), attributed to the enhanced proton conductivity at elevated temperatures. For instance, the baseline degradation sample (5-24) exhibited an R_Ω decrease from 193.37 ±0.09 $m\Omega.cm^2$ at 40 °C to 150.41 ±0.65 $m\Omega.cm^2$ at 75 °C.

Table 12: EIS results with absolute error for Nafion® 115 CCMs tested in PEMWE single cell at j=0.5 A.cm^{-2}

Temp (°C)	R_x (mΩ.cm^2)	5-24	5-48	5-72	15-24	15-48	15-72	30-24	30-48	30-72
40	R_Ω	193.37 ±0.09	199.54 ±0.17	200.97 ±0.09	205.41 ±0.17	210.87 ±0.34	211.32 ±0.25	212.85 ±0.19	239.95 ±0.30	239.43 ±0.42
	R_{ct}	56.63 ±0.46	57.27 ±1.03	80.60 ±0.46	75.74 ±1.03	55.82 ±2.27	52.71 ±1.54	59.80 ±1.96	62.05 ±2.28	45.97 ±1.57
	R_{mt}	125.37 ±1.48	43.63 ±2.91	23.99 ±1.48	33.92 ±2.91	45.44 ±6.06	66.93 ±5.86	27.84 ±3.87	144.95 ±6.58	92.03 ±5.57
60	R_Ω	169.25 ±0.60	164.57 ±0.29	171.61 ±0.12	169.31 ±0.10	170.18 ±0.33	153.24 ±0.03	152.95 ±0.03	171.58 ±0.02	164.80 ±0.07
	R_{ct}	67.52 ±2.17	58.91 ±2.49	83.52 ±0.44	78.13 ±0.63	56.85 ±2.77	48.41 ±0.24	52.11 ±0.31	45.20 ±0.11	44.26 ±0.35
	R_{mt}	38.64 ±7.55	26.90 ±6.60	16.40 ±1.37	21.91 ±1.96	28.91 ±6.37	36.39 ±0.92	19.85 ±0.60	98.84 ±0.44	47.98 ±0.89
75	R_Ω	150.41 ±0.65	146.90 ±0.29	153.54 ±0.14	151.67 ±0.11	149.73 ±0.34	134.55 ±0.04	127.67 ±0.03	149.05 ±0.03	137.45 ±0.08
	R_{ct}	64.44 ±5.01	59.03 ±2.89	84.16 ±0.56	79.18 ±0.78	56.55 ±3.19	48.89 ±0.32	51.43 ±0.45	49.49 ±0.19	44.54 ±0.46
	R_{mt}	31.54 ±7.90	24.46 ±6.47	16.23 ±1.84	19.55 ±2.29	25.86 ±6.03	29.05 ±0.88	19.92 ±0.66	70.46 ±0.66	40.09 ±1.02

The impact of degradation on R_Ω revealed a complex, temperature-dependent behaviour:

i) At 40 °C: Higher degradation intensity generally correlated with increased ohmic resistance. The most severely degraded sample series (30 ppm) exhibited significantly higher resistances (e.g., 30-48: 239.95 mΩ.cm^2 and 30-72: 239.43 mΩ.cm^2) compared to the mildest degradation (5-24: 193.37 mΩ.cm^2). This suggests that at lower temperatures, the loss of functional sulfonic acid groups or structural damage that hinders proton transport outweighs any membrane-thinning effects. [25, 30] ii) At 75 °C: This trend appeared reversed or convoluted. The 30 ppm samples often displayed lower R_Ω values (e.g., 30-24: 127.67 mΩ.cm^2) compared to the 5 ppm series. This could indicate that, at higher operating temperatures, membrane thinning dominates, reducing the proton transport path length despite chemical degradation.[70]

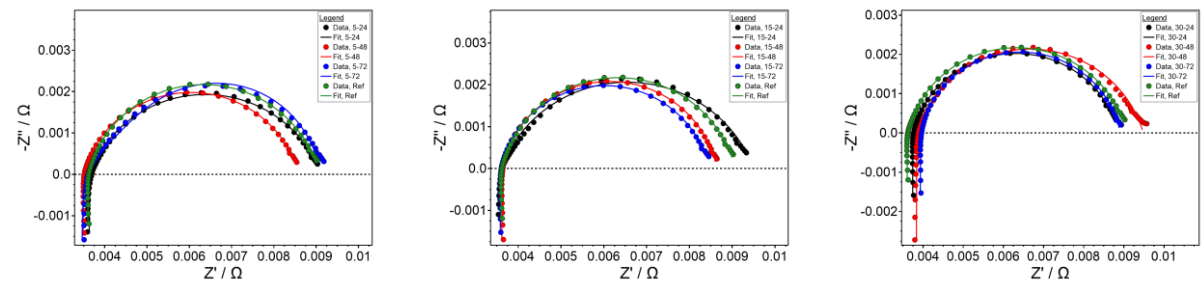
Similar trends were observed at the lower current density of 0.1 A.cm^{-2}, as shown in Table 13, where the 40 °C data consistently showed the highest resistance values (ranging from ~195 to 220 mΩ.cm^2) compared with the 75 °C data (ranging from ~143 to 161 mΩ.cm^2).

Table 13: EIS results with absolute error for Nafion® 115 CCMs tested in PEMWE single cell at j=0.1 A.cm^{-2}

Temp (°C)	R_x (mΩ.cm^2)	5-24	5-48	5-72	15-24	15-48	15-72	30-24	30-48	30-72
40	R_Ω	202.69 ±0.30	195.20 ±0.10	198.94 ±0.55	200.90 ±0.49	202.46 ±0.14	200.31 ±0.14	209.32 ±0.09	215.11 ±0.26	219.89 ±0.15
	R_{ct}	308.19 ±1.01	285.60 ±0.38	326.10 ±2.16	331.38 ±1.97	281.42 ±0.47	273.80 ±0.49	287.44 ±0.36	313.07 ±0.95	279.17 ±0.45
60	R_Ω	169.50 ±0.24	161.22 ±0.10	172.12 ±0.52	169.61 ±0.45	163.55 ±0.17	170.07 ±0.15	171.86 ±0.08	182.65 ±0.19	177.43 ±0.17
	R_{ct}	311.08 ±0.88	277.76 ±0.42	341.28 ±2.18	336.69 ±1.94	280.37 ±0.64	282.09 ±0.57	288.58 ±0.39	314.34 ±0.74	275.87 ±0.55
75	R_Ω	150.79 ±0.19	143.20 ±0.11	155.77 ±0.47	151.23 ±0.41	146.05 ±0.18	148.03 ±0.18	145.93 ±0.10	161.05 ±0.17	151.58 ±0.22
	R_{ct}	330.21 ±0.81	283.54 ±0.54	353.63 ±2.09	345.66 ±1.92	293.17 ±0.75	294.40 ±0.76	300.06 ±0.51	321.90 ±0.71	283.10 ±0.79

Charge Transfer (R_{ct}) and Mass Transport (R_{mt}) Resistances

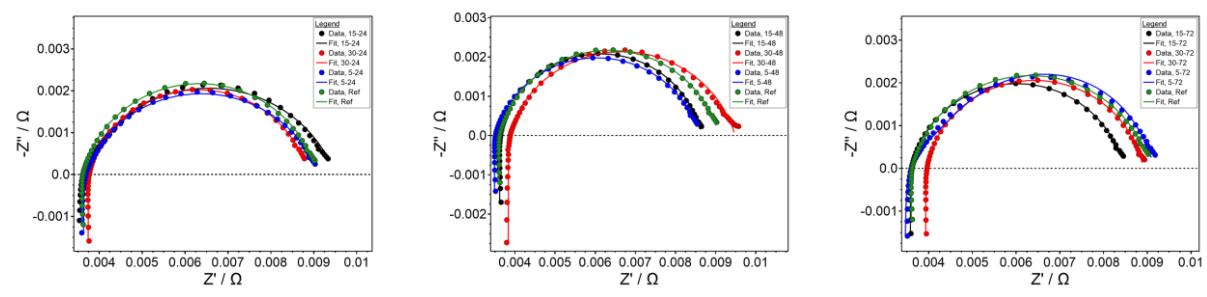
The kinetic performance, characterised by charge transfer resistance (R_{ct}), varied significantly with current density, consistent with Butler-Volmer kinetics. i) *j*=0.1 A.cm^{-2}: The cell operated in the kinetic region, resulting in high R_{ct} values ranging between 273 mΩ.cm^2 and 353 mΩ.cm^2 across all temperatures and degradation states. ii) *j*=0.5 A.cm^{-2}: R_{ct} values decreased to the 45-85 mΩ.cm^2 range. A notable abnormality was observed in the R_{ct} stability. While R_Ω maintained low absolute errors, R_{ct} and R_{mt} exhibited greater variability. For example, the 30-48 sample at 40 °C (0.5 A.cm^{-2}) showed a substantial mass transport resistance (R_{mt}) of 144.95 ±6.58 mΩ.cm^2, which was significantly higher than the previously defined outlier, the 30-24 sample (27.84 ±3.87 mΩ.cm^2) under the same conditions. This suggests that specific degradation conditions (30 ppm, 48h) may have induced structural changes at the catalyst interface. The Nyquist plots visually confirm the quantitative data. Figure 50 (at 40 °C) illustrates the evolution of impedance arcs with degradation time.



a) b) c)

Figure 50: Nyquist plot of reference cell vs a) 5 ppm, b) 15 ppm, and c) 30 ppm degraded cells at 40 °C

The arcs for 5-24, 5-48, and 5-72 (Figure 50 a) show distinct separation, with the total impedance (arc width + intercept) shifting, reflecting the changes in R_{ct} and R_{Ω} noted in Table 12. The 30 ppm Series (Figure 50 c) shows a higher overall impedance than the 5 ppm series, which correlates with the higher R_{Ω} and R_{mt} values recorded at 40 °C for these samples. Furthermore, the comparisons in Figures 50 and 51 demonstrate that the ECM used provided a robust fit to the experimental data, with the solid lines closely tracking the experimental points across the frequency spectrum.



a) b) c)

Figure 51: Nyquist plot of reference cell vs a) 24 h, b) 48 h, and c) 72 h degraded cells at 40 °C

In summary, there is no linear correlation between the extent of Fenton degradation and the loss of the EIS performance metric. The EIS analysis suggests that Fenton degradation induces a trade-off between increased material resistivity (likely due to chemical attack on ionic groups) and reduced resistance path length (due to thinning). This trade-off is thermally sensitive: chemical resistivity dominates at low temperatures (40 °C), whereas thinning effects appear to mitigate increases in resistance at high temperatures (75 °C).[70] Additionally, specific degradation conditions (e.g., 30-48) triggered anomalous spikes in mass transport resistance, highlighting the non-linear nature of the degradation mechanism.

4.3.2.4 Hydrogen Crossover

Hydrogen crossover data for the 5, 15, and 30 ppm Fe^{2+} degraded CCMs in Figure 52 align with the trends established in Section 4.3.1.3. It is important to note that in this work, hydrogen gas crossover is described by the concentration of H_2 measured in volume percent (and not in terms of the permeability constant). Specifically, the anodic hydrogen content exhibits an inverse relationship with temperature: it decreases as the cell temperature rises from 40 to 75 °C (at all tested current densities). It may be that at higher temperatures, due to lower ohmic drop, the production rate of oxygen is increased and the concentration of H_2 in O_2 is lower (as measured by GC). However, we observed that with an increase in current density concentration of H_2 in O_2 also increased. It can be attributed to structural modifications of the PFSA ionomer due to chemical degradation, but a clear explanation is difficult to propose due to the complex

simultaneous processes taking place in chemically degraded CCMs. The persistence of these trends, even in degraded samples, indicates the complexity of the gas crossover process in operational water electrolysers that also takes into account the membrane's structural condition.

As detailed previously, the reduction in measured anodic hydrogen concentration at higher temperatures (Figure 52 a),c) could be explained by the significant increase in water vapour partial pressure and an increase in overall gas production (dilution effect)[85] and the thermally activated kinetics of the parasitic hydrogen oxidation reaction at the anode. Conversely, the increase in crossover with current density (Figure 52 b), d) and 53 b)) could be explained by the so-called supersaturation of dissolved hydrogen at the cathode catalyst layer. This dissolved hydrogen continues to act as an additional driving force for diffusion.[93] This phenomenon was first hypothesised by Oberlin *et al*. (1982), who observed that hydrogen flux increases with current density due to a build-up of hydrogen oversaturation at the cathode catalyst.[94] While these values can reach the order of 20 bar at 1 A cm^{-2}, other estimations suggest the additional driving force can be represented at an additional 10 bar of pressure. According to Bessarabov, this supersaturation has a limited capacity that is a specific function of the catalyst layer structure, current collector morphology, and the ionomer pore network.[95]

Trinke *et al.,*[96] quantitatively demonstrated that hydrogen crossover in PEMWE is governed by Fickian diffusion driven by the dissolved hydrogen concentration gradient across the membrane, rather than membrane thickness alone. Supersaturated hydrogen concentrations within the cathode catalyst layer, arising from mass-transport limitations, increase this gradient and thus the crossover flux with increasing current density. They further attributed enhanced crossover at high current densities to elevated gas pressure, dissolved-gas supersaturation, and thermally induced changes in permeability. Notably, Trinke *et al*. demonstrated that the cathode ionomer content significantly influences this supersaturation effect; increasing the ionomer content from 10 wt% to 40 wt% resulted in higher mass transfer resistances and a corresponding increase in hydrogen crossover. As confirmed by our sample specifications (Table 6), our methodology uses a 40 wt% ionomer content in the cathode. This aligns with the ‘worst-case’ scenario identified in the literature, where high ionomer loadings hinder hydraulic gas transport and increase diffusion pathways, thereby promoting higher crossover rates.[96] They further attributed enhanced crossover at high current densities to elevated gas pressure, dissolved-gas supersaturation, and thermally induced changes in permeability. This framework directly supports the present observation that crossover remains strongly current-dependent even after chemical degradation, indicating that catalyst-layer transport phenomena remain operative despite membrane structural modification.[97]

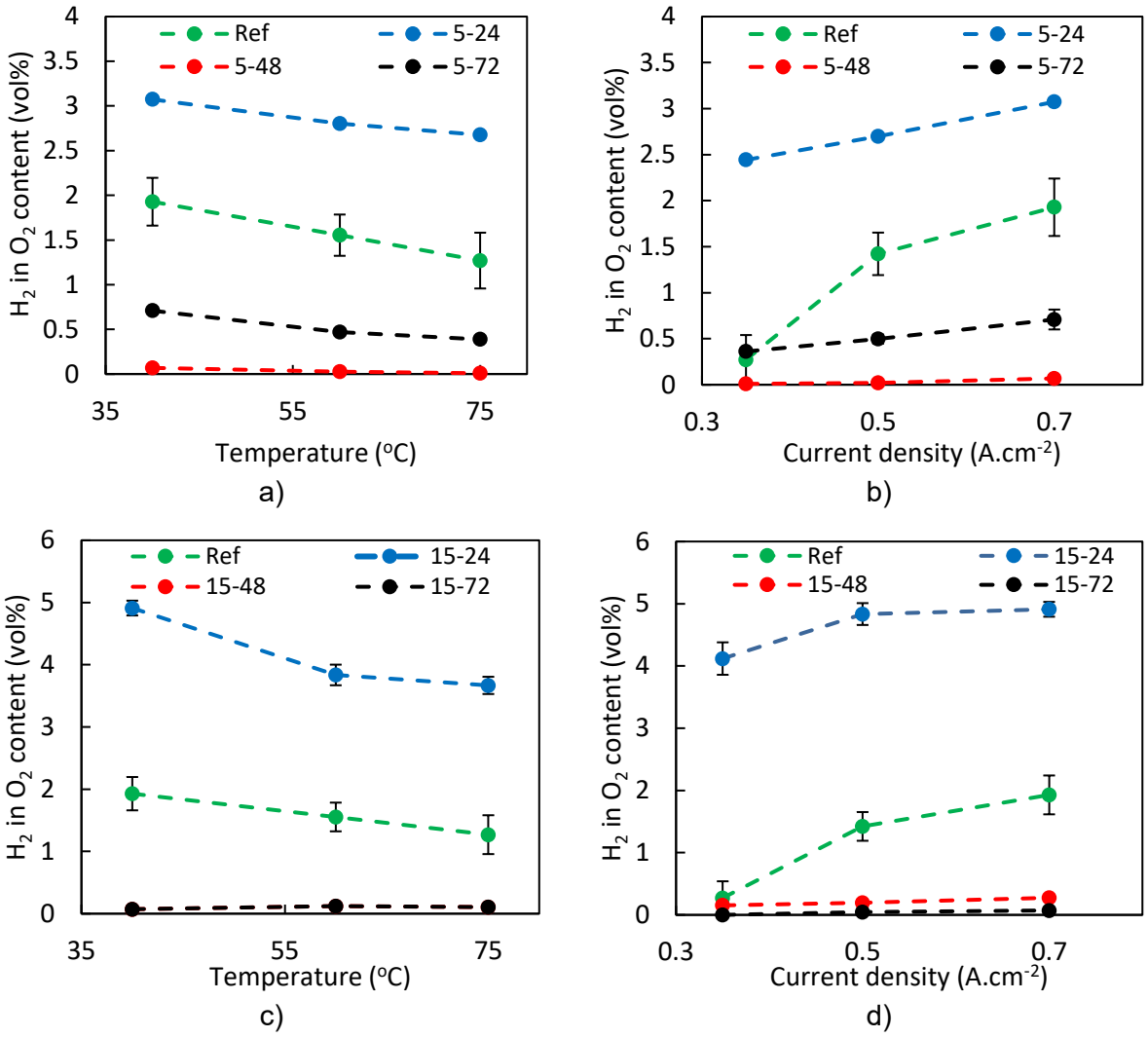


Figure 52: Hydrogen gas crossover data for 5 ppm Fe^{2+} degraded CCMs at variable a) temperature (T= 40, 60 and 75°C) and b) current density(*j*= 0.35, 0.5 and 0.7A.cm^{-2}), and 15 ppm Fe^{2+} degraded CCMs at variable c) temperature(T= 40, 60 and 75°C) and d) current density (*j*= 0.35, 0.5 and 0.7A.cm^{-2}).

Analysis of the low-to-moderate (5 and 15 ppm Fe^{2+} in Figure 52) degraded CCMs reveals distinct behaviour that depends on exposure duration. The 24 h exposure samples exhibit elevated H_2 crossover relative to the pristine baseline, a result consistent with Fickian diffusion principles and attributable to membrane thinning (driven by CF_{bb} scission) and the initiation of microstructural defects.

However, extending the degradation duration to 48 and 72 h reveals a non-monotonic trend, characterised by an unexpected decrease in crossover flux relative to the 24 h sample. This deviation suggests that although morphological thinning occurs, *ex-situ* Fenton degradation concurrently induces physicochemical changes, such as altered internal tortuosity, possibly crystallinity, and reduced water uptake capacity, that modify the membrane's effective diffusion

coefficient. The absence of a linear correlation between degradation duration and crossover magnitude indicates competition between membrane thinning (which enhances flux) and material-property alteration (which appears to impede flux in these samples).

This interpretation aligns with the analysis of Trinke et al.,[96, 97] who showed that hydrogen crossover flux depends on both the effective diffusion coefficient within the hydrated membrane and the dissolved hydrogen concentration at the cathode–membrane interface. Variations in transport coefficients or interfacial concentrations can therefore offset purely geometric effects such as membrane thickness. Accordingly, in the present degraded samples, a reduction in effective diffusivity due to partial structural collapse or reduced membrane water fraction would decrease crossover even in the presence of macroscopic thinning.

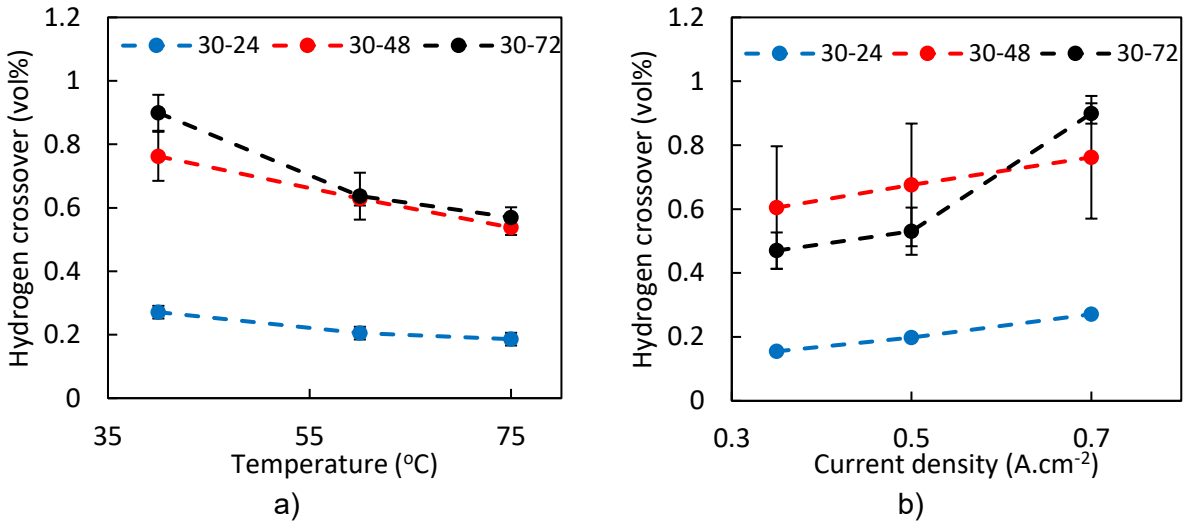


Figure 53: Hydrogen gas crossover data for 30 ppm Fe^{2+} degraded CCMs at variable a) temperature and b) current density.

In contrast, the 30 ppm Fe^{2+} degraded CCMs (Figure 53) exhibit a profound decrease in H_2 crossover magnitude. Despite the morphological degradation noted in Section 4.2.4, including cratering (manifesting as surface pitting and blisters) and irreversible membrane dimensional expansion (due to a loss of elastic modulus), the anodic H_2 content decreases and remains consistently below 1 vol%.

This suppression of H_2 crossover, which contradicts predictions based solely on membrane thinning, suggests that the transport properties of the membrane have been altered by the high concentration of Fenton reagents. While membrane thinning would theoretically increase flux according to Fick's Law, the observed decrease in crossover implies a substantial reduction in the effective H_2 diffusion coefficient. This reduction is attributed to the collapse of the hydrophilic cluster network caused by CF_{sc} (side-chain) scission.[98]

As discussed in Section 4.2.1, the 30 ppm samples experienced moderate IEC loss due to the cleavage of SO_3H groups. Since H_2 transport in PFSA membranes occurs primarily through water-filled ionic channels, the destruction of these hydrophilic domains leads to membrane dehydration and the collapse of the pathways required for gas diffusion. Consequently, the membrane transitions from a thin, conductive separator to a denser, hydrophobic barrier with low gas permeability, effectively reducing H_2 crossover despite the macroscopic surface degradation.[99]

Finally, it is critical to contextualise these findings within the broader electrolyser system. As noted by Trinke at the International Conference on Electrolysis (ICE) in 2025,[97] H_2 gas crossover is influenced by a complex matrix of factors beyond the membrane itself. This complexity is further highlighted by Kalinnikov *et al.*, whose work emphasises the intricate interplay of two-phase mass transfer across the PTLs and catalyst layers, which can significantly dictate overall cell performance and gas purity.[100] Key system parameters, including PTL design (pore size, thickness, coating) and electrode properties (ionomer content, catalyst loading, and support structure), simultaneously influence gas transport, highlighting the complexity of isolating membrane-specific degradation effects.

4.4 Correlating *Ex-Situ* Degradation with *In-Situ* Performance

Validating *ex-situ* degradation protocols requires establishing a correlation between the AST outcomes, specifically those from Fenton's reagent immersion, and the performance decay observed in the PEMWE cell. Table 14 summarises the key degradation metrics determined in this study, enabling direct comparison of the chemical stability and electrochemical durability of the tested Nafion® 115 CCMs.

Table 14: Compiled results of Nafion® 115 samples used in CCM fabrication.Negative values are representative of a performance improvement when compared to the reference cell, i.e., non-degraded CCMs.

Sample	5-24	5-48	5-72	15-24	15-48	15-72	30-24	30-48	30-72
IEC loss (%)	0.406 ±0.012	2.24 ±0.447	6.33 ±1.122	1.9 ±0.938	4.55 ±0.227	8.37 ±0.669	3.31 ±0.832	7.33 ±0.469	12.29 ±1.64
Fluoride release ($\mu mol.cm^{-2}$)	2.45	7.02	10.72	11.49	21.9	30.49	38.77	63.15	77.38
Sulfur emission ($\mu mol.cm^{-2}$)	0.01	0.1	1.44	0.02	1.7	3.24	1.51	2.95	4.16
Voltage loss at 1.85 V 75°C (mV)	-0.5 ±0.007	11 ±0.000	9.5 ±0.000	15.83 ±0.001	14.5 ±0.004	21.5 ±0.005	-24.17 ±0.004	102.17 ±0.013	107 ±0.012
Voltage loss ave 75°C (mV)	6.06 ±0.004	12.11 ±0.004	9.55 ±0.002	10.46 ±0.005	8.03 ±0.006	9.03 ±0.012	-16.68 ±0.006	46.29 ±0.036	70.04 ±0.037
R_{Ω} at 40°C ($m\Omega.cm^2$)	193.37	199.54	200.97	205.41	210.87	211.32	212.85	239.95	239.43
R_{ct} at 40°C ($m\Omega.cm^2$)	56.63	57.27	80.60	75.74	55.82	52.71	59.80	62.05	45.97
R_{mt} at 40°C ($m\Omega.cm^2$)	125.37	43.63	23.99	33.92	45.44	66.93	27.84	144.95	92.03

4.4.1 Fluoride Release Rate (FRR) and Voltage Degradation

As discussed in Sections 2.4.5.3 and 2.6, fluoride release originates predominantly from radical-induced cleavage of the PFSA backbone (CF_{bb}) and sidechain (CF_{sc}), producing perfluorinated fragments and ultimately HF in aqueous media.[101] •OH and •OOH radicals generated during Fenton reactions attack tertiary carbon sites and ether linkages in the side chain, initiating scission reactions and backbone unzipping.[25, 33, 102, 103] This degradation pathway is well established as a dominant chemical failure mechanism in PFSA membranes under oxidative environments.

The progressive loss of polymer mass and structural integrity leads to membrane thinning and the formation of pinholes or microdefects.[35] In operating PEMWE cells, such structural degradation compromises electronic isolation between electrodes, promoting mixed electrode

potentials. These parasitic reactions reduce Faradaic efficiency and require a higher cell voltage to maintain a constant current density. [29, 33]

Several studies have demonstrated that FRR is a reliable quantitative proxy for PFSA chemical degradation and strongly correlates with performance decay in both fuel cells and electrolyser systems.[101, 103]

A primary correlation is observed between the cumulative FRR measured *ex-situ* and the voltage degradation rate recorded during the *in-situ* hold. The membranes exhibiting the highest cumulative FRR in the *ex-situ* Fenton tests (Table 14) correspond to those showing the highest rate of voltage increase in the *in-situ* polarisation curves over time (Sections 4.3.2.1 and 4.3.2.2).

4.4.2 Correlation of *Ex-Situ* Degradation with Electrochemical Impedance Spectroscopy (EIS)

While polarisation curves provide a macroscopic view of performance decay, EIS enables deconvolution of voltage losses into distinct resistive components. Correlating *ex-situ* chemical degradation markers with *in-situ* impedance parameters (R_Ω and R_{ct}) provides mechanistic insight into how chemical attack translates into efficiency loss.

4.4.2.1 Ion Exchange Capacity (IEC) Loss and Ohmic Resistance (R_Ω)

IEC represents the concentration of fixed sulfonic acid groups ($-SO_3H$), which are responsible for proton conduction.[2] Radical attack preferentially cleaves PFSA side chains, leading to detachment of sulfonic acid groups and reducing the number of proton-conducting sites.[101] Since proton conductivity in PFSA membranes is strongly dependent on the density and connectivity of these ionic clusters, degradation of side chains directly reduces proton transport efficiency.[11, 62]

The most direct correlation observed is between *ex-situ* IEC loss and *in-situ* ohmic resistance (R_Ω). Membranes with greater IEC loss exhibit higher end-of-test R_Ω values.

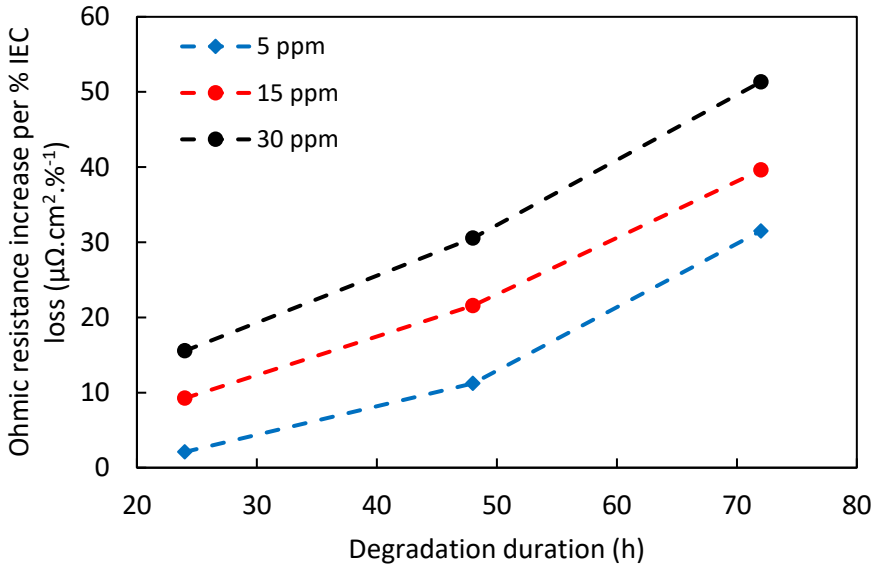


Figure 54: Ohmic resistance increase per % IEC loss as a function of degradation duration

Ohmic resistance in PEM electrolysers is largely determined by membrane proton conductivity, which depends on water content, temperature, and fixed-charge concentration.[11] The *ex-situ* Fenton's test induces radical attack (primarily •OH and •OOH radicals) on the polymer side-chains, leading to the scission of the C-S bonds and the subsequent detachment of -SO_3H groups.[101] Since the proton conductivity is directly proportional to the concentration of these fixed charge groups (represented by IEC), the chemical loss of -SO_3H groups results in a lower charge carrier density.[11] This creates a direct linear correlation where:

$$\Delta IEC_{ex-situ} \propto \Delta R_{\Omega,in-situ}$$

Although membrane thinning due to chemical degradation would, in theory, decrease resistance by shortening the proton transport path length, the experimental increase in R_Ω indicates that loss of intrinsic ionic conductivity dominates over geometric thickness effects. This observation is consistent with established PFSA degradation behaviour.[29]

4.4.2.2 Sulfur Emission and Ohmic Resistance (R_Ω)

While FRR primarily reflects backbone and overall polymer degradation, sulfur emission provides a more direct indicator of the loss of sulfonic acid groups.[101] Correlating cumulative SER with impedance evolution reveals degradation mechanisms that affect both bulk membrane properties and interfacial ionic transport. Figure 55 represents a continual increase in R_Ω and R_{ct} as sulfur is released.

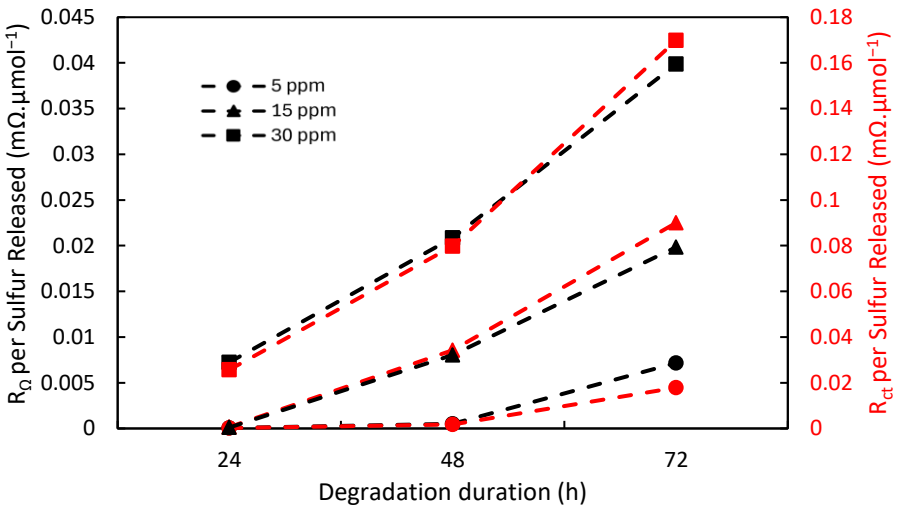


Figure 55: Sulfur emission per R_Ω and R_{ct} as a function of degradation duration

A near-linear relationship between cumulative sulfur release and increased R_Ω is observed across tested samples at low temperature (40 °C). Proton transport in PFSA membranes occurs through hydrated ionic clusters via both vehicular diffusion and Grotthuss proton hopping mechanisms. The detachment of sulfonic acid groups reduces the density of proton-conducting sites and disrupts the percolated ionic network.[11]

This relationship may be expressed using a specific resistivity increase parameter, defined as the ratio of the increase in ohmic resistance to the sulfur loss. A constant ratio would indicate conductivity loss driven primarily by side-chain degradation, whereas deviations from linearity may suggest concurrent morphological changes such as membrane thinning, phase separation, or micro-crack formation.[29]

$$\frac{\Delta R_\Omega}{n(S)_{loss}} = k_{cond}$$

A constant value of this ratio across membranes would indicate that the mechanism of conductivity loss is solely due to side-chain scission. Deviations from linearity suggest that structural changes (e.g., membrane thinning) compete with the loss of functional groups in altering the total cell resistance.

4.4.2.3 Sulfur Emission and Charge Transfer Resistance R_{ct}

A complex, nonlinear relationship exists between sulfur emission and the charge-transfer resistance (R_{ct}). Theoretically, sulfur-containing degradation fragments can migrate into catalyst layers and poison the ionomer films, reducing ionic accessibility to the active sites.[29, 104]

However, the experimental results indicate that this poisoning effect is secondary to morphological restructuring. As shown in Table 14, although sulfur emission peaked in the most degraded samples (4.16 μmol.cm^{-2} for Sample 30-72), R_{ct} decreased to 45.97 mΩ.cm^2, significantly lower than the baseline of 56.63 mΩ.cm^2.

This counterintuitive trend suggests that in the specific degradation regime tested, surface roughening (pitting) initially increases the effective interfacial surface area, temporarily lowering R_{ct} despite the lower IEC. Therefore, a high sulfur emission rate does not linearly predict increased R_{ct} in this setup; rather, it signals severe structural breakdown where the catalyst interface has been physically altered (pitted/roughened)

Bibliography

(1) Dorenbos, G.; Suga, Y. Simulation of equivalent weight dependence of Nafion morphologies and predicted trends regarding water diffusion. *Journal of Membrane Science* **2009**, *330* (1), 5-20. DOI: https://doi.org/10.1016/j.memsci.2008.11.056.

(2) Scott, K. MEMBRANE MATERIALS, PREPARATION AND CHARACTERISATION. In *Handbook of Industrial Membranes*, Scott, K. Ed.; Elsevier Science, 1995; pp 187-269.

(3) Jiang, B.; Wu, L.; Yu, L.; Qiu, X.; Xi, J. A comparative study of Nafion series membranes for vanadium redox flow batteries. *Journal of Membrane Science* **2016**, *510*, 18-26. DOI: https://doi.org/10.1016/j.memsci.2016.03.007.

(4) Hwang, S.; Lee, D.; Rho, Y.; Yoon, K. S.; Yu, D. M.; Yoon, S. J.; Kim, S.; Hong, Y. T.; So, S. Planar orientation of hydrophilic channels by biaxial deformation of perfluorinated sulfonic acid membranes for vanadium redox flow batteries. *Journal of Power Sources* **2021**, *489*, 229497. DOI: https://doi.org/10.1016/j.jpowsour.2021.229497.

(5) Mazzapioda, L.; Panero, S.; Navarra, M. A. Polymer Electrolyte Membranes Based on Nafion and a Superacidic Inorganic Additive for Fuel Cell Applications. In *Polymers*, 2019; Vol. 11.

(6) Tang, H.; Aili, D.; Tufa, R. A.; Kraglund, M. R.; Wu, Q.; Pan, C.; Cleemann, L. N.; Li, Q. Anion conductivity of cation exchange membranes in aqueous supporting electrolytes. *Solid State Ionics* **2022**, *383*, 115984. DOI: https://doi.org/10.1016/j.ssi.2022.115984.

(7) Evans, C. E.; Noble, R. D.; Nazeri-Thompson, S.; Nazeri, B.; Koval, C. A. Role of conditioning on water uptake and hydraulic permeability of Nafion® membranes. *Journal of Membrane Science* **2006**, *279* (1), 521-528. DOI: https://doi.org/10.1016/j.memsci.2005.12.046.

(8) Sharma, P. P.; Kim, D. A Facile and Sustainable Enhancement of Anti-Oxidation Stability of Nafion Membrane. *Membranes* **2022**, *12* (5), 521.

(9) Gruger, A.; Régis, A.; Schmatko, T.; Colomban, P. Nanostructure of Nafion® membranes at different states of hydration: An IR and Raman study. *Vibrational Spectroscopy* **2001**, *26* (2), 215-225. DOI: https://doi.org/10.1016/S0924-2031(01)00116-3.

(10) Korzeniewski, C.; Snow, D. E.; Basnayake, R. Transmission Infrared Spectroscopy as a Probe of Nafion Film Structure: Analysis of Spectral Regions Fundamental to Understanding Hydration Effects. *Applied Spectroscopy* **2006**, *60* (6), 599-604. DOI: 10.1366/000370206777670620 (acccessed 2025/07/21).

(11) Mauritz, K. A.; Moore, R. B. State of Understanding of Nafion. *Chemical Reviews* **2004**, *104* (10), 4535-4586. DOI: 10.1021/cr0207123.

(12) Liang, Z.; Chen, W.; Liu, J.; Wang, S.; Zhou, Z.; Li, W.; Sun, G.; Xin, Q. FT-IR study of the microstructure of Nafion® membrane. *Journal of Membrane Science* **2004**, *233* (1), 39-44. DOI: https://doi.org/10.1016/j.memsci.2003.12.008.

(13) Laporta, M.; Pegoraro, M.; Zanderighi, L. Perfluorosulfonated membrane (Nafion): FT-IR study of the state of water with increasing humidity. *Physical Chemistry Chemical Physics* **1999**, *1* (19), 4619-4628, 10.1039/A904460D. DOI: 10.1039/A904460D.

(14) Cable, K. M.; Mauritz, K. A.; Moore, R. B. Effects of hydrophilic and hydrophobic counterions on the Coulombic interactions in perfluorosulfonate ionomers. *Journal of Polymer Science Part B: Polymer Physics* **1995**, *33* (7), 1065-1072. DOI: https://doi.org/10.1002/polb.1995.090330710 (acccessed 2025/07/21).

(15) Robert, M.; El Kaddouri, A.; Perrin, J.-C.; Raya, J.; Lottin, O. Time-resolved monitoring of composite Nafion™ XL membrane degradation induced by Fenton's reaction. *Journal of Membrane Science* **2021**, *621*, 118977. DOI: https://doi.org/10.1016/j.memsci.2020.118977.

(16) Peng, Z.; Huguet, P.; Deabate, S.; Morin, A.; Sutor, A. K. Depth-resolved micro-Raman spectroscopy of tri-layer PFSA membrane for PEM fuel cells: how to obtain reliable inner water contents. *Journal of Raman Spectroscopy* **2013**, *44* (2), 321-328. DOI: https://doi.org/10.1002/jrs.4192.

(17) Böhm, T.; Moroni, R.; Breitwieser, M.; Thiele, S.; Vierrath, S. Spatially Resolved Quantification of Ionomer Degradation in Fuel Cells by Confocal Raman Microscopy. *Journal of The Electrochemical Society* **2019**, *166* (7), F3044. DOI: 10.1149/2.0051907jes.

(18) Chourdakis, N.; Voyiatzis, G. A. Molecular orientation study of uniaxially drawn nafion polymer electrolyte membranes utilizing polarized UV–Raman spectra. *Journal of Polymer Science Part B: Polymer Physics* **2007**, *45* (17), 2509-2517. DOI: https://doi.org/10.1002/polb.21250 (acccessed 2025/11/03).

(19) Nishiyama, H.; Takamuku, S.; Oshikawa, K.; Lacher, S.; Iiyama, A.; Inukai, J. Chemical States of Water Molecules Distributed Inside a Proton Exchange Membrane of a Running Fuel Cell Studied by Operando Coherent Anti-Stokes Raman Scattering Spectroscopy. *The Journal of Physical Chemistry C* **2020**, *124* (18), 9703-9711. DOI: 10.1021/acs.jpcc.0c00347.

(20) Maier, M.; Abbas, D.; Komma, M.; Mu'min, M. S.; Thiele, S.; Böhm, T. A comprehensive study on the ionomer properties of PFSA membranes with confocal Raman microscopy. *Journal of Membrane Science* **2023**, *669*, 121244. DOI: https://doi.org/10.1016/j.memsci.2022.121244.

(21) Bribes, J. L.; El Boukari, M.; Maillols, J. Application of Raman spectroscopy to industrial membranes. Part 2–Perfluorosulphonic membrane. *Journal of Raman Spectroscopy* **1991**, *22* (5), 275-279. DOI: https://doi.org/10.1002/jrs.1250220507 (acccessed 2025/11/03).

(22) Yena, M.; Ryeo Yun, H.; Sujeong, P.; Oc Hee, H. 1H NMR spectroscopy of degraded perfluorosulfonic acid membranes: A simple methodology for detecting onset of

degradation. *Journal of Electroanalytical Chemistry* **2023**, *932*, 117268. DOI: https://doi.org/10.1016/j.jelechem.2023.117268.

(23) Maximilian, M.; Dunia, A.; Miriam, K.; Muhammad Solihul, M. m.; Simon, T.; Thomas, B. A comprehensive study on the ionomer properties of PFSA membranes with confocal Raman microscopy. *Journal of Membrane Science* **2023**, *669*, 121244. DOI: https://doi.org/10.1016/j.memsci.2022.121244.

(24) Dennis, E. C.; Robert, D. L.; Timothy, J. H.; Paul, C. T.; Monica, E. T. Advanced materials for improved PEMFC performance and life. *Journal of Power Sources* **2004**, *131* (1), 41-48. DOI: https://doi.org/10.1016/j.jpowsour.2004.01.023.

(25) Frühwirt, P.; Kregar, A.; Törring, J. T.; Katrašnik, T.; Gescheidt, G. Holistic approach to chemical degradation of Nafion membranes in fuel cells: modelling and predictions. *Physical Chemistry Chemical Physics* **2020**, *22* (10), 5647-5666, 10.1039/C9CP04986J. DOI: 10.1039/C9CP04986J.

(26) Xunying, W.; Linsong, Z.; Guangfu, L.; Geng, Z.; Zhi-Gang, S.; Baolian, Y. The influence of Ferric ion contamination on the solid polymer electrolyte water electrolysis performance. *Electrochimica Acta* **2015**, *158*, 253-257. DOI: https://doi.org/10.1016/j.electacta.2015.01.140.

(27) Lorenz, G.; Sindy, M. D.; Willem, H. K. Radical (HO•, H• and HOO•) Formation and Ionomer Degradation in Polymer Electrolyte Fuel Cells. *Journal of The Electrochemical Society* **2011**, *158* (7), B755. DOI: 10.1149/1.3581040.

(28) Sethuraman, V. A.; Weidner, J. W.; Haug, A. T.; Protsailo, L. V. Durability of Perfluorosulfonic Acid and Hydrocarbon Membranes: Effect of Humidity and Temperature. *Journal of The Electrochemical Society* **2008**, *155* (2), B119. DOI: 10.1149/1.2806798.

(29) Kusoglu, A.; Weber, A. Z. New Insights into Perfluorinated Sulfonic-Acid Ionomers. *Chemical Reviews* **2017**, *117* (3), 987-1104. DOI: 10.1021/acs.chemrev.6b00159.

(30) Madhav, D.; Shao, C.; Mus, J.; Buysschaert, F.; Vandeginste, V. The Effect of Salty Environments on the Degradation Behavior and Mechanical Properties of Nafion Membranes. In *Energies*, 2023; Vol. 16, p 2256.

(31) Shah, A. A.; Ralph, T. R.; Walsh, F. C. Modeling and Simulation of the Degradation of Perfluorinated Ion-Exchange Membranes in PEM Fuel Cells. *Journal of The Electrochemical Society* **2009**, *156* (4), B465. DOI: 10.1149/1.3077573.

(32) Feng, M.; Qu, R.; Wei, Z.; Wang, L.; Sun, P.; Wang, Z. Characterization of the thermolysis products of Nafion membrane: A potential source of perfluorinated compounds in the environment. *Scientific Reports* **2015**, *5* (1), 9859. DOI: 10.1038/srep09859.

(33) Curtin, D. E.; Lousenberg, R. D.; Henry, T. J.; Tangeman, P. C.; Tisack, M. E. Advanced materials for improved PEMFC performance and life. *Journal of Power Sources* **2004**, *131* (1), 41-48. DOI: https://doi.org/10.1016/j.jpowsour.2004.01.023.

(34) Kuhnert, E.; Heidinger, M.; Bernroitner, A.; Kiziltan, Ö.; Berger, E.; Hacker, V.; Bodner, M. Fluoride emission rate analysis in proton exchange membrane water electrolyzer cells. *Frontiers in Energy Research* **2024**, *Volume 12 - 2024*, Original Research. DOI: 10.3389/fenrg.2024.1457310.

(35) Shi, S.; Sun, X.; Lin, Q.; Chen, J.; Fu, Y.; Hong, X.; Li, C.; Guo, X.; Chen, G.; Chen, X. Fatigue crack propagation behavior of fuel cell membranes after chemical degradation. *International Journal of Hydrogen Energy* **2020**, *45* (51), 27653-27664. DOI: https://doi.org/10.1016/j.ijhydene.2020.07.113.

(36) Lim, H. J.; Kim, G.; Yun, G. J. Durability and Performance Analysis of Polymer Electrolyte Membranes for Hydrogen Fuel Cells by a Coupled Chemo-mechanical Constitutive Model and Experimental Validation. *ACS Applied Materials \& Interfaces* **2023**, *15* (20), 24257-24270. DOI: 10.1021/acsami.2c15451 , note = PMID: 37179493.

(37) Madhav, D.; Shao, C.; Mus, J.; Buysschaert, F.; Vandeginste, V. The Effect of Salty Environments on the Degradation Behavior and Mechanical Properties of Nafion Membranes. In *Energies*, 2023; Vol. 16.

(38) Lim, H. J.; Kim, G.; Yun, G. J. Durability and Performance Analysis of Polymer Electrolyte Membranes for Hydrogen Fuel Cells by a Coupled Chemo-mechanical Constitutive Model and Experimental Validation. *ACS Appl Mater Interfaces* **2023**, *15* (20), 24257-24270. DOI: 10.1021/acsami.2c15451 From NLM.

(39) Tsuneda, T.; Singh, R. K.; Iiyama, A.; Miyatake, K. Theoretical Investigation of the H2O2-Induced Degradation Mechanism of Hydrated Nafion Membrane via Ether-Linkage Dissociation. *ACS Omega* **2017**, *2* (7), 4053-4064. DOI: 10.1021/acsomega.7b00594.

(40) Frensch, S. H.; Serre, G.; Fouda-Onana, F.; Jensen, H. C.; Christensen, M. L.; Araya, S. S.; Kær, S. K. Impact of iron and hydrogen peroxide on membrane degradation for polymer electrolyte membrane water electrolysis: Computational and experimental investigation on fluoride emission. *Journal of Power Sources* **2019**, *420*, 54-62. DOI: https://doi.org/10.1016/j.jpowsour.2019.02.076.

(41) Halalay, I. C.; Merzougui, B.; Mance, A. Three Mechanisms for Protecting the Fuel Cell Membrane, Plates and Catalysts. *ECS Transactions* **2008**, *16* (2), 969. DOI: 10.1149/1.2981937.

(42) Bosnjakovic, A.; Kadirov, M. K.; Schlick, S. Using ESR spectroscopy to study radical intermediates in proton-exchange membranes exposed to oxygen radicals. *Research on Chemical Intermediates* **2007**, *33* (8), 677-687. DOI: 10.1163/156856707782169372.

(43) Liu, H.; Coms, F. D.; Zhang, J.; Gasteiger, H. A.; LaConti, A. B. Chemical degradation: correlations between electrolyzer and fuel cell findings. Springer: 2009; Vol. 1.

(44) Gao, Y.; Salako, E.; Thompson, M. Synthesis of New Perfluorosulfonic Acids Against H2o2 Degradations. *Available at SSRN 4645297*.

(45) Hassan, M. K.; Nalawade, A.; Abukmail, A.; Patil, Y.; Mauritz, K. A. Analysis of Nafion Fuel Cell Membrane Chemical Durability Using Broadband Dielectric Spectroscopy. *ECS Transactions* **2011**, *41* (1), 1359.

(46) Vijay, A. S.; John, W. W.; Andrew, T. H.; Lesia, V. P. Durability of Perfluorosulfonic Acid and Hydrocarbon Membranes: Effect of Humidity and Temperature. *Journal of The Electrochemical Society* **2007**, *155* (2), B119. DOI: 10.1149/1.2806798.

(47) Patil, Y. P.; Jarrett, W. L.; Mauritz, K. A. Deterioration of mechanical properties: A cause for fuel cell membrane failure. *Journal of Membrane Science* **2010**, *356* (1), 7-13. DOI: https://doi.org/10.1016/j.memsci.2010.02.060.

(48) Crum, M.; Liu, W. Effective Testing Matrix for Studying Membrane Durability in PEM Fuel Cells: Part 2. Mechanical Durability and Combined Mechanical and Chemical Durability. *ECS Transactions* **2006**, *3* (1), 541. DOI: 10.1149/1.2356175.

(49) Mittal, V. O.; Kunz, H. R.; Fenton, J. M. Membrane Degradation Mechanisms in PEMFCs. *Journal of The Electrochemical Society* **2007**, *154* (7), B652. DOI: 10.1149/1.2734869.

(50) Wang, K.; Zhang, Z.; Wang, S.; Wang, Y.; Liu, Y.; Wu, H.; Shao, J.; Ye, J.; Cai, J. A compact and stable diagnostic system for major species concentration and temperature in the combustion flow field by Raman scattering. *Frontiers in Physics* **2025**, *Volume 13 - 2025*, Original Research. DOI: 10.3389/fphy.2025.1526350.

(51) Fang, X.; Shen, P. K.; Song, S.; Stergiopoulos, V.; Tsiakaras, P. Degradation of perfluorinated sulfonic acid films: An in-situ infrared spectro-electrochemical study. *Polymer Degradation and Stability* **2009**, *94* (10), 1707-1713. DOI: https://doi.org/10.1016/j.polymdegradstab.2009.06.015.

(52) Danilczuk, M.; Lancucki, L.; Schlick, S.; Hamrock, S. J.; Haugen, G. M. In-Depth Profiling of Degradation Processes in a Fuel Cell: 2D Spectral-Spatial FTIR Spectra of Nafion Membranes. *ACS Macro Letters* **2012**, *1* (2), 280-285. DOI: 10.1021/mz200100s.

(53) Coms, F. D.; Fuller, T. J.; Schaffer, C. P. A Mechanistic Study of Perfluorosulfonic Acid Membrane Water Permeance Degradation in Air. *Journal of The Electrochemical Society* **2018**, *165* (6), F3104. DOI: 10.1149/2.0141806jes.

(54) Agarwal, T.; Prasad, A. K.; Advani, S. G.; Babu, S. K.; Borup, R. L. Infrared spectroscopy for understanding the structure of Nafion and its associated properties. *Journal of Materials Chemistry A* **2024**, *12* (24), 14229-14244, 10.1039/D3TA05653H. DOI: 10.1039/D3TA05653H.

(55) Boyle, N. G.; McBrierty, V. J.; Douglass, D. C. The behavior of water in Nafion membranes. *Macromolecules* **1983**, *16* (1), 75-80. DOI: 10.1021/ma00235a015.

(56) Chen, Q.; Schmidt-Rohr, K. 19F and 13C NMR Signal Assignment and Analysis in a Perfluorinated Ionomer (Nafion) by Two-Dimensional Solid-State NMR. *Macromolecules* **2004**, *37* (16), 5995-6003. DOI: 10.1021/ma049759b.

(57) Kolodziejski, W.; Klinowski, J. Kinetics of Cross-Polarization in Solid-State NMR: A Guide for Chemists. *Chemical Reviews* **2002**, *102* (3), 613-628. DOI: 10.1021/cr000060n.

(58) Majsztrik, P. W.; Bocarsly, A. B.; Benziger, J. B. Viscoelastic Response of Nafion. Effects of Temperature and Hydration on Tensile Creep. *Macromolecules* **2008**, *41* (24), 9849-9862. DOI: 10.1021/ma801811m.

(59) Kundu, S.; Simon, L. C.; Fowler, M.; Grot, S. Mechanical properties of Nafion™ electrolyte membranes under hydrated conditions. *Polymer* **2005**, *46* (25), 11707-11715. DOI: https://doi.org/10.1016/j.polymer.2005.09.059.

(60) Tang, H.; Peikang, S.; Jiang, S. P.; Wang, F.; Pan, M. A degradation study of Nafion proton exchange membrane of PEM fuel cells. *Journal of Power Sources* **2007**, *170* (1), 85-92. DOI: https://doi.org/10.1016/j.jpowsour.2007.03.061.

(61) Lee, S.-Y.; Cho, E.; Lee, J.-H.; Kim, H.-J.; Lim, T.-H.; Oh, I.-H.; Won, J. Effects of Purging on the Degradation of PEMFCs Operating with Repetitive On/Off Cycles. *Journal of The Electrochemical Society* **2007**, *154* (2), B194. DOI: 10.1149/1.2403083.

(62) Healy, J.; Hayden, C.; Xie, T.; Olson, K.; Waldo, R.; Brundage, M.; Gasteiger, H.; Abbott, J. Aspects of the Chemical Degradation of PFSA Ionomers used in PEM Fuel Cells. *Fuel Cells* **2005**, *5* (2), 302-308. DOI: https://doi.org/10.1002/fuce.200400050.

(63) Wang, H. H.; Yuan, X.-Z.; Li, H. *PEM fuel cell diagnostic tools*; Taylor & Francis/CRC Press, 2012. DOI: 10.1201/b11100.

(64) Bessarabov, D.; Kozak, P. Measurement of gas permeability in SPE membranes for use in fuel cells. *Membrane Technology* **2007**, *2007* (12), 6-9. DOI: https://doi.org/10.1016/S0958-2118(07)70264-1.

(65) Kusoglu, A.; Calabrese, M.; Weber, A. Z. Effect of Mechanical Compression on Chemical Degradation of Nafion Membranes. *ECS Electrochemistry Letters* **2014**, *3* (5), F33. DOI: 10.1149/2.008405eel.

(66) Hensle, N.; Horstmann de la Viña, J.; Winterholler, N.; Hoffmann, J.; Armbruster, S.; Lindner, A.; Weber, A.; Smolinka, T. Understanding the Cell Performance Along the Channel for Industrial PEM Water Electrolysis Operation. *ACS Applied Energy Materials* **2025**, *8* (11), 7107-7124. DOI: 10.1021/acsaem.5c00505.

(67) Ahmed, K. W.; Jang, M. J.; Park, M. G.; Chen, Z.; Fowler, M. Effect of Components and Operating Conditions on the Performance of PEM Electrolyzers: A Review. In *Electrochem*, 2022; Vol. 3, pp 581-612.

(68) Padgett, E.; Yu, H.; Blair, S. J.; Cullen, D. A.; Ahluwalia, R. K.; Myers, D. J.; Pivovar, B.; Alia, S. M. Quantifying Sources of Voltage Decay in Long-Term Durability Testing for PEM Water Electrolysis. *Journal of The Electrochemical Society* **2025**, *172* (5), 054508. DOI: 10.1149/1945-7111/add184.

(69) Alkhaldi, S.; Aziz, M.; Amrite, A.; Prasad, A. K. Parametric study of PEM water electrolyzer performance. *Journal of Applied Electrochemistry* **2025**, *55* (2), 327-343. DOI: 10.1007/s10800-024-02187-9.

(70) Kuhnert, E.; Heidinger, M.; Sandu, D.; Hacker, V.; Bodner, M. Analysis of PEM Water Electrolyzer Failure Due to Induced Hydrogen Crossover in Catalyst-Coated PFSA Membranes. In *Membranes*, 2023; Vol. 13, p 348.

(71) Choi, Y.; Lee, W.; Na, Y. Effect of Gravity and Various Operating Conditions on Proton Exchange Membrane Water Electrolysis Cell Performance. In *Membranes*, 2021; Vol. 11, p 822.

(72) Beigzadeh Arough, P.; Moranda, A.; Niyati, A.; Paladino, O. Parametric Sensitivity of a PEM Electrolyzer Mathematical Model: Experimental Validation on a Single-Cell Test Bench. In *Energies*, 2025; Vol. 18, p 2217.

(73) Kozlova, M. V.; Moguchikh, E. A.; Alekseenko, A. A.; Pavlets, A. S.; Pankov, I. V.; Aydakov, E. E.; Kaichev, V. V.; Solovyev, M. A.; Pushkareva, I. V.; Bessarabov, D. G.; et al. Ir-based oxygen evolution reaction catalysts: Role of microstructure and activation protocols. *Chemical Engineering Journal* **2025**, *526*, 170888. DOI: https://doi.org/10.1016/j.cej.2025.170888.

(74) Karaca, A.; Galkina, I.; Sohn, Y. J.; Wippermann, K.; Scheepers, F.; Glüsen, A.; Shviro, M.; Müller, M.; Carmo, M.; Stolten, D. Self-Standing, Ultrasonic Spray-Deposited Membranes for Fuel Cells. In *Membranes*, 2023; Vol. 13, p 522.

(75) Park, E. J.; Arges, C. G.; Xu, H.; Kim, Y. S. Membrane Strategies for Water Electrolysis. *ACS Energy Letters* **2022**, *7* (10), 3447-3457. DOI: 10.1021/acsenergylett.2c01609.

(76) Li, H.; Yuan, S.; You, J.; Zhao, C.; Cheng, X.; Luo, L.; Yan, X.; Shen, S.; Zhang, J. Revealing the Oxygen Transport Challenges in Catalyst Layers in Proton Exchange Membrane Fuel Cells and Water Electrolysis. *Nanomicro Lett* **2025**, *17* (1), 225. DOI: 10.1007/s40820-025-01719-y From NLM.

(77) GENNARO, L. Experimental and modelling investigation on degradation of the low temperature electrolyser through Electrochemical Impedance Spectroscopy. POLITECNICO DI TORINO, 2022.

(78) Yue, C.; Zheng, W.; Wang, Q.; Wang, Z.; Li, B.; Zhang, C.; Ming, P. Challenges in membrane electrode assemblies at elevated temperatures for proton exchange membrane fuel cells: a review. *Energy & Environmental Science* **2025**, *18* (14), 6934-6982, 10.1039/D5EE01108F. DOI: 10.1039/D5EE01108F.

(79) Liu, C.; Padgett, E.; Arregui-Mena, J. D.; Shepherd, M.; Ware, S.; Pylypenko, S.; Cullen, D. A.; Bender, G. Performance improvement of proton exchange membrane water electrolysis by surface modification of porous transport layers. *Journal of Power Sources* **2025**, *652*, 237624. DOI: https://doi.org/10.1016/j.jpowsour.2025.237624.

(80) Omrani, R.; Shabani, B. Hydrogen crossover in proton exchange membrane electrolysers: The effect of current density, pressure, temperature, and compression. *Electrochimica Acta* **2021**, *377*, 138085. DOI: https://doi.org/10.1016/j.electacta.2021.138085.

(81) Treutlein, L.; Javed, A.; Wolf, N. L.; Kungl, H.; Karl, A.; Jodat, E.; Eichel, R.-A. Gas Crossover in Membrane Electrolyzers—The Impact of MEA Conditioning on Gas Permeability. *Journal of The Electrochemical Society* **2025**, *172* (6), 064507. DOI: 10.1149/1945-7111/ade00f.

(82) Springer, T. E.; Zawodzinski, T. A.; Gottesfeld, S. Polymer Electrolyte Fuel Cell Model. *Journal of The Electrochemical Society* **1991**, *138* (8), 2334. DOI: 10.1149/1.2085971.

(83) Schalenbach, M.; Hoefner, T.; Paciok, P.; Carmo, M.; Lueke, W.; Stolten, D. Gas Permeation through Nafion. Part 1: Measurements. *The Journal of Physical Chemistry C* **2015**, *119* (45), 25145-25155. DOI: 10.1021/acs.jpcc.5b04155.

(84) Gawas, R.; Kushner, D. I.; Peng, X.; Mukundan, R. Importance of hydrogen oxidation reaction current in quantifying hydrogen crossover in PEM water electrolyzers at high differential pressure. *Energy & Environmental Science* **2025**, *18* (10), 4625-4631, 10.1039/D5EE00048C. DOI: 10.1039/D5EE00048C.

(85) Trinke, P.; Haug, P.; Brauns, J.; Bensmann, B.; Hanke-Rauschenbach, R.; Turek, T. Hydrogen Crossover in PEM and Alkaline Water Electrolysis: Mechanisms, Direct Comparison and Mitigation Strategies. *Journal of The Electrochemical Society* **2018**, *165* (7), F502. DOI: 10.1149/2.0541807jes.

(86) Martin, A.; Trinke, P.; Bensmann, B.; Hanke-Rauschenbach, R. Hydrogen Crossover in PEM Water Electrolysis at Current Densities up to 10 A cm−2. *Journal of The Electrochemical Society* **2022**, *169* (9), 094507. DOI: 10.1149/1945-7111/ac908c.

(87) Carmo, M.; Fritz, D. L.; Mergel, J.; Stolten, D. A comprehensive review on PEM water electrolysis. *International Journal of Hydrogen Energy* **2013**, *38* (12), 4901-4934. DOI: https://doi.org/10.1016/j.ijhydene.2013.01.151.

(88) Toghyani, S.; Fakhradini, S.; Afshari, E.; Baniasadi, E.; Abdollahzadeh Jamalabadi, M. Y.; Safdari Shadloo, M. Optimization of operating parameters of a polymer exchange

membrane electrolyzer. *International Journal of Hydrogen Energy* **2019**, *44* (13), 6403-6414. DOI: https://doi.org/10.1016/j.ijhydene.2019.01.186.

(89) Belkhiri, Z.; Zeroual, M.; Moussa, H.; Bariza, Z. Effect of temperature and water content on the performance of PEM fuel cell. *Journal of Renewable Energies* **2023**, *14*. DOI: 10.54966/jreen.v14i1.246.

(90) Selamet, Ö. F.; Acar, M. C.; Mat, M. D.; Kaplan, Y. Effects of operating parameters on the performance of a high-pressure proton exchange membrane electrolyzer. *International Journal of Energy Research* **2013**, *37* (5), 457-467. DOI: https://doi.org/10.1002/er.2942 (acccessed 2026/01/08).

(91) Kesercioğlu, M. A.; Boyacı San, F. G.; Sözbir, N.; Çay, Y. Performance optimization of PEM electrolyzers: An experimental and Taguchi-based approach. *International Journal of Hydrogen Energy* **2025**, *152*, 150214. DOI: https://doi.org/10.1016/j.ijhydene.2025.150214.

(92) Nur Ozdemir, S.; Taymaz, I.; Okumuş, E.; Gül Boyacı San, F.; Akgün, F. Experimental investigation on performance evaluation of PEM electrolysis cell by using a Taguchi method. *Fuel* **2023**, *344*, 128021. DOI: https://doi.org/10.1016/j.fuel.2023.128021.

(93) Grigoriev, S. A.; Fateev, V. N.; Bessarabov, D. G.; Millet, P. Current status, research trends, and challenges in water electrolysis science and technology. *International Journal of Hydrogen Energy* **2020**, *45* (49), 26036-26058. DOI: https://doi.org/10.1016/j.ijhydene.2020.03.109.

(94) Oberlin, R. S., S.; Christen, H. J. Gas Permeation Through an SPE Membrane During Electrolysis. *Journal of Applied Electrochemistry* **1980**, *10* (1), 97-104.

(95) Bessarabov, D.; Millet, P.; Pollet, B. G. *PEM Water Electrolysis*; Academic Press, 2018.

(96) Trinke, P.; Keeley, G. P.; Carmo, M.; Bensmann, B.; Hanke-Rauschenbach, R. Elucidating the Effect of Mass Transport Resistances on Hydrogen Crossover and Cell Performance in PEM Water Electrolyzers by Varying the Cathode Ionomer Content. *Journal of The Electrochemical Society* **2019**, *166* (8), F465. DOI: 10.1149/2.0171908jes.

(97) Trinke, P. Review on Gas Crossover in Low Temperature Water Electrolysis. In *International Conference on Electrolysis (ICE)*, Freiburg, Germany, 2025.

(98) Kundu, S.; Simon, L. C.; Fowler, M. W. Comparison of two accelerated Nafion™ degradation experiments. *Polymer Degradation and Stability* **2008**, *93* (1), 214-224. DOI: https://doi.org/10.1016/j.polymdegradstab.2007.10.001.

(99) Sakai, T.; Kawami, Y.; Takenaka, H.; Torikai, E.; Wakabayashi, N. Gas permeation properties of solid polymer electrolyte (SPE) membranes. **1985**, *132:6*. DOI: 10.1149/1.2114111

Journal Name: J. Electrochem. Soc.; (United States) Journal Issue: 6 Journal Volume: 132:6.

(100) Kalinnikov, A. A.; Grigoriev, S. A.; Bessarabov, D. G.; Bouzek, K. Two-phase mass transfer in porous transport layers of the electrolysis cell based on a polymer electrolyte membrane: Analysis of the limitations. *Electrochimica Acta* **2021**, *387*, 138541. DOI: https://doi.org/10.1016/j.electacta.2021.138541.

(101) Ghassemzadeh, L. Polymer electrolyte membrane degradation and mobility in fuel cells. **2010**.

(102) Kinumoto, T.; Inaba, M.; Nakayama, Y.; Ogata, K.; Umebayashi, R.; Tasaka, A.; Iriyama, Y.; Abe, T.; Ogumi, Z. Durability of perfluorinated ionomer membrane against hydrogen peroxide. *Journal of Power Sources* **2006**, *158* (2), 1222-1228. DOI: https://doi.org/10.1016/j.jpowsour.2005.10.043.

(103) Gubler, L.; Dockheer, S. M.; Koppenol, W. H. Radical (HO•, H• and HOO•) Formation and Ionomer Degradation in Polymer Electrolyte Fuel Cells. *Journal of The Electrochemical Society* **2011**, *158* (7), B755. DOI: 10.1149/1.3581040.

(104) Wu, J.; Yuan, X. Z.; Martin, J. J.; Wang, H.; Zhang, J.; Shen, J.; Wu, S.; Merida, W. A review of PEM fuel cell durability: Degradation mechanisms and mitigation strategies. *Journal of Power Sources* **2008**, *184* (1), 104-119. DOI: https://doi.org/10.1016/j.jpowsour.2008.06.006.

CHAPTER 5: PROJECT EVALUATION AND FUTURE PROSPECTS

The project evaluation and prospects serve as a tool to determine whether the aim of this study was achieved. The project is evaluated based on the pre-determined objectives set for this study. Thereafter, recommendations for future research are provided as building blocks for the foundation laid by this work.

5.1 Project evaluation

This study aimed to elucidate the impact of chemically induced *ex-situ* Fenton degradation on the subsequent *in-situ* performance of PFSA membranes in a PEMWE system. To achieve this, an *ex-situ* Fenton-based AST was used to probe membrane chemical degradation and link this degradation to *in-situ* electrochemical performance losses. For self-evaluation, the study is assessed against the objectives set out in Section 1.3. Based on these objectives, the following conclusions may be made.

i) Subject Nafion® 115 and 117 membranes to controlled *ex-situ* Fenton degradation under varying Fe^{2+} concentrations and exposure durations, mimicking the accelerated chemical degradation induced by metallic contaminants and reactive radical species encountered during PEMWE operation.

This objective was fully achieved through the methodology presented in Section 3.3. A robust AST matrix was established in which Nafion® 115 and 117 membranes were exposed to Fe^{2+} concentrations of 5, 15, and 30 ppm for 24, 48, and 72 h at 80 °C. The *ex-situ* Fenton protocol successfully produced controlled, graded degradation severity, enabling systematic comparison of membrane chemical and physical changes across the test matrix.

ii) Characterise the alterations in the Nafion® 115 and 117 membranes resulting from the *ex-situ* Fenton degradation, focusing on key properties such as IEC, FRR, SER, surface morphology, and chemical structure alterations.

This objective was comprehensively achieved and is detailed in Section 4.2 through a multi-modal characterisation framework.

The chemical degradation was quantified by IEC loss, which increased with both Fe^{2+} concentration and exposure duration, confirming a dose-dependent response. Importantly, the IEC loss rate ($\%.h^{-1}$) was non-linear and accelerated at longer exposure times, indicating a self-accelerating degradation process, likely due to autocatalytic effects or the formation of new vulnerable sites following initial chain scission.

Effluent analysis of fluoride release and sulfur emission (FRR and SER) produced a key mechanistic result. The measured Fluoride-to-Sulfur (F:S) molar ratio of 18.62:1 in severely

degraded samples exceeded the theoretical 10:1 ratio expected for side-chain-only scission by a factor of 1.8. This provides quantitative evidence that degradation was not limited to sulfonic acid side chains, but also involved substantial main-chain (CF_{bb}) unzipping, which accounted for a large fraction of the material loss.

This dual-degradation mechanism was corroborated by vibrational spectroscopy. NMR and Raman spectroscopy proved highly effective, showing a dose-dependent loss of structural order and the concurrent attenuation of the side-chain S-O peak and main-chain (CF_{bb}) peak. This provided direct spectroscopic evidence for simultaneous side-chain and main-chain degradation. In contrast, ATR FT-IR was found to be insensitive for quantifying degradation under these conditions, as strong IR-active bonds (C-F and S-O) remained detectable even in fragmented material, limiting its utility for tracking structural loss.

Morphological analysis using profilometry further showed that degradation was chemo-mechanical and non-homogeneous. Physical damage, including blistering, pitting, and rupture, originated at pre-existing initiation sites. This was demonstrated by the severe and widespread blistering observed in small, mechanically cut (scalpel) samples, compared with the greater resistance of large, laser cut samples. These observations support a chemo-mechanical degradation pathway in which local mechanical flaws initiate localised chemical attack, leading to a feedback loop of progressive, non-uniform damage and eventual pinhole formation.

iii) Evaluate the *in-situ* electrochemical performance of PEMWE single cells employing Catalyst Coated Membranes (CCMs) fabricated from the pre-degraded Nafion® 115 membranes, assessing parameters including polarisation behaviour, hydrogen gas crossover, and Electrochemical Impedance Spectroscopy (EIS) under relevant operating conditions.

This objective was achieved by fabricating CCMs from the set of large-scale degraded Nafion® 115 membranes (Section 3.5.1), assembling them into PEMWE single cells, and testing them under relevant operating conditions (Section 4.3). The *in-situ* testing framework generated performance metrics needed to evaluate how *ex-situ* chemical degradation translated into electrochemical and transport penalties.

iv) Establish a correlation between the extent of *ex-situ* Fenton degradation, as determined by changes in membrane properties, and the resulting *in-situ* PEMWE performance metrics.

This objective was successfully addressed through the correlative analysis in Section 4.4, which bridged *ex-situ* degradation benchmarking and *in-situ* operational decay.

A clear linear relationship was observed between *ex-situ* IEC loss and the increase in *in-situ* ohmic resistance (R_Ω), quantitatively confirming that radical-induced scission of sulfonic acid groups directly translates to reduced proton conductivity. In addition, cumulative FRR served as a predictor of voltage penalties, with higher fluoride release corresponding to progressively larger increases in cell potential, reaching up to 107 mV at 75 °C for the most severely degraded membrane.

By contrast, hydrogen crossover showed a non-linear response to degradation. At low-to-moderate degradation levels, crossover trends followed Fickian expectations (increased flux with membrane thinning). However, at severe degradation (30 ppm Fe^{2+}), hydrogen crossover was unexpectedly suppressed. This was attributed to the structural collapse of hydrophilic ionic clusters, which hindered gas transport despite ongoing polymer mass loss. This finding demonstrates that severe chemical degradation cannot be interpreted solely as membrane thinning and that nanoscale morphological collapse must also be considered.

Overall, the study successfully achieved its overarching aim of elucidating how chemically induced *ex-situ* Fenton degradation impacts subsequent *in-situ* PEMWE membrane performance. The work established that PFSA membrane degradation under the applied AST conditions is dose-dependent, self-accelerating, and mechanistically dual in nature (side-chain and main-chain scission). It further demonstrated that degradation is chemo-mechanical, non-homogeneous, and strongly influenced by pre-existing mechanical defects. Most importantly, the study successfully linked *ex-situ* degradation metrics (IEC loss and FRR) to *in-situ* PEMWE performance losses (ohmic resistance and voltage penalty), thereby addressing an important gap between *ex-situ* chemical benchmarking and functional PEMWE performance decay.

5.2 Limitations Of The Study

While the study successfully achieved its objectives, the findings should be interpreted in the context of the methodological limitations. These limitations define the scope of the conclusions and provide a framework for future work.

5.2.1 The *Ex-Situ* Versus *In-Operando* Gap

The most significant limitation is the use of an *ex-situ* chemical bath (Fenton test) to simulate degradation in a functioning electrochemical device. Although the Fenton test is a powerful chemical proxy for radical attack, it does not replicate the full stress environment of an operating PEMWE, where chemical, electrochemical, mechanical, and thermal factors act simultaneously.

5.2.2 Aggressiveness and Mechanism of the AST

The AST conditions were intentionally severe to accelerate degradation, but this severity may activate degradation pathways that are not fully representative of long-term field operation.

The use of 30 wt% H_2O_2 and Fe^{2+} concentrations up to 30 ppm generates a highly aggressive radical environment. Under these conditions, substantial main-chain scission was observed, as evidenced by the ~18.6:1 F:S molar ratio. While this is a critical mechanistic finding, it remains uncertain whether main-chain unzipping is the dominant degradation mode under realistic PEMWE contamination levels (e.g., ppb-level Fe^{2+}), or whether side-chain scission would dominate over long operational lifetimes (e.g., ~20 000 h).

In addition, the study focused exclusively on Fe^{2+} as the contaminant species. This choice was justified because Fe^{2+} is widely reported as a highly catalytic cation for radical generation. However, practical PEMWE systems are more likely to be exposed to mixed contamination (e.g., Cu^{2+}, Ni^{2+}, Ca^{2+}, and other ions from feedwater and corrosion products). As such, the current study does not capture potential synergistic or antagonistic effects that may arise in multi-cation environments.

5.2.3 Scope of Materials and *In-Situ* Testing

The membrane materials investigated were unreinforced, relatively thick Nafion® 115 and 117 membranes. While these are well-established benchmark materials, they are not fully representative of the thin, mechanically reinforced composite membranes (e.g., ePTFE-reinforced PFSA membranes) used in modern commercial electrolysers. Consequently, some of the physical failure modes observed here, particularly blistering, pitting, and rupture, may not manifest in the same way in reinforced membranes designed to resist such mechanical damage.

The *in-situ* validation was also limited to single cell PEMWE testing. Although this was sufficient to establish correlations between *ex-situ* degradation and key *in-situ* metrics, it does not capture stack-level effects such as non-uniform compression, uneven flow distribution, or current-density gradients across multiple cells. These stack-scale factors may generate localised degradation hotspots that are not reproduced in a laboratory single cell setup.

5.3 Recommendations for Future Research

Based on the achievements and limitations of this study, the following recommendations are proposed to extend the work and strengthen its relevance to practical PEMWE operation.

5.3.1 Development of an In-Operando Contamination AST

A next possible step is to bridge the *ex-situ/in-operando* gap by introducing Fe^{2+} and other contaminants directly into the anode feedwater of an operating PEMWE single cell. This would allow degradation to be studied under simultaneous electrochemical, chemical, and mechanical stresses. By testing under different operational profiles (e.g., constant load, dynamic cycling, and OCV), the impact of contamination on in-operando membrane degradation could be quantified and compared directly with the *ex-situ* AST results established in this work.

5.3.2 Investigation of Contaminant Synergies

To address the single-contaminant limitation, the *ex-situ* Fenton AST protocol developed here should be extended to mixed-contaminant systems. Experimental matrices incorporating Fe^{2+} with other common cations (e.g., Cu^{2+}, Ni^{2+}, Ca^{2+}) would provide a more realistic assessment of membrane degradation in practical environments and could reveal synergistic or antagonistic effects not captured in single-cation studies.

5.3.3 Mapping Degradation Mechanisms at Realistic Contaminant Concentrations

The observed main-chain scission (high F:S ratio) is mechanistically significant, but its relevance under realistic PEMWE operating conditions remains uncertain. Long-duration studies using much lower Fe^{2+} concentrations (e.g., <1 ppm and into the ppb range) are required. By monitoring effluent chemistry (F:S ratio) together with membrane IEC loss over extended test periods, future work can determine whether a concentration threshold exists where the dominant degradation mechanism shifts from side-chain-only scission (functional failure) to main-chain unzipping (mechanical failure).

5.3.4 Evaluation of Modern Reinforced Membranes

The full experimental framework developed in this dissertation, from *ex-situ* AST through *in-situ* correlation, should be repeated using state-of-the-art, thin, mechanically reinforced composite membranes. This is important to determine: whether reinforcement (e.g., ePTFE) mitigates the chemo-mechanical failure modes (blistering, pitting, rupturing) identified in this study; and how ionomer degradation within a reinforcement matrix affects *in-situ* PEMWE performance, which may differ substantially from degradation behaviour in bulk, unreinforced PFSA films.

5.3.5 Study of Chemical Mitigation Strategies

This study focused on degradation mechanisms and their consequences. A logical extension is to evaluate mitigation strategies. Radical scavengers such as cerium and

manganese based additives are widely reported as effective stabilisers against radical-induced attack. Future work could therefore investigate the incorporation of CeO_2 nanoparticles into the membrane as a stabilising additive, and/or the addition of Ce^{3+} ions to the Fenton reagent bath as a chemical mitigant.

Repeating the AST under these modified conditions would allow direct quantification of mitigation effectiveness in terms of reduced IEC loss, lower FRR, and improved retention of membrane integrity.

5.3.6 Advanced *In-Situ* Diagnostics

The *in-situ* analysis in this work relied primarily on bulk electrochemical measurements (EIS and polarisation), which were effective for performance correlation but do not directly resolve evolving membrane morphology. Future studies should incorporate advanced *in-operando* diagnostics, such as X-ray Computed Tomography (X-ray CT), to non-destructively visualise membrane damage within an operating PEMWE cell. This would enable real-time, three-dimensional tracking of blister, pinhole, and crack formation and provide direct validation of the post-mortem morphological trends identified in this study.

CHAPTER 6: ANNEXURE

6.1 Annexure A: *Ex-situ* analysis

6.1.1 IEC Loss

Table 15: IEC loss at varying Fe^{2+} concentration and duration for small-scale 4 cm^2 samples.

Fe^{2+} Concentration ppm	Duration h	Total IEC loss (%)	IEC loss rate (%.h^{-1})	IEC loss rate (×10^{-2} %.h^{-1}.cm^{-2})
5	24	0.453 (±0.047)	0.052	1.297
	48	5.835 (±1.905)	0.122	3.039
	72	14.995 (±1.480)	0.208	5.207
15	24	2.459 (±0.970)	0.082	2.054
	48	6.653 (±1.741)	0.139	3.465
	72	19.996 (±0.948)	0.278	6.943
30	24	6.091 (±0.973)	0.116	2.897
	48	8.353 (±0.475)	0.174	4.351
	72	27.266 (±2.650)	0.379	9.467

Table 16: IEC loss at varying Fe^{2+} concentration and duration for large-scale 336.44 cm^2 samples.

Fe^{2+} Concentration ppm	Duration h	Total IEC loss (%)	IEC loss rate (×10^{-2} %.h^{-1})	IEC loss rate (×10^{-4} %.h^{-1}.cm^{-2})
5	24	0.406 (±0.012)	0.17	5.03
	48	2.24 (±0.447)	0.47	13.86
	72	6.33 (±1.122)	0.87	26.13
15	24	1.90 (±0.938)	0.79	23.58
	48	4.55 (±0.227)	0.94	28.15
	72	8.37 (±0.669)	1.16	34.56
30	24	3.31 (±0.832)	1.38	40.96
	48	7.33 (±0.469)	1.53	45.42
	72	12.29 (±1.64)	1.71	50.74

6.1.2 Fluoride Release Rate (FRR)

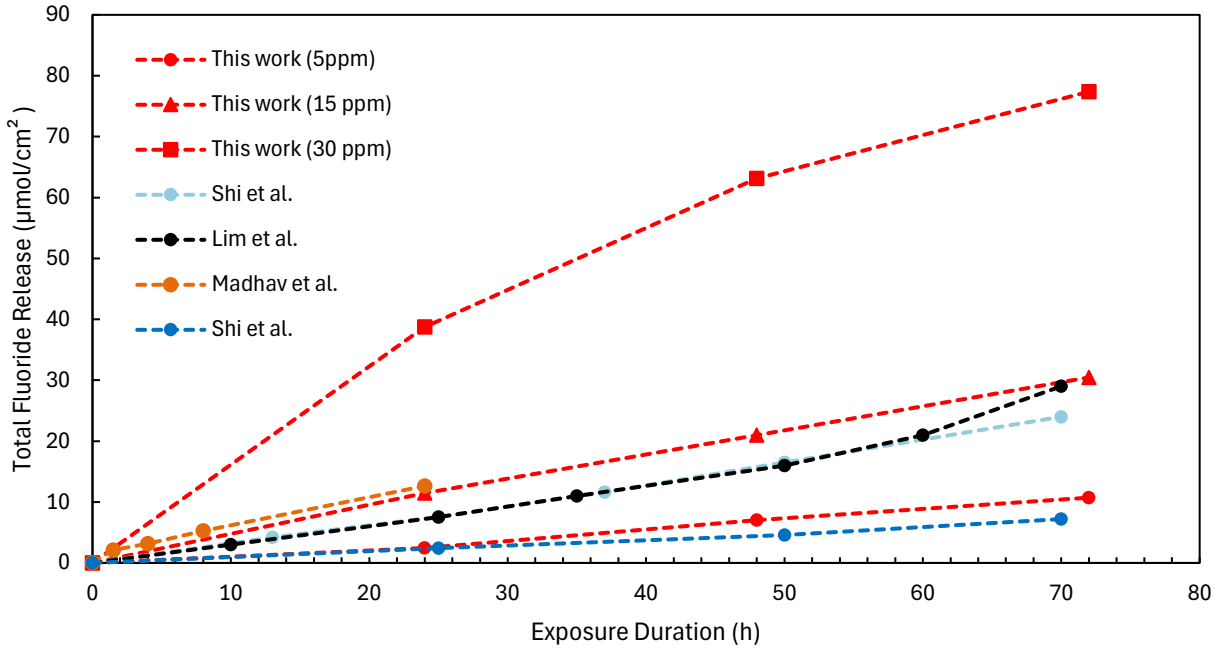
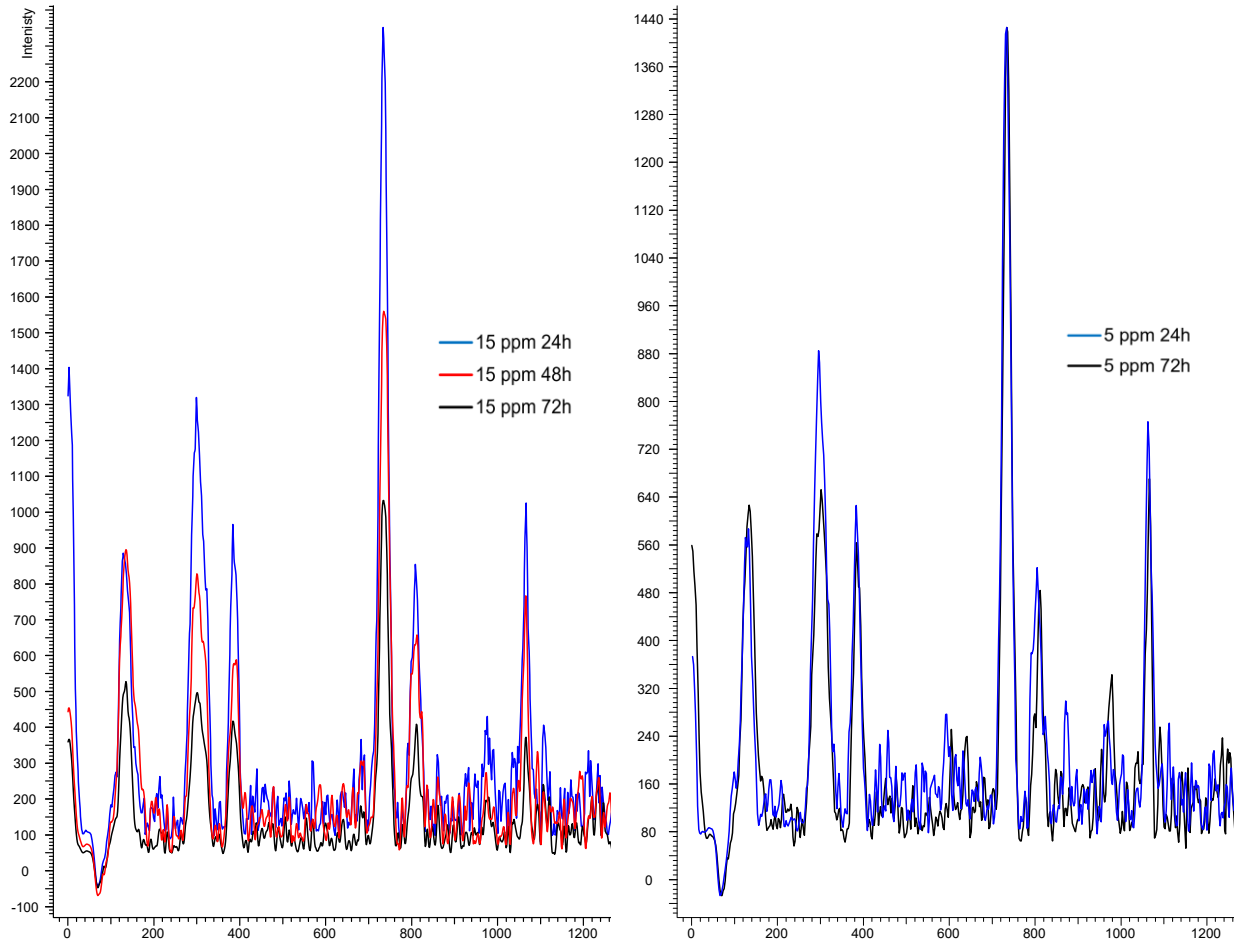


Figure 56: Comparative figure of previous studies of total fluoride release in terms of *ex-situ* Fenton test duration. This line graph compares the total fluoride release (µmol.cm^{-2}) of all samples done in this study with previous works.

6.1.3 Raman



a) b)

Figure 57: Raman spectrum of Fenton degraded Nafion® 117 at variable duration in the spectral range of 0-1340(cm^{-1}) This Figure overlays the Raman spectra for samples degraded at (15 ppm a) and 5 ppm b)

6.2 Annexure B: Programmed Break-In Script and I*n-Situ* Analysis

6.2.1 Automated Break-In Script

Table 17: Table of automation breaking-in script with comments

Row	Script	Comment
1	SET_STRING scattergraph_file_path "C:\Greenlight Innovation Datalogs\HySA CCMS\2025\Jason\N115_B(variable)\Breaking In\Automated\	Set File location
2	STEP_TIME 250 msec	
3	SET_VALUE anode_inlet_neartemp = 60	Set Anode Inlet Temp to 60 °C
4	SET pump_anode_dewpoint_on On 0.00	Activate the Anode Dewpoint pump
5	SET system.state_set PS-CTRL 1.00	Power Supply Control
6	SET Current_Adj 5.5 A 0.00	Initialise Current at 5.5 A
7	SET mode_set Current 1.00	Set Galvanostatic Mode
8	WAIT 5 sec	
9	DATALOG_CONFIG Default-Data-logger TEST_NAME = scattergraph_file_path; USER_NAME = "Jason"; TEST_COMMENT = "Test"; LOG_PERIOD = 10000 ms; END_CONFIG	Configuration of the datalogger
10	DATALOG_START Default-Data-logger	Start data logging
11		
12	**LABEL RAMP_UP**	Define Loop
13	IF (data_cell_001 > 2 V) THEN	
14	JUMP TOTAL_SHUTDOWN	Safety shutdown at >2V
15	END_IF	
16	IF (data_cell_001 >= 1.85 V) THEN	Define upper potential limit
17	JUMP RAMP_DOWN	
18	END_IF	Termination of the IF variable
19	MOD Current_Adj 0.1 A 0.00	Increase current by 0.1 A
20	WAIT 1 sec	Waiting period of 1s
21	IF (data_cell_001 < 1.85 V) THEN	Define the lower potential limit
22	JUMP RAMP_UP	
23	END_IF	Termination of the IF variable
24		
25	**LABEL RAMP_DOWN**	Define Loop
26	IF (data_cell_001 > 2 V) THEN	
27	JUMP TOTAL_SHUTDOWN	Safety shutdown at >2V
28	END_IF	
29	IF (data_cell_001 >= 1.851 V) THEN	Define Upper limit
30	MOD Current_Adj -0.1 A 0.00	Decrease current by 0.1 A
31	WAIT 1 sec	Waiting period of 1s
32	END_IF	Termination of the IF variable
33	IF (data_cell_001 <= 1.84 V) THEN	Define the lower potential limit
34	JUMP RAMP_UP	
35	END_IF	Termination of the IF variable
36	JUMP RAMP_DOWN	
37		
38	**LABEL TOTAL_SHUTDOWN**	Define Loop
39	SET Current_Adj 0 A 0.00	Cut current to 0 A (Safety Zero)
40	SET_VALUE temp_anode_inlet_set = 0 °C	Turn off heating (Set setpoint to 0 °C)
41	SET system.state_set SETUP 1.00	Return system state to SETUP/Standby mode
42	SET pump_anode_dewpoint_on Off 0.00	Deactivate the Anode Dewpoint pump
44	DATALOG_STOP Default-Data-logger	Stop data recording
45	END	End of Script

6.2.2 Virgin CCM Polarisation Data

Table 18: Baseline parameters for virgin non-degraded PEMWE cells.

Temperature (°C)	Current density ($mA.cm^{-2}$)	Potential (V)	Standard deviation (10^{-3})	Hydrogen Crossover (vol%)
40	0.1	1.56	9.25	-
	0.2	1.60	8.75	-
	0.3	1.64	8.50	-
	0.35	-	-	0.27
	0.4	1.67	8.50	1.42
	0.5	1.70	7.50	-
	0.6	1.73	6.75	-
	0.7	1.76	5.50	1.93
	0.8	1.78	4.75	-
	0.9	1.81	3.50	-
	1.0	1.84	1.75	-
	1.1	1.87	1.00	-
	1.2	1.90	4.50	-
	1.3	1.91	8.50	-
60	0.1	1.52	7.72	-
	0.2	1.56	8.83	-
	0.3	1.59	8.50	-
	0.4	1.62	8.73	-
	0.5	1.65	8.50	-
	0.6	1.68	8.38	-
	0.7	1.70	7.72	1.55
	0.8	1.72	7.13	-
	0.9	1.75	7.12	-
	1	1.77	6.13	-
	1.1	1.79	5.44	-
	1.2	1.82	5.31	-
	1.3	1.84	5.56	-
	1.4	1.86	7.32	-
	1.5	1.89	10.08	-
	1.6	1.90	11.08	-
75	0.1	1.50	7.07	-
	0.2	1.53	7.59	-
	0.3	1.56	8.81	-
	0.4	1.59	2.00	-
	0.5	1.61	2.00	-
	0.6	1.64	3.00	-
	0.7	1.66	2.00	1.27
	0.8	1.68	2.00	-
	0.9	1.70	1.50	-
	1	1.72	0.00	-
	1.1	1.74	1.00	-
	1.2	1.76	0.50	-
	1.3	1.78	1.00	-
	1.4	1.80	2.50	-
	1.5	1.82	4.50	-
	1.6	1.84	5.50	-
	1.7	1.86	8.00	-
	1.8	1.88	11.50	-
	1.9	1.90	14.00	-

6.2.3 Degraded CCM Polarisation Data

Table 19: Table of Polarisation results at 40, 60 and 75 °C for large-scale membranes

Fe^{2+} conc. (ppm)		Ref	5			15			30		
Duration (h)		0	24	48	72	24	48	72	24	48	72
Temp	*j* ($mA.cm^{-2}$)		Potential response (V)								
40	0.1	1.560	1.605	1.588	1.586	1.571	1.586	1.576	1.579	1.590	1.609
	0.2	1.603	1.649	1.631	1.631	1.617	1.631	1.617	1.621	1.638	1.653
	0.3	1.637	1.683	1.666	1.666	1.655	1.667	1.653	1.655	1.677	1.689
	0.4	1.668	1.715	1.698	1.700	1.689	1.700	1.683	1.686	1.717	1.725
	0.5	1.698	1.744	1.728	1.732	1.720	1.731	1.714	1.714	1.758	1.769
	0.6	1.727	1.772	1.757	1.762	1.750	1.762	1.746	1.741	1.804	1.816
	0.7	1.755	1.797	1.785	1.790	1.778	1.793	1.777	1.769	1.863	1.877
	0.8	1.783	1.822	1.814	1.817	1.807	1.823	1.809	1.794	1.940	1.951
	0.9	1.810	1.846	1.844	1.845	1.835	1.855	1.842	1.821		
	1	1.837		1.874	1.872	1.863	1.886	1.880	1.848		
	1.1	1.866		1.906	1.900	1.884	1.918	1.922	1.874		
	1.2	1.896		1.940		1.891		1.971	1.900		
	1.3	1.914				1.917			1.926		
60	0.1	1.521	1.559	1.525	1.536	1.537	1.535	1.527	1.522	1.543	1.561
	0.2	1.562	1.604	1.563	1.577	1.580	1.575	1.565	1.561	1.586	1.6
	0.3	1.594	1.636	1.593	1.610	1.613	1.608	1.597	1.592	1.621	1.633
	0.4	1.623	1.665	1.621	1.640	1.644	1.636	1.629	1.621	1.654	1.665
	0.5	1.650	1.691	1.648	1.669	1.672	1.664	1.656	1.647	1.687	1.698
	0.6	1.675	1.716	1.673	1.696	1.698	1.690	1.682	1.673	1.721	1.731
	0.7	1.700	1.739	1.698	1.721	1.724	1.716	1.710	1.697	1.756	1.769
	0.8	1.724	1.761	1.723	1.745	1.748	1.742	1.737	1.721	1.794	1.813
	0.9	1.747	1.782	1.746	1.768	1.772	1.767	1.764	1.744	1.838	1.859
	1	1.770	1.803	1.769	1.790	1.795	1.793	1.791	1.767	1.892	1.911
	1.1	1.793	1.823	1.792	1.813	1.819	1.818	1.819	1.790	1.943	1.964
	1.2	1.816	1.842	1.816	1.835	1.842	1.844	1.851	1.812		
	1.3	1.839	1.861	1.838	1.855	1.866	1.871	1.885	1.835		
	1.4	1.863		1.862	1.878	1.890	1.897	1.925	1.857		
	1.5	1.887		1.886	1.899	1.909			1.880		
	1.6	1.904		1.910	1.913				1.902		
75	0.1	1.495	1.524	1.500	1.500	1.495	1.503	1.496	1.4943	1.506	1.532
	0.2	1.534	1.567	1.536	1.540	1.535	1.540	1.532	1.5277	1.545	1.571
	0.3	1.564	1.596	1.578	1.572	1.567	1.569	1.562	1.5540	1.577	1.602
	0.4	1.590	1.624	1.604	1.599	1.595	1.594	1.588	1.5783	1.606	1.629
	0.5	1.614	1.647	1.628	1.625	1.621	1.618	1.612	1.6007	1.635	1.658
	0.6	1.637	1.670	1.651	1.648	1.645	1.641	1.636	1.6223	1.664	1.685
	0.7	1.659	1.692	1.672	1.671	1.669	1.662	1.659	1.6433	1.692	1.712
	0.8	1.680	1.713	1.695	1.693	1.691	1.683	1.681	1.6640	1.722	1.742
	0.9	1.702	1.732	1.718	1.714	1.713	1.705	1.704	1.6840	1.753	1.774
	1	1.722	1.751	1.739	1.735	1.734	1.725	1.726	1.7037	1.786	1.812
	1.1	1.743	1.770	1.759	1.754	1.755	1.747	1.748	1.7237	1.823	1.85
	1.2	1.763	1.788	1.779	1.773	1.776	1.768	1.770	1.7420	1.865	1.892
	1.3	1.782	1.805	1.789	1.792	1.795	1.789	1.792	1.7623	1.912	1.935
	1.4	1.802	1.823	1.810	1.812	1.816	1.811	1.814	1.7807		
	1.5	1.821	1.839	1.830	1.830	1.836	1.833	1.837	1.7997		
	1.6	1.840	1.855	1.851	1.849	1.855	1.854	1.861	1.8193		
	1.7	1.859	1.872	1.872	1.868	1.876	1.876	1.886	1.8373		
	1.8	1.880		1.893	1.886	1.896	1.898	1.912	1.8553		
	1.9	1.900		1.914	1.904	1.914	1.920	1.939	1.8740		

Table 20: Average potential difference in mV vs reference data at each datapoint with standard deviations shown. Negative values are representative of a performance improvement when compared to the reference cell. Data based on 3 repeats

Fe^{2+} concentration (ppm)	Duration (h)	Temperature (°C)		
		40	**60**	**75**
5	**24**	12.67 (±0.004)	10.87 (±0.003)	6.06 (±0.004)
	48	32.79 (±0.004)	-0.17 (±0.002)	12.11 (±0.004)
	72	32.80 (±0.003)	17.46 (±0.003)	9.55 (±0.002)
15	**24**	20.77 (±0.004)	23.14 (±0.003)	10.46 (±0.005)
	48	37.32 (±0.008)	19.87 (±0.007)	8.03 (±0.006)
	72	25.23 (±0.012)	18.83 (±0.017)	9.03 (±0.012)
30	**24**	13.08 (±0.004)	-2.95 (±0.001)	-16.68 (±0.006)
	48	69.67 (±0.041)	61.59 (±0.040)	46.29 (±0.036)
	72	82.50 (±0.040)	77.03 (±0.044)	70.04 (±0.037)

Table 21: Potential difference in mV at 1.85V vs reference data with standard deviations Negative values are representative of a performance improvement when compared to the reference cell. Data based on 3 repeats

Fe^{2+} concentration (ppm)	Duration (h)	Temperature (°C)		
		40	**60**	**75**
5	**24**	14.00 (±0.015)	6.33 (±0.000)	-0.50 (±0.007)
	48	34.00 (±0.017)	-0.67 (±0.005)	11.00 (±0.000)
	72	35.33 (±0.001)	16.00 (±0.004)	9.50 (±0.000)
15	**24**	26.50 (±0.019)	26.33 (±0.006)	15.83 (±0.001)
	48	45.00 (±0.000)	28.33 (±0.010)	14.50 (±0.004)
	72	32.00 (±0.001)	35.33 (±0.009)	21.50 (±0.005)
30	**24**	11.50 (±0.007)	-5.67 (±0.010)	-24.17 (±0.004)
	48	108.00 (±0.005)	90.67 (±0.009)	102.17 (±0.013)
	72	141.33 (±0.003)	112.00 (±0.019)	107.00 (±0.012)

6.2.4 Degraded CCM Electrochemical Impedance (EIS) Data

Table 22: EIS data for degraded CCMs at j=0.1 A.cm^{-2}

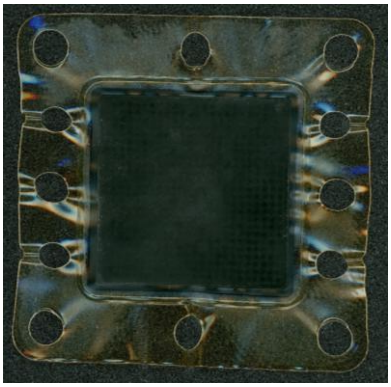
	Fe^{2+} conc. (ppm)	5			15			30		
	Duration (h)	**24**	**48**	**72**	**24**	**48**	**72**	**24**	**48**	**72**
40 C	**Capacitance (F)**	1.54	2.68	2.30	2.34	2.05	2.70	4.23	2.21	1.56
	τ_1 (s)	0.01	0.01	0.01	0.01	0.01	0.01	0.02	0.01	0.01
	f_1 (Hz)	18.74	11.64	11.89	11.49	15.42	12.06	7.34	12.88	20.45
	R_Ω (mΩ.cm^2)	202.69	195.20	198.94	200.90	202.46	200.31	209.32	215.11	219.89
	R_{ct} (mΩ.cm^2)	308.19	285.60	326.10	331.38	281.42	273.80	287.44	313.07	279.17
60 C	**Capacitance (F)**	1.74	3.30	2.05	2.29	2.39	2.57	4.88	2.25	1.69
	τ_1 (s)	0.01	0.02	0.01	0.01	0.01	0.01	0.03	0.01	0.01
	f_1 (Hz)	16.43	9.73	12.73	11.56	13.30	12.28	6.34	12.60	19.15
	R_Ω (mΩ.cm^2)	169.50	161.22	172.12	169.61	163.55	170.07	171.86	182.65	177.43
	R_{ct} (mΩ.cm^2)	311.08	277.76	341.28	336.69	280.37	282.09	288.58	314.34	275.87
75 C	**Capacitance (F)**	2.09	3.67	1.96	2.23	2.44	2.76	5.12	2.24	1.74
	τ_1 (s)	0.01	0.02	0.01	0.01	0.01	0.01	0.03	0.01	0.01
	f_1 (Hz)	12.93	8.57	12.87	11.59	12.46	10.99	5.80	12.35	18.08
	R_Ω (mΩ.cm^2)	150.79	143.20	155.77	151.23	146.05	148.03	145.93	161.05	151.58
	R_{ct} (mΩ.cm^2)	330.21	283.54	353.63	345.66	293.17	294.40	300.06	321.90	283.10

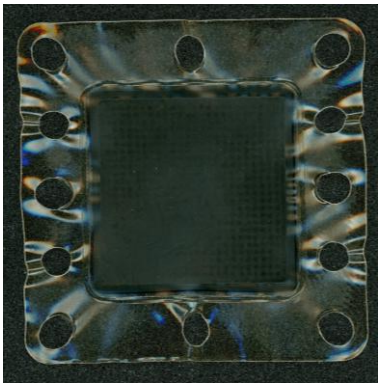
Table 23: EIS data for degraded CCMs at j=0.5 A.cm^{-2}

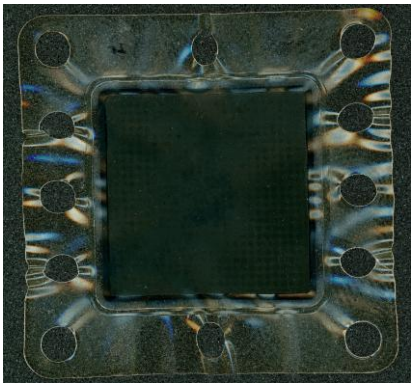
	Fe^{2+} conc. (ppm)	5			15			30		
	Duration (h)	**24**	**48**	**72**	**24**	**48**	**72**	**24**	**48**	**72**
40 C	**Capacitance1 (F)**	1.49	2.44	1.69	1.81	2.08	2.73	3.98	1.89	1.66
	Capacitance2 (F)	31677.83	913.55	3472.55	2229.00	784.22	1244.41	1053.88	435.12	512.39
	τ_1 (s)	0.00	0.00	0.00	0.00	0.00	0.00	0.00	0.00	0.00
	τ_2 (s)	70.92	0.71	1.49	1.35	0.64	1.49	0.52	1.13	0.84
	f_1 (Hz)	105.85	63.77	65.34	65.12	76.89	61.97	37.48	76.11	116.63
	f_2 (Hz)	0.00	0.22	0.11	0.12	0.25	0.11	0.30	0.14	0.19
	R_Ω (mΩ.cm^2)	193.37	199.54	200.97	205.41	210.87	211.32	212.85	239.95	239.43
	R_{ct} (mΩ.cm^2)	56.63	57.27	80.60	75.74	55.82	52.71	59.80	62.05	45.97
	R_{mt} (mΩ.cm^2)	125.37	43.63	23.99	33.92	45.44	66.93	27.84	144.95	92.03
60 C	**Capacitance1 (F)**	1.33	2.66	1.39	1.81	2.25	2.45	4.16	2.33	1.70
	Capacitance2 (F)	2997.08	1596.12	4664.49	3268.16	915.70	1875.73	1195.18	798.12	486.35
	τ_1 (s)	0.00	0.00	0.00	0.00	0.00	0.00	0.00	0.00	0.00
	τ_2 (s)	2.07	0.77	1.37	1.28	0.47	1.39	0.48	1.61	0.48
	f_1 (Hz)	99.40	56.88	76.79	63.02	69.63	65.88	36.00	74.06	103.85
	f_2 (Hz)	0.08	0.21	0.12	0.12	0.34	0.11	0.33	0.10	0.33
	R_Ω (mΩ.cm^2)	169.25	164.57	171.61	169.31	170.18	153.24	152.95	171.58	164.80
	R_{ct} (mΩ.cm^2)	67.52	58.91	83.52	78.13	56.85	48.41	52.11	45.20	44.26
	R_{mt} (mΩ.cm^2)	38.64	26.90	16.40	21.91	28.91	36.39	19.85	98.84	47.98
75 C	**Capacitance1 (F)**	1.60	2.85	1.35	1.73	2.32	2.51	4.42	2.26	1.77
	Capacitance2 (F)	430.18	1291.88	4856.82	3338.76	650.20	1191.03	630.49	873.44	415.92
	τ_1 (s)	0.00	0.00	0.00	0.00	0.00	0.00	0.00	0.00	0.00
	τ_2 (s)	0.24	0.56	1.41	1.17	0.30	0.71	0.26	1.26	0.34
	f_1 (Hz)	86.43	52.97	78.41	64.95	67.93	63.46	34.32	69.84	99.08
	f_2 (Hz)	0.66	0.28	0.11	0.14	0.53	0.23	0.62	0.13	0.47
	R_Ω (mΩ.cm^2)	150.41	146.90	153.54	151.67	149.73	134.55	127.67	149.05	137.45
	R_{ct} (mΩ.cm^2)	64.44	59.03	84.16	79.18	56.55	48.89	51.43	49.49	44.54
	R_{mt} (mΩ.cm^2)	31.54	24.46	16.23	19.55	25.86	29.05	19.92	70.46	40.09

6.2.5 Post-Mortem Imaging

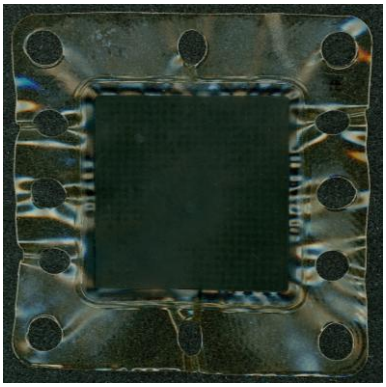
5 ppm

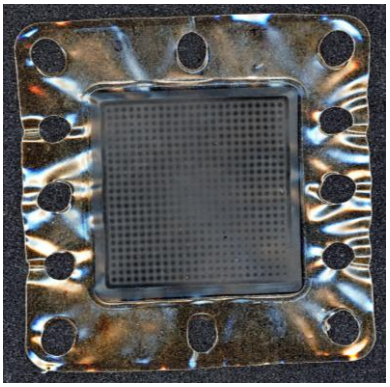

24h


48h


72h

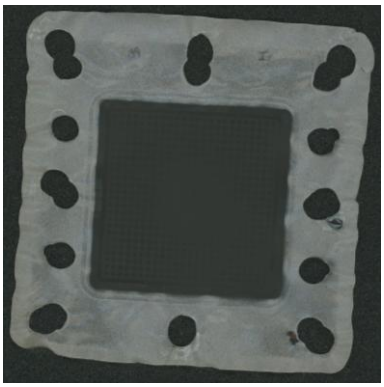
15 ppm

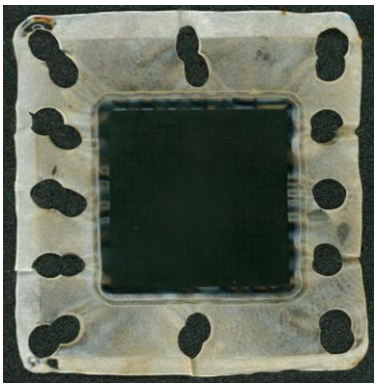

24h

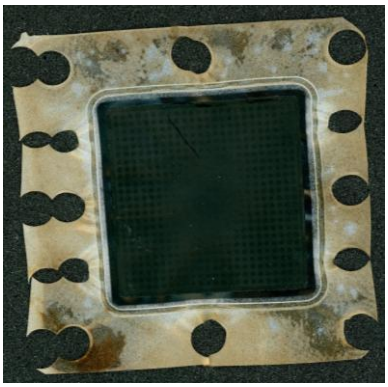

48h


72h

30 ppm


24h


48h


72h

6.3 Annexure C: Membrane Physical Parameters and Experimental Conditions

Table 24: Parameters for large-scale Nafion® 115 virgin membranes and their corresponding experimental conditions								Exp conditions	
Sample	**Wet Mass (g)**	**Dry Mass (g)**	**Water mass (g)**	**WU (%)**	**Hydration number (λ)**	**EW**	**IEC (meq/g)**	**Fe (ppm)**	**Duration (h)**
LN115_BA	4.927	3.981	0.947	23.777	13.87	1050.594	0.952	30	24
LN115_BB	5.228	4.239	0.989	23.325	14.249	1100.234	0.909	0	48
LN115_BC	5.161	4.12	1.042	25.284	15.652	1114.912	0.897	5	24
LN115_BD	5.03	4.012	1.018	25.366	14.181	1006.876	0.993	5	72
LN115_BE	5.208	4.089	1.119	27.376	15.694	1032.449	0.969	15	24
LN115_BF	4.464	3.979	0.485	12.201	8.138	1201.208	0.832	5	24
LN115_BG	5.301	4.229	1.072	25.337	15.866	1127.733	0.887	15	72
LN115_BH	4.858	3.887	0.972	24.995	15.443	1112.711	0.899	15	48
LN115_BI	4.898	3.961	0.936	23.634	15.067	1148.203	0.871	30	72
LN115_BJ	4.953	3.951	1.002	25.372	15.912	1129.471	0.885	30	48
LN115_BK	5.105	4.076	1.03	25.262	15.409	1098.571	0.91	5	48
LN115_BL	5.226	4.172	1.054	25.273	16.485	1174.715	0.851	15	72
LN115_BM	4.954	3.924	1.03	26.238	16.611	1140.2	0.877	15	48
LN115_BN	5.039	3.943	1.096	27.805	17.083	1106.5	0.904	30	72
LN115_BO	5.024	3.918	1.106	28.232	17.779	1134.17	0.882	30	48

Table 25: Parameters for small-scale Nafion® 117 virgin membranes and their corresponding experimental conditions

Sample	Wet Mass (g)	Dry Mass (g)	Water mass(g)	WU (%)	HN (λ)	EW	IEC (meq/g)	Exp conditions	
								Fe (ppm)	Duration (h)
N117_BA	0.163	0.131	0.032	24.068	14.130	1057.384	0.946	10	24
N117_BB	0.168	0.132	0.036	27.398	16.356	1075.173	0.930	15	24
N117_BC	0.168	0.138	0.030	21.916	13.024	1070.291	0.934	30	24
N117_BD	0.162	0.130	0.032	24.981	15.911	1147.080	0.872	30	72
N117_BE	0.162	0.131	0.031	23.457	11.189	859.051	1.164	30	48
N117_BF	0.162	0.131	0.031	23.523	15.345	1174.916	0.851	5	24
N117_BG	0.144	0.131	0.013	9.547	5.931	1118.723	0.894	5	72
N117_BH	0.155	0.128	0.027	20.886	12.888	1111.333	0.900	5	48
N117_BI	0.155	0.132	0.023	17.123	10.917	1148.286	0.871	15	48
N117_BJ	0.152	0.132	0.020	15.099	9.670	1153.362	0.867	5	72
N117_BK	0.147	0.127	0.020	15.539	10.188	1180.789	0.847	10	24
N117_BL	0.161	0.139	0.022	15.936	9.694	1095.621	0.913	30	72
N117_BM	0.162	0.133	0.029	21.549	13.084	1093.579	0.914	10	48
N117_BN	0.165	0.134	0.031	23.521	14.738	1128.448	0.886	10	72
N117_BO	0.159	0.129	0.030	22.808	14.029	1107.765	0.903	15	72
N117_BP	0.161	0.134	0.027	20.266	12.834	1140.532	0.877	30	48
N117_BQ	0.158	0.131	0.027	21.054	14.549	1244.529	0.804	5	24
N117_BR	0.160	0.130	0.030	22.831	14.024	1106.242	0.904	30	24
N117_BS	0.160	0.130	0.030	23.533	14.342	1097.627	0.911	15	24
N117_BT	0.167	0.136	0.031	22.605	13.985	1114.192	0.898	30	48
N117_BU	0.165	0.136	0.029	21.440	14.621	1228.203	0.814	10	48
N117_BV	0.167	0.135	0.032	23.475	13.679	1049.467	0.953	5	72
N117_BW	0.155	0.133	0.021	16.074	10.097	1131.269	0.884	5	48
N117_BX	0.160	0.134	0.026	19.421	12.179	1129.442	0.885	30	24
N117_BY	0.162	0.131	0.030	23.199	13.937	1081.979	0.924	30	72

Table 25: Parameters for small-scale Nafion® 117 virgin membranes and their corresponding experimental conditions

Sample	Wet Mass (g)	Dry Mass (g)	Water mass(g)	WU (%)	HN (λ)	EW	IEC (meq/g)	Exp conditions	
								Fe (ppm)	Duration (h)
N117_BZ	0.159	0.131	0.028	21.129	11.797	1005.561	0.994	5	24
N117_AA	0.3681	0.3315	0.0366	11.0273	6.4037	1045.8675	0.9561	5	72
N117_AB	0.3591	0.3168	0.0423	13.3447	8.1584	1101.0599	0.9082	5	24
N117_AC	0.2221	0.2013	0.0208	10.3428	6.2185	1082.8402	0.9235	5	48
N117_AD	0.3901	0.3507	0.0394	11.2318	6.8994	1106.3091	0.9039	15	24
N117_AE	0.2851	0.2549	0.0302	11.8351	7.3634	1120.5275	0.8924	15	72
N117_AF	0.4239	0.3803	0.0436	11.4567	6.9693	1095.5708	0.9128	15	48
N117_AG	0.3389	0.3014	0.0376	12.4705	7.6363	1102.8362	0.9068	30	24
N117_AH	0.4737	0.4320	0.0418	9.6652	5.9364	1106.1716	0.9040	30	48
N117_AI	0.3587	0.3220	0.0367	11.4082	6.9724	1100.7179	0.9085	30	72
N117_AJ	0.3859	0.3544	0.0315	8.8893	5.4614	1106.5105	0.9037	10	24
N117_AK	0.4596	0.4204	0.0392	9.3221	5.7203	1105.1525	0.9049	10	48
N117_AL	0.2662	0.2457	0.0206	8.3774	4.7415	1019.3361	0.9810	10	72
N117_AM	0.1851	0.1536	0.0315	20.5183	12.4747	1094.9733	0.9133	10	48
N117_AN	0.2102	0.1773	0.0329	18.5459	11.1235	1080.2133	0.9257	5	72
N117_AO	0.2057	0.1742	0.0315	18.1077	11.2098	1114.9304	0.8969	30	72
N117_AP	0.3151	0.2673	0.0478	17.8750	10.8840	1096.6154	0.9119	10	48
N117_AQ	0.2465	0.2107	0.0358	17.0037	10.4817	1110.1976	0.9007	5	72
N117_AR	0.3320	0.2841	0.0479	16.8685	10.5533	1126.7427	0.8875	5	24
N117_AS	0.0935	0.0796	0.0139	17.4416	10.5033	1084.5656	0.9220	5	48

6.4 Annexure D: Recent Development in Hydrocarbon-Based PEMs

Table 26: A comparison of physicochemical properties of fluorinated and hydrocarbon-based PEMs
(Reprint from [1] with permission from KeAi publishing under CC BY-NC-ND license: https://creativecommons.org/licenses/by-nc-nd/4.0/)

Membrane		Water Uptake %	Swelling ratio (%)	Oxidative stability			Tensile strength (MPa)	Conductivity ($mS.cm^{-1}$)	Ref.
				Breaking time (h)	Dissolve time (h)	Residual weight (%)			
Commercial perfluorosulfonic acid membranes	Nafion 115	38	10	-	-	-	43	≥100	[2]
	Nafion 211	50.0 ±5.0	10	-	-	-	23	60 ±5	[2]
Commercial hydrocarbon membrane	PF1-HLF8-15-X (Pemion)	110-140	<7	-	-	-	>50	>90	[3]
Main-chain-type hydrocarbon membranes with ether and ketone units	SPDPEKK-7	>30	15.2	4.2	8.7	-	48	125	[4]
	SP-BNP-10	12.2	4.6	3	6	-	63	103	[5]
	tCr-SPEK	62.1	11.9	6.5	-	-	42.2	146.7	[6]
	Hex-BP-2	-	-	-	-	91	25.9	>100	[7]
	SPAESK-15	85.6	<50	3	-	97.5	43.72	181.0	[8]
	tt-SPAE-1.94	61.4	20.9	6	-	96.1	51.8	77.0	[9]
	SPAES/ATP/P–CNOs-2	68	10.5	-	-	98.4	39.5	195.6	[10]
	SPAES-2CST3	43.9	5.9	5.03	-	99.8	52.9	128.1	[11]
	SPAES/SP-CNOs-1.5	65.3	11.3	3.27	-	98.8	>30	181.2	[12]
	C-SPAEKS/IUSN-3%	44.24	29.37	-	-	96.97	48.67	234	[13]
	Si-SPEEK(0.8wt%)	80.91	78.65			96	23.73	23.5	[14]
	SCTF-7.5@SPP-3	>30	<28			99	24	139	[15]
	SPAES/D-sPOSS-2	>60	<20	2.9	-	-	60.01	243	[16]
	SPEEK/0.1 OH-BN	39.153	16.237	-	-	95.817	43.3	25.057	[17]
	1.3%NU6@PPNF-SPEEK	>22.5	14	-	-	82.8	23.8	133	[18]
	SPEEK/ZCN-2.5	40.2	8.6	-	-	-			[19]
	SPEEK-co-PEK-75	>14	2.5	2	-	95.33	47.66	173	[20]
	t-SPEEK/SPAES(1:2:2)	52.7	13.9	2.45	4	-	46	149.6	[21]
Main-chain-type	sPBT-E62.5/SGO3	>55	12.3	5.2	-	94.2	68.5	139	[22]

Table 26: A comparison of physicochemical properties of fluorinated and hydrocarbon-based PEMs
(Reprint from [1] with permission from KeAi publishing under CC BY-NC-ND license: https://creativecommons.org/licenses/by-nc-nd/4.0/)

Membrane		Water Uptake %	Swelling ratio (%)	Oxidative stability			Tensile strength (MPa)	Conductivity (mS.cm^{-1})	Ref.
				Breaking time (h)	Dissolve time (h)	Residual weight (%)			
hydrocarbon membranes with aromatic heterocyclic compounds	MSOPBI	11	1.52	-	-	-	62.6	7	[23]
	SPI-B40	4836	29.7	-	24	97.2	102.76	146	[24]
	3wt% Cu-TMA/sABPBI	21.58	10	-	-	>89	7.7	39	[25]
	S-PBI-100	32.7	5.8	-	-	-	246.0	-	[26]
Main-chain-type hydrocarbon membranes with aromatic compounds	NEXAR-1.5	29.0	-	-	-	-	-	250	[27]
	SPP-QP	-	-	-	-	99	40.8	220	[28]
	SPP-BP (No. 4)	-	-	-	-	99	42.6	-	[29]
	P(AA-*alt*-*m*TP)	50	-	-	-	-	80	5	[30]
	sPPB-H+	119.2	77.7	-	-	99.31	59.6	172	[31]
	sPPN-H+	183.3	109.9	-	-	99.91	53.3	268	[31]
Non-fluorinated microphase separation membranes	HF3DP1-PS	40	21	-	-	>80	15.5	88.56	[32]
	Gel-PBI-PS-3	-	-	-	-	>70	47.1	162	[33]
	SPBPI-0.10M	>40	>8	-	-	94	>30	>150	[34]
	PBI-PS 200%	41	13	-	-	-	34	-	[35]
	PTMIm-C3-QA	10.6	-	250	-	-	31.7	-	[36]
	PC-SBPIMs-0.10	-	-	-	-	>90	-	200	[37]
Membranes with rigid-twisted structure	sPIM-SBF-1.40	61.5	15.6	-	-	-	46.4	19.5 [a]	[38]
	SCTF-BP	-	<5	-	-	-	29	54.9[a]	[39]
	SPDI-100	-	13.5	-	-	98.2	37.5	233	[40]

[a] Refers to ion conductivity of K^+

Bibliography

(1) Song, P.; Zhang, Y.; Zhang, X.; Liu, J.; Wu, L.; Fisher, A. C.; An, Q.-F. Recent progress on the development of non-fluorinated proton exchange membrane-A review. *Green Energy & Environment* **2025**. DOI: https://doi.org/10.1016/j.gee.2025.03.003.

(2) Products, N. *Nafion™ Membranes, Dispersions, and Resins*. https://www.nafion.com/en/products (accessed 2025 15 April).

(3) Inc., P. P. E. M. I. I. *Durable, High Performance Cation Exchange*. https://ionomr.com/solutions/pemion/ (accessed 2025 15 April).

(4) Liu, Q.; Zhang, S.; Sun, F.; Xu, P.; Wang, C.; Zhuo, L.; Li, Z.; Niu, K.; Wang, Z.; Jian, X. Proton exchange membrane deriving from sulfonated N-heterocyclic poly(aryl ether ketone)s containing ether-free proton conducting units and performing enhanced physicochemical stability and conduction properties. *Journal of Membrane Science* **2024**, *694*, 122402. DOI: https://doi.org/10.1016/j.memsci.2023.122402.

(5) Liu, Q.; Li, X.; Zhang, S.; Wang, Z.; Chen, Y.; Zhou, S.; Wang, C.; Wu, K.; Liu, J.; Mao, Q.; et al. Novel sulfonated N-heterocyclic poly(aryl ether ketone ketone)s with pendant phenyl groups for proton exchange membrane performing enhanced oxidative stability and excellent fuel cell properties. *Journal of Membrane Science* **2022**, *641*, 119926. DOI: https://doi.org/10.1016/j.memsci.2021.119926.

(6) Liu, D.; Xie, Y.; Zhong, J.; Yang, F.; Pang, J.; Jiang, Z. High methanol resistance semi-crystalline sulfonated poly(ether ketone) proton exchange membrane for direct methanol fuel cell. *Journal of Membrane Science* **2022**, *650*, 120413. DOI: https://doi.org/10.1016/j.memsci.2022.120413.

(7) Kyeong, M.; Chae, J. E.; Lee, S. Y.; Lim, T.-H.; Kim, M.; Lee, S.-S.; Song, K. H.; Kim, H.-J. Development of Poly(Arylene ether Sulfone)-Based blend membranes containing aliphatic moieties for the low-temperature decal transfer method. *Journal of Membrane Science* **2022**, *660*, 120853. DOI: https://doi.org/10.1016/j.memsci.2022.120853.

(8) Zhao, Z.; Liu, D.; Zhong, J.; Li, J.; Lin, Z.; Zhao, Z.; Pang, J. Poly(aryl ether sulfone ketone) with densely sulfonated structural units facilitate microphase separation to promote proton transport. *Journal of Membrane Science* **2024**, *693*, 122319. DOI: https://doi.org/10.1016/j.memsci.2023.122319.

(9) Liu, D.; Xie, Y.; Cui, N.; Han, X.; Zhang, J.; Pang, J.; Jiang, Z. Structure and properties of sulfonated poly(arylene ether)s with densely sulfonated segments containing mono-, di- and tri-tetraphenylmethane as proton exchange membrane. *Journal of Membrane Science* **2021**, *620*, 118856. DOI: https://doi.org/10.1016/j.memsci.2020.118856.

(10) Liu, L.; Wang, Y.; Liu, S.; Li, N.; Hu, Z.; Chen, S. Novel bifunctional fillers (ATP/P–CNOs) for sulfonated poly(aryl ether sulfone) matrix for improved power output and durability of H2/O2 fuel cell at low humidity. *Journal of Membrane Science* **2022**, *660*, 120774. DOI: https://doi.org/10.1016/j.memsci.2022.120774.

(11) Liu, L.; Pu, Y.; Lu, Y.; Li, N.; Hu, Z.; Chen, S. Superacid sulfated SnO2 doped with CeO2: A novel inorganic filler to simultaneously enhance conductivity and stabilities of proton exchange membrane. *Journal of Membrane Science* **2021**, *621*, 118972. DOI: https://doi.org/10.1016/j.memsci.2020.118972.

(12) Liu, L.; Lu, Y.; Pu, Y.; Li, N.; Hu, Z.; Chen, S. Highly sulfonated carbon nano-onions as an excellent nanofiller for the fabrication of composite proton exchange membranes with enhanced water retention and durability. *Journal of Membrane Science* **2021**, *640*, 119823. DOI: https://doi.org/10.1016/j.memsci.2021.119823.

(13) Chen, X.; Ren, Q.; Xu, J.; Ju, M.; Meng, L.; Wang, Z. Design, transport efficiency and structure-activity relationship of sulfonated poly (aryl ether ketone) proton exchange membrane based on multi-functional MOFs. *Electrochimica Acta* **2023**, *469*, 143210. DOI: https://doi.org/10.1016/j.electacta.2023.143210.

(14) Sharma, V.; Upadhyay, P.; Rathod, N. H.; Sharma, J.; Mishra, S.; Raj, S. K.; Kishore, V.; Kulshrestha, V. Silica modified sulphonated Poly(ether ether ketone) proton exchange membranes for DMFC application. *International Journal of Hydrogen Energy* **2023**, *48* (96), 37784-37795. DOI: https://doi.org/10.1016/j.ijhydene.2022.11.146.

(15) Cui, W.; Zhou, S.; Bai, J.; Qian, H.; Zheng, J.; Li, S.; Zhang, S. SCTF nanosheets@sulfonated poly (p-phenylene-co-aryl ether ketone) composite proton exchange membranes for passive direct methanol fuel cells. *International Journal of Hydrogen Energy* **2021**, *46* (69), 34344-34355. DOI: https://doi.org/10.1016/j.ijhydene.2021.07.218.

(16) Zhang, P.; Li, W.; Wang, L.; Gong, C.; Ding, J.; Huang, C.; Zhang, X.; Zhang, S.; Wang, L.; Bu, W. Polydopamine-modified sulfonated polyhedral oligomeric silsesquioxane: An appealing nanofiller to address the trade-off between conductivity and stabilities for proton exchange membrane. *Journal of Membrane Science* **2020**, *596*, 117734. DOI: https://doi.org/10.1016/j.memsci.2019.117734.

(17) Michel Myures, X.; Suresh, S.; Arthanareeswaran, G. Construction of thermal, chemical and mechanically stable ion exchange membranes with improved ion selectivity for vanadium redox flow batteries applications. *Journal of Power Sources* **2024**, *591*, 233818. DOI: https://doi.org/10.1016/j.jpowsour.2023.233818.

(18) Zhu, B.; Sui, Y.; Wei, P.; Wen, J.; Cao, H.; Cong, C.; Meng, X.; Zhou, Q. NH2-UiO-66 coated fibers to balance the excellent proton conduction efficiency and significant dimensional

stability of proton exchange membrane. *Journal of Membrane Science* **2021**, *628*, 119214. DOI: https://doi.org/10.1016/j.memsci.2021.119214.

(19) Sun, H.; Tang, B.; Wu, P. Two-Dimensional Zeolitic Imidazolate Framework/Carbon Nanotube Hybrid Networks Modified Proton Exchange Membranes for Improving Transport Properties. *ACS Applied Materials & Interfaces* **2017**, *9* (40), 35075-35085. DOI: 10.1021/acsami.7b13013.

(20) Li, J.; Cui, N.; Liu, D.; Zhao, Z.; Yang, F.; Zhong, J.; Pang, J. SPEEK-co-PEK-x proton exchange membranes with controllable sulfonation degree for proton exchange membrane fuel cells. *International Journal of Hydrogen Energy* **2024**, *50*, 606-617. DOI: https://doi.org/10.1016/j.ijhydene.2023.08.334.

(21) Haragirimana, A.; Li, N.; Hu, Z.; Chen, S. A facile, effective thermal crosslinking to balance stability and proton conduction for proton exchange membranes based on blend sulfonated poly(ether ether ketone)/sulfonated poly(arylene ether sulfone). *International Journal of Hydrogen Energy* **2021**, *46* (29), 15866-15877. DOI: https://doi.org/10.1016/j.ijhydene.2021.02.022.

(22) Wang, G.; Yang, S.; Kang, N. Y.; Lu, M.; Hua, B.; Wei, H.; Kang, J.; Tang, W.; Lee, Y. M. Sulfonated graphene oxide doped sulfonated polybenzothiazoles for proton exchange membrane fuel cells. *Journal of Membrane Science* **2023**, *668*, 121239. DOI: https://doi.org/10.1016/j.memsci.2022.121239.

(23) Subhadarshini, S.; Sravan, J. S.; Sarkar, O.; Venkata Mohan, S.; Roy, T. K.; Jana, T. Sulfonated Polybenzimidazole as a PEM in a Microbial Fuel Cell: An Efficient Strategy for Green Energy Generation and Wastewater Cleaning. *ACS Applied Energy Materials* **2023**, *6* (3), 1422-1438. DOI: 10.1021/acsaem.2c03238.

(24) Yang, J.; Guo, Y.; Liu, L.; Guo, L.; Sun, Z.; Wang, C. Preparation of proton exchange membrane with intrinsic micropores constructing efficient ion transport channels based on segmented copolymer (sulfonated polyimide). *Journal of Energy Storage* **2023**, *72*, 108407. DOI: https://doi.org/10.1016/j.est.2023.108407.

(25) Moorthy, S.; Maria Mahimai, B.; Kannaiyan, D.; Deivanayagam, P. Synthesis and fabrication of Cu-trimesic acid MOF anchored sulfonated Poly(2,5-benzimidazole) membranes for PEMFC applications. *International Journal of Hydrogen Energy* **2023**, *48* (92), 36063-36075. DOI: https://doi.org/10.1016/j.ijhydene.2023.05.362.

(26) Wang, Y.; Geng, K.; Tan, Q.; Guo, T.; Hu, X.; Tang, H.; Liu, L.; Li, N. Highly Ion Selective Proton Exchange Membrane Based on Sulfonated Polybenzimidazoles for Iron–Chromium Redox Flow Battery. *ACS Applied Energy Materials* **2022**, *5* (12), 15918-15927. DOI: 10.1021/acsaem.2c03471.

(27) Hwang, M.; Nixon, K.; Sun, R.; Willis, C.; Elabd, Y. A. Sulfonated pentablock terpolymers as membranes and ionomers in hydrogen fuel cells. *Journal of Membrane Science* **2021**, *633*, 119330. DOI: https://doi.org/10.1016/j.memsci.2021.119330.

(28) Miyake, J.; Taki, R.; Mochizuki, T.; Shimizu, R.; Akiyama, R.; Uchida, M.; Miyatake, K. Design of flexible polyphenylene proton-conducting membrane for next-generation fuel cells. *Science Advances* **2017**, *3* (10), eaao0476. DOI: doi:10.1126/sciadv.aao0476.

(29) Shiino, K.; Miyake, J.; Miyatake, K. Highly stable polyphenylene ionomer membranes from dichlorobiphenyls. *Chemical Communications* **2019**, *55* (49), 7073-7076, 10.1039/C9CC02475A. DOI: 10.1039/C9CC02475A.

(30) Künzel-Tenner, A.; Kirsch, C.; Dolynchuk, O.; Rößner, L.; Wach, M.; Kempe, F.; von Unwerth, T.; Lederer, A.; Sebastiani, D.; Armbrüster, M.; et al. Proton-Conducting Membranes from Polyphenylenes Containing Armstrong's Acid. *Macromolecules* **2024**, *57* (3), 1238-1247. DOI: 10.1021/acs.macromol.3c02123.

(31) Adamski, M.; Skalski, T. J. G.; Britton, B.; Peckham, T. J.; Metzler, L.; Holdcroft, S. Highly Stable, Low Gas Crossover, Proton-Conducting Phenylated Polyphenylenes. *Angewandte Chemie International Edition* **2017**, *56* (31), 9058-9061. DOI: https://doi.org/10.1002/anie.201703916 (acccessed 2025/04/15).

(32) Xu, F.; Chen, Y.; Li, J.; Han, Y.; Lin, B.; Ding, J. Robust poly(alkyl–fluorene isatin) proton exchange membranes grafted with pendant sulfonate groups for proton exchange membrane fuel cells. *Journal of Membrane Science* **2022**, *664*, 121045. DOI: https://doi.org/10.1016/j.memsci.2022.121045.

(33) Zhu, T.; Zhu, D.; Liang, J.; Zhang, L.; Huang, F.; Xue, L. Gel-state polybenzimidazole proton exchange membranes with flexible alkyl sulfonic acid side chains for a wider operating temperature range (25–240 °C). *Journal of Energy Chemistry* **2023**, *85*, 91-101. DOI: https://doi.org/10.1016/j.jechem.2023.05.045.

(34) Shen, X.; Liang, X.; Xu, Y.; Yu, W.; Li, Q.; Ge, X.; Wu, L.; Xu, T. In-situ growth of PPy/MnOx radical quenching layer for durability enhancement of proton exchange membrane in PEMFCs. *Journal of Membrane Science* **2023**, *675*, 121556. DOI: https://doi.org/10.1016/j.memsci.2023.121556.

(35) Yan, X.; Dong, Z.; Di, M.; Hu, L.; Zhang, C.; Pan, Y.; Zhang, N.; Jiang, X.; Wu, X.; Wang, J.; et al. A highly proton-conductive and vanadium-rejected long-side-chain sulfonated polybenzimidazole membrane for redox flow battery. *Journal of Membrane Science* **2020**, *596*, 117616. DOI: https://doi.org/10.1016/j.memsci.2019.117616.

(36) Mu, T.; Tang, W.; Shi, N.; Wang, G.; Wang, T.; Wang, T.; Yang, J. Novel ether-free membranes based on poly(p-terphenylene methylimidazole) for vanadium redox flow

battery applications. *Journal of Membrane Science* **2022**, *659*, 120793. DOI: https://doi.org/10.1016/j.memsci.2022.120793.

(37) Xu, Y.; Liang, X.; Shen, X.; Yu, W.; Yang, X.; Li, Q.; Ge, X.; Wu, L.; Xu, T. In situ construction of ultra-thin PANI/CeOx layer on proton exchange membrane for enhanced oxidation resistance in PEMFC. *Journal of Membrane Science* **2024**, *689*, 122167. DOI: https://doi.org/10.1016/j.memsci.2023.122167.

(38) Ye, C.; Wang, A.; Breakwell, C.; Tan, R.; Grazia Bezzu, C.; Hunter-Sellars, E.; Williams, D. R.; Brandon, N. P.; Klusener, P. A. A.; Kucernak, A. R.; et al. Development of efficient aqueous organic redox flow batteries using ion-sieving sulfonated polymer membranes. *Nature Communications* **2022**, *13* (1), 3184. DOI: 10.1038/s41467-022-30943-y.

(39) Zuo, P.; Ye, C.; Jiao, Z.; Luo, J.; Fang, J.; Schubert, U. S.; McKeown, N. B.; Liu, T. L.; Yang, Z.; Xu, T. Near-frictionless ion transport within triazine framework membranes. *Nature* **2023**, *617* (7960), 299-305. DOI: 10.1038/s41586-023-05888-x.

(40) Wang, Q.; Huang, L.; Guan, J.; Sang, L.; Zheng, J.; Zhang, Q.; Qin, G.; Li, S.; Zhang, S. Side chain sulfonic acid polymers with intrinsic pores in the main chain as proton exchange membranes for fuel cells and redox flow battery. *Journal of Membrane Science* **2023**, *687*, 122036. DOI: https://doi.org/10.1016/j.memsci.2023.122036.